Theoretical and observational aspects of relativistic cosmology

Di Dio, Enea

UNIVERSITÉ DE GENÈVE
Section de Physique
Département de Physique théorique

FACULTÉ DES SCIENCES
Professeure Ruth DURRER

Theoretical and Observational Aspects of Relativistic Cosmology

THÈSE

présentée à la Faculté des sciences de l'Université de Genève
pour obtenir le grade de
Docteur ès sciences, mention physique

par

Enea DI DIO

de

Vogorno (TI)

Thèse N° 4704

GENÈVE

Atelier de reproduction de la Section de Physique
2014

Abstract

Durant ma thèse j'ai travaillé sur des aspects théoriques et observationnels de la cosmologie relativiste. D'un point de vue théorique, j'ai considéré deux possibles solutions au problème de l'énergie sombre: les effets des inhomogénéités induits, par rétroaction, sur des échelles cosmologiques, et l'introduction d'un champ scalaire qui peut expliquer l'accélération de l'expansion de l'univers. Du côté observationnel, j'ai étudié la distribution des galaxies en fonction des quantités réellement observables et considérant tous les effets relativistes au premier ordre dans la théorie des perturbations. J'ai analysé avec quelle précision de futures expériences pourront estimer les paramètres cosmologiques et j'ai calculé la contribution des différents effets à la distribution des galaxies.

Remerciements

En premier lieu, je tiens à remercier ma directrice de thèse Ruth Durrer. Grâce à sa disponibilité et compréhension, j'ai eu l'énorme, et probablement unique, chance de bénéficier de toutes ses compétences scientifiques. Voir sa passion pour la physique, son désir de comprendre les phénomènes fondamentaux, a été très motivant pour moi. En particulier, je suis reconnaissant de la façon dont elle m'a supervisé pendant ma thèse, en me montrant comme avancer dans la recherche, mais en même temps, sans me priver de ma liberté. Au-delà du côté scientifique, elle s'est toujours engagée pour maintenir une ambiance très agréable dans tout le groupe de cosmologie.

Je tiens aussi à remercier toutes les personnes avec qui j'ai collaboré pendant ces quatre ans: Julian Adamek, Jose Beltran Jimenez, Martin Kunz, Julien Lesgourgues, Giovanni Marozzi, Francesco Montanari et Marc Vonlanthen. J'ai eu la chance de travailler et discuter avec eux.

J'aimerais également remercier tous les membres du groupe de cosmologie qui ont créé un ambiance agréable, sans oublier les deux secrétaires du département, Francine Gennai-Nicole et Cécile Jaggi, qui ont été toujours disponibles. Je ne peux manquer de citer mes amis qui ont rendu inoubliables ces dernières années: Francesco, Giovanni, Guillermo, Hidéki, Jose, Kwan, Marc et Matteo. En particulier, je dois un remerciement spécial à Hidéki qui a corrigé l'introduction en français de ma thèse.

Enfin, je veux remercier de cœur Alba pour son soutien, sa compréhension, son aide dans tous les moments. Avec sa présence tout est paru plus simple, et sans doute, plus agréable.

Examinateurs

Le jury de cette thèse se compose de

- Prof. Ruth Durrer, Université de Genève, Suisse.
- Dr. Martin Kunz, Université de Genève, Suisse.
- Prof. Julien Lesgourgues, EPFL Lausanne and CERN Genève, Suisse.
- Prof. Alexandre Refregier, ETH Zürich, Suisse.

Je les remercie d'avoir accepté de faire partie du jury et surtout d'avoir consacré du temps à la lecture de ma thèse.

Résumé

La cosmologie est la science qui étudie l'univers dans son ensemble. Elle pose ses fondations sur la théorie de la Relativité Générale pour décrire la force de gravitation et sur le Modèle Standard des particules pour la matière. Ces deux théories ont été confirmées par différentes expériences et observations et sont, sans doute, les plus importantes conquêtes de la physique théorique du XX^{e} siècle. Cependant, quelques observations cosmologiques ne concordent pas avec les prédictions théoriques. Afin de développer un modèle cosmologique consistant avec toutes les observations il est nécessaire de modifier, ou d'étendre, au moins une de ces théories. À ce jour, toutes les observations convergent vers le modèle ΛCDM, qui décrit un univers homogène et isotrope, sans courbure, avec une constante cosmologique Λ et de la matière sombre (Cold Dark Matter). Le besoin d'introduire la matière sombre, notamment un type de matière non-relativiste insensible à la force électromagnétique, s'est présenté déjà en 1933 lorsque Zwicky [1] a mesuré la vitesse des galaxies de l'Amas de Coma, et montré que la matière lumineuse n'était pas suffisante pour justifier ces vitesses. En 1998, deux collaborations ont mesuré la distance lumineuse avec des supernovae [2, 3, 4], et montré que l'univers n'est pas seulement en expansion, mais également que l'expansion est en train d'accélérer. Cet effet répulsif de la gravité ne peux pas être expliqué par de la matière ordinaire. La solution la plus simple consiste à introduire une constante cosmologique, Λ, dans les équations d'Einstein. Ce terme est compatible avec les symétries de la Relativité Générale et il est équivalent à un type de matière satisfaisant $\rho = -p$. Grâce à cette pression négative de la constante cosmologique, la force gravitationnelle agit de façon répulsive et produit une accélération.

Si d'un point de vue observationnel, l'introduction de la constante cosmologique est bien motivée, elle est complètement énigmatique du point de vue théorique. En effet, la valeur mesurée est plus petite de plusieurs ordres de magnitude que ce qu'on attendrait naïvement de la contribution des fluctuations quantiques du vide. Après la mesure de la distance lumineuse des supernovae, différents modèles ont été considérés pour expliquer l'accélération de l'expansion de l'univers. Généralement, ces modèles n'essaient pas d'expliquer pour quelle raison la valeur mesurée est si petite.

L'espoir est que des effets quantiques puissent annuler la contribution de l'énergie du vide. Dans cette perspective, il faut trouver un autre mécanisme physique qui puisse produire la récente accélération. Les différentes tentatives peuvent être classifiées en trois catégories. La première possibilité consiste à introduire un nouveau degré de liberté, généralement décrit par un champ scalaire avec une pression négative, qui produit la récente accélération de l'univers. On parle dans ce cas d'énergie sombre (Dark Energy). Une autre approche étudie la possibilité de modifier la théorie de la Relativité Générale à grandes échelles. Une force gravitationnelle plus faible à des échelles cosmologiques peut induire une accélération de l'expansion de l'univers. La troisième idée, plus conservatrice, est fondée sur le fait que l'univers est homogène en moyenne, mais qu'il est fortement perturbé à petites échelles. Ces perturbations peuvent reproduire, par rétroaction (Back-Reaction), une (apparente) accélération sur des échelles cosmologiques. Cet effet peut se produire parce que les équations d'Einstein ne sont pas linéaires et elles ne commutent donc pas avec la moyenne.

Dans ma thèse, j'ai pris en considération surtout cette dernière idée. J'ai considéré [5] un modèle avec une symétrie plane et une distribution inhomogène de matière non-relativiste le long d'une direction. Clairement, ce modèle n'est pas réaliste, mais grâce à ses symétries il possède des solutions aux équations d'Einstein. J'ai étudié comment les perturbations peuvent modifier la propagation de la lumière et donc la distance lumineuse dans un régime complètement relativiste. J'ai trouvé que la distance est perturbée autour de la valeur de fond, mais elle ne manifeste pas d'effet global qui peut être confondu avec l'énergie sombre. À cause de l'absence de pression dans la matière non-relativiste, tous les profils de densité réalistes forment des singularités. Pour cette raison, je me suis limité à des petites amplitudes initiales des perturbations. Pour éliminer cette limitation j'ai réétudié [6] ce modèle utilisant un nouveau code numérique relativiste [7] qui peut traiter correctement la distribution de matière, évitant la formation des singularités. Ces projets m'ont permis de conclure que, si les résultats de ce modèle peuvent être généralisés, les effets de rétroaction (Back-Reaction) ne sont pas suffisants pour expliquer l'accélération de l'expansion de l'univers. Cependant, ces effets sont certainement présents et on doit les prendre attentivement en considération. Ces dernières années, les fluctuations de la distance lumineuse au premier ordre dans la théorie des perturbations autour d'une métrique de fond homogène et isotrope (FLRW) ont été calculées [8, 9, 10], montrant que les fluctuations sont deux ordres de grandeur plus grands que ce qu'on aurait pu imaginer naïvement. Des calculs au deuxième ordre [11] ont aussi montré des fluctuations de même amplitude. Dans ma thèse, j'ai dérivé la contribution aux fluctuations de la distance lumineuse induites par des perturbations vectorielles et tensorielles [12]. J'ai appliqué ce formalisme à un spectre primordial de perturbations tensorielles et montré que l'effet sur la distance est beaucoup plus petit que celui induit par les perturbations scalaires. Ceci s'explique par le fait que les perturbations tensorielles décroissent quand elles entrent dans l'horizon, tandis que les perturbations scalaires grandissent. Puisque l'effet des perturbations tensorielles au première ordre est si petit, on s'attend à ce que la plus grande contribution vienne des perturbations tensorielles au deuxième ordre générées à partir des perturbations

scalaires au premier ordre. Ce résultat peut être pertinent dans les récentes analyses des fluctuations de la distance lumineuse au deuxième ordre [13, 14].

Dans un autre projet [15], j'ai étudié le comportement et la quantification d'une théorie, le champ de Pais-Uhlenbeck [16], avec deux dérivées temporelles dans le lagrangien. Contrairement à ce que l'on puisse penser naïvement, on a montré que cette théorie peut être quantifiée en éliminant, du spectre des états physiques, les instabilités liées au théorème d'Ostrogorsky. On a introduit le champ de Pais-Uhlenbeck comme champ de Stückelberg pour restaurer l'invariance de jauge dans l'action d'un champ vectoriel sans masse avec un terme cinétique non-standard. Cela m'a permis d'identifier la composante longitudinale du champ vectoriel avec le champ de Pais-Uhlenbeck. De plus, interpréter le champ de Pais-Uhlenbeck comme un champ de Stückelberg m'a permis de considérer le champ de Pais-Uhlenbeck comme le médiateur de l'interaction de jauge. Cette interaction naturelle amène une dynamique pour le champ de Pais-Uhlenbeck indépendamment des champs scalaires ou fermioniques aux quels il est couplé. Grâce à cette propriété, on peut être sûr que les problèmes d'instabilité ne sont pas réintroduits par l'interaction, une fois qu'ils ont été éliminés de la théorie libre. J'ai aussi vu que le champ de Pais-Uhlenbeck peut avoir une importance cosmologique. En effet, il induit une constante cosmologique effective dont la valeur est liée à l'échelle énergétique de l'inflation. En étudiant l'influence des perturbations du champ de Pais-Uhlenbeck sur les observables cosmologiques, on a la possibilité de distinguer ce modèle d'énergie sombre de la constante cosmologique.

Après les incroyables succès obtenus par les observations du fond diffus cosmologique (CMB), plusieurs expériences destinées à mesurer la distribution des structures à grandes échelles vont nous fournir la possibilité d'étudier la nature de l'énergie sombre dans les années qui viennent. On est en train de s'approcher de l'ère de la cosmologie de précision. Une précision de l'ordre du pour-cent sur les paramètres cosmologiques nous permettra de distinguer les différents modèles. Afin d'obtenir cette précision, il faudra non seulement dessiner des expérience meilleures, mais également développer un formalisme théorique fondé sur les quantités vraiment observables et des instruments numériques pour calculer et comparer les prédictions théoriques avec les observations.

Récemment, un nouveau formalisme pour décrire la distribution des galaxies en fonction des quantités réellement observables, comme la direction angulaire et le *redshift* (décalage vers le rouge), a été développé [17, 18]. Pour calculer les observables de la structure à grande échelle, j'ai donc développé un code numérique CLASSgal [19], à partir d'un code de Boltzmann, CLASS [20], écrit surtout pour calculer les anisotropies du fond diffus cosmologique. Grâce à CLASSgal j'ai analysé avec quelle précision de futures expériences pourront estimer les paramètres cosmologiques. En particulier j'ai montré que cette méthode, qui utilise uniquement des quantités réellement observables, est compétitive par rapport à la méthode traditionnellement utilisée. De plus, la méthode traditionnelle néglige des effets, qui pouvaient être négligés pour des experiences à petites échelles, mais qui pourront être

significatifs en future. J'ai également calculé la contribution des différents termes à la distribution des galaxies, et montré que le terme qui décrit l'effet de lentille gravitationnelle faible devient important pour des expériences qui vont jusqu'à des grands *redshifts*. Cette constatation nous permettra d'utiliser les expériences futures pour tester des modèles de gravité modifiée qui prévoient souvent une différence entre les deux potentiels de Bardeen. Puisque la contribution du terme qui décrit l'effet de lentille gravitationnelle faible devient important indépendamment de la résolution de l'expérience, je pense qu'il est possible d'appliquer cette idée aux présents catalogues de radiogalaxies.

Liste de publications

- E. Di Dio, M. Vonlanthen and R. Durrer, *Back Reaction from Walls*, JCAP **1202** (2012) 036, [arXiv:1111.5764]
- E. Di Dio and R. Durrer, *Vector and Tensor Contributions to the Luminosity Distance*, Phys. Rev. **D86** (2012) 023510, [arXiv:1205.3366]
- J. B. Jimenez, E. Di Dio and Ruth Durrer, *A longitudinal gauge degree of freedom and the Pais Uhlenbeck field*, JHEP **1304** (2013) 030, [arXiv:1211.0441]
- E. Di Dio, F. Montanari, J. Lesgourgues and R. Durrer, *The* CLASS*gal code for Relativistic Cosmological Large Scale Structure*, JCAP **1311** (2013) 044, [arXiv:1307.1459]
- E. Di Dio, F. Montanari, R. Durrer and J. Lesgourgues, *Cosmological Parameter Estimation with Large Scale Structure Observations*, JCAP **1401** (2014) 042 , [arXiv:1308.6186]
- J. Adamek, E. Di Dio, R. Durrer and M. Kunz, *The distance redshift relation in plane symmetric Universes*, Phys. Rev. **D89** (2014) 063543 , [arXiv:1401.3634]

Contents

1

Introduction

Cosmology is the science which studies the universe as a whole, describing its dynamical evolution. In the history of the humanity, different civilizations had been interested and amazed by the perfection and periodicity of the events on the celestial sphere. They had a good knowledge about the motion of the planets and the stars, but their explanations were completely based on mythology and religion. The first attempts to explain the astronomical observations with a rational approach (even if yet not scientific) are attributed to the ancient Greeks. Aristotle's geocentric model has been adopted and used for many centuries until the Copernican revolution[1] in 16th century. Modern cosmology has been developed starting from the first decades of 20th century. In 1915 Einstein published [21] the theory of General Relativity which describes the gravity geometrically and determines how the geometry is coupled to the energy density. Only two years later, he applied his theory of gravity to the whole universe[2]. He was convinced that the universe were static and so he introduced in his equations the famous cosmological constant [23] to find a static solution. The same year de Sitter [24] proposed an alternative solution to Einstein's field equations describing an universe without matter. A few years later, Friedmann found the first cosmological solution [25] to Einstein's field equations, describing an expanding homogenous and isotropic universe. The Friedmann prediction had been experimentally confirmed first [26] by Lemaître[3] in 1927 and then [33] by Hubble in

[1] We often forget that, already in the ancient Greece, Aristarchus developed a heliocentric model.

[2] At that time there was a controversy, the so called Great Debate or Shapley–Curtis Debate, about the size of our universe and the nature of galaxies, until Hubble, in 1925, measured [22] the distance to Andromeda prooving that it was an independent galaxy.

[3] The first redshift measurements had been performed [27] by Slipher in 1913. He interpreted them as radial velocities through the Doppler effect. Wirtz [28] in 1922 noticed that the recession velocities of nebulae could be described as a dispersion motion with respect to our position. Then, in 1924 [29] he gave the first cosmological interpretation of the redshift measurements trying to fit the predicted redshift of de Sitter's model [24]. Lemaître was unaware of the Friedmann results, and he re-derived his dynamical solutions to Einstein's field equations. By using the Slipher redshift [30] and the Hubble distance measurements [31] he confirmed his prediction for a linear relation between the radial velocities and the distances of galaxies. He was the first one who suggested and supported with observational data the concept of the expanding universe. Interesting details about the history of the discovering of the expanding universe can be found in [32].

1929. In 1932, a decade after Friedmann's publication [25], Einstein and de Sitter accepted the idea of the expanding universe and they wrote a two-page paper [34] describing the so-called Einstein-de Sitter model which has been adopted as cosmological model until the end of 20th century. During the same decades also particle physics had been revolutionized by the rising of quantum mechanics which will lead in the second half of the century to the Standard Model of particle physics.

Modern cosmology is based on the two following pillars: the theory of General Relativity, to describe the gravitational force, and the Standard Model of particle physics for the matter sector. These two pillars are independently very solid, having passed many different experimental tests. Nevertheless some cosmological observations do not agree with their theoretical predictions. The first puzzling problem had been revealed by Zwicky already in 1933. By measuring the amount of visible matter in the Coma galaxy cluster and applying the virial theorem, he observed that the visible matter was not enough to explain[4] the measured galaxy velocities [1, 35]. This discrepancy between the theoretical predictions and the observations had forced cosmologists to modify (or extend) at least one of the two pillars on which is based the modern cosmology. On the gravitational side, different theories[5] of Modified Gravity on galactic scales had been developed to fit the observed galaxy rotation curves [39]. On the matter sector, without modifying gravity, it is necessary to postulate the existence of a new kind of matter, the so called Dark Matter, which does not interact electromagnetically[6]. This idea had been proposed already by Zwicky. Later, independent and complementary, cosmological observations support the evidences in favor of the existence of Dark Matter to explain the anisotropies in the Cosmic Microwave Background (CMB), the Big Bang nucleosynthesis (BBN), the growth of structures, the light deflection or the cluster collisions. At the same time, not all of them can be explained with the proposed theories of Modified Gravity. Nowadays Dark Matter is considered as the most convincing explanation. A second, and probably more serious, problem arised from the measurements [2, 3, 4] of the distance-redshift relation for type Ia Supernovae (SNIa) in 1998 and which was awarded with the Nobel Prize[7] in 2011. These observations, together with the cosmological principle[8] assumption, lead to an accelerating expansion of the universe. Since then, cosmologists are trying to find a physical understanding for the

[4]His calculations were Newtonian, but at these scales General Relativity reduces with a good precision to Newtonian gravity.

[5]See for example Modified Newtonian Dynamics (MoND) [36, 37] or the relativistic generalization Tensor–Vector–Scalar gravity (TeVeS) [38].

[6]In the standard paradigm of thermal decoupling, Dark Matter particles are described as cold relics of the early universe. In this picture, these species freeze-out once their interaction is no longer competitive with the Hubble expansion. The amount of Dark Matter is then determined by the strength of the interaction. Interestingly, the current measured density of Dark Matter can be explained by a cold relic with an interaction at the weak scale. This supports the idea of Weak Interacting Massive Particles (WIMP) as candidate for Dark Matter and it is often called WIMP-miracle.

[7]`http://www.nobelprize.org/nobel_prizes/physics/laureates/2011/`

[8]The cosmological principle is a generalization of the Copernican principle and it postulates that the universe is (statistically) spatially homogeneous and isotropic.

unexpected acceleration of the expansion of the universe. The proposed solutions can be divided in three categories. A first approach consists in modifying the matter sector by postulating the existence of Dark Energy, i.e. a new kind of matter which interacts only gravitationally and with a negative pressure. This last condition is necessary to obtain accelerating solutions to Friedmann's equations. A second approach aims to modify gravity on cosmological scales, indeed a weaker gravitational force on large scales could explain the observed acceleration of the expansion of the universe. Since the Einstein equations relate the gravity and the matter sectors, some Dark Energy models could be considered as well as theories of Modified Gravity and vice versa. The simplest solution, which fits to very good accuracy the different cosmological observations, is the introduction (or re-introduction) of the cosmological constant[9]. Even if the cosmological constant agrees well with various cosmological probes, it is very puzzling from the theoretical point of view. As already noticed by Einstein, the cosmological constant can be added to the field equations respecting all the symmetries of General Relativity. It is actually a term expected from a low energy effective field theory approach. So the real problem is not the presence of this term, but its very small value. Indeed the bare value of the cosmological constant induced by quantum vacuum energy fluctuations is many orders of magnitude larger than the measured one. In other words the cosmological constant leads to a fine tuning problem[10]. The third approach questions the validity and the interpretation of the cosmological principle. There are indeed very strong constraints on the spatial isotropy, but the homogeneity is always only assumed[11]. It has been shown that inhomogenous models can fit the supernova data. Generically they predict that the Earth is surrounded by an underdense region of the size of the Hubble scale and they are often ruled out by a second cosmological probe. Another approach that enters in the same category is based on the consideration that the our universe is spatial homogenous and isotropic in a statistical sense only. This means that homogeneity and isotropy are recovered through an averaging procedure. Because Einstein's equations are non-linear, they do not commute with the averaging procedure. The so-called Back-Reaction is the idea that a correct analysis might explain the supernova data without the need of the cosmological constant. Interesting this idea solves the coincidence problem, i.e. the fact that the acceleration of the expansion happened only very recently. Indeed Back-Reaction relates naturally the growth of structures with the acceleration of the expansion of the universe. Even if it seems unlikely that Back-Reaction can replace the cosmological constant, it describes an effect that we need to consider carefully when interpreting the data from future surveys to enter the so-called precision era of cosmology, where

[9]The cosmological constant can be considered as a modification of gravity or as a new field, i.e. Dark Energy, in the matter sector.

[10]The naive expectation for the bare contribution of vacuum quantum fluctuations to the cosmological constant ranges between 10^{76} GeV^4 for a cutoff at Planck scale to 10^{10} GeV^4 for a much more conservative cutoff at the electroweak scale, while the measured value in cosmological observations is $\rho_\Lambda = \Lambda/(8\pi G) \sim 10^{-47}$ GeV^4.

[11]To be able to test the spatial homogeneity we should observe an isotropic universe from a second point in space.

the cosmological parameters will be constrained within the percent level.

In the last decade, different probes converged towards the concordance model of cosmology, which is characterized by few parameters only. This model astonishingly agrees with the cosmological observations and it starts to play the role of the standard model of cosmology, also known as ΛCDM model. Unfortunately it does not enlighten[12] us about the underlying physics. At the same time cosmology has become a data driven science. In particular, future surveys will allow us to search for violations of the standard cosmological model. The missions planed for the next decade[13] will be focused on Large Scale Structures (LSS). In this scenario cosmologists will have access to an impressive large amount of data. This will permit to release some assumption and to proceed in a model independent way. This is necessary to rule out many different theories and to constrain the available parameter space.

In my thesis I have been working on different theoretical and observational aspects of relativistic cosmology. In a first series of papers [5, 6, 12] I have studied how inhomogeneities affect light propagation in the universe. These works are motived by the Back-Reaction idea to explain the distance-redshift relation measured with supernovae. I have considered both a toy model, for which we know an exact relativistic solution to Einstein's equations, and linear perturbations on a homogenous and isotropic FLRW metric.

In a second series of papers [19, 41] I have worked on Large Scale Structure observables, developing a numerical code CLASSgal, which allows to compute them to first order including all the relativistic corrections. I have then performed a Fisher matrix forecast to analyze how future surveys, like Euclid, can constrain cosmological parameters. I have also studied the contributions of the different terms to the Large Scale Structure observables, to understand which configuration can enhance some particular effect.

In a third more theoretical project [15] I have studied a higher derivative theory, the Pais-Uhlenbeck field [16], as a Dark Energy candidate by showing that we can consistently quantize it, such that the interactions with charged scalars and fermions do not spoil the stability of the theory. I have argued that such a degree of freedom can only be excited by gravitational effects during the inflationary era in the early universe and may play the role of Dark Energy in the form of an effective cosmological constant whose value is linked to the inflation scale.

[12] This is not, of course, a necessary requirement for a (effective) physical theory. If future surveys will be consistent with a Dark Energy equation of state parameter $w_{DE} = -1$ we will be stuck to a pure cosmological constant.

[13] After the first detection of B-mode CMB polarization [40], there will probably be many experiments which will open, if this detection will be confirmed, a new, exciting and perhaps unique window on very high energy physics.

1.1 Distance-redshift relation

The distance-redshift relation is a fundamental observable in cosmology. Historically it has been the first observable, measured by Lemaître [26] in 1927 and two years later by Hubble [33], that showed the expansion of the universe and discarded the cosmological constant introduced by Einstein to find a static solution to his equations. It led also to another revolutionary discovery in cosmology, when two collaborations observed the acceleration of the expansion of the universe in 1998 [2, 3, 4] suggesting to reintroduce the cosmological constant[14].

In cosmology there are different notions of observable distances, which coincide in a Euclidian space, but not in an expanding universe. Probably the most intuitive definition is the angular diameter distance. Indeed if we know the physical size s of an object in the sky and we measure the angle α under which we see it, we can define the angular diameter distance as

$$d_A = \frac{s}{\alpha} \qquad \text{for} \quad \alpha \ll 1\,. \tag{1.1}$$

To be able to measure it, it is necessary to know some standard rulers in the universe. The Baryonic Acoustic Oscillations (BAO) that we observe in Large Scale Structure (LSS) are a good candidate. They are the imprint on the galaxy distribution of the acoustic oscillations in the plasma before its decoupling from CMB photons. They are the LSS-equivalent to the acoustic peaks in the CMB anisotropies. Nevertheless they do not describe exactly the same physical scale, whereas the first peak of the CMB angular power spectrum is determined by the sound horizon at the photon decoupling, the BAO are characterized by the size of the horizon at the drag epoch[15]. The knowledge of the physical scale of BAO determines the angular diameter distance measuring the separation angle in the galaxy correlation function [42].

Another definition of distance is based on the idea of standard candles instead of standard rulers. Indeed if we know the intrinsic luminosity L of an object, by measuring the flux F, we can infer the luminosity distance

$$d_L = \sqrt{\frac{L}{4\pi F}}\,. \tag{1.2}$$

The best known candidates for standard candles are type Ia supernovae. This type of supernovae are generated by a binary systems where one of the stars is a white dwarf. This implies that type Ia supernovae depend only weakly on the previous configuration of the system and they can be considered standard candles[16]. These

[14]The cosmological constant introduced by Einstein had the opposite sign with respect to the current observed value.

[15]The drag epoch is defined as the era when baryon perturbations can start growing. This happens only when photon pressure can no longer support the gravitational instability of baryon perturbations. Because of the low baryon density, the drag epoch takes place after the photon decoupling leading to a slightly larger BAO scale compared to the CMB anisotropy scale.

[16]To be more precise they should be considered as standardizable candles. The correction to apply is described by the Phillips relation [43], which relates the peak luminosity to the luminosity time evolution.

two definitions of observable distances are not independent, they are indeed related via the Etherington's reciprocity relation [44]

$$d_L = (1+z)^2 \, d_A \tag{1.3}$$

where z is the redshift of the source. It holds[17] not only in General Relativity, but in any metric theory of gravity under the assumptions of the conservation of photon number and that photons travel along null geodesic. For this reason we can combine luminosity and angular diameter distances to get rid of possible systematics in the observations.

In a FLRW universe the luminosity distance

$$d_L(z) = \frac{1+z}{\sqrt{|\Omega_K|}H_0}\chi\left[\sqrt{|\Omega_K|}H_0\int_0^z \frac{dz'}{H(z')}\right] \tag{1.4}$$

$$\text{where} \quad \chi(r) = \begin{cases} \sin(r) & \text{for } K>0, \\ r & \text{for } K=0, \\ \sinh(r) & \text{for } K<0, \end{cases} \tag{1.5}$$

is directly related to the Hubble parameter

$$H(z) = H_0\sqrt{\Omega_R(1+z)^4 + \Omega_M(1+z)^3 + \Omega_\Lambda + \Omega_K(1+z)^2}. \tag{1.6}$$

The measurement of the luminosity distance reveals the dynamics of the universe and its matter content. In this way it has been possible to measure the acceleration[18] of the expansion of the universe. This result implicitly assumes that the universe is correctly described by a FLRW metric. It is important to study how robust is this assumption and how the conclusions could depend on it. Moreover almost all the evidences in favor of Dark Energy rely on the distance-redshift relation valid in a FLRW metric [47]. Only recently some independent measurements [48] of the Hubble parameter have been provided. An exact treatment requires the knowledge of the metric, as a solution to Einstein's equations, and the ability of tracking photon geodesics in this metric. Then to determine the distance, one has to solve the Sachs focusing equation [49, 50]

$$\frac{d^2 d_A}{ds^2} = -\left(|\sigma|^2 + \mathcal{R}\right) d_A \,. \tag{1.7}$$

Here s is an affine parameter along the photon geodesic,

$$\mathcal{R} = \frac{1}{2}R_{\mu\nu}n^\mu n^\nu = 4\pi G T_{\mu\nu}n^\mu n^\nu, \tag{1.8}$$

and σ is the complex shear of the light bundle defined in Eq. (2.29). In practice we need to make some approximation. In my thesis I have been exploring different approximations and assumptions.

[17] Tests on the Etherington's reciprocity relation have been discussed in [45].

[18] There are different meanings and definitions of the acceleration of the expansion of the universe, see Ref. [46] for details.

In the first paper [5], reproduced in Chapter 2, we have considered a universe filled with 'walls' of pressure-less dust separated by under dense regions. Since Einstein's equations for this plane symmetric universe can be solved exactly, we could study how the inhomogeneities affect the light propagation in a non-perturbative regime in a full relativistic framework. The aim of the project was to consider this plane symmetric universe as a toy model, and study if in this scenario we can observe a Back-Reaction effect from small scales, where there is a considerable density contrast, back to large distances to mimic the measured distance-redshift relation. We have considered various density profiles, with the only constraint that they do not form singularity before the present time. Indeed, since this plane symmetric universe is filled with pressure-less dust, any realistic initial density profile will lead to singularities at some point. In particular, we have studied some cases in which the dust forms singularities just after the present time, such that the photons really travel across over densities in a non-perturbative regime. We have found that the luminosity distance fluctuates around the unperturbed value. These fluctuations are at the level of few percent. It is clear that they do not lead to a global effect that could mimic the observed distance-redshift relation. The fluctuations are mainly determined by the metric perturbations at the source position, while the integrated effects seem to average out along the line of sight and hence to be negligible.
In the same paper we have also solved the inverse problem. Namely, given the observed distance-redshift relation, we have determined the density profile which reproduces it. It is not surprising that it possible to solve the inverse problem, since the considered toy model has an additional degree of freedom necessary to describe the inhomogenous matter distribution. To fit the observed supernova data is indispensable to live at the center of a void of the Hubble size. Because the additional free parameter has been adapted such that the model fits the data, a second independent observable should be able to distinguish this model from a FLRW universe. Indeed, we have computed the redshift drift, i.e. the rate of change of the redshift of a co-moving source per unit of observer time. Comparing, then, the redshift drift for this toy model and ΛCDM we noticed that they are very different.

In a following project [6], we have revisited the same problem. The aim was to go beyond to the pressure-less dust assumption which led to the formation of singularities. The singularities are a consequence of shell-crossing caustics, which can not be treated in the fluid approximation. In the previous work we had to choose small initial fluctuation amplitudes to avoid the formation of singularities before the present time. In [6] we were interested in understanding the consequences of this limitation, due to the fluid approximation, on the final results. This problem can be resolved by using N-body simulations that avoid the caustic formation. This was also a good opportunity to test the agreement between the exact solution and a novel general relativistic N-body scheme which was recently presented in [7]. As shown in detail in Chapter 3, the N-body scheme agrees too high precision with the exact solution before the formation of singularities in the fluid approximation scheme. We understand this good agreement from the fact that, while the synchronous comoving gauge breaks down when shell-crossing occurs, the metric perturbations in

longitudinal gauge remain small. We then have analyzed, in the N-body scheme, the distance-redshift relation for large initial fluctuation amplitudes. We have found larger fluctuations around the unperturbed distance, but again we did not see a global effect that can mimic the supernova data. This result also shows that once shell-crossing happens, the luminosity distance is in general not single valued, as already pointed out in [51]. We have then considered the effect on photons traveling at the center of the void, parallel to the walls. The lack of matter along the photon path leads to a continuous defocussing of the light beam, at the same time this is partially compensated by the presence of a non-zero shear (generated by the Weyl tensor). In this case we have found an increase of the distance-redshift relation, but not enough to mimic the ΛCDM model. So in these two projects we have concluded that, if we can generalize the results of this toy model, the inhomogeneities do affect the distance-redshift relation, but they can not be mistaken for Dark Energy. In other words, the Back-Reaction does affect the precision of the future measurements, but it can not explain, by itself, the acceleration of the universe.

As we have seen the luminosity distance is modified by the metric perturbations. In the last years the angular and redshift fluctuations of the luminosity distance [8, 9, 10] have been studied in linear perturbation theory on FLWR background metric. Naively we expect these fluctuations to be of the order of the metric perturbation, i.e. about 10^{-5}, while it has been shown in [9] that they are 2 orders of magnitude larger, i.e. about 10^{-3}. In [11] the contribution of about 10^{-3} for some terms at second order[19] in perturbation theory has been computed. Considering that the second order contribution is as large as the first order, we may wonder if perturbation theory can be trusted. On the other hand we know that the considered toy models show only small modifications to the distance-redshift relation. In [12], reproduced in Chapter 4, we have derived the vector and tensor contributions to the luminosity distance in terms of gauge-invariant quantities. The study of these contributions is interesting for different reasons. First of all, as recent observations [40] indicate, gravitational waves are produced during inflation with a relatively high amplitude. We also know that binary systems source gravitational waves which may affect the luminosity distance. Moreover vector and tensor perturbations are produced at second order by scalar perturbations at linear order. In particular, since the second order effects seem to be as larger as the linear one they can play a role and they have to be considered for completeness. Later, our results have been shown to agree with the vector and tensor contributions at second order computed in [13]. After deriving these linear contributions, we have expanded them in spin weighted spherical harmonics and computed the redshift dependent angular power spectrum $c_\ell\left(z,z'\right)$ defined through

$$\left\langle \Delta_L\left(z,\mathbf{n}\right)\Delta_L\left(z',\mathbf{n}'\right)\right\rangle = \frac{1}{4\pi}\sum_\ell \left(2\ell+1\right)c_\ell(z,z')P_\ell\left(\mathbf{n}\cdot\mathbf{n}'\right), \tag{1.9}$$

where $\Delta_L\left(z,\mathbf{n}\right)$ relative difference in the luminosity distance and $\langle . \rangle$ denotes the

[19] More recently two different groups have independently derived the full expression for the luminosity distance at second order [13, 14].

statistical average. For tensor perturbations we have applied this formalism to a primordial scale-invariant power spectrum. Naively one may think that the tensor angular power spectrum is suppressed with respect to the scalar one by the tensor-to-scalar ratio of the primordial fluctuations generated during inflation. We have, instead, found that the tensor contributions are suppressed by about 8 orders of magnitude more. This is due to the fact that tensor perturbations decay once they enter the horizon, while the scalar perturbations start growing. Since the first order signal is so small we may expect that the second order contributions, sourced by linear scalar perturbations, dominate. Hence, the vector and tensor contributions might play a role at second order in perturbation theory.

1.2 Large Scale Structure Observables

From the unexpected observation of the acceleration of the expansion of the universe in 1998, it has become clear that cosmology turned into a data driven science, challenging cosmologists to develop theoretical and numerical tools to fully profit of these datasets. This process allows, on one hand, to determine the cosmological parameters with higher and higher precision, and on the other hand, to test for deviations from the standard cosmological model. The quantity and the quality of current and future data will permit to analyze them in a model independent way. This approach has been successfully adopted to handle the CMB anisotropy data, measured by different and independent experiments, until the astonishing agreement between observations and theoretical predictions, based on the standard cosmological model, reached by the last Planck release [52]. To reach this amazing result it has been necessary to develop a theoretical formalism [53] based on observable quantities and numerical tools [20, 54, 55, 56] to compute, efficiently and accurately, the theoretical predictions. The aim for the next decades is to repeat the same steps for Large Scale Structures observables, i.e. for the galaxy distribution. LSS contain in principle much more information than CMB anisotropies, because the galaxy distribution is 3-dimensional while the CMB information comes mainly from the 2-dimensional last scattering surface. On the other hand, this is a much harder effort to handle. The difficulties arise from different effects, including the galaxy bias, i.e. the fact that we predict fluctuations of a continuous density field, i.e. Dark Matter distribution, but we observe a discrete galaxy distribution, i.e. a biased tracer of the underling smooth density field. Moreover, on small scales density perturbations become non-linear and perturbation theory fails. Since the non-linear regime contains a wealth of cosmological information, different attempts have been performed to describe, at least, the middle non-linear regime [57, 58, 59, 60]. This will be a fundamental and necessary step to really profit of LSS datasets from future surveys.

The traditional LSS analysis is performed computing the 3-dimensional matter power spectrum $P(k)$. This approach has some evident advantages: it can be easily measured in galaxy catalogs since it only depends on a single variable and the different k Fourier modes are independent in linear perturbation theory. Nevertheless it is not an observable quantity. One needs to assume a fiducial set of cosmological pa-

rameters to convert the observable 2-point correlation function in the 3-dimensional matter power spectrum $P(k)$. If iteratively repeated this approach can determine the best fit of the cosmological parameters, but it is much more difficult to correctly estimate the errors. An underestimation of errors can lead to wrong conclusions discarding valuable models. Recently a novel approach based only on observable quantities, namely the redshift and the angles under which we observe the galaxies on the sky, has been presented [17, 18]. In this approach the fundamental quantity is the so-called galaxy number count

$$\Delta\left(\mathbf{n}, z\right) \equiv \frac{N\left(\mathbf{n}, z\right) - \langle N\rangle\left(z\right)}{\langle N\rangle\left(z\right)} \tag{1.10}$$

as a function of the observed number of galaxies N in direction $\mathbf{n}$ and at redshift z. To correctly compute the galaxy number counts one needs to consider many different effects like the fact that observations are made on our past light-cone, that the measured redshifts are perturbed by the motion of the galaxies, that light is deflected and the volume distorted by the perturbed geometry. In the past, these effects could be neglected, but this may no longer be the case for future surveys which go deeper in redshift and cover a larger fraction of the sky. A careful treatment leads to

$$\begin{aligned}\Delta(\mathbf{n}, z) \;=\;& D_g + \Phi + \Psi + \frac{1}{\mathcal{H}}\left[\Phi' + \partial_r(\mathbf{V}\cdot\mathbf{n})\right] \\ &+ \left(\frac{\mathcal{H}'}{\mathcal{H}^2} + \frac{2}{r_S\mathcal{H}}\right)\left(\Psi + \mathbf{V}\cdot\mathbf{n} + \int_0^{r_S} dr(\Phi' + \Psi')\right) \\ &+ \frac{1}{r_S}\int_0^{r_S} dr\left[2 - \frac{r_S - r}{r}\Delta_\Omega\right](\Phi + \Psi).\end{aligned} \tag{1.11}$$

Hence the galaxy number counts not only describe the matter density, but also the redshift space distortions (RSD), the lensing and the gravitational potential (or relativistic) terms. In other words the galaxy number counts contain, at least potentially, information about the large scale matter distribution, the cosmic velocity field and the geometry. All these quantities are related through the Einstein equations, so by measuring them, we can test General Relativity and the cosmological standard model against different theories of Modified Gravity, which usually predict a different lensing potential. Since the galaxy number counts depend sensitively and in several different ways on dark energy, on the matter and baryon densities, bias, and so on, their measurements provide a new estimation of cosmological parameters, without the need of assuming a fiducial cosmology.

As the galaxy number counts (1.11) are defined, for each redshift, on the unit sphere, it is convenient to expand them in multipoles,

$$\Delta\left(\mathbf{n}, z\right) = \sum_{\ell m} a_{\ell m}\left(z\right) Y_{\ell m}\left(\mathbf{n}\right) \tag{1.12}$$

with redshift dependent coefficients

$$a_{\ell m}\left(z\right) = \int d\Omega_{\mathbf{n}} Y^*_{\ell m}\left(\mathbf{n}\right)\Delta\left(\mathbf{n}, z\right). \tag{1.13}$$

We can then define the redshift dependent angular power spectrum

$$C_\ell(z_1, z_2) = \langle a_{\ell m}(z_1)\, a^*_{\ell m}(z_2)\rangle \tag{1.14}$$

and the redshift dependent angular correlation function

$$\xi(\theta, z_1, z_2) = \sum_\ell \frac{2\ell+1}{4\pi} C_\ell(z_1, z_2)\, P_\ell(\cos(\theta)), \tag{1.15}$$

where P_ℓ are the Legendre polynomials. Comparing the theoretical predicted angular power spectrum, which contains all the statistical information for Gaussian perturbations, with the LSS data we can extract from them the information needed to estimate the cosmological parameters. This comparison requires to scan the parameter space, computing and comparing the predictions with observations many times to find the best fit for the cosmological parameters. To achieve this requirement it is necessary to develop numerical codes which compute, accurately and efficiently, the LSS observables. We have decided to implement CLASS [20], a public Boltzmann code oriented on computing very efficiently the CMB angular power spectrum, to compute the LSS observables including all the relativistic corrections derived in [17, 18] and described in Eq. (1.11). This code is called CLASSgal and publicly available[20], all the details about CLASSgal can be found in Ref. [19], which is reproduced in Chapter 5. Since any survey can only determine the redshift of galaxies with finite accuracy, we can not compare directly the measurements with the theoretical redshift dependent angular power spectrum $C_\ell(z_1, z_2)$ defined through Eq. (1.14). We need, indeed, to convolve the theoretical predicted angular power spectra with a window (or selection) function. By introducing the window functions, we split the redshift range of the survey in many redshift bins. Depending on the redshifts z_1 and z_2 of the sources, they can belong to the same redshift bin or to two different bins. Splitting the full survey in $N_{\rm bins}$, the full information is arranged in a symmetric matrix $\left(C_\ell^{ij}\right)$ with $N_{\rm bins}(N_{\rm bins}+1)$ independent angular power spectra. This is also the final output of our code CLASSgal. Observationally we need to measure $N_{\rm bins}$ autocorrelated[21] angular power spectra, which are affected by shot-noise, because we sample a smooth field with a discrete set of galaxies. In order to have larger amplitudes of the angular power spectra we should consider narrow redshift bins, this avoids to smear out the signal by large window functions. On the other hand too narrow redshift bins lead to a signal which is completely dominated by shot-noise which scales as the inverse of the number of galaxies per redshift bin. As we have shown in [19], the optimal configuration determined by the spectroscopic[22] redshift resolution can not be reached because shot-noise starts to dominate earlier.

[20] `http://cosmology.unige.ch/tools/`. The main features of CLASSgal have been merged with the main code CLASS starting from version 2.1 publicly available at `http://class-code.net`.

[21] With autocorrelation we mean the correlation between galaxies in the same redshift bin. In case of correlation between galaxies in different redshift bins we refer to cross-correlation.

[22] The situation is different for photometric surveys. At their redshift resolutions shot-noise is almost negligible for current or future surveys.

In the past, data from galaxy surveys have been analyzed considering only the matter power spectrum, corrected by the Kaiser formula [61] to describe the redshift space distortions, considering the other effects as negligible. This approximation has worked well, but for future surveys, like Euclid which observes larger scales and deeper in redshift, it may be not good enough. In [19] we have quantified the errors made in the angular power spectrum by neglecting the contributions of the different terms. These errors in the power spectra can induce a bias limiting the accuracy in the cosmological parameter estimation. In particular, as we have shown in [41], the lensing becomes a detectable signal for deep surveys. Therefore, by correctly considering the lensing contribution, we can not only estimate the cosmological parameters with a better precision, but we have an important cosmological probe to test for deviations from General Relativity. We have pointed out that a measure of the lensing potential would require only a deep survey independently of its redshift resolution. Indeed, the lensing signal becomes important at high redshift because it is coherently integrated along the line of sight smearing out the redshift information of the sources. We think that one may apply this idea to radio galaxy catalogs, which have a very poor redshift resolution but cover a deep redshift range.

In order to estimate the contribution of the different effects described in Eq. (1.11), we determine the parametrical order of all contributions by writing them in terms of metric perturbations through the Einstein equations

$$D_g \sim \left(\frac{k}{\mathcal{H}}\right)^2 \Phi\,, \qquad \mathbf{V}\cdot\mathbf{n} \sim \frac{k}{\mathcal{H}}\Phi\,, \tag{1.16}$$

and considering the contribution of the derivatives as[23]

$$\partial_r \sim k, \qquad \Delta_\Omega \sim \left(\frac{k}{\mathcal{H}}\right)^2 . \tag{1.17}$$

At sub-Hubble scales ($k \gg \mathcal{H}$) the leading terms are:

$$D_g \sim \left(\frac{k}{\mathcal{H}}\right)^2 \Phi \qquad \text{(density)},$$

$$\frac{1}{\mathcal{H}}\partial_r\left(\mathbf{V}\cdot\mathbf{n}\right) \sim \left(\frac{k}{\mathcal{H}}\right)^2 \Phi \qquad \text{(redshift-space distortion)},$$

$$\int_0^{r_S} dr \frac{r_S - r}{r_S r}\Delta_\Omega\left(\Phi+\Psi\right) \sim 2\int_0^{r_S} dr \frac{r_S - r}{r_S r}\left(\frac{k}{\mathcal{H}}\right)^2 \Phi \qquad \text{(lensing)}.$$

[23] To estimate the parametric order of the angular Laplacian Δ_Ω we re-express the definition (1.1) of angular distance as

$$d_A = \sqrt{\frac{dA}{d\Omega}}\,.$$

Then the solid angle Ω can be approximated as

$$\Omega \sim \frac{\lambda^2}{d_A^2} \sim \left(\frac{\mathcal{H}}{k}\right)^2 ,$$

where λ characterizes the size of the observed object in the sky at the angular diameter distance d_A, which goes roughly like $\mathcal{H}^{-1}$.

It is therefore not surprising that the lensing contribution becomes important for some configurations, since it appears at the same parametrical order as the density and the redshift space distortion terms. The other terms, i.e. gravitational potential (or relativistic) contributions, have a smaller power in the parametric expansion in $k/\mathcal{H}$ and they can become important only at larger scales. Indeed, since these terms are purely relativistic[24] contributions, they become naturally relevant at super-Hubble scales ($k \ll \mathcal{H}$) where Newtonian gravity fails. However cosmological observations at very large scales are strongly affected by cosmic variance which induces a large theoretical uncertainty. This suggests that their contribution to LSS observables is weaker than all the other terms. In all the configurations analyzed in our work their contribution was always negligible. Nevertheless there are some novel methods [62] that can enhance their effects. It might be possible that the gravitational potential (or relativistic) terms are completely negligible in the standard analysis to estimate the cosmological parameters, but at the same time a different analysis could lead to their detection.

This model independent approach is based on several 2-dimensional redshift dependent angular power spectra. An important question that we have studied in [41], and that had been already addressed in [63], is if one can recover the whole 3-dimensional information. We have performed a Fisher matrix analysis constraining some pairs of ΛCDM cosmological parameters marginalizing over the remaining ones, for an Euclid-like and a DES-like galaxy surveys. We have paid particular attention in translating a non-linear cutoff in real space to a sharp cutoff in the multipole space depending on the bin correlations. We have then shown that considering only autocorrelated redshift dependent angular power spectra we can not recover the information of the traditional 3-dimensional analysis based on the matter power spectrum $P(k)$ in redshift space. This is not surprising, one needs to consider the cross-correlations between different redshift bins to have access to the information along the radial direction. Indeed we have found that including cross-correlations we can recover the full information of the traditional 3-dimensional analysis. In particular our results show that for a spectroscopic surveys the same information is reached roughly when the size of the redshift bins is given by the non-linear cutoff in the analysis. So the minimal number of redshift bins will depend on the redshift range of the survey, requiring more and more redshift bins for a survey which goes deep in redshift. Hence, performing a Markov Chain Monte Carlo (MCMC) analysis to estimate the cosmological parameters will be numerically very expansive, because the number of redshift dependent angular power spectra scales like $N_{\rm bins}^2$. If we consider photometric surveys the 3-dimensional information is recovered when the width of the redshift bins roughly coincides with the photometric resolution. In this case the number of power spectra permits an accurate numerical analysis.

This analysis has shown that an approach only based on observable quantities is competitive with the traditional method based on the 3-dimensional matter power spectrum $P(k)$. On top of that, this novel approach fully describes all the relativistic

[24] Obviously also the lensing is a general relativistic contribution and the redshift space distortions are as well (special) relativistic contributions.

terms. In particular, the lensing potential may be detected in galaxy surveys. This work, including the code CLASSgal, also helps to determine optimal observational specifications for future surveys.

1.3 Pais Uhlenbeck field as Dark Energy candidate

Since 1998, the efforts of many cosmologists have been focused on trying to explain the underlying physics which leads to the acceleration of the expansion of the universe. Up to now all cosmological probes are consistent with the simplest model based on a cosmological constant. A crucial step [64] will be to constrain as precise as possible the Dark Energy equation of state. Different surveys have been designed to optimize this measurement. As long as $w_{\rm DE}$ will be consistent with -1 without any time dependence, it will be impossible to distinguish between a cosmological constant and a Dark Energy model. Generically Dark Energy models replace the cosmological constant with a dynamical degree of freedom described by a scalar field. They do not attempt to solve the original cosmological constant problem. The (speculative) attitude is to hope that quantum gravity effects will lead to a cancellation of the vacuum energy. With this hope, it seems more natural to obtain directly a vanishing renormalized cosmological constant, instead of the small, but finite, observed value. In this framework, these models try to explain with physical mechanisms the observed acceleration. Through their dynamical evolution they often claim to resolve the coincidence problem[25]. Among the Dark Energy models, physicists have considered also theory with higher (than first order) derivatives in the Lagrangian like $f(R)$ [68, 69] or galileon theories [70, 71, 72, 73]. According to the Ostrogradski theorem [74, 75] these theories do not have an energy functional bounded from below and they are expected to develop instabilities. Generically, such theories are characterized by the presence of ghosts, i.e. fields whose kinetic term has the wrong sign. The ghost appears as a new degree of freedom in the equation of motion with higher than second order time derivatives. The aforementioned $f(R)$ and galileon theories do not exhibit the Ostrogradski instability, indeed their higher derivative Lagrangians, thanks to their specific form, reduce to only second order equations of motion.

The puzzling and unsolved Dark Energy problem, after many failed attempts in the last decade, may force us to carefully reconsider theories that at first sight might look dangerous. Higher derivative theories have been considered in the past [76] since they allow to absorb the divergences which arise by quantizing General Relativity, leading to renormalizable theories of quantum gravity[26]. In this framework we have

[25] Tracker solutions for quintessence models have been found [65]. But it is important to stress that they solve only apparently the coincidence problem, because they require a strong fine-tuning of the parameters of the Lagrangian. K-essence models [66] do not generically require a fine-tuning of the parameters, but they lead to superluminal propagation and violate causality [67].

[26] In this approach the price to pay for the renormalization of quantum gravity is to introduce

considered the (degenerate) Pais-Uhlenbeck field described by the action

$$S = \int d^4x \, (\Box\phi)^2 \,, \tag{1.18}$$

where $\Box = \partial_\mu \partial^\mu$ is the d'Alembertian operator, which induces the equation of motion

$$\Box^2 \phi = 0, \tag{1.19}$$

solved by

$$\phi = \int \frac{\mathrm{d}^3 k}{(2\pi)^{3/2}} \frac{1}{(2k)^{3/2}} \left[(a_k + i b_k kt) e^{i(\vec{k}\cdot\vec{x} - kt)} + (a_k^* - i b_k^* kt) e^{-i(\vec{k}\cdot\vec{x} - kt)} \right]. \tag{1.20}$$

It is not surprising that it does not exhibit any instability. Indeed free theories have an unitarity evolution even if the ghost mode, induced by the Ostrogradski instability, is present. The Hamiltonian is unbounded from below, but as long as the system is free and energy is conserved the system evolves in closed orbits in phase space. Classically the instability appears only once we introduce an interaction with other fields. Through the interaction the coupled system can extract an infinite amount of energy from the unbounded one. Nevertheless the details are controlled by the explicit form of the interaction. To consistently quantize this theory we have made used of the presence of another symmetry. Looking at the equation of motion (1.19) it is clear that the field ϕ can be shifted by an arbitrary harmonic function. This implies that the a_k mode in Eq. (1.20) can be gauged away. We quantize the system by promoting a_k, b_k to operators $\mathbf{a}_k$, $\mathbf{b}_k$. The relevance of the mentioned symmetry becomes evident writing the Hamiltonian function

$$H = \int d^3x : \mathcal{H}_0 := \int d^3k \; k \left[\mathbf{b}_k^\dagger \mathbf{b}_k - \frac{1}{2} \left(\mathbf{a}_k^\dagger \mathbf{b}_k + \mathbf{b}_k^\dagger \mathbf{a}_k \right) \right]. \tag{1.21}$$

Gauging away the $\mathbf{a}_k$ mode, the energy spectrum of physical states is bounded from below. We can fix the gauge by eliminating the ghost state from the physical spectrum and quantize only the physical mode or we can impose an additional subsidiary condition à la Gupta-Bleuler to define the physical Hilbert space. The quantization of the free theory does not guarantee that the ghost is not reintroduced once we include interactions with other fields. This is actually the fundamental problem for higher derivative theories.

In our work we have shown that the Pais-Uhlenbeck field can be identified with a Stückelberg field to restore the $U(1)$ gauge invariance of an action for a massless vector field with a modified kinetic term

$$S = \int d^4x \left[-\frac{1}{4} F_{\mu\nu} F^{\mu\nu} + \frac{1}{2} \xi \left(\partial_\mu A^\mu \right)^2 \right]. \tag{1.22}$$

massive ghosts spoiling unitarity of the theory. Nevertheless it has been claimed [77] that the massive ghosts could disappear in the asymptotic states due to quantum corrections, restoring unitary.

Once the residual gauge is fixed, this action propagates 3 degrees of freedom, namely 2 traverse modes and a longitudinal mode associated to $\partial_\mu A^\mu$. By restoring the $U(1)$ gauge invariance, the longitudinal vector mode becomes a scalar mode described by the Pais-Uhlenbeck field. Motivated by the introduction of the Pais-Uhlenbeck field as Stückelberg field, we interpret the Pais-Uhlenbeck field as gauge field which mediates the interaction. We have considered both charged scalars and fermions whose interaction is mediated by the Pais-Uhlenbeck field as gauge field. We have shown that the equation of motion for the Pais-Uhlenbeck field is sourced by the current of the charged fields, which is conserved thanks to the $U(1)$ global symmetry of the considered theory. This implies that the dynamics of the Pais-Uhlenbeck field is not affected by the charged scalars or fermions to which it couples, and moreover that once the ghost mode is eliminated from the spectrum of physical states of the free theory it is not reintroduced by this interaction.

From the equation of motion (1.19) we notice that $\Box\phi$ satisfies the Klein-Gordon equation for a massless scalar field. It is well-known that a massless scalar field in an expanding universe is frozen on super-Hubble scale. This leads to an energy-momentum tensor given by

$$T_{\mu\nu} = \frac{1}{2}\left(\Box\phi\right)^2 g_{\mu\nu} \tag{1.23}$$

which plays the role of an effective cosmological constant with the value $\Lambda = 4\pi G\left(\Box\phi\right)^2$. Since it behaves like a massless scalar field, we argue that it can be generated during the inflationary phase with a scale-invariant power spectrum determined by $P_{\Box\phi} \simeq H_I^4$. The value of the effective cosmological constant induced by the Pais-Uhlenbeck field is set by the energy scale of inflation and to agree with observations it requires an inflationary scenario about 1 TeV, which corresponds to the electroweak scale[27]. As shown in [78] this interesting feature is shared[28] by all the Dark Energy models with scalar fields produced during inflation provided that their mass does not exceed the Hubble parameter today. These scalar fields, including the Pais-Uhlenbeck one, have to be generated from a non-standard mechanism. Indeed a standard scalar field is diluted by the very rapid expansion during inflation. Even if at the background level the Pais-Uhlenbeck field behaves like an effective cosmological constant, its dynamical evolution can have an imprint on cosmological probes. By studying its cosmological perturbations we have a mechanism to discriminate between this Dark Energy model and a pure cosmological constant.

[27]Recent B-mode polarization detection [40] would indicate a much higher inflationary energy scale, namely about 10^{16} GeV which interestingly coincides with the Grand Unification Theory (GUT) scale. If this first detection will be confirmed by independent experiments and any other non-primordial source of B-mode will be excluded, this will rule out the Pais-Uhlenbeck field as Dark Energy candidate.

[28]B-mode polarization detection [40], if confirmed, rules out all Dark Energy models described by massless scalar fields sourced during inflation.

2

Back Reaction from Walls

JOURNAL OF ASTROPHYSICS AND ASTROPARTICLE PHYSICS **02** 036
(2012)

Back Reaction from Walls

Enea Di Dio, Marc Vonlanthen, Ruth Durrer

We study the distance–redshift relation in a universe filled with 'walls' of pressureless dust separated by under dense regions. We show that as long as the density contrast of the walls is small, or the diameter of the under dense regions is much smaller than the Hubble scale, the distance–redshift relation remains close to what is obtained in a Friedmann universe. However, when arbitrary density contrasts are allowed, every prescribed distance–redshift relation can be reproduced with such models.

2.1 Introduction

Since more than a decade, cosmology research is facing the dark energy problem: the present Universe seems to be in an accelerating phase. This conclusion was first drawn from measurements of the distance–redshift relation from type Ia Supernovae (SNIa) [2, 4, 79, 80, 81, 82] and is confirmed by many other datasets, from the cosmic microwave background [83] to baryon acoustic oscillations and other aspects of large scale structure. Until very recently the measurements inferring the existence of dark energy rely mainly on the distance–redshift relation which is valid in a Friedmann Universe [47]. New *independent* measurements of, e.g. the expansion rate $H(z)$ are now being performed see e.g. [48]. Hence this situation is changing, so that we shall soon know both, $d_A(z)$ and $H(z)$ with good accuracy. The general opinion is that fluctuations on large scales are small so that they can be treated with linear perturbation theory and linear perturbations average out in the mean over many directions and large scales, and therefore fluctuations are not relevant for the determination of quantities like $d_A(z)$ and $H(z)$. This expectation has been confirmed by perturbative calculations. Within linear perturbation theory, the fluctuations of the distance–redshift relation for redshift $z > 0.2$ is on the level of a few percent [9].

However, perturbations on smaller scales can become very large, density fluctuations e.g. in galaxies are $\delta\rho/\rho \sim \rho_{\rm gal}/\rho_m \sim 10^8$. Since the relation between metric perturbations, or more precisely the Christoffel symbols, and density fluctuations is non-linear, it is not evident that large amplitude, non-linear, small scale density fluctuations cannot add up to affect the distance–redshift relation on large scales.

To study the real problem one would need to analyse light rays passing through a realistic Universe with high density fluctuations. So far, this has been done only within Newtonian N-body simulations, see e.g. [84, 85]. However, it is well known that Newtonian gravity misses the terms which are relevant for the back reaction

problem [86], hence a full, non-linear relativistic treatment is needed. Since this is very difficult, so far mainly toy models which mimic reality to a certain extent have been studied.

The present work inscribes in this framework. Instead of considering spherically symmetric solutions of general relativity (GR), the so called Lemaître [87]-Tolman [88]-Bondi (LTB) models, for recent reviews see [89, 90], we study a Universe containing high density walls. We shall consider infinitely extended parallel walls. The considered model is a sub-case of the Szekeres solution [91]. Light propagation in general Szekeres model has been studied recently [92, 93]. This is of course a gross over-simplification, but we know that galaxies tend to be aligned in filaments and photons coming to us from a far away supernova, might experience a geometry similar to the one of such a symmetric wall universe. The weakest point of our toy model is that all the walls are parallel while we expect a typical photon to traverse filaments which are aligned in different directions. We shall take this into account to some extent by studying photons coming in from different directions with respect to the walls.

Such walls have been studied in the past [94], but only perturbatively. Since we know that the effects are small within linear perturbation theory, we cannot trust higher order perturbation theory if it predicts large deviations from the Friedmann distance-redshift relation. For this reasons we analyse exact, fully relativistic wall-universes in this work.

In the next section we present the wall metric and the Einstein equations. We also study the conditions on the parameters which have to be satisfied so that no singularity apart from the Big Bang is present in the backward light cone of the observer. In section 2.3 we present the results for the distance-redshift relation for 'realistic' walls and for a wall universe which mimics the observed relation. In section 2.4 we conclude.

2.2 Wall Universes

In this section we study universes containing only pressure-less matter (dust) and which are symmetric under translations and rotations in a plane which we call the y-plane. They have the same number of symmetries as LTB models and can be solved analytically, see [95]. The metric is of the form

$$ds^2 = -dt^2 + a^2(t,x)dx^2 + b^2(t,x)(dy_1^2 + dy_2^2)\,. \tag{2.1}$$

Note that the only difference to the LTB geometry is that our symmetrical 2d manifolds are planes, $dy_1^2 + dy_2^2 = dr^2 + r^2 d\phi^2$ while those of LTB are spheres, $d\Omega^2 = d\theta^2 + \sin^2\theta d\phi^2$. We denote the spatial coordinates by $\mathbf{x} = (x, y_1, y_2)$ in order to reserve the letter z for the redshift. In the following a prime denotes a derivative w.r.t. x while a dot denotes derivative w.r.t. t. The Einstein equations for this

geometry and for pure dust matter yield [91, 95, 96]

$$\partial_t \left(\frac{b'}{a}\right) \equiv \partial_t E = 0\,, \tag{2.2}$$

$$\dot{b}^2 - \left(\frac{b'}{a}\right)^2 = 2\frac{M(x)}{b}\,, \tag{2.3}$$

$$M' = 4\pi G\rho b^2 b' = 4\pi G\rho b^2 a E(x)\,. \tag{2.4}$$

In Eq. (2.2) we have introduced the time-independent function

$$E(x) = b'/a \tag{2.5}$$

and Eq. (2.3) defines $M(x)$ which is also time-independent. In LTB models M/G can be interpreted as mass density (Note that in the LTB case a term $b/(2G)$ has to be added to M which is a consequence of the curvature of the 2-sphere. For more details see [96].), and $(M'/G)r^2dr$ is the mass in a shell of thickness dr. However as the mass in an infinite plane is not well defined, this interpretation is not meaningful in the planar case. In our case it is therefore not unreasonable that M may become negative even though a, b and ρ are supposed to be positive at all times.

From the matter conservation equation we also obtain $\partial_t(\rho b^2 a) = 0$, which, on the other hand, is a consequence of Eq. (2.4).

2.2.1 The solutions

Eq. (2.3) can we rewritten as

$$\dot{b}^2 = \frac{2M(x)}{b} + E(x)^2\,, \tag{2.6}$$

with parametric solutions [91, 95]

$$\text{for } E \neq 0 \;:\quad b = \frac{M}{E^2}(\cosh\eta - 1) = \frac{2M}{E^2}\sinh^2(\eta/2)\,, \tag{2.7}$$

$$t = \frac{M}{E^3}(\sinh\eta - \eta) + t_B(x), \quad \text{for } M > 0\,; \tag{2.8}$$

$$b = -\frac{M}{E^2}(\cosh\eta + 1) = -\frac{2M}{E^2}\left(\sinh^2(\eta/2) + 1\right)\,, \tag{2.9}$$

$$t = -\frac{M}{E^3}(\sinh\eta + \eta) + t_B(x), \quad \text{for } M < 0\,; \tag{2.10}$$

$$b = |E|(t - t_B(x)) \quad \text{for } M = 0\,; \tag{2.11}$$

$$\text{for } E = 0 \;:\quad b = \left(\frac{3}{2}\sqrt{2M}(t - t_B(x))\right)^{2/3}, \text{ for } M > 0\,, \tag{2.12}$$

$$b = b_0 = \text{ const. }, \text{ for } M = 0\,. \tag{2.13}$$

Note that for $E = 0$ Eq. (2.6) implies that $M \geq 0$. This equation also implies

$$b \geq -\frac{2M}{E^2}$$

at all times, in all cases.

The function $t_B(x)$ is arbitrary; it is called the 'bang time'. For $M \geq 0$, at $t = t_B$, i.e $\eta = 0$, we have $b = 0$ which represents the Big Bang singularity. Positions with $M < 0$ have no Big Bang singularity but a 'bounce' at $t = t_B$. We shall simplify below to the case $t_B \equiv 0$, i.e., uniform bang time. Note that we have chosen expanding solutions. From these we can obtain the collapsing solutions simply by changing the sign of t. Since in the Einstein equations only $\dot{b}^2$ appears they are invariant under $t \to -t$.

Of course the $\{t$ =const.$\}$ hypersurfaces are not parallel to the $\{\eta$ =const.$\}$ hypersurfaces, but their position depends on x. For fixed position x, Eqs. (2.7,2.8) and (2.12) correspond to Friedmann solutions with curvature $K = -E^2 \leq 0$ and $M = 4\pi G\rho b^3/3$. Note that unlike in the Friedmann case, wall solutions with $M < 0$ need not be unphysical.

The parametric representation with η is chosen in order to express the solutions in terms of elementary functions, but it is of course not necessary. For example, for $M > 0$, setting

$$\tau(t,x) = -E^2\left(\frac{t}{6M}\right)^{2/3} \quad \text{and}$$

$$S(\tau) = (-3\tau)^{-1}\sinh^2\left(\frac{1}{2}\left[\sinh -\mathrm{id}\right]^{-1}\Big(6\,(-\tau)^{3/2}\Big)\right)$$

we obtain

$$b(t,x) = -\frac{M}{E^2}6\tau S(\tau)\,.$$

Note that in the definition of S, $[\sinh -\mathrm{id}]^{-1}$ denotes the inverse of the function in brackets, and id is the identity function, $\mathrm{id(x)} = \mathrm{x}$. One can check that S solves the differential equation [97]

$$\frac{4}{3}\left(S + \tau S'\right)^2 + 3\tau - \frac{1}{S} = 0, \tag{2.14}$$

with initial condition $S(0) = \left(\frac{3}{4}\right)^{1/3}$. Note that this is the only regular solution, i.e solution with $S'(0) \neq \infty$. This expression will be useful in Section 2.3.3.

The function $a(x,\eta)$ can be obtained from Eq. (2.5). For example for $M > 0$ we find

$$a = E^{-1}\left(\frac{\partial b}{\partial x}\right)_t$$

$$\text{for } E \neq 0 \;: a = \frac{2}{E}\left(\frac{M}{E^2}\right)'\sinh^2\left(\frac{\eta}{2}\right) - \coth\left(\frac{\eta}{2}\right)\left[t_B' + \left(\frac{M}{E^3}\right)'(\sinh\eta - \eta)\right], \tag{2.15}$$

$$\text{for } E = 0 \;:\; a = \frac{(t-t_B)^{2/3}}{M^{1/3}6^{1/3}}\left[M^{-1/3}\frac{M'}{E} + \frac{9(t-t_B)^{2/3}E'}{5\times 6^{1/3}}\right]. \tag{2.16}$$

(The suffix t in $\partial b/\partial x$ indicates that we have to interpret b as function of (t, x), not (x, η), in this derivative.) Even if $E = 0$, Eq. (2.4) implies that $0 < M'/E < \infty$, so that the r.h.s. of Eq. (2.16) is well defined. Below, we shall choose the x-coordinate such that $M'/E =$constant.

Note that $M(x)$ and $E(x)$ can pass through zero so that in general different solutions from above have to be glued together at the boundary of their validity. We have checked that this gluing process can be performed in a smooth way and does not induce singularities in the scale factor b. However, for $M \to 0$ the scale factor $a \to \infty$. Nevertheless, we believe this to be a coordinate singularity, since, as we have checked, both, the Kretschmann scalar, $K \equiv R_{\alpha\beta\mu\nu}R^{\alpha\beta\mu\nu}$ and the scalar curvature remain finite for $M \to 0$. In our examples below we shall have $M > 0$ throughout and therefore we do not encounter this problem. However, when computing a from Eq. (2.5), one has to be careful to use the result (2.15) and take the limit $E \to 0$ for fixed t, hence also $\eta \to 0$. One cannot use (2.12) and (2.5), since for $E = 0$ we have $M' = 0$ so that Eq. (2.5) is identically satisfied and cannot be used to obtain $a(t, x)$.

2.2.2 Singularities

Singularities can occur when a, b or ρ become either infinite or zero. To have no singularities (apart from the Big Bang) which occurs at $t = t_B$, hence $b = 0$, in the past light cone of every possible observer we might be interested in, we must demand that all singularities lie in the future. In more precise models, when one specifies the observer location, one can relax this condition to the one that no singularity lies within the background lightcone of the specific observer.

In general, the question of singularities depends on the choice of the functions $M(x)$ and $E(x)$. From our solutions it is clear that b behaves monotonically as a function of time for fixed x. This is to be expected since no clustering goes on in the directions y_1 and y_2 described by this scale factor. Since we are interested in an expanding b, a singularity is present when the the scale factor a of the x-direction tends to zero. From Eq. (2.15) we infer that for $t_B \equiv 0$, $a = 0$ implies

$$\frac{2}{E}\frac{(M/E^2)'}{(M/E^3)'} = \frac{\cosh(\eta/2)}{\sinh^3(\eta/2)}\,(\sinh\eta - \eta) \geq 4/3\,.$$

It is easy to verify that the right hand side is an even positive function with minimum $4/3$ at $\eta = 0$. Hence there is a singularity at some finite value of η if the l.h.s. ever becomes larger than $4/3$ or, equivalently, if

$$\frac{E'}{E}\frac{M/E^3}{(M/E^3)'} = \frac{\cosh(\eta/2)}{2\sinh^3(\eta/2)}\,(\sinh\eta - \eta) - 1 > -1/3$$

for some value of x.

We now consider a simple ansatz motivated by the perturbative analysis presented in Ref. [95]. We choose

$$M(x) = \frac{2}{9t_0^2}\,(1 + \epsilon h(x)) \tag{2.17}$$

and

$$4\pi G\rho b^2 a = \frac{M'}{E} = \frac{2}{3}t_0^{-2} = \text{const.} \tag{2.18}$$

so that

$$E = \epsilon\frac{h'}{3}\,. \tag{2.19}$$

In full generality $M'/E = f(x)$ could be an arbitrary positive function of x. But we can always make a coordinate transformation to $\tilde{x}(x)$ determined by

$$\frac{dx}{d\tilde{x}} = \frac{1}{6\pi G\rho b^2 a t_0^2},$$

so that with respect to the new coordinate M'/E =constant. Hence we just fix the coordinate x (up to a constant shift) by this choice. In addition, we have chosen uniform bang time, $t_B(x) \equiv 0$. This is a true restriction. With this we have reduced the three free functions of x to one, $h(x)$ which defines the density profile. Furthermore, we have introduced the parameter ϵ such that for $\epsilon = 0$ we reproduce the matter dominated Friedmann solution. We may also require $|h(x)| \leq 1$ so that ϵ indicates the amplitude of the perturbations. We do this in one of the examples below.

The above requirement for a singularity at some time $t \neq 0$ now reduces to $MM'' < M'^2/3$. (Strictly our derivation applies only for $M' \neq 0$. For $M' \propto E = 0$, one sees directly from Eq. (2.16) that $M'' \propto E' < 0$ is the necessary and sufficient condition for $a = 0$ at some time $t > t_B$.) We have found that most interesting mass profiles satisfy this condition for some values of x and therefore have singularities at some time in some places. This is not surprising but actually expected from gravitational collapse. However, when over densities become very high and we approach the collapse, pressure forces and heating become important and our simple pressure-less dust model for matter no longer holds. In order to be able to stay within the present framework, we therefore demand that such singularities be in the future and not in the past for the density profiles under consideration.

Let us consider as a first example

$$h(x) = \cos(kx)\,.$$

Then the condition for the existence of a singularity (at $t \neq 0$) becomes

$$-\left(\epsilon\cos(kx) + \epsilon^2\cos^2(kx)\right) < (\epsilon^2/3)\sin^2(kx)\,,$$

which is always satisfied for some values of x, irrespective of k and ϵ. A similar behavior is expected whenever h is not a convex function, but a function representing several under- and over-densities cannot be convex.

However, this is not so important for our considerations. As we have said, the requirement of singularities to be absent is mainly a technical one and it is actually sufficient not to have a singularity in the past.

Using the above expression for a (for $M > 0$) and the ansatz (2.17,2.19) for M and E, we find that $a = 0$ is equivalent to

$$\frac{(1+\epsilon h)h''}{\epsilon h'^2 - 3(1+\epsilon h)h''} = \frac{-1}{3}\frac{1}{1-\frac{\epsilon h'^2}{3(1+\epsilon h)h''}} = \frac{1}{2}\frac{\cosh(\eta/2)}{\sinh^3(\eta/2)}(\sinh\eta - \eta) - 1 > -\frac{1}{3}\,. \quad (2.20)$$

Interestingly, in extremal positions of h, with $h' = 0$, the l.h.s. of the above expression is exactly $-1/3$. This comes from the fact that for this case $\eta = 0\ \forall\ t$ and we have to replace the condition that there is no singularity before some given time t_0 by $a(t) > 0$ for $t < t_0$ using expression (2.16) for $a(t)$. If $h''' = 0$ when $h' = 0$ (as in our example) one can show that in the positions where h has a maximum, hence $h' = 0$ and $h'' < 0$, $1 + \epsilon h > 0$, singularities occur first. Furthermore, when $1 + \epsilon h > 0$ and $h'' < 0$, the denominator of the l.h.s. of Eq. (2.20) is larger than 1 and hence the l.h.s. becomes larger than $-1/3$. Therefore, there exists a finite value $\eta_s(x)$ where Eq. (2.20) is satisfied and $a(x, \eta_s(x)) = 0$. If, on the contrary, $1+\epsilon h > 0$ and $h'' > 0$ the l.h.s. of Eq. (2.20) is smaller than $-1/3$. For positions in the vicinity of an extremum this implies that if the extremum is a minimum of h, the position x does not encounter a singularity in the future while positions close to maxima do.

Let us study in more detail the request that the second singularity (not the big bang one) lies in the future, $t > t_0$. Using the expression (2.8) for t, we can rewrite the condition $a(x, \eta_s) = 0$ as

$$\frac{(1+\epsilon h)h''}{\epsilon h'^2 - 3(1+\epsilon h)h''} = \frac{9}{4}\frac{\cosh(\eta_s/2)}{\sinh^3(\eta_s/2)}\frac{t_0^2 t(x,\eta_s)\epsilon^3 h'^3}{(1+\epsilon h)} - 1\,.$$

The condition $t(x, \eta_s) > t_0$, for $h' < 0$ which we shall consider hence $\eta_s < 0$ for $t(x, \eta_s) > 0$, then becomes

$$\frac{(1+\epsilon h)}{\epsilon^3 h'^3}\left[1 + \frac{(1+\epsilon h)h''}{\epsilon h'^2 - 3(1+\epsilon h)h''}\right]\frac{4}{9t_0^3} < \frac{\cosh(\eta_s/2)}{\sinh^3(\eta_s/2)}\,.$$

This equation for $\eta_s(x)$ can only be solved numerically. However, often we realize that the l.h.s. is smallest at small $|h'|$ i.e. for small values of $|E(x)|$. Hence singularities will develop first in positions with small $|h'|$. This requires also small $|\eta_s|$ so that we may develop the scale factor a and t in η_s. The above inequality then leads to power law relations and inserting the above expression for $E = (3/2)M' t_0^2$ yields the constraint

$$1 + \frac{(3t_0^2)^{7/3}3^{1/3}2^{2/3}}{80}\left(6M''M^{1/3} - \frac{M'^2}{M^{2/3}}\right) > 0\,,$$
$$1 - \frac{1}{20}(t_0 k)^{2/3}\Big(6\epsilon\cos(kx)\left(1+\epsilon\cos(kx)\right)^{1/3} + \frac{\epsilon^2\left(\sin\left(kx\right)\right)^2}{\left(1+\epsilon\cos\left(kx\right)\right)^{2/3}}\Big) > 0. \quad (2.21)$$

The first inequality is general while for the second inequality we have chosen $h = \cos(kx)$. In Fig. 2.1 we plot the constraint for this case together with the condition to use the limiting solution for $E = 0$, (2.16), (which is not necessary for our analysis) in the ϵ–λ plane, where λ denotes the wavelength of the perturbation $\lambda = 2\pi/k$.

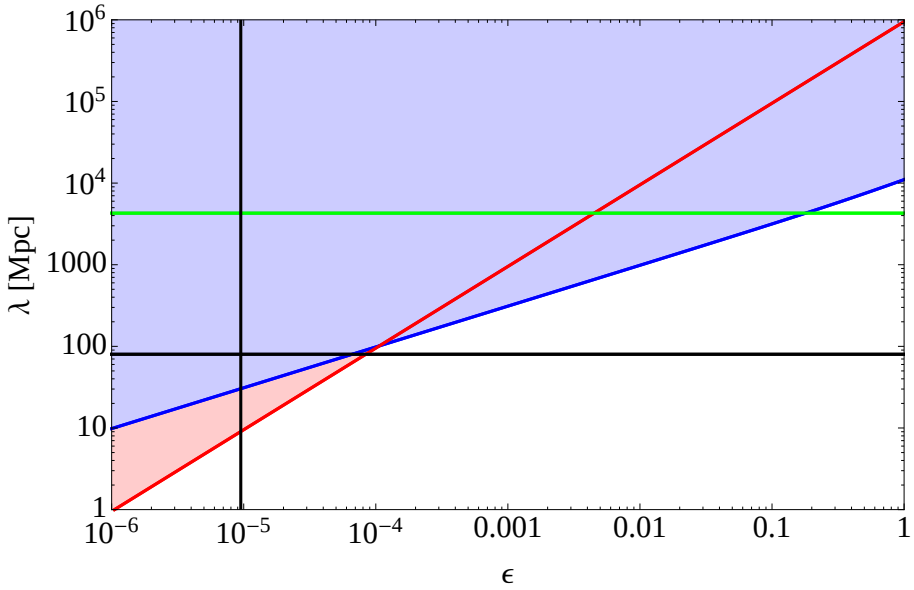

Figure 2.1: The region above the blue line has singularities in the future only. While the red line describes the condition to use the limiting solution for $E = 0$, (2.16). This can be used when $tE^3/M \ll 1$, where with "$\ll$" we mean at least two orders of magnitude smaller. The two black lines describe the physical parameters $\epsilon = 9.5 \times 10^{-6}$ and $\lambda = 80$ Mpc. The green line is the Hubble scale H_0^{-1}. With physical parameters we mean an amplitude as determined by WMAP [98] observations and a wavelength agrees with the size of the largest observed voids [99] which is about 40-90 Mpc. More precisely we find ϵ requiring that at early time there is only a single density fluctuation in each Hubble distance. This leads, at first order, to $\delta = 8\pi^2\epsilon/15$, and the matter density fluctuation at early times, $\delta \cong 5 \times 10^{-5}$ can be inferred from WMAP observations. For more details see [94].

2.3 The distance redshift relation in a wall universe

2.3.1 Generalities

Redshift

We now consider a photon emitted from a source at some position and time $(t_s, \mathbf{x}_s)$ arriving in our telescope at position and time $(t_0, \mathbf{x}_0)$. We denote the matter 4-velocity field, hence the 4-velocity of source and observer by $u(t, \mathbf{x})$ and the photon 4-velocity by n. The redshift of the source, z is then given by

$$1 + z = \frac{g(n,u)|_s}{g(n,u)|_0}\,. \tag{2.22}$$

We consider a co-moving source and observer, hence $u = \partial_t$ and normalize the affine parameter of the photon, s, such that $n^0(s_0) = 1$. The redshift then reduces to

$$1 + z = n^0|_s \tag{2.23}$$

for our geometry with $g_{00} = -1$ and $g_{0i} = 0$. From the geodesic equation for the photon we infer that its momenta in y_1- and y_2-direction are simply redshifted so that

$$J_1 \equiv b^2 n^1 = b^2 \frac{dy_1}{ds} = \text{const.} \qquad \text{and} \qquad J_2 \equiv b^2 n^2 = b^2 \frac{dy_2}{ds} = \text{const.} \tag{2.24}$$

hence

$$(n^x)^2 = \left(\frac{n^0}{a}\right)^2 - \frac{1}{a^2 b^2}\left(J_1^2 + J_2^2\right). \tag{2.25}$$

From the geodesic equation for n^0 we can now derive the evolution of the redshift:

$$\frac{dz}{ds} = -\frac{dn^0}{ds} = (1+z)^2 \frac{\dot{b}'}{b'} + \frac{J_1^2 + J_2^2}{b^2}\left(\frac{\dot{b}}{b} - \frac{\dot{b}'}{b'}\right). \tag{2.26}$$

Here we have used $a = b'/E$ to eliminate the scale factor a. Note also that the prime and the dot in the above equation denote partial derivatives while d/ds is a total derivative along the path of the photon.

Distance

The evolution of the distance to the source is given by the Sachs focussing equation [49],

$$\frac{d^2 D}{ds^2} = -\left(|\sigma|^2 + \mathcal{R}\right) D\,. \tag{2.27}$$

D is the angular diameter distance to the source, σ is the complex scalar shear of the light bundle which we define below and

$$\mathcal{R} = \frac{1}{2} R_{\mu\nu} n^\mu n^\nu = 4\pi G T_{\mu\nu} n^\mu n^\nu = 4\pi G (1+z)^2 (\rho + \bar{P})\,. \tag{2.28}$$

Here $\bar{P}$ is the pressure in the direction of the photon. The important point is that this quantity is non-negative for any energy momentum tensor which satisfies the dominant energy condition $\rho \geq \bar{P}$ in all directions, hence also for a cosmological constant where we have $\mathcal{R} \equiv 0$. In terms of the affine parameter of the photon, the growth of the angular diameter distance to the source is not accelerated. If the dominant energy condition is satisfied $D(s)$ is always a concave function. Furthermore, clustering which leads to the production of non-vanishing shear is only increasing the deceleration of D as function of the affine parameter s. But of course we do not measure this function but $D(z)$ which can behave very differently.

The complex shear of the light ray bundle is defined as follows (appendix 7.7.3. in [50]): We consider two spatial orthonormal vectors e_1 and e_2 which are normal

to both, u and n at the observer and are parallel transported along n, such that $\nabla_n e_a = 0$ for $a = 1, 2$. The vectors e_1, e_2 are a basis of the so called 'screen'. Note that we do not require that u be parallel transported along n, hence e_1, e_2 are in general not normal to u elsewhere than at the observer, where we have given their initial conditions. The complex shear is defined by

$$\sigma = \frac{1}{2} g(\epsilon, \nabla_\epsilon n)\,, \qquad \epsilon \equiv e_1 + i e_2. \tag{2.29}$$

In order to compute the shear we must know n not only along the photon geodesic itself but we must determine its derivatives in directions normal to n. We shall directly use the transport equations [50]. For a vorticity free ray bundle (which is the case here) with expansion rate $\theta \equiv \frac{1}{2} n^{\mu}_{;\mu}$ these are

$$\dot{\theta} + \theta^2 + \sigma_1^2 + \sigma_2^2 = -\mathcal{R}, \tag{2.30}$$

$$\dot{\sigma}_1 + 2\theta\sigma_1 = -\mathrm{Re}\,(\mathcal{F})\,, \tag{2.31}$$

$$\dot{\sigma}_2 + 2\theta\sigma_2 = \mathrm{Im}\,(\mathcal{F})\,, \tag{2.32}$$

where $\sigma_1 = \mathrm{Re}\,(\sigma)$, $\sigma_2 = \mathrm{Im}\,(\sigma)$, and $\mathcal{F} = \frac{1}{2} R_{\alpha\mu\beta\nu} \bar{\epsilon}^{\alpha} \bar{\epsilon}^{\beta} n^{\mu} n^{\nu}$. To determine the shear σ we need to know the initial conditions for the differential equations (2.30) to (2.32). It is possible to determine the behavior of the shear and the expansion of the light near the vertex [100]. Choosing the affine parameter of the photon to vanish at the observer position, $s_0 = 0$, these are

$$\sigma(s) = -\frac{s}{3} \bar{\mathcal{F}}_0 + O\left(s^2\right), \tag{2.33}$$

$$\theta(s) = \frac{1}{s}\left(1 - \frac{1}{3}\mathcal{R}_0 s^2\right) + O\left(s^3\right). \tag{2.34}$$

$\mathcal{F}_0$ and $\mathcal{R}_0$ are the values of $\mathcal{F}$ and $\mathcal{R}$ at the observer position. The light bundle expansion θ diverges at the observer position, but we can consider an initial condition not exactly at the observer. This choice can affect the numerical precision. After determining $\mathcal{R}$, ϵ and $\mathcal{F}$ for a given geometry and photon direction, we can solve the system (2.30) to (2.32) together with the Sachs focusing equation (2.27) numerically.

2.3.2 'Realistic' walls

We want to investigate whether the system of equations derived above for $z(s)$ and $D(s)$ can lead to a distance-redshift relation close to the one observed. For wall universes we consider,

$$\mathcal{R} = 4\pi G\rho(1+z)^2 = \frac{2(1+z)^2}{3t_0^2 b^2 a}\,. \tag{2.35}$$

For a chosen density contrast $h(x)$ we can determine $b(t, x)$ and $a(t, x)$ and solve the photon geodesic Eq. (2.26) for a given angle θ_0 of the observed photon w.r.t. the y-plane,

$$\cos\theta_0 = \frac{\sqrt{J_1^2 + J_2^2}}{b(x_0, t_0) n^0(0)}\,. \tag{2.36}$$

We again set the initial value of the affine parameter to 0, hence $x_0 = x(0)$ etc.

We have investigated two choices for $M(x)$. The first is simply

$$M(x) = \frac{2}{9t_0^2}\left(1 + \epsilon\cos(kx)\right)$$

which we have already discussed before. The results for this case are shown in Fig. 2.2.

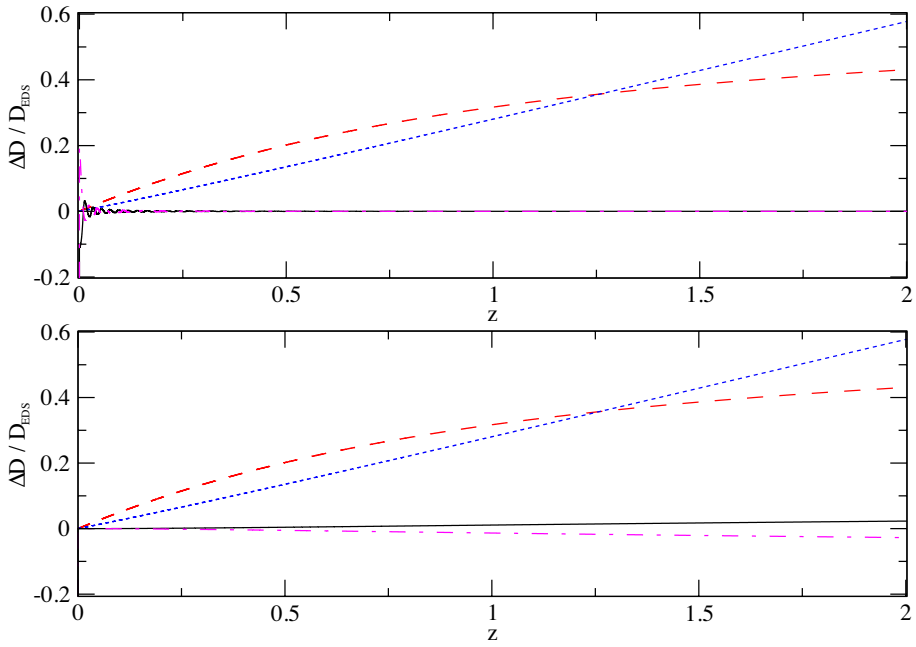

Figure 2.2: We show the relative luminosity distance redshift relation $\frac{\Delta D(z)}{D_{EdS}(z)} = \frac{D(z)-D_{EdS(z)}}{D_{EDS}(z)}$, for different models with luminosity distance $D(z)$. The blue dotted curve is for a Milne Universe, the red dashed curve is for ΛCDM universe with $\Omega_\Lambda = 0.7$ and $\Omega_M = 0.3$. The remaining two lines are our wall universe. The black solid line is in an under density while the purple dot-dashed line is in an over density. In the top panel, we consider light propagating in the x-direction only. The bottom panel is the same but for light propagating in the y-direction. The parameters for the wall model are the physical ones, $\epsilon = 9.5 \times 10^{-6}$ and $\lambda = 80$ Mpc.

The result is quite striking: The deviation from the Einstein-de Sitter distance-redshift relation is very small. On the level of a few percent in the most extreme case. Much smaller than the deviation for an open (Milne) Universe or even for ΛCDM. Hence voids and walls with the chosen parameters cannot simulate the observed distance redshift relation. We have also studied different values of the parameters (ϵ, k), but all cases which are such that there is no singularity before t_0 lead to small deviation from Einstein-de Sitter. Only for wavelengths of approximately Hubble scale, $k \sim H_0$, where we can choose $\epsilon \sim 10^{-3}$ do the deviations become relatively large. But the density profile chosen here does not at all lead to a relation that resembles the observations.

As a second profile we consider thin, highly concentrated over-dense walls with an exponential profile:

$$h\left(x\right)=\frac{\lambda}{\sqrt{2\pi\sigma^{2}}}\sum_{i}\exp\left(\frac{-\left(x-x_{i}\right)^{2}}{2\sigma^{2}}\right)-1, \tag{2.37}$$

where $\lambda=x_{i+1}-x_{i}$. In the limit $\sigma\ll\lambda$ the mean of $h\left(x\right)$ vanishes and $\min_{x}h\left(x\right)=-1$. Again, we choose ϵ such that there is no singularity before t_{0}. The results for this profile are shown in Fig. 2.3.

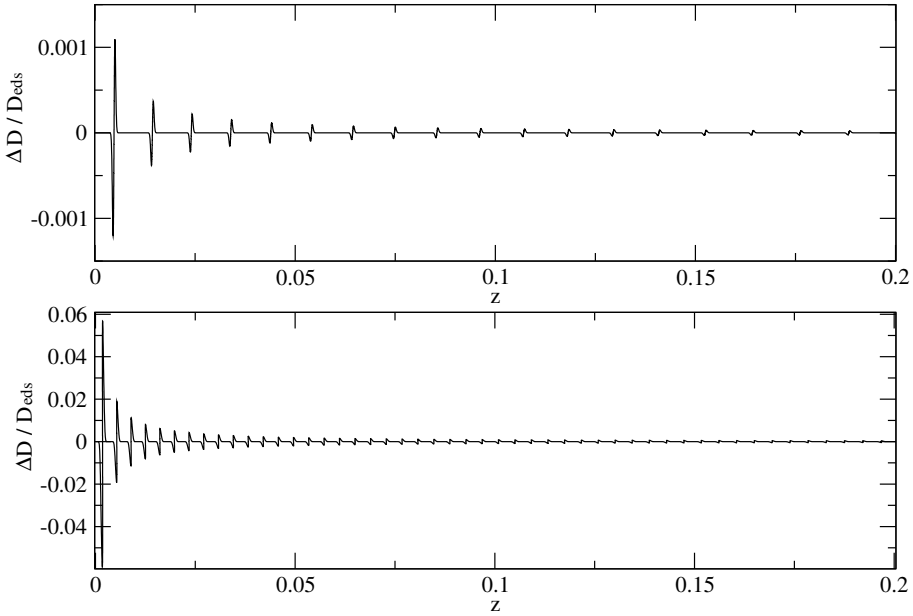

Figure 2.3: We show the relative difference between the distances in 'realistic' wall models and in EdS universe for photons propagating in x-direction. The top panel is obtained with $\epsilon=10^{-9}$, $\lambda=40$ Mpc and $\sigma=1$ Mpc, while the bottom one with $\epsilon=5\times10^{-8}$, $\lambda=15$ Mpc and $\sigma=1$ Mpc. In both cases the observer is at the center of the void. We have checked that the order of magnitude does not change for an observer in an over density. In the second case, we see that we obtain an effect of the same order of magnitude as the swiss cheese universe discussed in [101].

We have obtained the following result in these two examples (and other profiles which we do not present here explicitly): The modification of $D(z)$ never goes beyond the case of the open universe. We do not obtain acceleration by a series of dense walls. Even though we present here only two simple profiles, we think the conclusion is valid beyond these cases: if a photon passes through many *compensated* under- and over-densities in the integrated distance $D(z)$ the effect is minute as long as the time the photon spends inside a wall is much smaller than the time scale at which the gravitational potential of the wall evolves. A perturbative (first order) calculation gives a flavour of this effect. Indeed, at first order in the perturbed direction, the difference between $D(z)$ in our models and $D_{EdS}(z)$ of a matter dominated universe

can be written as

$$D_L(z_e) - D_L^{EdS} = (1+z_e)(\eta_o - \eta_e)\left(\frac{\epsilon}{3}(h(\eta_o) + h(\eta_e))\right) - (1+z_e)\int_{\eta_e}^{\eta_o} \frac{2\epsilon}{3} h(\eta)\, d\eta + (1+z_e)\int_{\eta_e}^{\eta_o} d\eta \int_{\eta_e}^{\eta} d\eta' \frac{\epsilon}{15} h''(\eta')\,\eta' - \frac{1+z_e}{\mathcal{H}_e}\int_{\eta_e}^{\eta_o} d\eta\ \frac{\epsilon}{15} h''(\eta)\,\eta, \quad (2.38)$$

where the subscripts e and o respectively mean that the conformal time is evaluated at the source (emission) or at the observer and expresses the perturbation of the energy density in under and over densities (see Appendix C for a derivation of the linearized result). From this expression, valid in the linear regime only, and for a periodic perturbation, it becomes clear that the deviation of $D_L(z)$ with respect to D_L^{EdS} depends on the amplitude ϵ of the perturbation and on the values of the conformal time at the source and at the observer. In the case of periodic perturbations, the contributions from photon path are mostly cancelled in the integral terms. Of course in the full non-linear calculation there is no simple relation between the matter over density h and the gravitational potential. In this case in principle the full non-linear Einstein equation have to be solved and Eqs. (2.26) and (2.27) govern $D_L(z)$.

Surprisingly, however, our non-linear simulations show that this result holds also to some extent in the non-linear regime. Note that, even though our value of ϵ is small, the over densities in the walls are large at late times, such that they develop singularities soon after today and we are deeply in the non-linear regime. While we do not have a proof that our conclusion holds in all cases, we have tested this also with other periodic wall profiles.

In Fig. 2.4 we show the deviations of the expansion rates with respect to the Hubble expansion in EdS universe. We note that the deviations in the unperturbed directions are small. However, in the perturbed direction these deviations can be large locally inside a wall, and they would be measurable by direct, local measurements of $H(z)$. However, they compensate when averaged over a wall thickness and do not show up in integrated quantities like $D(z)$.

2.3.3 Mimicking dark energy

Yoo et al. [97] have shown that in an LTB model every given distance–redshift relation can be mimicked by a suitable choice of the density profile. The same is true for a wall universe. For a given function $D(z)$ we can find a density profile which leads to exactly this distance–redshift relation for a photon coming in x-direction. First of all, for such a photon the shear vanishes for symmetry reasons and $\mathcal{R}$ is given by (2.35). To find the density profile, which is equivalent to finding $M(x)$ or $M(z) \equiv M(x(z))$ we have to solve the following coupled system of six ordinary differential equations (in principle none of the other equations couples to (2.41) since both, F_M and F_β do not depend on x explicitly), which is very similar to the system

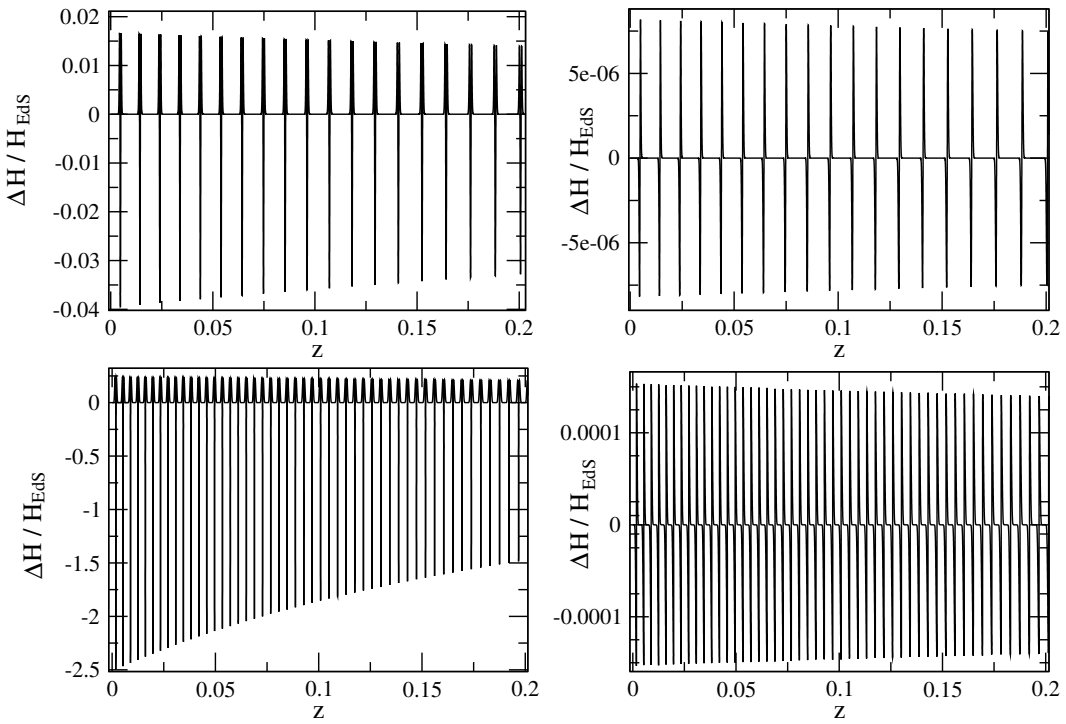

Figure 2.4: We show the relative differences between the expansion rates in the thin, highly concentrated over-dense wall model and the Hubble expansion in EdS universe. The top panels are obtained with $\epsilon = 10^{-9}$, $\lambda = 40$ Mpc and $\sigma = 1$ Mpc, while the bottom ones with $\epsilon = 5 \times 10^{-8}$, $\lambda = 15$ Mpc and $\sigma = 1$ Mpc. In both cases the observer is at the center of the void. The left panels show the expansion rates in the perturbed direction, while the right ones in the y-direction. The results for the cosine profile not shown here are similar to the two top panels.

solved in Ref. [97]:

$$\frac{dM}{ds} = F_M\left(t, z, M, \beta, \zeta\right), \tag{2.39}$$

$$\frac{d\beta}{ds} = F_\beta\left(t, z, M, \beta, \zeta\right), \tag{2.40}$$

$$\frac{dx}{ds} = \frac{F_M\left(t, z, M, \beta, \zeta\right)}{\beta}, \tag{2.41}$$

$$\frac{dt}{ds} = 1 + z, \tag{2.42}$$

$$\frac{dz}{ds} = \frac{\zeta}{\frac{dD}{dz}}, \tag{2.43}$$

$$\frac{d\zeta}{ds} = -4\pi\left(1+z\right)^2 \rho D, \tag{2.44}$$

where we have defined

$$\zeta = \frac{dz}{ds}\frac{dD}{dz} \quad \text{and} \quad \beta = \frac{\frac{dM}{ds}}{\frac{dx}{ds}} = M' = \frac{2}{3t_0^2}E\,. \tag{2.45}$$

In Appendix 2.5.1 we give the derivation of this system and the detailed expressions for F_M and F_β. There, we also explain the method used to specify the initial conditions at the observer. All the constraints are fixed by requiring the system to have no critical points. Note also that $z(s)$ need not to be monotonic. If $dz/ds = 0$ at a value of s where $\zeta = dD/ds \neq 0$, the derivative dD/dz is not well defined. This is, however, not the case of a ΛCDM Universe which we want to mimic here. We are then left with one initial condition, which we choose by requiring

$$H_0 = \left.\frac{\dot{a}}{a}\right|_{s_0} = \left.\frac{\dot{b}}{b}\right|_{s_0}\,, \tag{2.46}$$

i.e. the value of the Hubble rate at the observer today does not depend on direction. In Fig. 2.5 we show $M(x)$ as well as its derivative with respect to the x coordinate, $\beta\,(x)$, for the solution mimicking the ΛCDM expression for $D(z)$, for $\Omega_K = 0$, $\Omega_m = 0.3$ and $\Omega_{DE}(z) = 0.7$ =constant.

$$\begin{aligned} D(z) &= \frac{1}{1+z}\chi_K\left(\int_0^z \frac{dz'}{H(z')}\right) \quad \text{where} \\ \chi_K(r) &= \frac{1}{\sqrt{K}}\sin(r\sqrt{K})\,, \quad \text{and} \\ H(z) &= H_0\Big(\Omega_m(1+z)^3 + \Omega_K(1+z)^2 + \Omega_r(1+z)^4 + \Omega_{DE}(z)\Big)^{1/2}\,. \end{aligned} \tag{2.47}$$

In Fig. 2.6, we show how the luminosity distance deviates when the observer looks at photons coming in with different angles θ_0. For $\theta_0 = 90$ degrees, we have photons traveling in x-direction, in this case the luminosity distance is fitted to the one of ΛCDM by solving the system of Eqs. (2.39-2.44) with the functions $M(x)$ and $\beta(x)$ shown in Fig. 2.5. It is interesting to remark that a given angle of $\theta_0 \in [0; 90]$ degrees at the observer corresponds to an angle at the emission $\theta_e > \theta_0$. This is a consequence of the spacetime geometry induced by the walls: due to the clustering in direction x, corresponding to $\theta = 90^o$, its expansion slows down in time.

In Fig. 2.7, we present the density profile corrected by the isotropic expansion rate, $(1+z)^{-3}\rho(z)/\rho_0$, $\rho_0 = \rho(z=0)$, obtained for our model to mimic ΛCDM luminosity distance. Finally, in Fig. 2.8, we plot the expansion rates in the longitudinal and transverse directions, $H_a = \dot{a}/a$ and $H_b = \dot{b}/b$. It is interesting to estimate roughly the features of the under density needed to fit ΛCDM luminosity distance. For example, if one considers the highest redshift for which we have data from supernovae, at around $z \sim 1.7$. This roughly corresponds to a size $\sim H_0^{-1}$. (Of course we have another data point from the CMB. The angular size of the acoustic oscillations provides an excellent measure of the angular diameter distance to the

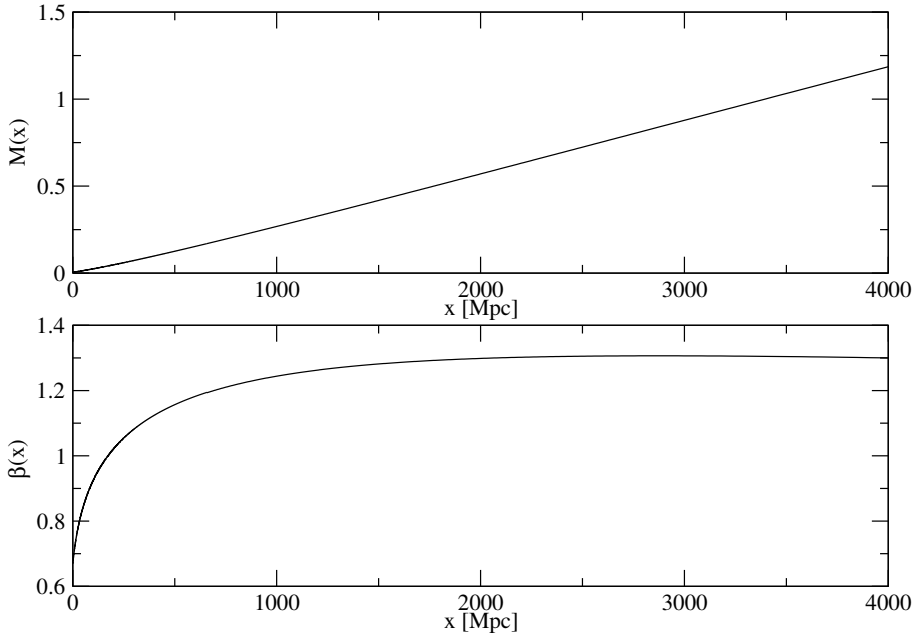

Figure 2.5: We show the function $M(x)$, top panel, and its derivative $\beta(x)$, bottom panel. In principle, there is a entire family of functions $M(x)$ parametrized by the initial value $M(0) = M_0$ that we are free to choose (appendix A). Here, we present the solutions corresponding to $H_0 = \frac{\dot{a}}{a}\big|_{s_0} = \frac{\dot{b}}{b}\Big|_{s_0}$.

last scattering surface, $z \simeq 1090$. But this is not very relevant in our context as the Universe is to a good approximation matter dominated from $z = 2$ to $z = 1090$.) An under density of the size of the order of the Hubble distance is necessary to mimic ΛCDM with our walls. Moreover, we can also determine the ratio of the energy density normalized at the observer to the energy density in an Einstein-de Sitter model at $z \sim 1.7$ which is about 4. At high redshift, $z \gtrsim 10$ the anisotropy is very small and the Universe is close to a Friedmann Universe with about 5 times the matter density obtained from local estimates.

2.3.4 Redshift drift

In the previous section we have fixed $M(x)$ to reproduce the distance redshift relation of ΛCDM universe. Of course, having one free function to play with, namely $M(x)$, we expect to be able to fit one function, in our case $D(z)$. If we now proceed to another, independent observable, we shall most probably not fit it. We have done this by looking at the redshift drift, defined as the rate of change of the redshift of a co-moving source per unit of observer time. In a Friedmann Universe the redshift drift is simply

$$\frac{dz}{dt_0} \equiv \lim_{\Delta t_0 \to 0} \frac{z(t_s + \Delta t_s) - z(t_s)}{\Delta t_0} = H_0(1+z) - H(z)\,, \tag{2.48}$$

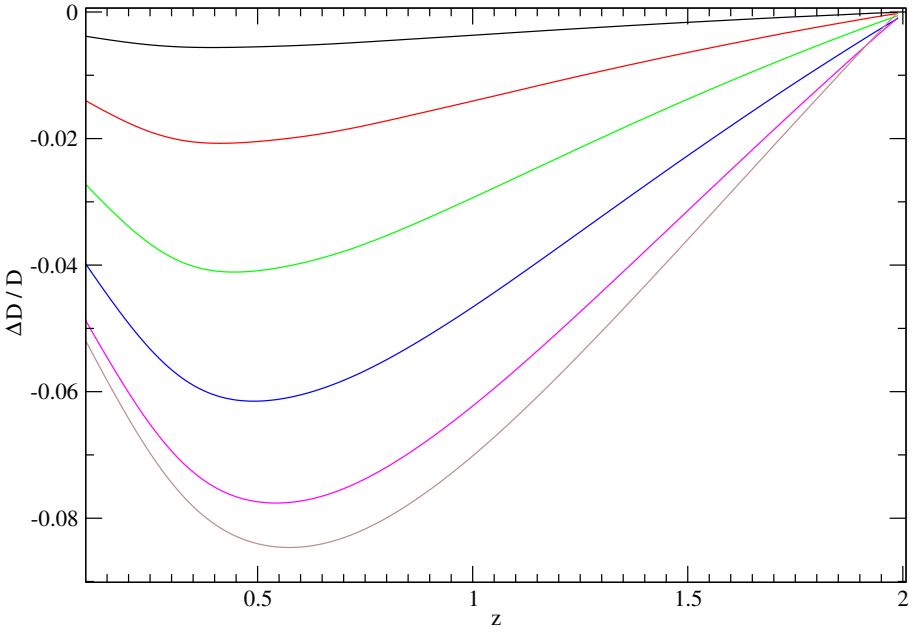

Figure 2.6: We show the relative differences between luminosity distances for photons traveling in the x-direction (perpendicular to the walls) and photons observed with an angle θ_0 (see Eq.(2.36)). From the top to the bottom, we respectively have $\theta_0 = 75$, 60, 45, 30, 15, 5 degrees.

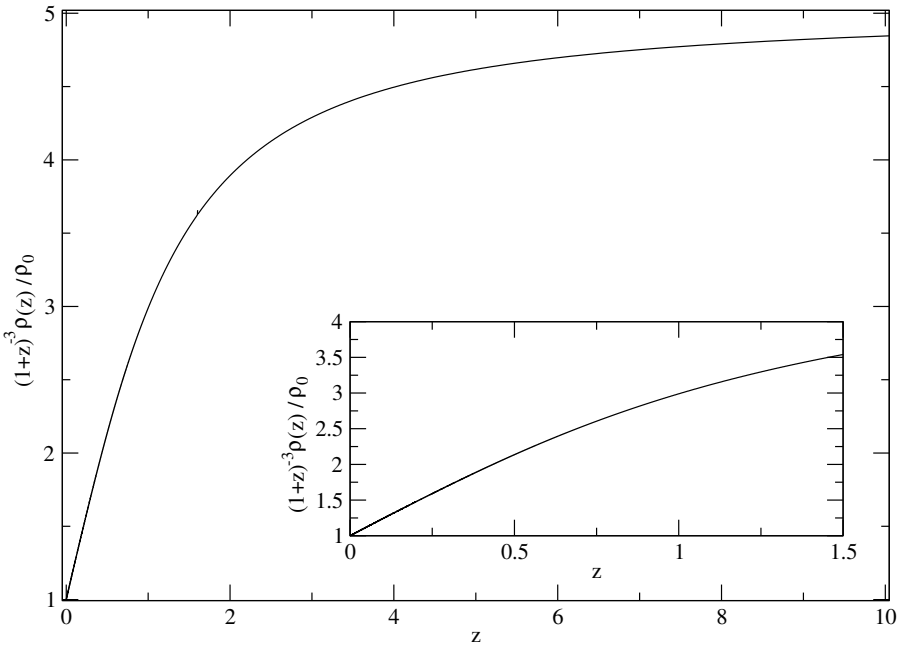

Figure 2.7: We show the ratio of our density profile to the Einstein-de Sitter one as a function of the cosmological redshift.

where $H(z) = H(t_s)$ and H_0 denote the Hubble parameter at the source position at time t_s and at the observer at the moment t_0. We have computed the correspond-

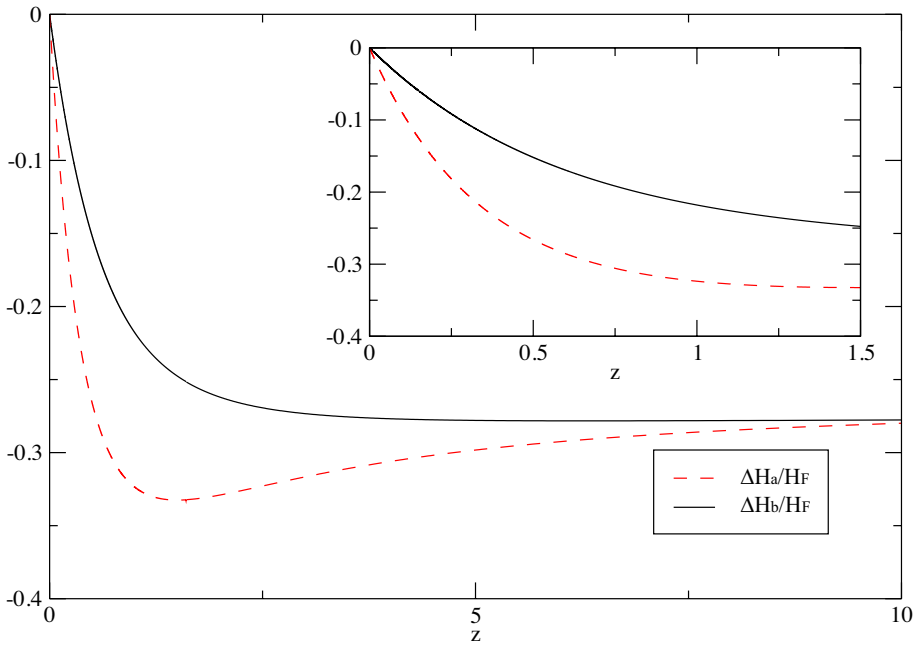

Figure 2.8: We show the relative expansion rates in the transverse and longitudinal directions as functions of the cosmological redshift. We use the following notation: $\Delta H_{a,b} = H_{a,b} - H_F$, where H_F is the expansion rate in an Einstein-de Sitter universe, and $H_{a,b}$ are the expansion rates in the longitudinal and transverse directions, normalized to the their values at the observer.

ing function (for light rays in x-direction) from our solution $M(x)$. The general expression for the redshift drift of a wall Universe in x–direction is (see Appendix 2.5.2),

$$\begin{aligned} \frac{dz}{dt_0} &= (1+z)\int_0^z \left(\frac{\ddot{b}'}{\dot{b}'}\right)(1+z')^{-2}\,dz' \\ &= -(1+z)\int_0^z \left(4\pi G\rho - \frac{2M}{b^3}\right)\frac{a}{\dot{a}}\,(1+z')^{-2}\,dz' \ . \end{aligned} \tag{2.49}$$

Since we do not require $M_0 = 0$ as in LTB model, we can in principle have a positive redshift drift at low redshift; but we do not obtain this for our best fit profile $M(x)$ with $t_B(x) \equiv 0$. The result is compared with ΛCDM in Fig. 2.9.

Clearly the redshift drift for the two cosmologies are very different. We do have a second function to play with, the bang time $t_B(x)$, so that we could probably fix this observable. This has been done for LTB models in [102]. However, as it is shown there, models which have both, the same redshift distance relation and the same redshift drift as ΛCDM can be ruled out with a third observable, the kinematic Sunyaev-Zel'dovich effect which comes from the recession velocity of clusters.

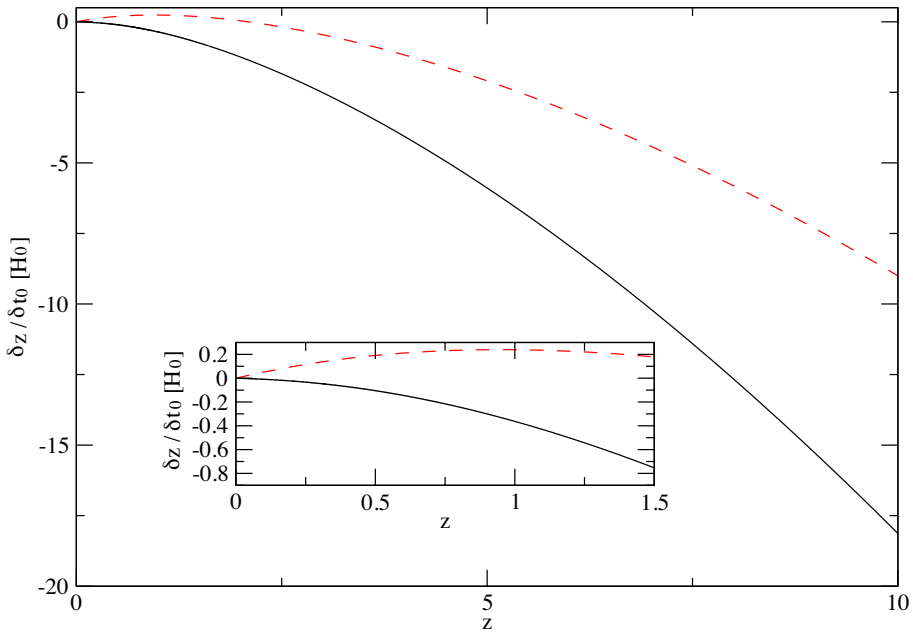

Figure 2.9: We show the redshift drift for the wall Universe (black solid line) which mimics the distance redshift relation of ΛCDM and compare it with the redshift drift of the latter (red dashed line).

2.4 Conclusions

We have studied the effect of matter perturbations on the luminosity distance in a model with planar symmetry described by the metric (2.1). Considering 'realistic' walls we find that the effect from density inhomogeneities is very small, it nearly averages out. It leads to fluctuations of the luminosity distance around the 'background' distance, but not to a significant global shift. Our results (Fig. 2.3) show that these fluctuations are due to matter inhomogeneities at the source and the observer positions, without any relevant contribution from the integrated effects of light propagation, like in the linear approach (2.38). Hence we can not mimic acceleration with many dense walls which grow by gravitational instability. Since we consider pressure-less matter only, the amplitude of density fluctuations is limited by the presence of singularities. This is a limitation of the model.

After having shown that 'realistic' wall models can not reproduce the observed distance-redshift relation, we have determined the density profile which can mimic it. We have fixed the free function of our model, $M(x)$, to mimic the luminosity (or angular) distance of the ΛCDM universe. We have shown that the observation of the redshift drift can distinguish between this model and ΛCDM. Abandoning the assumption of an uniform bang time we could arrange the second degree of freedom, $t_B(x)$, to fit the redshift drift too. We have found that the redshift drift in our model can be positive at low redshift, contrarily to the LTB model [103].

With our solution $M(x)$ we can fit ΛCDM distance for photons coming in x-direction for positive x only. This preferred direction corresponds to the radial incoming direction for LTB model. The deviation from ΛCDM for photons coming from different angles is typically a few percent (see Fig. 2.6).

Acknowledgements

This work is supported by the Swiss National Science Foundation.

2.5 Appendix

2.5.1 Derivation of the system of differential equations and initial conditions

The system

Here we derive in more detail the system (2.39) to (2.44) and give the initial conditions used for the solution.

Since we choose the photon affine parameter such that $n^0|_0 = 1$ we have

$$1 + z(s) = n^0(s) = \frac{dt}{ds}.$$

Furthermore, the null condition for a light ray in x–direction implies

$$\left(\frac{dt}{ds}\right)^2 = \left(\frac{b'}{E}\right)^2 \left(\frac{dx}{ds}\right)^2 = \left(\frac{2b'}{3t_0^2 M'}\right)^2 \left(\frac{dx}{ds}\right)^2. \tag{2.50}$$

The geodesic equation gives

$$\frac{dz}{ds} = \frac{d^2t}{ds^2} = -\frac{\dot{a}}{a}(1+z)^2 = -\frac{\dot{b}'}{b'}(1+z)^2\,. \tag{2.51}$$

Hence, when the expansion in x-direction changes into contraction, $\dot{a} = 0$, also dz/ds passes through zero. However, this does not happen in our case which mimics ΛCDM. Noting that geodesics in x-direction have no shear, the Sachs focusing equation yields

$$\frac{d^2z}{ds^2}\frac{dD}{dz} + \left(\frac{dz}{ds}\right)^2 \frac{d^2D}{dz^2} = -4\pi G\rho\,(1+z)^2\,D, \tag{2.52}$$

where we have used $\mathcal{R} = 4\pi G\,(1+z)^2\,\rho$. We can now rewrite these equations in terms of the system (2.39) to (2.44). To find the functions F_M and F_β we first derive

the following useful relations

$$\dot{\tau} = \frac{2}{3t}\tau, \tag{2.53}$$

$$\tau' = \tau\left(2\frac{\frac{d\beta}{ds}}{\frac{dM}{ds}} - \frac{2}{3}\frac{\beta}{M}\right), \tag{2.54}$$

$$b' = -\frac{8}{9t_0^4}\frac{\tau}{\beta}\left(S - 2\tau S'\right) - \frac{16}{3t_0^4}\tau^2\frac{M}{\beta^2}\frac{\frac{d\beta}{ds}}{\frac{dM}{ds}}S', \tag{2.55}$$

$$\dot{b}' = -\frac{16}{27t_0^4}\frac{\tau}{t}\frac{1}{\beta}\left(S - 3\tau S' - 2\tau^2 S''\right) - \frac{32}{9t_0^4}\frac{M}{\beta^2}\frac{\frac{d\beta}{ds}}{\frac{dM}{ds}}\frac{\tau^2}{t}\left(2S' + \tau S''\right). \tag{2.56}$$

Here S' always indicates the derivative of S with respect to its argument τ while as for all other functions of (t, x) the prime denotes the partial derivative w.r.t. x and the dot the one w.r.t. t. The null condition for the light ray can be written as

$$\frac{dM}{ds}A_1 + \frac{d\beta}{ds}B_1 = \pm 1,$$

with

$$A_1 = -\frac{16}{27t_O^6}\frac{\tau}{\beta^3\left(1+z\right)}\left(S - 2\tau S'\right), \tag{2.57}$$

$$B_1 = -\frac{32}{9t_O^6}\frac{\tau^2 M}{\beta^4\left(1+z\right)}S'. \tag{2.58}$$

The geodesic equation takes the form

$$\frac{dM}{ds}A_2 + \frac{d\beta}{ds}B_2 = 0, \tag{2.59}$$

where

$$A_2 = -\frac{\zeta}{\frac{dD}{dz}}\frac{8}{9t_0^4}\frac{\tau}{\beta}\left(S - 2\tau S'\right) - \left(1+z\right)^2\frac{16}{27t_0^4}\frac{\tau}{t}\frac{1}{\beta}\left(S - 3\tau S' - 2\tau^2 S''\right), \tag{2.60}$$

$$B_2 = -\frac{\zeta}{\frac{dD}{dz}}\frac{16}{3t_O^4}\tau^2\frac{M}{\beta^2}S' - \left(1+z\right)^2\frac{32}{9t_0^4}\frac{M}{\beta^2}\frac{\tau^2}{t}\left(2S' + \tau S''\right), \tag{2.61}$$

with $\zeta = \frac{dD}{ds} = \frac{dz}{ds}\frac{dD}{dz}$. From this we infer

$$F_M\left(t, z, M, \beta, \zeta\right) = \pm\frac{B_2}{A_1B_2 - A_2B_1}, \tag{2.62}$$

$$F_\beta\left(t, z, M, \beta, \zeta\right) = \mp\frac{A_2}{A_1B_2 - A_2B_1}. \tag{2.63}$$

Since τ is a function of M, β and t, we now have expressed everything in terms of our variables (t, z, M, β, ζ) and the given function $D(z)$. Explicitly, F_M and F_β are

given by

$$F_M = \pm\frac{3t_O^2}{4}\beta\left(\frac{6M}{t}\right)^{2/3}\frac{\frac{\zeta}{\frac{dD}{dz}}\frac{3t}{2}\frac{S'}{1+z}+(1+z)\left(2S'+\tau S''\right)}{SS'+\tau SS''-\tau S'^2}\,, \tag{2.64}$$

$$F_\beta = \pm\frac{1}{18t_O^2}\frac{1}{M}\left(\frac{6M}{t}\right)^{4/3}\frac{\frac{\zeta}{\frac{dD}{dz}}\frac{3t}{2}\frac{(S-2\tau S')}{1+z}+(1+z)\left(S-\tau S'-2\tau^2 S''\right)}{SS'+\tau SS''-\tau S'^2}\,. \tag{2.65}$$

Initial conditions

Let us now turn to the initial conditions at $s_0 = 0$. Without loss of generality we can set $x(0) = 0$. Clearly also $z(0) = 0$. From definition (2.45) we have

$$\zeta(0) = \left.\frac{dD}{ds}\right|_{s=0}. \tag{2.66}$$

Since this is an initial condition for the Sachs focusing equation, we have consistently with our affine parameter normalization [100, 104],

$$\zeta(0) = -1. \tag{2.67}$$

From (2.43) we note that our system of coupled differential equations has a critical point z_{cr} defined by

$$\left.\frac{dD}{dz}\right|_{z=z_{cr}} = 0. \tag{2.68}$$

For our ΛCDM parameters $z_{cr} \approx 1.6$. To obtain a regular solution we must therefore impose $\zeta(z_{cr}) = 0$. We remark that Eqs. (2.67) and (2.51) imply

$$\frac{\dot{a}}{a} = H_0, \tag{2.69}$$

where we have used

$$\left.\frac{dD}{dz}\right|_{z=0} = H_0^{-1}.$$

Hence the rate expansion in x-direction coincides with the measured Hubble expansion. In order to solve the system of five differential equations (Eq. (2.41) is an independent equation, since the solution $x(s)$ can also be inferred from Eq. (2.42) via the null condition), five initial conditions are needed. However, we only have two of them

$$z(0) = 0 \qquad \zeta(0) = -1. \tag{2.70}$$

We have two other constraints which we must satisfy at the critical point where (2.68) holds. Denoting the affine parameter at the critical point by s_{cr}, we have

$$z(s_{cr}) = z_{cr} \qquad \zeta(s_{cr}) = 0. \tag{2.71}$$

These lead to two other initial conditions which can be determined using the shooting method. One remaining constraint is needed and we fix it by requiring

$$\left.\frac{\dot{a}}{a}\right|_0 = \left.\frac{\dot{b}}{b}\right|_0 = H_0. \tag{2.72}$$

This last condition fixes $M(0)$ and makes sure that the Hubble rate measured today is the same in any direction. We then numerically integrate the system from the critical point to the observer by varying the three remaining conditions at the critical point until the initial conditions (2.70) and (2.72) are satisfied. This matching is obtained by using the three dimensional Newton-Raphson method. Once the desired precision has been reached, the two remaining initial conditions $\beta(0)$ and $t(0)$ can simply be read from the numerical data.

2.5.2 Derivation of the system of differential equations for the redshift drift

The redshift drift for a LTB model has been derived in [103]. This approach can also be applied to our model. The null condition for the light ray (in x-direction) and the geodesic equation lead to

$$\frac{dz}{dx} = \frac{\dot{b}'}{E}(1+z), \qquad \frac{dt}{dx} = -\frac{b'}{E}. \tag{2.73}$$

We consider two infinitesimally close geodesics at fixed comoving position x, parameterized by

$$\{z_c, t_c\} \quad \text{and} \quad \{z_c + \delta z, t_c + \delta z\}.$$

Since the geodesic $\{z_c, t_c\}$ satisfies (2.73), it follows

$$\begin{aligned} \frac{d\delta z}{dx} &= \frac{\ddot{b}'}{E}(1+z)\,\delta t + \frac{\dot{b}'}{E}\delta z, \\ \frac{d\delta t}{dx} &= -\frac{\dot{b}'}{E}\delta t. \end{aligned}$$

Then, inserting (2.73) we obtain

$$\frac{d\delta z}{dz} = \frac{\ddot{b}'}{\dot{b}'}\delta t + \frac{\delta z}{1+z}, \tag{2.74}$$

$$\frac{d\delta t}{dz} = -\frac{\delta t}{1+z}. \tag{2.75}$$

Integrating (2.75) we find

$$\delta t = \frac{\delta t_0}{1+z}.$$

This solution together with (2.74) leads to

$$\frac{d}{dz}\left(\frac{\delta z}{\delta t_0}\right) = \frac{1}{1+z}\left(\frac{\ddot{b}'}{\dot{b}'} + \frac{\delta z}{\delta t_0}\right).$$

This equation is solved by (2.49). Deriving the Einstein equation (2.3) twice (once w.r.t. x and once w.r.t. t), we obtain

$$\ddot{b}' = \frac{2Mb'}{b^3} - \frac{M'}{b^2}. \tag{2.76}$$

With (2.2) and (2.4) this results in the second line of (2.49).

2.5.3 The linearized approach

We determine the luminosity distance within linear perturbation theory for small deviations from a Friedmann–Lemaître background. Let us define

$$\begin{aligned} a(t,x) &= \bar{a}(t)\left(1+\epsilon f(t,x)\right), && (2.77)\\ b(t,x) &= \bar{a}(t)\left(1+\epsilon g(t,x)\right), && (2.78)\\ \rho(t,x) &= \bar{\rho}(t)\left(1+\epsilon \delta(t,x)\right), && (2.79) \end{aligned}$$

where the unperturbed quantities $\bar{a}(t)$, $\bar{\rho}(t)$ satisfy the Einstein equations for a flat matter dominated Friedmann universe (EdS). The perturbed quantities are determined by the Einstein equations at first order in ϵ,

$$\begin{aligned} \frac{-6t_0^{4/3}g'' + 4t^{1/3}\left(\dot{f}+2\dot{g}\right)}{3t^{4/3}} &= 8\pi G\bar{\rho}\delta, && (2.80)\\ \dot{g}' &= 0, && (2.81)\\ t^{1/3}\left(2\dot{g}+t\ddot{g}\right) &= 0, && (2.82)\\ t_0^{4/3}g'' - t^{1/3}\left(2\dot{f}+2\dot{g}+t\left(\ddot{f}+\ddot{g}\right)\right) &= 0. && (2.83) \end{aligned}$$

Neglecting the decaying mode and imposing that at the beginning the scale factors in all three directions agree, we obtain [94],

$$\begin{aligned} g &= \frac{\delta_O}{3}, && (2.84)\\ f &= \frac{3}{10}\delta_O'' t_O^{4/3} t^{2/3} + \frac{\delta_O}{3}, && (2.85) \end{aligned}$$

where $\delta_O(x) = \delta(t,x) + f(t,x) + 2g(t,x)$ is independent of time. This is a consequence of energy conservation and can also be derived by combining (2.80) to (2.83).

We are interested in finding the relation between δ_O and M, E in the perturbative regime. Following [95] we expand the solution (2.7, 2.8) around $\eta = 0$ in terms of

$\frac{t_B(x)}{t} \ll 1$ and $\frac{E^3 t}{M} \ll 1$. Comparing the expanded solution with the linear one we find

$$M = \frac{2}{9t_0^2}\left(1+\epsilon\delta_O\right), \quad E = \frac{\epsilon\delta_O'}{3}. \tag{2.86}$$

With the ansatz (2.17, 2.19) we can identify $\delta_O(x)$ with $h(x)$ in the perturbative regime.

The angular distance is determined by Sachs focusing equation (2.27). We note that the shear term does not contribute to first order. Since light propagation is not affected by a conformal transformation, it is convenient to work with the conformally related geometry

$$ds^2 = -d\eta^2 + (1+2\epsilon f)\,dx^2 + (1+2\epsilon g)\left(dy_1^2 + dy_2^2\right). \tag{2.87}$$

From this, we compute the Christoffel symbols (here we denote the derivative w.r.t. the conformal time η by a dot)

$$\begin{array}{ccc} & \Gamma^0_{11} \cong \epsilon\dot{f}, & \Gamma^0_{22} = \Gamma^0_{33} \cong \epsilon\dot{g}, \\ \Gamma^1_{10} \cong \epsilon\dot{f}, & \Gamma^1_{11} \cong \epsilon f', & \Gamma^1_{22} = \Gamma^1_{33} \cong -\epsilon g', \\ & \Gamma^2_{20} = \Gamma^3_{30} \cong \epsilon\dot{g}, & \Gamma^2_{21} = \Gamma^3_{31} \cong \epsilon g', \end{array}$$

and the Ricci tensor

$$\begin{aligned} R_{00} &\cong -\epsilon\left(\ddot{f} + 2\ddot{g}\right), \\ R_{10} &\cong -2\epsilon\dot{g}', \\ R_{11} &\cong \epsilon\left(\ddot{f} - 2g''\right), \\ R_{22} = R_{33} &\cong \epsilon\left(\ddot{g} - g''\right). \end{aligned}$$

At 0-order we are free to parametrize the affine parameter s such that $\bar{n}^0 = 1$ and $\bar{n}^i = \delta^{i1}$ (we are interested in the distance in x-direction). With this we obtain the coefficient $\mathcal{R}$

$$\mathcal{R} = -\epsilon\left(\ddot{g} + g'' + 2\dot{g}'\right).$$

Consistently with the parametrization of the affine parameter s such that $n^0(s_0) = 1$, the initial conditions are $D(s_o) = 0$ and $D'(s_o) = -1$. After an integration by parts we find the solution to Sachs focusing equation (2.27),

$$D(s) = (s_o - s)\left(1 + \epsilon g(s_o) + \epsilon g(s)\right) + 2\int_{s_o}^{s} ds'\epsilon g(s'). \tag{2.88}$$

With the above initial conditions for the Sachs focusing equation, we consider a thin light bundle with the vertex at the observer position. Hence the solution (2.88) is the angular diameter distance, see [100]. To determine the luminosity distance we have to compute also the redshift, using the geodesic equation for n^0,

$$1 + z = \frac{g_{\mu\nu}n^\mu u^\nu\big|_e}{g_{\mu\nu}n^\mu u^\nu\big|_o} = n^0\big|_e = 1 - \int_{s_o}^{s_e} ds\ \epsilon\dot{f}, \tag{2.89}$$

where $|_e$ denotes the emission point, the source, and we denote the affine parameter at the source by s_e. With the same geodesic equation we derive the relation between the conformal time η and the affine parameter s, $n^0 = d\eta/ds$,

$$\eta_o - \eta_e = s_o - s_e + \int_{s_o}^{s_e} ds \int_{s_o}^{s} ds' \epsilon \dot{f}(s'). \tag{2.90}$$

In terms of conformal time the luminosity distance then becomes

$$D_L(\eta_e) = (\eta_o - \eta_e)\left(1 + \epsilon g_o + \epsilon g_e - 2\int_{\eta_o}^{\eta_e} d\eta\ \epsilon \dot{f}\right) + 2\int_{\eta_o}^{\eta_e} d\eta\ \epsilon g - \int_{\eta_o}^{\eta_e} d\eta \int_{\eta_o}^{\eta} d\eta' \epsilon \dot{f}. \tag{2.91}$$

All of this is valid in the conformal geometry, where the expansion of the Universe is divided out. Taking into account the expansion of the universe, changes the relation between the affine parameter and conformal time. The luminosity distance scales as [9]

$$\tilde{D}_L = \frac{\bar{a}^2(\eta_o)}{\bar{a}(\eta_e)} D_L = \frac{D_L}{\bar{a}(\eta_e)} = (1 + \bar{z}_e) D_L.$$

Since conformal time is not an observable quantity, we rewrite the distance in term of the observed redshift. We define the observed redshift as $z_e = \bar{z}_e + \delta z_e$ and we compute the correction term. The same calculation as presented in Ref. [9] leads to

$$\left(\frac{d}{dz}\tilde{D}_L\right)\delta z_e = \left((\eta_o - \eta_e) + \mathcal{H}_e^{-1}\right)\delta z_e, \tag{2.92}$$

where

$$\delta z_e = -(1 + z_e)\int_{\eta_o}^{\eta_e} d\eta\ \epsilon \dot{f}. \tag{2.93}$$

Subtracting (2.92) we obtain the distance–redshift relation

$$\begin{aligned} \tilde{D}_L(z_e) &= (1 + z_e)(\eta_o - \eta_e)\left(1 + \epsilon g_o + \epsilon g_e - \int_{\eta_o}^{\eta_e} d\eta\ \epsilon \dot{f}\right) \\ &+ (1 + z_e)\left(2\int_{\eta_o}^{\eta_e} d\eta\ \epsilon g - \int_{\eta_o}^{\eta_e} d\eta \int_{\eta_o}^{\eta} d\eta' \epsilon \dot{f}\right) + \frac{1 + z_e}{\mathcal{H}_e}\int_{\eta_o}^{\eta_e} d\eta\ \epsilon \dot{f}. \end{aligned} \tag{2.94}$$

With

$$-\int_{\eta_o}^{\eta_e} d\eta \int_{\eta_o}^{\eta} d\eta' \epsilon \dot{f} = (\eta_e - \eta_o)\int_{\eta_e}^{\eta_o} d\eta\ \epsilon \dot{f} + \int_{\eta_e}^{\eta_o} d\eta \int_{\eta_e}^{\eta} d\eta' \epsilon \dot{f},$$

we can rewrite the above expression in the form as

$$\begin{aligned} \tilde{D}_L(z_e) &= (1 + z_e)(\eta_o - \eta_e)(1 + \epsilon g_o + \epsilon g_e) \\ &+ (1 + z_e)\left(-2\int_{\eta_e}^{\eta_o} d\eta\ \epsilon g + \int_{\eta_e}^{\eta_o} d\eta \int_{\eta_e}^{\eta} d\eta' \epsilon \dot{f}\right) - \frac{1 + z_e}{\mathcal{H}_e}\int_{\eta_e}^{\eta_o} d\eta\ \epsilon \dot{f}\ . \end{aligned} \tag{2.95}$$

Using the solutions (2.84, 2.85) we express the distance in terms of $\delta_O(\eta)$. Conformal time is defined as

$$d\eta = \frac{dt}{\bar{a}(t)} \quad \Rightarrow \quad \eta(t) = 3t^{1/3}t_0^{2/3}, \quad \text{setting} \quad \eta(0) = 0.$$

This leads to

$$\begin{aligned} g(\eta, x(\eta)) &= \frac{\delta_O(x(\eta))}{3}, \\ f(\eta, x(\eta)) &= \frac{1}{30}\delta_O''(x(\eta))\eta^2 + \frac{\delta_O(x(\eta))}{3}, \\ \dot{f}(\eta, x(\eta)) &= \frac{1}{15}\delta_O''(x(\eta))\eta, \end{aligned}$$

and consequently to the following distance–redshift relation

$$\begin{aligned} D_L(z_e) &= (1+z_e)(\eta_O - \eta_e)\left(1 + \frac{\epsilon}{3}(\delta_O(x(\eta_o)) + \delta_O(x(\eta_e)))\right) \\ &- (1+z_e)\int_{\eta_e}^{\eta_o}\frac{2\epsilon}{3}\delta_O(x(\eta))\,d\eta + (1+z_e)\int_{\eta_e}^{\eta_o}d\eta\int_{\eta_e}^{\eta}d\eta'\frac{\epsilon}{15}\delta_O''(x(\eta'))\,\eta' \\ &- \frac{1+z_e}{\mathcal{H}_e}\int_{\eta_e}^{\eta_o}d\eta\;\frac{\epsilon}{15}\delta_O''(x(\eta))\,\eta. \end{aligned} \tag{2.96}$$

3

The distance-redshift relation in plane symmetric universes

PHYSICAL REVIEW D **89**, 063543 (2014)

The distance-redshift relation in plane symmetric universes

Julian Adamek, Enea Di Dio, Ruth Durrer, Martin Kunz

Distance measurements are usually thought to probe the 'background' metric of the universe, but in reality the presence of perturbations will lead to deviations from the result expected in an exactly homogeneous and isotropic universe. At least in principle the presence of perturbations could even explain the observed distance–redshift relation without the need for dark energy. In this paper we re-investigate a toy model where perturbations are plane symmetric, and for which exact solutions are known in the fluid limit. However, if perturbations are large, shell-crossing occurs and the fluid approximation breaks down. This prevents the study of the most interesting cases. Here we use a general-relativistic N-body simulation that does not suffer from this problem and which allows us to go beyond previous works. We show that even for very large plane-symmetric perturbations we are not able to mimic the observed distance-redshift relation. We also discuss how the synchronous comoving gauge breaks down when shell-crossing occurs, while metric perturbations in the longitudinal gauge remain small. For this reason the longitudinal (Newtonian) gauge appears superior for relativistic N-body simulations of large-scale structure formation.

3.1 Introduction

The Physics Nobel Prize 2011 has been given "for the discovery of the accelerated expansion of the Universe" [2, 3, 4, 79, 80, 81, 82]. Interpreting this finding within the model of a Friedmann–Lemaître (FL) universe requires that the energy density of the Universe is presently dominated by a component with strongly negative pressure, $p = w\rho$ with $w \sim -1$. The nature of this so-called Dark Energy (DE) remains largely unexplained to date, and is considered as one of the grand challenges of cosmology. In the cosmological standard model it is addressed by introducing a cosmological constant Λ which is equivalent to a vacuum energy $\rho_\Lambda = \Lambda/(8\pi G)$ and obeys the equation of state $p_\Lambda = -\rho_\Lambda$. However, the required value of this vacuum energy is considered unnatural, as it is much smaller than all known fundamental scales in particle physics and there is no established mechanism which protects it from large quantum corrections. Therefore, although formally possible, this explanation of DE remains unsatisfactory.

So far, the measurements pointing to the existence of DE rely mainly on the distance–redshift relation which is valid in an FL universe [47]. Independent measurements of, e.g. the expansion rate $H(z)$ are underway, but at present they are

still relatively weak, see, e.g., [48]. In the future however, for instance with the Euclid satellite[1] [105], it will be possible to measure $H(z)$ and the luminosity distance $d_L(z)$ independently to sufficient accuracy to test whether they obey the relation predicted in an FL universe [106].

There are many ways to address the DE problem. Most of them can be classified either as 'Dark Energy' or 'Dark Gravity' by specifying whether they modify the right hand side of Einstein's equation, by introducing a new contribution to the energy momentum tensor, or its left hand side by modifying the laws of gravity, making gravity weaker on large scales. For a review see, e.g. [107].

However, there is also the 'coincidence problem': why did DE start to become important roughly at the time when non-linear structures have formed? This leads to the question whether one might be completely misled by using the distance–redshift relation of a homogeneous FL universe when actually the true Universe is lumpy, inhomogeneous. If this were true, DE does not exist but is inferred from an oversimplified, and hence inappropriate interpretation of the data. This would certainly be the most conservative solution to the DE problem, requiring no new physics at all (although it does not explain why vacuum energy is not large, as there is no obvious reason why zero should be a preferred value).

One might argue that on large scales over- and underdensities compensate and the distance–redshift relation is similar to the one in an FL universe. However, since General Relativity is non-linear, the relation between metric and density perturbations is not so simple. Unfortunately, so far nobody has been able to address this problem in full generality and most attempts rely either on approximations or on toy models. The latter are fully relativistic solutions which, however, impose symmetries which are not found in the observed Universe.

In the past some of us have considered plane symmetric dust universes to study the effect of large overdensities on the distance–redshift relation, $d_L(z)$, and on the Hubble parameter, $H(z)$ [5]. We found that even though the Hubble parameter becomes strongly fluctuating in these solutions, in its integral, $d_L(z)$, the fluctuations average out and the deviations from the Einstein-de Sitter result are small. They can become somewhat larger for a line of sight parallel to the plane of symmetry along a sheet-like void, but they never exceed the luminosity distance for an empty (Milne) universe which up to about $z = 1$ is still smaller than the observed distance $d_L(z)$, which is well fitted by the cosmological Lambda-cold-dark-matter standard model, ΛCDM, dominated by a cosmological constant.

The problem of the exact plane symmetric dust solution is the fact that we have to choose relatively small initial density perturbations, otherwise we encounter a singularity before the present time. This singularity is a consequence of shell-crossing caustics which cannot be handled properly in a fluid approach and which become relevant as soon as density perturbations are large, which is exactly where we expect deviations of $d_L(z)$ from the FL relation to become relevant. This prompted us to study the problem with a method which can handle shell crossings but is still relativistic. This is what we attempt in this paper:

[1] `http://www.euclid-ec.org`

We re-examine the wall-universe scenario with a new approach, using the novel general relativistic N-body scheme which was recently presented in [7].

In section 3.2 we briefly summarize the key points of the two approaches, and in section 3.3.1 we compare the relativistic N-body results with the exact solution in the regime where both coexist. As soon as the evolution of dust leads to the formation of caustics, the exact solution becomes singular due to the breakdown of the fluid description and of the synchronous gauge. Nothing serious happens though within the N-body scheme, which employs longitudinal gauge. It is therefore possible to study the solutions in the highly non-linear regime beyond the formation of caustics, as is presented in section 3.3.2. We also comment on the comparison with traditional Newtonian N-body schemes in section 3.3.3. We present our conclusions in section 3.4.

3.2 Relativistic and semi-relativistic wall universes

3.2.1 Description in synchronous comoving gauge

We consider a model where the Universe contains only dust and is invariant under transformations (translations, rotations) of the two-dimensional Euclidean group. In other words, two of the three space dimensions are homogeneous and isotropic. Perturbations occur only in the form of plane-parallel sheets of over- and underdense regions. By construction, all perturbations (linear or nonlinear) are confined to the scalar sector. In synchronous gauge, the metric takes the form

$$ds^2 = -dt^2 + \alpha^2(t,\mathrm{x})d\mathrm{x}^2 + \beta^2(t,\mathrm{x})\left[d\mathrm{y}_1^2 + d\mathrm{y}_2^2\right] . \tag{3.1}$$

The Einstein equations for this geometry and for pure dust matter yield [5, 91, 95, 96, 108]

$$\partial_t\left(\frac{\beta'}{\alpha}\right) \equiv \partial_t E = 0 , \tag{3.2}$$

$$(\partial_t\beta)^2 - \left(\frac{\beta'}{\alpha}\right)^2 = 2\frac{M(\mathrm{x})}{\beta} , \tag{3.3}$$

$$M' = 4\pi G\rho\beta^2\beta' = 4\pi G\rho\beta^2\alpha E(\mathrm{x}) . \tag{3.4}$$

Here a prime denotes a derivative w.r.t. x. In Eq. (3.2) we have introduced the time-independent function

$$E(\mathrm{x}) = \beta'/\alpha \tag{3.5}$$

and Eq. (3.3) defines $M(\mathrm{x})$ which is also time-independent. Here we have assumed that matter is comoving. As long as the perfect fluid description is valid, this can always be achieved by a suitable choice of coordinates [96]. We therefore call this the synchronous comoving gauge. In Ref. [5] some of us have considered overdense "walls" separated by underdense regions of different sizes. There we also present the parametric solutions of Eqs. (3.2) to (3.4) for a given initial density profile. High

overdensities turn the initial expansion of the fluid into contraction and rapidly lead to a shell-crossing singularity. In Ref. [5] we had to choose the initial overdensities such that no singularity was encountered up to the present time. In these Universes, the directions normal to the collapse, i.e. parallel to the wall, (y_1, y_2) always expand.

3.2.2 Description in longitudinal gauge

The synchronous comoving gauge is useful as long as the dust can be described as a perfect fluid, in which case the evolution equations reduce to a tractable set of differential equations as we have seen above. However, the fluid description usually breaks down during nonlinear evolution due to the formation of caustics, i.e. the convergence of world lines of different fluid elements in the same space-time point. This problem can be avoided by employing a particle description of the dust, which samples the full phase space. In general we do not try to work at the level of the fundamental particles but instead use an N-body simulation that samples the phase-space distribution by following the evolution of a relatively small set of "representatives".

In this approach, the equations become much more involved, and in general we are not able to find exact solutions but have to resort to numerical simulations. N-body simulations traditionally employ Newton's laws of gravity rather than full General Relativity. There is, of course, at best an approximate correspondence between Newtonian and relativistic cosmologies. On the formal level, this correspondence has been elaborated in recent years [109, 110], leading to a deeper understanding of the impressive success of Newtonian simulations within the cosmological standard model. In general terms, this success rests upon the standard model assumptions that gravitational fields are weak (on the relevant scales) and velocities are small. Furthermore, the effect of a cosmological constant can be taken into account simply by adjusting the background.

Scenarios which potentially violate one of these assumptions can not be tested reliably with Newtonian simulations. Examples include various models of dynamical DE or, to some extent, warm dark matter. Some of us have therefore started to develop the numerical techniques for relativistic N-body simulations, which incorporate a truly dynamical spacetime [7]. Since we want to remain within the cosmological context, we employ a weak-field approximation which is described in detail in [7] and which is closely related to the approach of [109]. The equations are solved in longitudinal gauge, in which metric perturbations indeed remain small on the relevant scales. For the plane-symmetric setup studied in this paper, the metric in longitudinal gauge reads

$$ds^2 = a^2(\tau)\left[-\left(1+2\Psi(\tau,x^1)\right)d\tau^2 + \left(1-2\Phi(\tau,x^1)\right)\delta_{ij}dx^i dx^j\right] . \qquad (3.6)$$

In the scheme implemented numerically, we assume that the gravitational potentials Φ and Ψ are small, of order ϵ, but may fluctuate on small spatial scales. This is taken into account by giving spatial derivatives a weight $\epsilon^{-1/2}$. We then include all terms in Einstein's equations up to order ϵ. In this scheme CDM velocities are

of order $\epsilon^{1/2}$, while density fluctuations are large, of order ϵ^0. This scheme is fully relativistic up to the order described here. It just cannot handle large gravitational potentials, but these are not observed on cosmologically interesting scales $\lambda \gtrsim 0.1$ Mpc. Relativistic velocities $v \sim 1$ can be accommodated within the scheme, but since they do not arise, we simply truncate the stress-energy tensor and geodesic equation for CDM particles at order $v^2 \sim \epsilon$. More details are given in Ref. [7], where also the explicit equations can be found.

Here we identify the spacetime directions perpendicular to the plane of symmetry, (t, x) in Eq. (3.1), with the (τ, x^1)-plane. Note, however, that the *coordinates* x and x^1 should not be identified. As long as the perfect fluid description of dust is valid, the two metrics (3.1) and (3.6) are related by a gauge transformation which eventually becomes nonlinear as matter perturbations grow, see section 3.2.3.

While the relativistic N-body approach does not have issues with shell crossing as it samples the full phase space, it relies on the assumption that the metric perturbations remain small so that they can be treated perturbatively in a weak-field limit. In section 3.3.2 we investigate whether this condition remains valid for the wall universes studied here.

3.2.3 Transformations between the two gauges

At early times the Universe is close to Friedmann and we can write

$$\alpha(t,\mathrm{x}) = a(t)\,(1+g(t,\mathrm{x}))\ ,\ \ \beta(t,\mathrm{x}) = a(t)\,(1+h(t,\mathrm{x}))\ , \tag{3.7}$$

where g and h denote small perturbations. In conformal time $\tilde{\tau}$ defined by $d\tilde{\tau} = a^{-1}dt$ we obtain

$$ds^2 = a^2(\tilde{\tau})\left[-d\tilde{\tau}^2 + (1+2g)d\mathrm{x}^2 + (1+2h)(dy_1^2+dy_2^2)\right] \tag{3.8}$$

To determine the initial Bardeen potentials corresponding to this perturbation, we have to transform it to longitudinal gauge. We choose $\tilde{\tau} = \tau + T$ and $\mathrm{x} = x^1 + L$. In order for this to transform from synchronous to longitudinal gauge we must require

$$g_{\mathrm{long}} = g_{\mathrm{syn}} + L_X \bar{g}\,,$$

where $X = (T, L, 0, 0)$ is the vector field inducing the gauge transformation, $\bar{g} = a^2(-,+,+,+)$ is the background metric, g_{long} and g_{syn} are the perturbed metric in longitudinal respectively synchronous gauge. L_X denotes the Lie derivative in direction X. A brief calculation of the different terms yields

$$\Psi + \mathcal{H}T + \dot{T} = 0\,, \qquad \dot{L} - T' = 0\,, \tag{3.9}$$

$$-\Phi + \mathcal{H}T + L' = g\,, \qquad -\Phi + \mathcal{H}T = h\,, \tag{3.10}$$

$$\text{hence} \qquad L' = g - h\,, \qquad T'' = \dot{g} - \dot{h}\,. \tag{3.11}$$

Here $\mathcal{H} = (da/d\tau)a^{-1}$, and a dot denotes the derivative w.r.t. τ. Hence Φ and Ψ are the solutions of

$$\Phi'' = -h'' + \mathcal{H}(\dot{g} - \dot{h}) \quad \text{and} \tag{3.12}$$

$$\Psi'' = \mathcal{H}(\dot{h} - \dot{g}) + \ddot{h} - \ddot{g}\,. \tag{3.13}$$

For our simulations, we choose initial density profiles which deviate from a constant by the addition of a periodic plane-wave perturbation of small amplitude, see Ref. [5]. We then determine the initial Bardeen potentials via Eqs. (3.12), (3.13). Note that the assumption of a flat FL background in Eq. (3.6) puts a constraint on the total matter density. This constraint finds its counterpart in Eqs. (3.12), (3.13) by the requirement that they have appropriate periodic solutions. The perfect fluid solutions in comoving synchronous gauge introduced above are more general, allowing for arbitrary deviations from critical density. To study such general solutions within the N-body framework would require to extend the simulations to handle arbitrary background curvature.

At late times, the coordinate transformations are not simple linear gauge transformations. Finally, at shell-crossing, the synchronous, comoving gauge breaks down, while the longitudinal gauge is still well defined. In the fluid approximation, shell crossing corresponds to a real singularity in the density and therefore also in the curvature. But since this singularity is sheet-like, the Christoffel symbols only have a jump and the metric components have a kink at the singularity. Such sheet-like singularities can be handled with the Israel junction method [111]. In the N-body approach such singular sheets do not lead to a divergent density on the grid; the finite lattice unit acts as a regulator. It should be noted that the singularity is introduced by the fluid approximation in the first place, and will be regulated in a similar fashion by fluid imperfection as soon as one considers a physical dark matter model.

3.2.4 Observables

Comparing quantities which have been calculated in different gauges can be quite subtle. The safest approach is to use observables, as they are uniquely defined through a physical prescription, and therefore are gauge invariant by design. Two common observables are redshifts and distances, which allow to construct the distance–redshift relation. It was this relation that led to the discovery of the accelerated expansion of the Universe.

To determine the redshift and the distance to a source at some position $\mathbf{x}_*$, we consider a photon emitted from the source at time t_* arriving at the location of the observer, today, $(t_0, \mathbf{x}_0)$. We denote the matter 4-velocity field, hence the 4-velocity of source and observer by $u(t, \mathbf{x})$ and the photon 4-velocity by n. The redshift of the source, z, is simply given by

$$1 + z = \frac{g(n, u)|_*}{g(n, u)|_0} \,. \tag{3.14}$$

The evolution of the distance to the source is determined by the Sachs focussing equation [49, 50],

$$\frac{d^2 d_A}{ds^2} = -\left(|\sigma|^2 + \mathcal{R}\right) d_A \,. \tag{3.15}$$

Here s is an affine parameter along the photon geodesic, and

$$\mathcal{R} = \frac{1}{2} R_{\mu\nu} n^\mu n^\nu = 4\pi G T_{\mu\nu} n^\mu n^\nu \,. \tag{3.16}$$

The complex shear σ of the light bundle is defined by

$$\sigma = \frac{1}{2} g(\epsilon, \nabla_\epsilon n)\,, \text{ where } \epsilon \equiv e_1 + i e_2 \,. \tag{3.17}$$

The spatial orthonormal vectors e_1 and e_2 which are normal to both u and n at the observer are parallel transported along n, such that $\nabla_n e_j = 0$. They form a basis of the so called 'screen'. For the explicit expressions see Appendix 3.5.1.

The angular diameter distance d_A to the source is defined as the solution of Eq. (3.15) with final conditions

$$d_A|_0 = 0, \qquad \left.\frac{d\, d_A}{ds}\right|_0 = g(n,u)|_0. \tag{3.18}$$

The luminosity distance is related to the angular diameter distance via Etherington's reciprocity relation [44]

$$d_L(z) = (1+z)^2 d_A(z)\,.$$

In the discussion of the results below we plot the distance modulus $\mu(z)$ (the log of the luminosity distance) and subtract the value one would obtain in the homogeneous model,

$$\mu(z) - \mu_{\rm EdS}(z) = 5 \log_{10}\left(\frac{d_L(z)}{d_L^{\rm EdS}(z)}\right)\,, \tag{3.19}$$

where $d_L^{\rm EdS}$ is the luminosity distance in an Einstein-de Sitter Universe, i.e. in a matter dominated FL Universe with vanishing curvature. We shall compare our result to the distance in a Milne Universe, i.e. an empty FL Universe with negative curvature and to the standard ΛCDM case. The expressions for the distances in these universes are

$$\begin{aligned} d_L^{\rm EdS}(z) &= \frac{2}{H_0}\left(1+z-\sqrt{1+z}\right)\,, \\ d_L^{\rm Milne}(z) &= \frac{1}{H_0}\left(z+\frac{z^2}{2}\right)\,, \\ d_L^{\Lambda{\rm CDM}}(z) &= \frac{1+z}{H_0}\int_0^z \frac{dz'}{\sqrt{\Omega_m(1+z')^3+\Omega_\Lambda}}\,. \end{aligned}$$

A second observable is given by the image distortion which is induced by the shear alone. This distortion can be measured with the help of weak lensing observations. It can be characterized by a complex quantity e whose absolute value measures the ellipticity acquired by an infinitesimal light bundle with circular cross-section at the observer when traced back along the photon path [104]. The phase angle of e, on

the other hand, encodes the orientation of the principal axis of the elliptical cross section with respect to the screen vectors. This complex quantity is obtained by integrating the shear according to

$$\frac{de}{ds} = 2\sigma\sqrt{|e|^2 + 4}\,, \tag{3.20}$$

with final condition $e|_0 = 0$.

We will plot the absolute value of e (in cases where it is not zero by symmetry) as a function of observed redshift. The direct interpretation of this quantity is the ellipticity of the observed image of a source with intrinsically circular shape, located at the given redshift. If the ratio of the principle axes of the observed elliptical image is r then $|e| = |r - (1/r)|$, so that $r = 2$ corresponds to $|e| = 3/2$. We will not plot the phase angle of e, because it is already fully determined by the symmetry of our setup.

3.3 Comparison and interpretation of the results

3.3.1 Exact relativistic and N-body solutions

In Fig. 3.1 we show the distance–redshift relation for a plane wave perturbation initially described by a cosine-function with a comoving wavelength of 70 Mpc/h, for an observer located at the center of the underdense region and a photon coming in perpendicular to the plane of symmetry. We show both the exact solution for a perfect dust fluid (blue dashed) and the relativistic N-body simulation (red solid). The two distances agree extremely well over the entire redshift range which provides an important check of the accuracy of the relativistic N-body approach.

Comparing the result to Milne (purple dotted line) or ΛCDM (green dot-dashed curve), we find that for $z \gtrsim 0.2$ the deviations from EdS are much too small to mimic observations which are in good agreement with ΛCDM. They also have the wrong shape. It is however possible that this changes when we allow for larger initial perturbations that become non-linear and undergo shell-crossing before the present time. This situation can only be modeled in the N-body approach, and we show the result in Fig. 3.2, where we used an initial perturbation that is five times larger than the one shown in Fig. 3.1. In this case the fluctuations are indeed larger by a factor of about 2, but at high redshift ($z \gtrsim 0.3$) they are still too small, and again they have the wrong shape.

As discussed in more detail below, the most important contribution to the fluctuations in the luminosity distance comes from the Doppler effect, i.e. the peculiar velocity of the object emitting the light. This is visible in Fig. 3.1, where we also plot the luminosity distance without this term (red dashed curve). Once shell-crossing has occurred, there is no longer a single, well-defined velocity field at each point in space. Instead we now have a velocity dispersion. As the Doppler effect is so important, one might hope that taking into account velocity dispersion could help yield a better fit to the ΛCDM curve. But as shown by the gray area in Fig. 3.2,

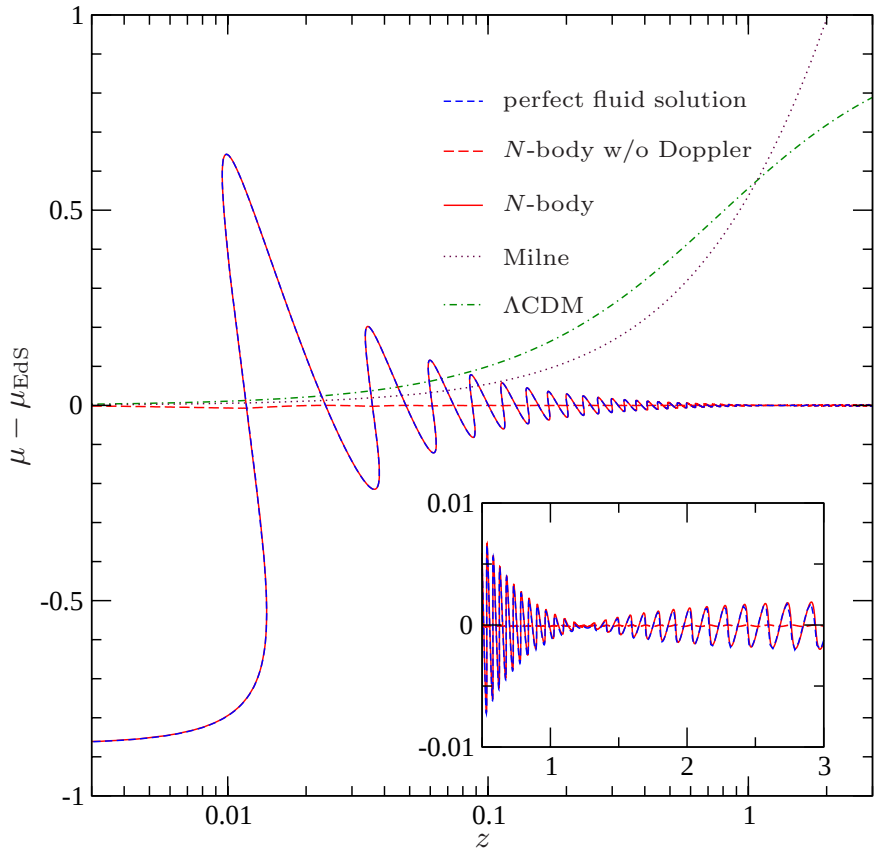

Figure 3.1: (Color online) We plot the observed distance–redshift relation for a plane symmetric setup with an initial plane-wave perturbation of comoving wavelength $\lambda = 70$ Mpc$/h$. More precisely, we plot the distance modulus minus the one of an Einstein-de Sitter background. We compare the perfect fluid description (blue, dashed) with a relativistic N-body simulation with the same initial conditions (red, solid). The observer sits at the center of an underdense region and the line of sight is chosen perpendicular to the plane of symmetry. In this case, within the longitudinal gauge employed in the N-body framework, the fluctuations of the distance are dominated by the peculiar motion (Doppler) of the sources, which are assumed to follow the bulk flow of CDM. To illustrate this, we also plot the luminosity distance with the Doppler term subtracted (red, long-dashed). For a better assessment of the size of the effects, we also indicate the distance–redshift relation for two well-known FL models: the Milne universe (purple, dotted) and a ΛCDM model with $\Omega_\Lambda = 2/3$ (green, dot-dashed). The inset shows a zoom into the region $z > 0.5$ and has a linear z-axis

which represents the velocity dispersion, this is not the case. Velocity dispersion is mainly relevant at low redshift, $z < 0.1$, while the deviation from ΛCDM is most significant at larger redshift.

We also see that the luminosity distance is in general not single valued (as pointed out previously e.g. in [51]). It seems intriguing that the impact of the fluctuations

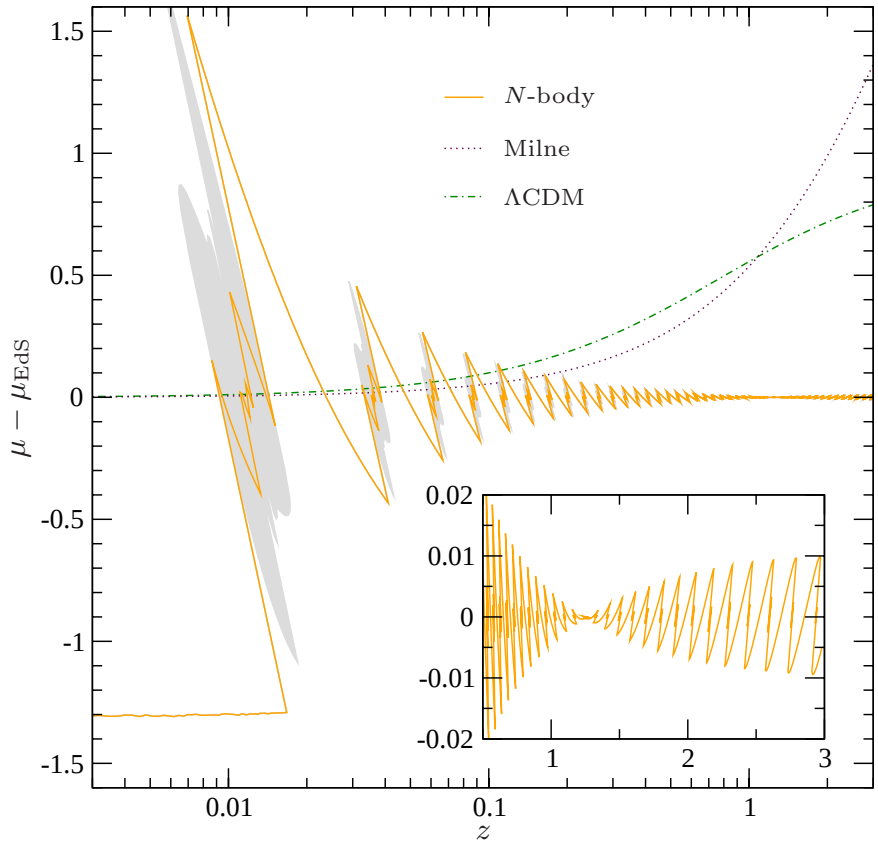

Figure 3.2: (Color online) Same as Fig. 3.1, but with an initial perturbation amplitude which is five times larger. In this case the perfect fluid description breaks down due to the formation of caustics before the end of the simulation. We therefore only show the N-body result (orange, solid). In the regions where shell-crossing has occurred, the phase space distribution of particles shows a considerable velocity dispersion (see Fig. 3.5). One may expect a similar dispersion for the sources: the gray areas correspond to the possible observed scatter of the distance modulus induced by the typical standard deviation of source velocities with respect to the bulk flow (at 1σ).

on the distance is minimal around $z = 1.25$, cf. the inset of Figs. 3.1 and 3.2, which happens to be also the redshift at which the angular diameter distance in the Einstein-de Sitter model is maximal. However, in the longitudinal gauge, this can be easily understood from the fact that the main effect (in these particular cases) is caused by peculiar motions: a perturbation of the redshift (as caused by the Doppler effect) changes our observable $\mu(z) - \mu_{\rm EdS}(z)$ at first order by $\delta z \times d \ln d_A^{\rm EdS}/dz$. This expression becomes zero at the maximum of $d_A^{\rm EdS}$.

Instead of looking at photons that propagate in the direction perpendicular to the plane of symmetry (i.e. 'across' the perturbations), we can also consider photons that move along the symmetry directions, i.e. that follow a trough of the density along the y-direction. In this case the lack of matter along the photon path leads

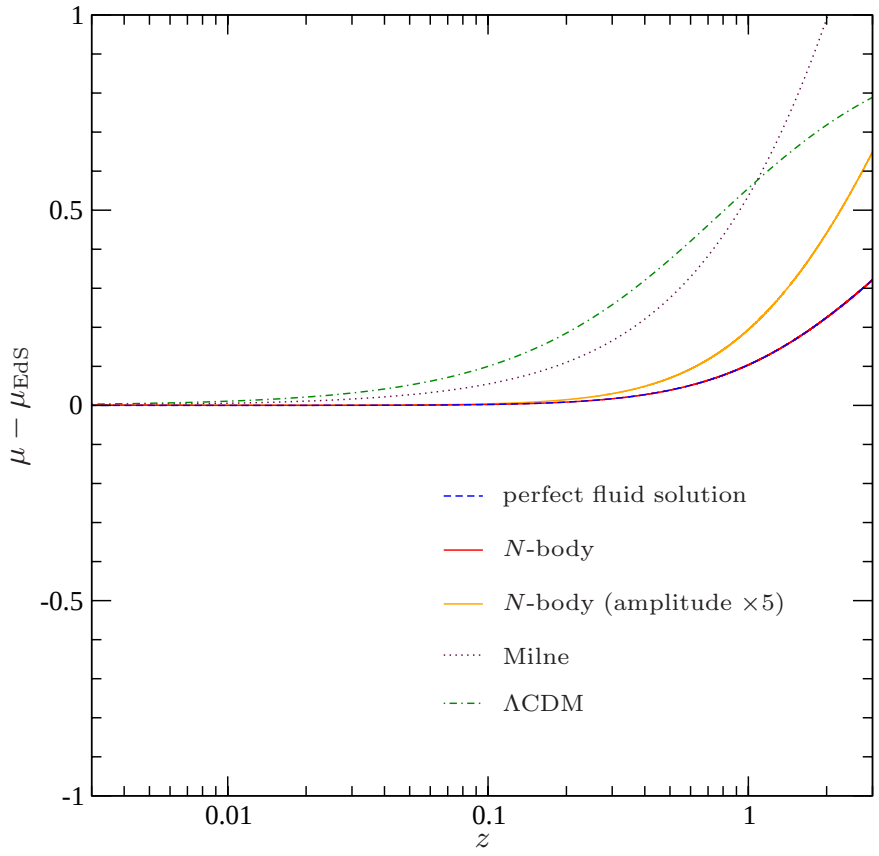

Figure 3.3: (Color online) Same as Figs. 3.1 and 3.2, but with the line of sight parallel to the plane of symmetry. In this case, the photon trajectory runs within the center of an underdense sheet, and the peculiar motion of sources is zero by construction also in longitudinal gauge. However, since the beam is continuously defocussed due to the underdensity, a considerable deviation from the unperturbed distance–redshift relation is accumulated. The deviation remains below the one for the Milne universe and would be too small to account for DE.

to a continuous defocussing of the light beam which is only slightly counteracted by the presence of a non-zero shear (generated through the Weyl tensor). However, as shown in Fig. 3.3, this increase of the luminosity distance is still not sufficient to mimic ΛCDM. In fact, the luminosity distance remains strictly smaller than the one of the Milne Universe.

The non-zero complex shear generates an ellipticity for light bundles propagating along the symmetry directions, and we plot the absolute value of the ellipticity as a function of observed redshift in Fig. 3.4. As this is a cumulative effect, the ellipticity can become very large at redshifts of order unity.

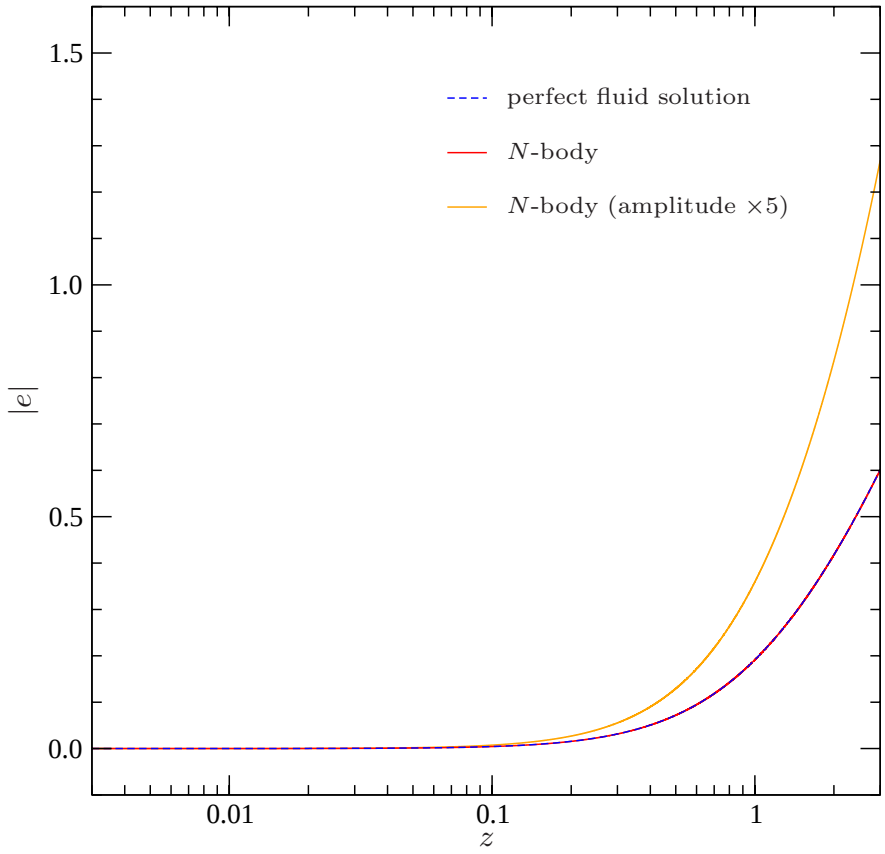

Figure 3.4: (Color online) Image distortion, measured by the ellipticity $|e|$ observed for small circular sources with redshift z. We consider the same scenarios as in Fig. 3.3. An ellipticity of $|e| = 3/2$ implies that one principle axis is twice as long as the other.

3.3.2 Shell-crossing and singularities

The orange solid curve in Figs. 3.2 and 3.3 shows the distance-redshift relation in the more extreme setup where shell-crossing occurs before today. This section investigates in more detail what happens in this situation.

A caustic formally leads to a divergent stress-energy tensor. The divergence, however, occurs in the form of a delta-function on a $(2+1)$-dimensional (timelike) worldsheet and can in principle be handled with the Israel junction method [111]. The particle acceleration remains small everywhere but is discontinuous on the caustic. In the N-body treatment, the discontinuity is smeared out by the finite spatial dispersion of the N-body particles. This is similar to physical reality, but on the scale of the N-body particles which are much larger than the true microscopic CDM particles.

In the phase space representation at the present time given in Fig. 3.5 we see that shell-crossing has happened by today in this setup (orange line) while it is just about to happen in the setup with 5 times smaller initial density contrast (red

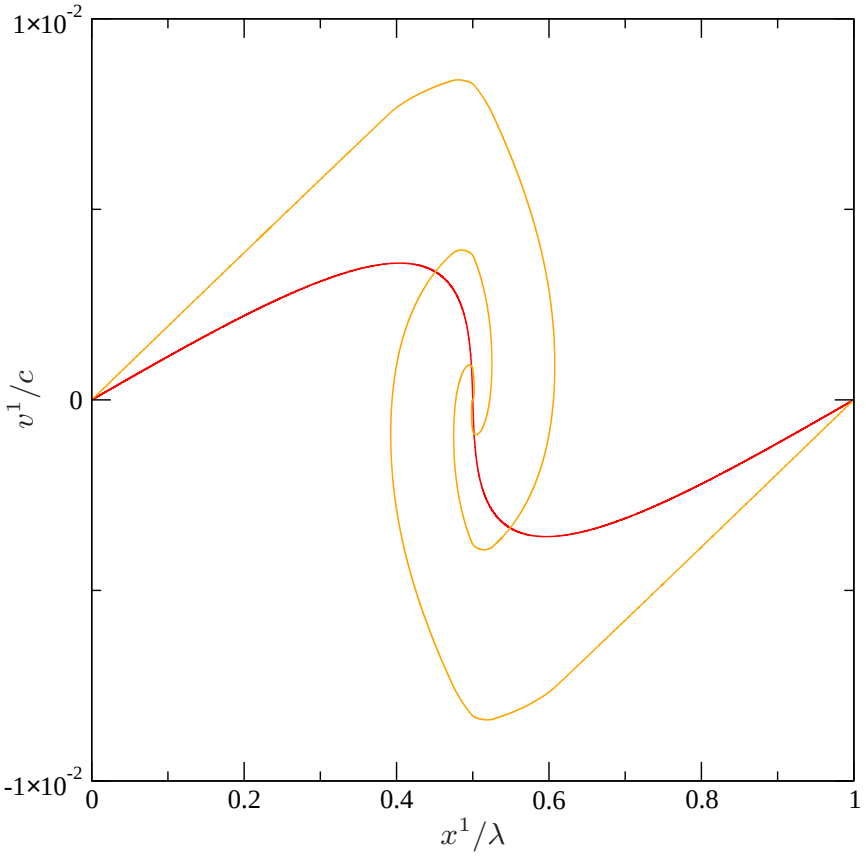

Figure 3.5: (Color online) Phase space diagram at the end of the simulation for the setup used for Fig. 3.1 (red curve) and Fig. 3.2 (orange curve). In the first case shell-crossing does not occur and the velocity is single-valued everywhere. In the second case on the other hand shell-crossing has occurred, and near the central overdensity the velocity field is multi-valued. In this case there is a velocity dispersion that leads to a dispersion also in the luminosity distance, see Fig. 3.2.

line). In Fig. 3.6 we show, in addition to the phase space, also the acceleration, the matter density and the gravitational potential just before and just after shell crossing happens. We can observe the jump in the acceleration (red-dashed) after shell crossing occurs (right panel) which is induced by a kink in the gravitational potential Ψ (purple dotted in the lower panel). The only quantity that becomes large at shell crossing is the density.

The comoving synchronous gauge becomes singular at shell crossing, since the fluid rest frame is no longer well-defined. It is remarkable that the longitudinal gauge does not only remain finite, but the metric potentials stay small and safely in the perturbative regime. Therefore, our relativistic N-body simulation in longitudinal gauge is well adapted to describe non-linear structure formation.

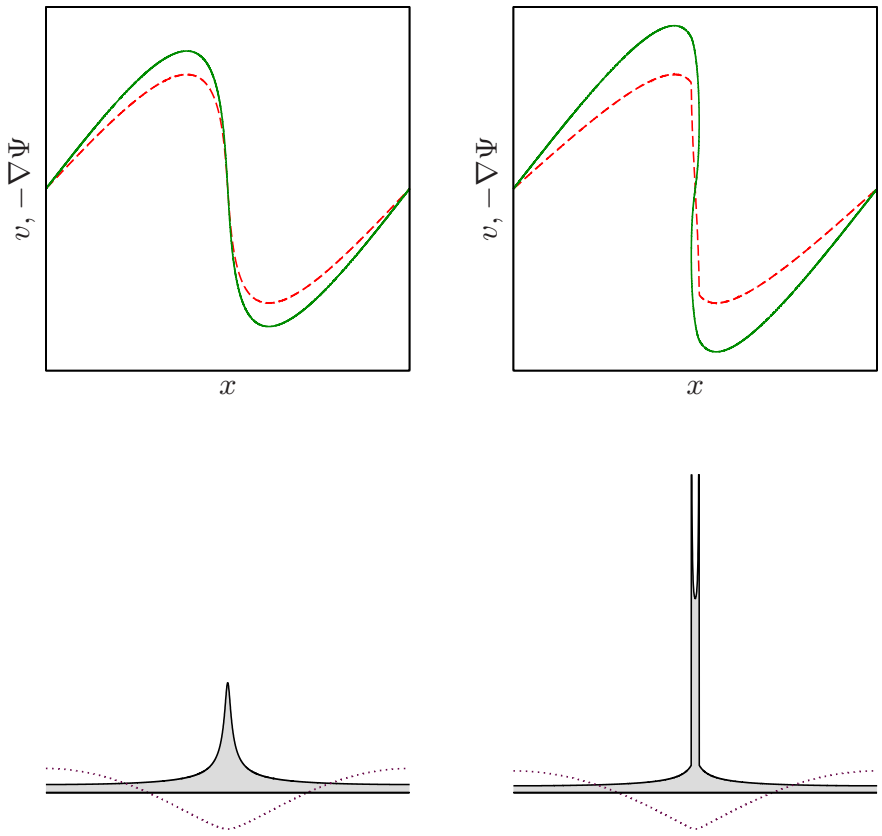

Figure 3.6: (Color online) Sketch of the situation shortly before and after shell crossing. The upper panels show the phase space distribution (green, solid) and the local acceleration, given by the gradient of Ψ (red, dashed). The lower panels show the density (black, solid) and the potential Ψ itself (purple, dotted) – the potential Φ is for all practical purposes indistinguishable from Ψ for the cases studied here. On the left side, shell crossing has not yet occurred: the perfect fluid description (zero velocity dispersion) is still valid and all quantities are regular and smooth. On the right side, two caustics have formed as a result of shell crossing. The density on the caustics diverges like a delta-function on a sheet. However, the potential itself remains small everywhere. Its gradient, which corresponds to the acceleration, also remains small, but it is discontinuous on the caustics. Only the second derivative of Φ becomes large.

3.3.3 Interpretation in longitudinal gauge

When we compare the result of the relativistic N-body simulation with a Newtonian N-body simulation for the scenario shown in Fig. 3.1, we find that the two agree extremely well if we use the relativistic distance formula including the Doppler term for both cases. The reason is that in longitudinal gauge the result is entirely dominated by the contributions from peculiar velocities, see Fig. 3.1. The contributions from the metric potentials are sub-dominant, and vector and tensor perturbations

are absent in an exactly plane-symmetric universe. We do expect velocities which are of order $\epsilon^{1/2}$ to dominate over the gravitational potentials which are of order ϵ in our counting scheme.

This dominance of the Doppler contribution is however gauge- and situation-dependent. In the synchronous co-moving gauge the particles are by definition at rest with respect to the coordinate system. Also, if we look along a symmetric direction y rather than in the transverse direction x, the velocities are zero also in longitudinal gauge. In this case, perturbations of the distance modulus are entirely governed by the gravitational potentials.

3.4 Conclusions

In this paper we have analyzed the distance–redshift relation for plane symmetric universes. We have used general relativistic fluid solutions as well as relativistic N-body simulations. The fluid approach suffers from singularities due to the formation of caustics and cannot be used for high overdensities: when particle trajectories cross, the comoving synchronous coordinate system used for these exact solutions breaks down. The N-body approach, which is a phase-space method, remains regular at all times. Furthermore, in this approach the gravitational potentials remain small so that our approximation is consistent.

Both approaches give consistent results where they are both regular: wall inhomogeneities, even though they do modify the distance–redshift relation, cannot mimic Dark Energy. This is also true for high density fluctuations where the fluid approach breaks down, treated with our relativistic N-body code developed in Ref [7]. The excellent agreement with the exact relativistic solution in the scenarios without shell crossing provides an important test for the accuracy of our code.

It is well known that inhomogeneous models can in principle reproduce any given distance–redshift relation by carefully adjusting the matter distribution. Such fine-tuned models typically violate the cosmological principle. In a model where the Universe has a homogeneity scale well within the observed patch (which is the only case where one can talk about the cosmological principle being respected), the distance–redshift relation can still be affected by the lumpiness of matter. However, fluctuations induced by peculiar motion are expected to average out when considering a large enough sample of observations. Defocussing of light beams, which for realistic observations are biased towards travelling mostly through underdense regions, does not seem to give a strong enough effect to be mistaken for Dark Energy. In fact, we were not even able to reach the level of defocussing found in the Milne model, even when considering light beams which travelled through essentially depleted regions only.

If the results from this toy model can be generalized, we have to conclude that structures in the Universe – over- and underdensities – cannot be responsible for the observed acceleration and Dark Energy or Dark Gravity is needed to explain it. Nevertheless, they certainly do affect the distance–redshift relation and therefore they have to be taken into account when interpreting measurements precisely.

Acknowledgments

It is a pleasure to thank Philip Bull for interesting discussions. J.A. acknowledges funding from the German Research Foundation (DFG) through the research fellowship AD 439/1-1. This work is supported by the Swiss National Science Foundation. Some of the simulations for this paper used the Andromeda cluster of the University of Geneva.

3.5 Appendix

3.5.1 Computing the distance redshift relation

In this appendix we explain in more detail how we calculate the luminosity distance in the N-body code. Details for the exact relativistic fluid solution can be found in Ref. [5].

The relativistic N-body scheme we use has the advantage that the metric is explicitly computed, and one can therefore directly integrate the null geodesic equation numerically to obtain the path of a photon in the perturbed geometry. The difficulty, when constructing observables like the distance–redshift relation, is that they are defined on the past light cone of an observer, whereas the simulation, on the other hand, evolves forward in time. In the perturbed Universe, one does not know exactly whether a point lies on the past light cone of an event until one has actually found a photon path which connects the two. Naturally, one would do this construction backwards in time, starting form the observer, but for this one needs to save a part of the four-dimensional geometry with high resolution in space and time. Although this is a possible way to go, we chose a different approach which one may call a "shooting method".

Somewhere close to the highest redshift which we want to plot in the distance–redshift diagram, we choose an initial point located at spacetime coordinates which would be connected to the observer event by a null ray in the *unperturbed* geometry. This location can simply be read off from the distance–redshift relation obtained in an exact FL universe. We then shoot a light ray directed at the observer by integrating the null geodesic equation in the perturbed geometry, along with the N-body simulation. When the simulation reaches the observer event, we usually find that we have missed the observer by some small spacelike distance due to the perturbations of the photon path. We then restart the simulation, correcting the coordinates of the initial point by the amount by which we have missed the observer. Rerunning the simulation will now bring the perturbed light ray almost to the observer event, up to second-order perturbations. This procedure can be iterated to close in on the observer event to arbitrary precision. For our purposes, a single iteration was enough.

At the last iteration, we also save the change of the photon energy and some information about the geometry, in particular the terms which enter the Sachs equation, along the light ray with high resolution. Additionally, we also save the peculiar

velocities of sources which lie on the path. Since baryonic physics are completely neglected in our simple setup, we assume that observable sources have the same distribution as CDM particles. With this set of data, once we have reached the end of the simulation, we can integrate the Sachs equations backwards in time along the line of sight given by the light ray. Eliminating the affine parameter s in the equations in favor of the coordinate time τ, the angular distance evolves according to

$$\ddot{d_A} + \frac{\dot{n}^0}{n^0}\dot{d_A} + \left(|\sigma|^2 + \mathcal{R}\right)\frac{d_A}{(n^0)^2} = 0\,, \tag{3.21}$$

where $n^0 = d\tau/ds$ is the τ-component of the photon null vector which has to be determined from the null geodesic equation,

$$\dot{n}^0 + \left(\dot{\Phi} - \dot{\Psi} + 2\nabla_{\mathbf{n}}\Psi + 2\mathcal{H}\right)n^0 = 0\,, \tag{3.22}$$

where $\mathbf{n}$ denotes the spatial direction of the photon vector. This equation takes care of the path-dependent contribution to the redshift. The total redshift (the ratio between photon energies measured in the rest frames of source and observer) is given by Eq. (3.14), which yields

$$1 + z = \frac{\left[n^0 a\left(1 + \Psi - \mathbf{n}\cdot\mathbf{v} + \frac{\mathbf{v}^2}{2}\right)\right]\Big|_*}{\left[n^0 a\left(1 + \Psi - \mathbf{n}\cdot\mathbf{v} + \frac{\mathbf{v}^2}{2}\right)\right]\Big|_0}\,. \tag{3.23}$$

Here, $\mathbf{v}$ is the peculiar velocity vector in the longitudinal gauge, $\mathbf{n}\cdot\mathbf{v}$ denotes its projection on the photon direction, and the subscripts $*$ and 0 indicate that the entire expression has to be evaluated at the source and observer event, respectively. The last two equations have been truncated at our approximation order.

We finally need an evolution equation for the complex shear, see [49, 50]. For the purpose of solving Eq. (3.21), it is useful to write it as

$$\frac{d}{d\tau}\left(\frac{\sigma}{n^0}\right) + \left(\frac{\dot{n}^0}{n^0} + 2\frac{\dot{d_A}}{d_A}\right)\frac{\sigma}{n^0} + \frac{\mathcal{F}}{(n^0)^2} = 0\,, \tag{3.24}$$

where $\mathcal{F} = \frac{1}{2}C_{\kappa\lambda\mu\nu}\epsilon^\kappa n^\lambda \epsilon^\mu n^\nu$ is a contraction of the Weyl tensor with the complex screen vector ϵ and the photon four velocity.

In order to solve this coupled system of differential equations, it is sufficient to know four real-valued quantities along the line of sight (as a function of τ) which can all be obtained from the knowledge of the metric and the photon direction: $\dot{n^0}/n^0$, $\mathcal{R}/(n^0)^2$, and $\mathcal{F}/(n^0)^2$. The last quantity is complex in general and therefore corresponds to two real-valued quantities. However, for the particular lines of sight we chose to study in this work, owing to the symmetry of our setup, we can choose the screen vectors such that $\mathcal{F}/(n^0)^2$ remains real-valued. In particular, for the light

ray perpendicular to the plane of symmetry, we find

$$\begin{aligned}\frac{\mathcal{R}}{(n^0)^2} &= 4\pi G a^2 \left[-\left(1+2\Psi\right) T_0^0 + 2T_0^1 + T_1^1\right] , \\ \frac{\mathcal{F}}{(n^0)^2} &= 0 , \end{aligned} \tag{3.25}$$

up to terms which are neglected in our approximation scheme. In this case, the shear remains zero and the angular distance is entirely governed by convergence. For the light ray parallel to the plane of symmetry, we can choose an orthogonal basis of the screen where one basis vector remains orthogonal to the plane of symmetry, while the other basis vector remains parallel to it. This is possible because the center of the underdense region has an additional $\mathbb{Z}_2$ symmetry which guarantees that the ray remains parallel to the plane of symmetry (even though this path is unstable under small perturbations). Using such a basis, we find

$$\begin{aligned}\frac{\mathcal{R}}{(n^0)^2} &= -4\pi G a^2 \left(1+2\Psi\right) T_0^0 , \\ \frac{\mathcal{F}}{(n^0)^2} &= \left(\frac{1}{2} + 2\Phi + \Psi\right) \Delta\Phi + \left(\frac{1}{2} + \Phi\right) \Delta\Psi . \end{aligned} \tag{3.26}$$

In all these explicit expressions we have used the symmetries of our setup to simplify them. Note also that we assume T_0^1 is of order $\epsilon^{1/2}$ and T_1^1 is of order ϵ; components with spatial indices 2, 3 vanish by symmetry. Using this information, the distance–redshift relation is constructed by integrating Eqs. (3.21), (3.22), (3.24) backwards in time. To this end, the final conditions are fixed at the observer as $d_A(\tau_0) = 0$, $\dot{d}_A(\tau_0) = -a(1 + \Psi - \mathbf{n}\cdot\mathbf{v} + \mathbf{v}^2/2)|_0$, $\sigma(\tau_0) = 0$, and $n^0(\tau_0) > 0$ (arbitrary). The solution for the ellipticity e in terms of the real-valued shear follows from Eq. (3.20):

$$e = 2\sinh\left(2\int_{\tau_0}^{\tau_*} \frac{\sigma}{n^0} d\tau\right) . \tag{3.27}$$

4

Vector and Tensor Contributions to the Luminosity Distance

PHYSICAL REVIEW D **86**, 023510 (2012)

Vector and Tensor Contributions to the Luminosity Distance

Enea Di Dio and Ruth Durrer

We compute the vector and tensor contributions to the luminosity distance fluctuations in first order perturbation theory, and we expand them in spherical harmonics. This work presents the formalism with a first application to a stochastic background of primordial gravitational waves.

4.1 Introduction

The distance–redshift relation for far away objects plays an important role in cosmology. It has led Hubble, or rather Lemaître [32], to discover the expansion of the Universe; and the distance–redshift relation to far away Supernovae type Ia is at the origin of last year's Nobel Prize in physics for the discovery of the accelerated expansion of the Universe [2, 3, 4, 79, 81, 82].

A next step that has been initiated recently considers the angular and redshift fluctuations of the luminosity distance, which may also contain important information about our Universe [8, 9, 10]. One important unsolved problem is the question how strongly the distance–redshift relation may be affected by the fact that the actual Universe is not homogeneous and isotropic, but the matter distribution and also the geometry have fluctuations. To first order in perturbation theory these fluctuations can average out in the mean and are therefore expected to be small.

However, it has been found that they are significantly larger than the naively expected value that would be of the order of the gravitational potential, namely, $\sim 10^{-5}$. An analysis in first order gave fluctuations of the order of 10^{-3}, hence 100 times larger than the naive estimate [9]. Recently, Ben-Dayan et al. [11] have calculated a second order contribution to the distance–redshift relation of the order of $\sim 10^{-3}$. Evidently, if the second order term is as large as the first order, this means that perturbation theory cannot be trusted. On the other hand, fully nonlinear toy models, which have been studied in the past, always gave relatively small modifications of the luminosity distance if the size of the fluctuations, spherical voids [112] or parallel walls [5], is small compared to the Hubble scale. Hence the problem remains open.

So far, the perturbative analyses of the distance–redshift relation have concentrated on scalar perturbations. In this work, we want to study the contributions from vector and tensor perturbations on a Friedmann–Lemaître (FL) universe. This is interesting for several reasons. First of all, tensor perturbations are generically

produced during inflation, and hence their contribution has to be added for completeness. Second, a passing gravitational wave from some arbitrary source does generate a tensor perturbation in the distance–redshift relation to any far away object and could, at least in principle, be detected in this way. For single binary sources we have found that this effect is very small [113]; however, a stochastic background might lead to a detectable effect. Even though vector perturbations are usually not generated during inflation (and if they are they decay during the subsequent radiation dominated phase), they are relevant in many models with sources like, e.g., cosmic strings or primordial magnetic fields. A third important motivation to study vector and tensor contributions comes from the fact that at second order in perturbation theory, scalars also generate vector and tensor perturbations [114, 115]. In a complete second order treatment these have to be included. With the formalism developed in this work, such an inclusion is straight forward. We plan to report on the result of these second order contributions in a forthcoming paper [116]. A similar program is carried out in Refs. [117, 118]. There the authors discuss scalar, vector, and tensor perturbations and split them into E and B modes. The treatment of these papers is, however, more adapted to describe distortions of surveys and weak lensing, but the convergence calculated there is related to our distance fluctuations.

The paper is organized as follows. In the next section we discuss the luminosity-redshift relation perturbatively at first order. In Sec. 4.3 we apply these results to tensor perturbations. We first derive the general first order expressions, which we then expand in spherical harmonics. We also give a numerical example for the gravitational wave background from inflation. In Sec. 4.4 we treat vector perturbations and in Sec. 4.5 we conclude. Some lengthy calculations and some details are deferred to four Appendices.

Notation: We use the metric signature $(-,+,+,+)$. We denote the derivative w.r.t. the conformal time η with a dot.

4.2 The distance–redshift relation

For an arbitrary geometry, defined through the metric g, a distance measure D from a source moving with 4-velocity $u_S = u(x_S)$ and an observer moving with 4-velocity $u_O = u(x_O)$ can be obtained as a solution of the Sachs focusing equation [49]:

$$\frac{d^2D}{d\lambda^2} = -\left(\mathcal{R} + |\Sigma|^2\right) D. \tag{4.1}$$

Here λ is the affine parameter of a lightlike geodesic $x^\mu(\lambda)$ from the source to the observer, $x^\mu(\lambda_S) = x^\mu_S$, $x^\mu(\lambda_O) = x^\mu_O$, and

$$\mathcal{R} = \frac{1}{2} R_{\mu\nu} k^\mu k^\nu \qquad \text{with} \quad k^\mu = \frac{dx^\mu}{d\lambda}, \tag{4.2}$$

k^μ is the 4-velocity of the lightlike geodesic, and Σ is the complex shear of the 'screen' defined below. The source and observer are made out of baryons; hence we identify the 4-velocity field $u^\mu(x)$ with the (baryonic and dark) matter velocity field.

Considering a thin light bundle with vertex at the source, the luminosity distance is given by

$$D_L = (1+z)\, D\ , \tag{4.3}$$

where z denotes the source redshift, defined by

$$1+z = \frac{g_{\mu\nu}k^\mu u^\nu|_S}{g_{\mu\nu}k^\mu u^\nu|_O} = \frac{\omega_S}{\omega_O}. \tag{4.4}$$

We are considering past light cones without caustics between the observer and source positions. This is well justified as we are treating small perturbations on a Friedmann background. See Ref. [119] for more details on the effect of caustics in the past light cone.

The complex shear of the light ray bundle, Σ, is defined as follows [50]: Consider two spatial orthonormal vectors e_1 and e_2, which are normal to both the 4-velocity u_O and k at the observer position and which are parallel transported along k, such that $\nabla_k e_a = 0$ for $a = 1, 2$. The vectors e_1, e_2 are a basis of the so-called 'screen'. Note that we do not require that u be parallel transported along k; hence e_1, e_2 are in general not normal to u elsewhere than at the observer. The complex shear is defined by

$$\Sigma = \frac{1}{2} g\left(\epsilon, \nabla_\epsilon k\right) = -\frac{1}{2} g\left(\nabla_\epsilon \epsilon, k\right), \quad \text{with} \quad \epsilon = e_1 + i e_2. \tag{4.5}$$

We consider a light bundle with vertex at the source[1]. This leads to the following initial conditions (more details are found in Appendix 4.6.1) for the Sachs focusing equation (4.1)

$$D\left(\lambda_S\right) = 0, \qquad D'\left(\lambda_S\right) = \omega_S = -\left. g_{\mu\nu}k^\mu u^\mu\right|_S. \tag{4.6}$$

In a perturbed FL metric the Sachs focusing equation (4.1) reduces, at first order, to

$$\frac{d^2 D}{d\lambda^2} = -\mathcal{R} D. \tag{4.7}$$

Since the complex scalar shear Σ vanishes for a conformally flat spacetime, $|\Sigma|^2$ contributes only at second order. To first order in $\mathcal{R}$, Eq. (4.7) with initial conditions (4.6) is solved by

$$\begin{aligned} \frac{D(\lambda_O)}{\omega_S} &= (\lambda_O - \lambda_S) - \int_{\lambda_S}^{\lambda_O} d\lambda \int_{\lambda_S}^{\lambda} d\lambda' \mathcal{R}\left(\lambda - \lambda_S\right) \\ &= (\lambda_O - \lambda_S) - \int_{\lambda_S}^{\lambda_O} d\lambda (\lambda - \lambda_S)(\lambda_O - \lambda)\mathcal{R}, \end{aligned} \tag{4.8}$$

where we have used the identity

$$\int_{\eta_S}^{\eta_O} d\eta \int_{\eta_S}^{\eta} d\eta' f\left(\eta'\right) = \int_{\eta_S}^{\eta_O} d\eta \left(\eta_O - \eta\right) f\left(\eta\right) \tag{4.9}$$

[1] A light bundle with vertex at the observer yields the angular diameter distance, which is related by a factor $(1+z)^2$ to the luminosity distance which we determine here.

for the second equal sign.

Of course, in a perturbed FL universe $\mathcal{R}$ is not first order; it also has a zeroth order contribution. But a perturbed FL universe is conformally related by the scale factor a to a perturbed Minkowski spacetime and lightlike geodesics are invariant under conformal transformations. Two conformally related metrics,

$$\tilde{g}_{\mu\nu} = a^2 g_{\mu\nu}$$

have the same lightlike geodesic curves, and only the affine parameter changes, $d\tilde{\lambda} = a^2 d\lambda$, such that $\tilde{k}^\mu = a^{-2} k^\mu$. Also the (normalized) matter 4-velocity changes, $\tilde{u}^\mu = a^{-1} u^\mu$ so that the redshifts are related by

$$\tilde{z} + 1 = \frac{a_O}{a_S} (\delta z + 1) \ , \quad \text{where} \ \ \frac{a_O}{a_S} \equiv \bar{z} + 1 \tag{4.10}$$

is the background redshift, i.e., the redshift in an unperturbed Friedmann–Lemaître universe, and δz is the source redshift according to definition (4.4) w.r.t. to the perturbed Minkowski metric g, while $\tilde{z}$ is the one w.r.t. to the perturbed FL metric $\tilde{g}$. We remark that $\tilde{z}$ is the true (observed) redshift. In what follows we shall normalize the scale factor at the observer to one, $a_O = 1$. The distance D is not affected by a conformal factor, so that the effect of the expansion on the distance simply leads to a rescaling [9]

$$\tilde{D}_L = (1 + \bar{z}) \, D_L \, . \tag{4.11}$$

We now compute the luminosity distance in a perturbed Minkowski spacetime, D_L, and then relate it to the one in a FL spacetime, $\tilde{D}_L$, by the above rescaling. Let $(1, n^i)$ be the 0-order term of the lightlike velocity vector k^μ (in the nonexpanding Minkowski spacetime). The lightlike condition implies $|\mathbf{n}|^2 = 1$. We normalize the affine parameter λ such that $\omega_S = k^0_S = 1$ at 0th order. To determine the redshift δz, we have to solve the perturbed geodesic equation for $\mu = 0$ only (in order to determine k^0_O to first order), since the peculiar velocities are already first order. The Christoffel symbols of Minkowski space vanish, so that the geodesic equation for $\mu = 0$ to first order is simply

$$\frac{dk^0}{d\lambda} + \Gamma^0_{00} + 2\Gamma^0_{i0} n^i + \Gamma^0_{ij} n^i n^j = 0. \tag{4.12}$$

We normalize the affine parameter λ such that $k^0_S = 1$, and Eq. (4.12) is solved by

$$k^0_O = 1 - \int_{\lambda_S}^{\lambda_O} d\lambda \left(\Gamma^0_{00} + 2\Gamma^0_{i0} n^i + \Gamma^0_{ij} n^i n^j \right) . \tag{4.13}$$

The geodesic equation (4.12) will be useful also in order to express the distance D in terms of the conformal time η instead of the affine parameter λ. For this we use

$$k^0 = \frac{d\eta}{d\lambda} = 1 - \int_{\lambda_S}^{\lambda} d\lambda' \left(\Gamma^0_{00} + 2\Gamma^0_{i0} n^i + \Gamma^0_{ij} n^i n^j \right) , \tag{4.14}$$

which, in first order, leads to

$$\lambda_O - \lambda_S = \eta_O - \eta_S + \int_{\eta_S}^{\eta_O} d\eta \int_{\eta_S}^{\eta} d\eta' \left(\Gamma^0_{00} + \Gamma^0_{i0} n^i + \Gamma^0_{ij} n^i n^j\right). \tag{4.15}$$

The conformal time and the background redshift are not observable. We want to write the distance as a function of the true (observed) redshift $\tilde{z} = \bar{z} + \delta\tilde{z}$, where $\delta\tilde{z} \equiv (1+\bar{z})\,\delta z$ according to Eq. (4.10). Following the approach presented in [9] we compute

$$\tilde{D}_L(\eta_S, \mathbf{n}) = \tilde{D}_L(\eta(\bar{z}), \mathbf{n}) \equiv \tilde{D}_L(\bar{z}, \mathbf{n}) = \tilde{D}_L(\tilde{z}, \mathbf{n}) - \left.\frac{d}{d\tilde{z}}\tilde{D}_L(\tilde{z}, \mathbf{n})\right|_{\tilde{z}=\bar{z}} \delta\tilde{z}, \tag{4.16}$$

with

$$\begin{aligned} \left.\frac{d}{d\tilde{z}}\tilde{D}_L(\tilde{z}, \mathbf{n})\right|_{\tilde{z}=\bar{z}} &= \frac{d}{d\bar{z}}\tilde{D}_L(\bar{z}, \mathbf{n}) + \text{first order} \\ &= \frac{\tilde{D}_L}{1+\tilde{z}} + \mathcal{H}_S^{-1} + \text{first order}, \quad \text{where} \quad \mathcal{H}_S = \left.\frac{\dot{a}}{a}\right|_S. \end{aligned} \tag{4.17}$$

In other words, we evaluate the distance at the true (observed) redshift $\tilde{D}_L(\tilde{z}, \mathbf{n})$ by using Eqs. (4.16, 4.17) in order to relate $\tilde{D}_L(\tilde{z}, \mathbf{n})$ to $\tilde{D}_L(\eta_S, \mathbf{n})$.

From Sec. 4.3 on, to simplify the notation, we denote the true (observed) redshift with z instead of $\tilde{z}$. We shall not use $\tilde{z}$ anymore.

4.3 The distance–redshift relation from tensor perturbations

We first consider a perturbed Minkowski metric with tensor perturbations only, defined by

$$ds^2 = -d\eta^2 + (\delta_{ij} + 2H_{ij})\,dx^i dx^j, \tag{4.18}$$

where the tensor perturbations are divergence-free $H^i_{j,i} = 0$, traceless $H^i_i = 0$, symmetric $H_{ij} = H_{ji}$, and spatial $H_{\mu 0} = 0$. By definition, a spin-2 perturbation is gauge–invariant. To use a notation consistent with the next section, we introduce the gauge invariant shear on the $\{t = \text{constant}\}$ hypersurfaces $\sigma_{ij} = \dot{H}_{ij}$ (see, e.g., [53, 120]).

4.3.1 The perturbation equations

From the Ricci tensor calculated in Appendix 4.6.2 we obtain

$$\mathcal{R} = -\frac{1}{2} n^i n^j \Box H_{ij}, \qquad \text{where} \quad \Box = \partial^\mu \partial_\mu. \tag{4.19}$$

Note that this is the Minkowski space d'Alembertian, without expansion. The geodesic equation (4.13) for $\mu = 0$ leads to (see Appendix 4.6.2 for details)

$$k_O^0 = 1 - \int_{\lambda_S}^{\lambda_O} d\lambda \; \sigma_{ij} n^i n^j. \tag{4.20}$$

We consider the 4-velocity $(u^\mu) = (1, \mathbf{0})$ because the spin-2 perturbations can not source peculiar velocities at linear order, so that we obtain the redshift to first order

$$1 + \delta z = \frac{1}{k_O^0} = 1 + \int_{\lambda_S}^{\lambda_O} d\lambda \; \sigma_{ij} n^i n^j. \tag{4.21}$$

With Eqs. (4.8, 4.11, 4.15) we find the luminosity distance in a perturbed FL universe with $d\tilde{s}^2 = a^2 ds^2$, as a function of the background redshift

$$\begin{aligned} \tilde{D}_L(\bar{z}, \mathbf{n}) &= (1+\bar{z})(\eta_O - \eta_S)\left(1 + \int_{\eta_S}^{\eta_O} d\eta \; \sigma_{ij} n^i n^j \right. \\ &\left. + \int_{\eta_S}^{\eta_O} d\eta \frac{\eta_O - \eta}{\eta_O - \eta_S} \sigma_{ij} n^i n^j - \int_{\eta_S}^{\eta_O} d\eta \frac{(\eta - \eta_S)(\eta_O - \eta)}{\eta_O - \eta_S} \mathcal{R}\right). \end{aligned} \tag{4.22}$$

We have again used (4.9) to reduce the double integral. We finally express the luminosity distance in terms of the true, observed redshift z. Using Eqs. (4.16,4.17), we obtain

$$\begin{aligned} \tilde{D}_L(z, \mathbf{n}) &= (1+z)(\eta_O - \eta_S) \\ &\times \left(1 - \frac{\mathcal{H}_S^{-1}}{\eta_O - \eta_S} \int_{\eta_S}^{\eta_O} d\eta \; \sigma_{ij} n^i n^j \right. \\ &+ \int_{\eta_S}^{\eta_O} d\eta \frac{\eta_O - \eta}{\eta_O - \eta_S} \sigma_{ij} n^i n^j \\ &\left. - \int_{\eta_S}^{\eta_O} d\eta \frac{(\eta - \eta_S)(\eta_O - \eta)}{\eta_O - \eta_S} \mathcal{R}\right). \end{aligned} \tag{4.23}$$

The origin of the different terms in the redshift–distance relation is as follows: the first line is the unperturbed expression for the luminosity distance in a FL universe at the observed redshift z, the term on the second line derives from the redshift correction, the one on the third line from the relation between the conformal time η and the affine parameter λ, and the one on the last line from the Sachs focusing equation. We can interpret this last term as a lensing effect. The first two terms come from the perturbation of the redshift.

For a fluid with a vanishing anisotropic stress the redshift–distance relation becomes

$$\begin{aligned} \tilde{D}_L(z, \mathbf{n}) &= (1+z)(\eta_O - \eta_S) \\ &\times \left(1 - \frac{\mathcal{H}_S^{-1}}{\eta_O - \eta_S} \int_{\eta_S}^{\eta_O} d\eta \; \sigma_{ij} n^i n^j + \int_{\eta_S}^{\eta_O} d\eta \frac{\eta_O - \eta}{\eta_O - \eta_S} \sigma_{ij} n^i n^j \right. \\ &\left. + \int_{\eta_S}^{\eta_O} d\eta \frac{(\eta - \eta_S)(\eta_O - \eta)}{\eta_O - \eta_S} \mathcal{H} \; n^i n^j \sigma_{ij}\right), \end{aligned} \tag{4.24}$$

where we used the Einstein equation [53, 120]

$$\ddot{H}_{ij} + 2\mathcal{H}\dot{H}_{ij} - \nabla^2 H_{ij} = 0, \tag{4.25}$$

and Eq. (4.19) to replace $\mathcal{R}$. If the cosmic fluid is not ideal, but has anisotropic stresses, these add to the right-hand side of Eq. (4.25) (see [53, 120]) and correspondingly to the last line in Eq. (4.24), the lensing term.

4.3.2 Spherical harmonic analysis

We want to determine the power spectrum of the luminosity distance. In the unperturbed FL background the luminosity distance to the redshift z is given by

$$\bar{D}_L(z) = (1+z)(\eta_O - \eta_S). \tag{4.26}$$

We define the relative difference in the luminosity distance as

$$\begin{aligned}\Delta_L(z,\mathbf{n}) &= \frac{\tilde{D}_L(z,\mathbf{n}) - \bar{D}_L(z)}{\bar{D}_L(z)} \\ &= \frac{1}{\eta_O - \eta_S}\int_{\eta_S}^{\eta_O} d\eta\Big[-\mathcal{H}_S^{-1} + (\eta_O - \eta) + \\ &\quad + (\eta - \eta_S)(\eta_O - \eta)\mathcal{H}\Big]\sigma_{ij}n^i n^j .\end{aligned} \tag{4.27}$$

Note that we evaluate the unperturbed distance at the true, observable redshift.

We are interested in the angular power spectrum of this observable, $c_\ell(z,z')$, which depends on the redshift of the two sources and is defined by the two point correlation function

$$\langle \Delta_L(z,\mathbf{n})\,\Delta_L(z',\mathbf{n}')\rangle = \frac{1}{4\pi}\sum_\ell (2\ell+1)\,c_\ell(z,z')P_\ell(\mathbf{n}\cdot\mathbf{n}'). \tag{4.28}$$

In the distance–redshift relation (4.23) [and, in particular, in Eq. (4.24) for an ideal fluid] we have several times the term $n^i n^j \sigma_{ij}(\eta, \mathbf{x}(\eta))$ where $\mathbf{x}(\eta) = \mathbf{x}_O - \mathbf{n}(\eta_O - \eta)$. In terms of its Fourier transform this is

$$n^i n^j \sigma_{ij}(\eta, \mathbf{x}(\eta)) = \int \frac{d^3k}{(2\pi)^3}\hat{\sigma}_{ij}(\eta,\mathbf{k})\,n^i n^j e^{-i\mathbf{k}\cdot\mathbf{x}(\eta)}. \tag{4.29}$$

Without loss of generality we choose $\mathbf{x}_O = \mathbf{0}$. Setting

$$\mathbf{k} = \hat{\mathbf{k}}\,|\mathbf{k}| = \hat{\mathbf{k}}k, \quad \mu = \hat{\mathbf{k}}\cdot\mathbf{n}, \quad \Delta\eta = \eta_O - \eta, \tag{4.30}$$

we obtain

$$n^i n^j \sigma_{ij}(\eta, \mathbf{x}(\eta)) = \int \frac{d^3k}{(2\pi)^3}\,\hat{\sigma}_{ij}(\eta,\mathbf{k})\,n^i n^j\; e^{i\mu k\Delta\eta}. \tag{4.31}$$

Writing the exponential in terms of spherical Bessel functions

$$e^{i\mu k\Delta\eta} = \sum_{l=0}^{\infty} (2\ell+1)\, i^{\ell}\; j_{\ell}\left(k\Delta\eta\right) P_{\ell}\left(\mu\right), \tag{4.32}$$

we find

$$n^i n^j \sigma_{ij} = \int \frac{d^3k}{\left(2\pi\right)^3} n^i n^j \hat{\sigma}_{ij} \sum_{\ell=0}^{\infty} \left(2\ell+1\right) i^{\ell} j_{\ell}\left(k\Delta\eta\right) P_{\ell}\left(\mu\right). \tag{4.33}$$

With respect to a helicity basis in Fourier space

$$\left\{\mathbf{e}^{(+)}, \mathbf{e}^{(-)}, \hat{\mathbf{k}}\right\} \;, \quad \mathbf{e}^{(\pm)} = \frac{1}{\sqrt{2}}\left(\mathbf{e}_1 \pm i\mathbf{e}_2\right) \;, \tag{4.34}$$

such that

$$\mathbf{e}^{(\pm)} \cdot \mathbf{n} = \sqrt{\frac{1-\mu^2}{2}} e^{\pm i\phi}, \tag{4.35}$$

we have

$$\hat{\sigma}_{ij}\; \mathbf{e}^i \otimes \mathbf{e}^j = \hat{\sigma}^+\; \mathbf{e}^{(+)} \otimes \mathbf{e}^{(+)} + \hat{\sigma}^-\; \mathbf{e}^{(-)} \otimes \mathbf{e}^{(-)}. \tag{4.36}$$

We introduce the spherical harmonics with respect to some arbitrary z direction given by a unit vector $\mathbf{e}$ as $Y_{\ell m}(\mathbf{n}, \mathbf{e})$, since we shall use them w.r.t. different z axes. The addition theorem of spherical harmonics is

$$P_{\ell}\left(\mu\right) = \frac{4\pi}{2\ell+1} \sum_{m} Y^*_{\ell m}\left(\hat{\mathbf{k}}, \mathbf{e}\right) Y_{\ell m}\left(\mathbf{n}, \mathbf{e}\right). \tag{4.37}$$

Using the following spherical harmonics definition

$$Y_{2,\pm 2}\left(\mathbf{n}, \hat{\mathbf{k}}\right) = \sqrt{\frac{15}{8\pi}} \sin^2\theta e^{\pm 2i\phi} = \sqrt{\frac{15}{2\pi}} \frac{1-\mu^2}{2} e^{\pm 2i\phi}, \tag{4.38}$$

we can rewrite Eq. (4.33) as

$$\begin{aligned} n^i n^j \sigma_{ij} \;\; = \;\; & \int \frac{d^3k}{\left(2\pi\right)^3} \left(\hat{\sigma}^+ Y_{22}\left(\mathbf{n}, \hat{\mathbf{k}}\right) + \hat{\sigma}^- Y_{2-2}\left(\mathbf{n}, \hat{\mathbf{k}}\right)\right) \\ & \times \sqrt{\frac{2\pi}{15}} \sum_{\ell,m} 4\pi i^{\ell} j_{\ell}\left(k\Delta\eta\right) Y^*_{\ell m}\left(\hat{\mathbf{k}}, \mathbf{e}\right) Y_{\ell m}\left(\mathbf{n}, \mathbf{e}\right). \end{aligned} \tag{4.39}$$

We now introduce the initial tensor power spectrum $P_H\left(k\right)$ through

$$\langle \hat{H}^{\pm}\left(\eta_S, \mathbf{k}\right) \hat{H}^{\pm *}\left(\eta_{S'}, \mathbf{k}'\right)\rangle = \left(2\pi\right)^3 \delta^{(3)}\left(\mathbf{k}-\mathbf{k}'\right) P_H\left(k\right) T_k\left(\eta_S\right) T_k\left(\eta_{S'}\right), \tag{4.40}$$

where $T_k\left(\eta\right)$ is the transfer function with the initial condition $T_k(\eta) \rightarrow_{(k\eta\rightarrow 0)} 1$. The $\delta^{(3)}(\mathbf{k}-\mathbf{k}')$ is a consequence of stochastic homogeneity. For the shear we then have

$$\langle \hat{\sigma}^{\pm}\left(\eta_S, \mathbf{k}\right) \hat{\sigma}^{\pm *}\left(\eta_{S'}, \mathbf{k}'\right)\rangle = \left(2\pi\right)^3 \delta^{(3)}\left(\mathbf{k}-\mathbf{k}'\right) P_H\left(k\right) \dot{T}_k\left(\eta_S\right) \dot{T}_k\left(\eta_{S'}\right). \tag{4.41}$$

Next, we express the terms in the distance–redshift relation with the help of the power spectrum of the integrand,

$$\langle n^i n^j \sigma_{ij} n'^l n'^k \sigma_{lk} \rangle = \frac{1}{4\pi} \sum_\ell (2\ell+1)\, \bar{c}_\ell(\eta,\eta') P_\ell\left(\mathbf{n}\cdot\mathbf{n}'\right). \tag{4.42}$$

A lengthy but straight forward calculation yields [53, 121]

$$\bar{c}_\ell = \frac{1}{\pi}\frac{(\ell+2)!}{(\ell-2)!}\int dk\, k^2 P_H(k)\dot{T}_k(\eta)\dot{T}_k(\eta')\frac{j_\ell(k\Delta\eta)}{(k\Delta\eta)^2}\frac{j_\ell(k\Delta\eta')}{(k\Delta\eta')^2}. \tag{4.43}$$

Using the Limber approximation (see Appendix 4.6.4) for the time integrals in Eq. (4.24), and, in particular, Eqs. (4.130), (4.131) and (4.132), we can simplify the time integrals, and we find the coefficients (under the ideal fluid assumption)

$$\begin{aligned} c_\ell(z,z') \;\simeq\; & \frac{1}{\pi}\frac{(\ell+2)!}{(\ell-2)!}\frac{I_\ell^2}{\ell^4}\frac{1}{\Delta\eta_S}\frac{1}{\Delta\eta_{S'}} \\ & \times \int_{k^*}^{\infty} dk\, P_H(k)\dot{T}^2(\eta_{\ell,k})\left(A + B\mathcal{H}(\eta_{\ell,k}) + C\mathcal{H}^2(\eta_{\ell,k})\right), \end{aligned} \tag{4.44}$$

where we have introduced

$$\Delta\eta_S = \eta_O - \eta_S, \qquad \Delta\eta_{S'} = \eta_O - \eta_{S'}, \tag{4.45}$$

$$\eta_{\ell,k} = \eta_O - \frac{\ell}{k}, \qquad I_\ell^2 = \frac{1.58}{\ell}, \tag{4.46}$$

$$k^* = \max\left\{\frac{\ell}{\Delta\eta_S}, \frac{\ell}{\Delta\eta_{S'}}\right\}, \tag{4.47}$$

and

$$A = \mathcal{H}_S^{-1}\mathcal{H}_{S'}^{-1} + \frac{\ell^2}{k^2} - \frac{\ell}{k}\left(\mathcal{H}_S^{-1} + \mathcal{H}_{S'}^{-1}\right), \tag{4.48}$$

$$B = -\frac{\ell}{k}\left(\mathcal{H}_S^{-1}\Delta\eta_{S'} + \mathcal{H}_{S'}^{-1}\Delta\eta_S\right) - 2\frac{\ell^3}{k^3} + \frac{\ell^2}{k^2}\left(\Delta\eta_S + \Delta\eta_{S'} + \mathcal{H}_S^{-1} + \mathcal{H}_{S'}^{-1}\right) \tag{4.49}$$

$$C = \frac{\ell^2}{k^2}\Delta\eta_S\Delta\eta_{S'} - \frac{\ell^3}{k^3}\left(\Delta\eta_S + \Delta\eta_{S'}\right) + \frac{\ell^4}{k^4}. \tag{4.50}$$

More details can be found in Appendix 4.6.4.

4.3.3 Application

As an example, we consider a flat primordial tensor power spectrum as expected from inflation $P_H(k) = \alpha/k^3$. If r denotes the tensor to scalar ratio, the scalar amplitude as measured by the Wilkinson Microwave Anisotropy Probe experiment [122] yields $\alpha \simeq r \times 10^{-9}$, such that the tensor power spectrum becomes

$$P_H(k) \simeq \frac{r}{k^3}\, 10^{-9}. \tag{4.51}$$

Considering an ideal fluid, the transfer function $T_k(\eta)$ is the solution of the differential equation (4.25),

$$\ddot{T}_k(\eta) + 2\mathcal{H}\dot{T}_k(\eta) + k^2 T_k(\eta) = 0, \tag{4.52}$$

with initial condition $T_k(\eta_{\rm in}) = 1$ and $\dot{T}_k(\eta_{\rm in}) = 0$ for $k\eta_{\rm in} \ll 1$. In a matter (or radiation) dominated universe this differential equation can be solved analytically in terms of Bessel functions. The growing (not decaying) mode is given by

$$T_k(\eta) = (k\eta)^{1/2-q} Y_{1/2-q}(k\eta), \quad \text{where} \quad a \propto \eta^q, \tag{4.53}$$

and Y_ν is the Bessel function of the second kind of order ν. At late times, when the cosmological constant dominates, we cannot write the scale factor $a(\eta)$ as a power law and we have no analytic solution to (4.52). To determine the c_ℓ coefficients, we have solved the differential Eq. (4.52) numerically.

The resulting power spectrum $c_\ell(z,z)$ for different source redshifts is shown in Fig. 4.1.

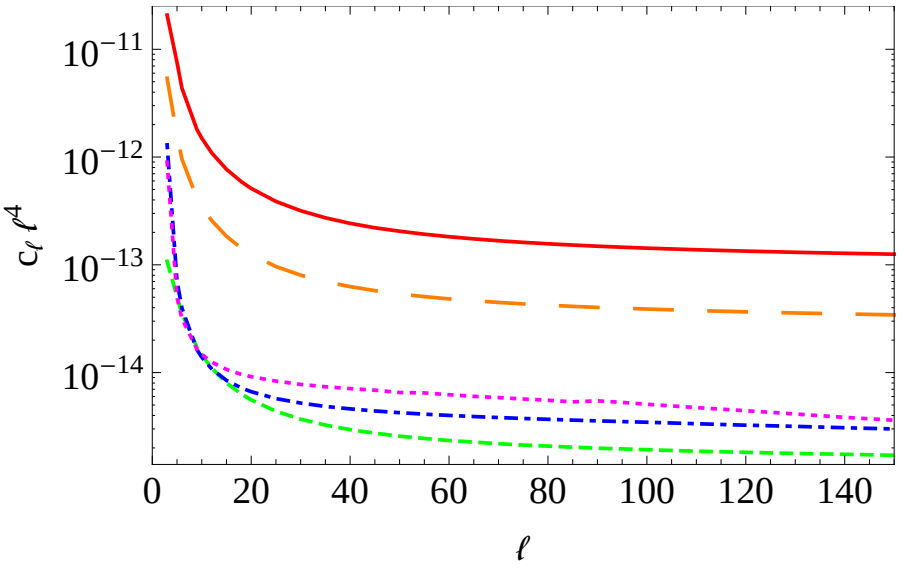

Figure 4.1: We show the tensor power spectrum rescaled by ℓ^4 for the fluctuations in the luminosity distance for different values of the source redshift ($z = 0.5$, dotted pink line; $z = 1$, dot-dashed blue line; $z = 2$, dashed green line; $z = 3$, long-dashed orange line; $z = 4$, solid red line). In the figure we have set $r = 1$.

Clearly, for sufficiently large ℓ, $c_\ell(z,z) \propto \ell^{-4}$. The simplest way to understand this scaling is to note that once a mode enters the horizon, the tensor fluctuations scale like $\int \sigma d\eta \sim H \propto a_k/a \propto (k\eta)^{-q}$, where $a_k = a(\eta = 1/k)$ denotes the value of the scale factor at horizon entry. For modes that enter during the radiation era $q = 1$, while for modes that enter during the matter era $q = 2$. Hence $\int \sigma d\eta \propto H \propto H_{\rm in}/k^q$ is acquiring a factor k^{-q} with respect to the scale invariant initial spectrum. This leads to a red spectrum, $k^3 \left(\int \sigma\right)^2 \propto k^{-2q}$ and $\ell^2 c_\ell(z,z) \propto \ell^{-2q}$. This spectrum turns

from $c_\ell \propto \ell^{-4}$ for scales that enter the horizon in the radiation era to $c_\ell \propto \ell^{-6}$ for scales that enter the horizon in the matter era. For $z = 4$ this happens roughly at $\ell \sim 20$. Of course, the transition is quite gradual.

Comparing Fig. 4.1 with the results from scalar perturbations [9], we see first that the tensor contribution is much smaller, nearly 8 orders of magnitude. We obtain $\ell^4 c_\ell(z) \sim 5 \times 10^{-13}$ for $z = 4$ and $\ell \gtrsim 40$ while scalar perturbations yield $\ell^2 c_\ell(z) \sim 10^{-5}$ for $z = 4$ and $\ell \gtrsim 100$. Furthermore, despite also being proportional to the lensing term, it scales differently with ℓ. This comes from the fact that the scalar lensing term is determined by the spectrum of $k^2\Psi$, where Ψ is the scale invariant Bardeen potential, while for scales that enter during radiation dominated expansion, $\sigma_{ij} n^i n^j$ is suppressed by a factor of $1/k$.

Interestingly the tensor signal is not monotonic in redshift up to $z \simeq 2$. It has a sharp minimum at $z \simeq 1.65$. To illustrate this, we also plot $c_\ell(z, z)$ as a function of the source redshift for different values of ℓ in Fig. 4.2.

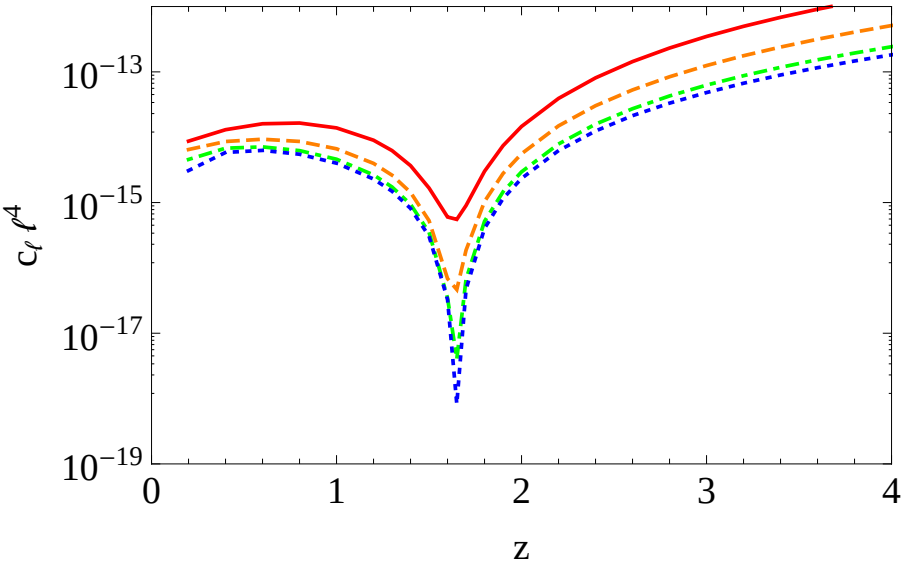

Figure 4.2: We show the tensor power spectrum rescaled by ℓ^4 for the fluctuations in the luminosity distance as a function of the source redshift for different values ℓ ($\ell = 60$, dotted blue line; $\ell = 40$, dot-dashed green line; $\ell = 20$, dashed orange line; $\ell = 10$, solid red line). Also here $r = 1$.

The signal drops to 0 at $z_c = 1.65$. This comes from the fact that it is dominated by two terms with opposite sign. To see this, we also show the contributions from the three terms in the square bracket of (4.27) individually in Fig. 4.3.

If the source redshift is small, $\eta_S \sim \eta_O$, the first term $\propto -\mathcal{H}_S^{-1} \sim -\eta_S/2$ dominates, while for large redshifts, $\eta_S \ll \eta_O$, the second term $\propto (\eta_O - \eta)$ dominates. If $\sigma_{ij} n^i n^j$ has a definite sign, the result inherits this sign for small redshifts and the opposite sign for large redshifts. The sign changes happens around $\eta_S = \eta_O/2$ corresponding to a redshift $z_c \sim 3$. This is not expected to be very precise; in particular, we have neglected the time dependence of the transfer function in this argument.

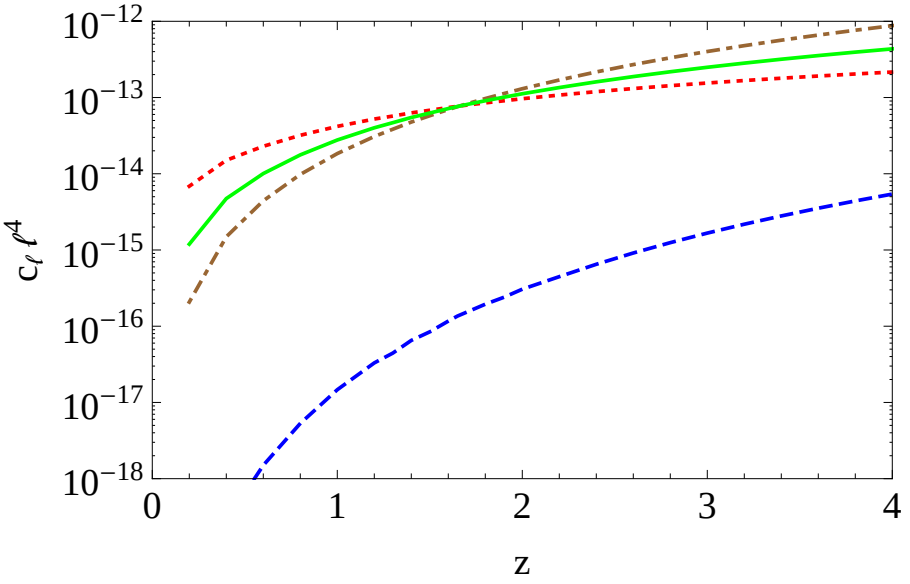

Figure 4.3: We show the contributions from the different terms of Eq. (4.27) to the tensor power spectrum rescaled by ℓ^4 for the fluctuations in the luminosity distance as a function of the source redshift for $\ell = 40$. (First term: dotted red line; second term: dot-dashed brown line; third term: dashed blue line; correlator of the first and second term: solid green line). The third term is always subdominant. We plot the correlator between the first and the second term (solid line) with the opposite sign since it is negative. The second and the first terms have opposite signs, and they cross at $z_c \simeq 1.65$.

The more precise numerical evaluation gives $z_c \simeq 1.65$. Interestingly this redshift is close to the maximum of the angular diameter distance $D_A(z) = (\eta_O - \eta_S)/(1+z)$.

The results shown in Figs. 4.1 to 4.3 have been calculated with the following cosmological parameters: $h = 0.7$, $H_O^{-1} = 2997.9 h^{-1}$Mpc, $\Omega_m h^2 = 0.13$, $\Omega_r h^2 = 4.17 \times 10^{-5}$, and $\Omega_\Lambda = 1 - \Omega_m - \Omega_r$.

4.4 The distance–redshift relation from vector perturbations

We now consider vector perturbations. As for tensor perturbations, we can divide out the cosmic expansion for lightlike geodesics. Hence we can consider Minkowski space with purely vector perturbations. The metric is then given by

$$ds^2 = -d\eta^2 - 2B_i dx^i d\eta + (\delta_{ij} + H_{i,j} + H_{j,i})\, dx^i dx^j, \tag{4.54}$$

where the perturbations are divergence-free, $B^i_{,i} = H^i_{,i} = 0$. Using $B_{ij} = B_{(i,j)}$ and $H_{ij} = H_{(i,j)}$, where $(\ )$ denotes symmetrization, the shear on the constant time hypersurface is given by [53, 120] $\sigma_{ij} = B_{ij} + \dot{H}_{ij}$ or in 3-vector notation $\sigma_i = B_i + \dot{H}_i$, and $\sigma_{ij} = \sigma_{(i,j)}$. This quantity is gauge invariant [53, 120].

4.4.1 The perturbation equations

With the Ricci tensor calculated in Appendix 4.6.3 we obtain for vector perturbations

$$\mathcal{R} = \frac{1}{2}\left(\nabla^2\left(\sigma_i n^i\right) + \dot{\sigma}_{ij} n^i n^j\right). \tag{4.55}$$

To determine the redshift we first evaluate the geodesic solution (4.13) with the Christoffel symbols derived in Appendix 4.6.3,

$$k_O^0 = 1 - \int_{\lambda_S}^{\lambda_O} d\lambda\ \sigma_{ij} n^i n^j. \tag{4.56}$$

Vector perturbations can have a nonvanishing peculiar velocity term. We define the observer 4-velocity $(u^\mu) = (1, B^i + v^i)$. The peculiar velocity v^i defined in this way is gauge invariant. It is the vorticity of the matter flow. We now obtain

$$1 + \delta z = \frac{-1 + n_i v_S^i}{-k_O^0 + n_i v_O^i} = 1 + n_i\left(v_O^i - v_S^i\right) + \int_{\lambda_S}^{\lambda_O} d\lambda\ \sigma_{ij} n^i n^j. \tag{4.57}$$

After a short calculation, using the results of Sec. 4.2, we find the luminosity distance

$$\begin{aligned}\tilde{D}_L\left(\bar{z}, \mathbf{n}\right) &= \left(1 + \bar{z}\right)\left(\eta_O - \eta_S\right) \\ &\times \left(1 + n_i v_O^i - 2 n_i v_S^i + \int_{\eta_S}^{\eta_O} d\eta\ \sigma_{ij} n^i n^j \right. \\ &\left. + \int_{\eta_S}^{\eta_O} d\eta \frac{\eta_O - \eta}{\eta_O - \eta_S} \sigma_{ij} n^i n^j - \int_{\eta_S}^{\eta_O} d\eta \frac{\left(\eta - \eta_S\right)\left(\eta_O - \eta\right)}{\eta_O - \eta_S} \mathcal{R}\right).\end{aligned} \tag{4.58}$$

Since we are interested in expressing the luminosity distance as a function of the true redshift, we have to evaluate Eq. (4.58) at z and subtract the correction term defined through Eqs. (4.16) and (4.17),

$$\begin{aligned}\tilde{D}_L\left(z, \mathbf{n}\right) &= \left(1 + z\right)\left(\eta_O - \eta_S\right) \\ &\times \left(1 - \frac{\mathcal{H}_S^{-1}}{\eta_O - \eta_S} n_i v_O^i - n_i v_S^i \left(1 - \frac{\mathcal{H}_S^{-1}}{\eta_O - \eta_S}\right)\right. \\ &- \frac{\mathcal{H}_S^{-1}}{\eta_O - \eta_S} \int_{\eta_S}^{\eta_O} d\eta\ \sigma_{ij} n^i n^j + \int_{\eta_S}^{\eta_O} d\eta \frac{\eta_O - \eta}{\eta_O - \eta_S} \sigma_{ij} n^i n^j \\ &\left. - \int_{\eta_S}^{\eta_O} d\eta \frac{\left(\eta - \eta_S\right)\left(\eta_O - \eta\right)}{\eta_O - \eta_S} \mathcal{R}\right),\end{aligned} \tag{4.59}$$

$$\begin{aligned}\Delta_L\left(z, \mathbf{n}\right) &= -\frac{\mathcal{H}_S^{-1}}{\eta_O - \eta_S} n_i v_O^i - n_i v_S^i \left(1 - \frac{\mathcal{H}_S^{-1}}{\eta_O - \eta_S}\right) \\ &- \frac{\mathcal{H}_S^{-1}}{\eta_O - \eta_S} \int_{\eta_S}^{\eta_O} d\eta\ \sigma_{ij} n^i n^j \\ &+ \frac{1}{\eta_O - \eta_S} \int_{\eta_S}^{\eta_O} d\eta (\eta_O - \eta) \sigma_{ij} n^i n^j \\ &- \int_{\eta_S}^{\eta_O} d\eta \frac{\left(\eta - \eta_S\right)\left(\eta_O - \eta\right)}{\eta_O - \eta_S} \mathcal{R}.\end{aligned} \tag{4.60}$$

This expression depends only on the gauge-invariant quantities v^i and σ_{ij} as it should. We note also that we did not assume any gravitational theory yet. Indeed the procedure used so far is completely geometrical. If one is interested in general relativity (GR), then the two gauge-invariant variables v^i and σ_{ij} are not independent but related via Einstein's equations [53, 120],

$$\nabla^2 \sigma_i = -16\pi G a^2 v_i \left(\bar{\rho} + \bar{p}\right), \tag{4.61}$$

where $\bar{\rho}$ and $\bar{p}$ are the background density and pressure, respectively.

4.4.2 Spherical harmonic analysis

As for the tensor perturbations, we are interested in the term $n^i n^j \sigma_{ij}$. The main difference is that in the vector case we have $\sigma_{ij} = \sigma_{(i,j)}$ in real space and $\hat{\sigma}_{ij} = -ik_{(i}\hat{\sigma}_{j)}$ in Fourier space. This leads to

$$n^l n^j \hat{\sigma}_{lj} e^{i\mu k \Delta\eta} = -k n^j \hat{\sigma}_j \frac{\partial\, e^{i\mu k \Delta\eta}}{\partial\left(k\Delta\eta\right)}. \tag{4.62}$$

With this we can write Eq. (4.33) as

$$n^i n^j \sigma_{ij} = -\int \frac{d^3k}{\left(2\pi\right)^3} k\; n^j \hat{\sigma}_j \sum_{\ell=0}^{\infty} \left(2\ell+1\right) i^\ell\; j'_\ell\left(k\Delta\eta\right) P_\ell\left(\mu\right). \tag{4.63}$$

With the helicity basis defined in Sec. 4.3, the addition theorem of the spherical harmonics (4.37), and

$$Y_{1,\pm1}\left(\mathbf{n}, \hat{\mathbf{k}}\right) = \mp\sqrt{\frac{3}{8\pi}} \sin\theta\; e^{\pm i\phi} = \mp\sqrt{\frac{3}{4\pi}}\sqrt{\frac{1-\mu^2}{2}} e^{\pm i\phi}, \tag{4.64}$$

we obtain

$$\begin{aligned} n^i n^j \sigma_{ij} \;\; = \;\; & \int \frac{d^3k}{\left(2\pi\right)^3} k \left(Y_{1,1}\left(\mathbf{n}, \hat{\mathbf{k}}\right)\hat{\sigma}^+ - Y_{1,-1}\left(\mathbf{n}, \hat{\mathbf{k}}\right)\hat{\sigma}^-\right) \\ & \times\; 4\pi\sqrt{\frac{4\pi}{3}} \sum_{\ell,m} i^\ell\; j'_\ell\left(kr\right) Y^*_{\ell m}(\hat{\mathbf{k}}, \mathbf{e}) Y_{\ell m}(\mathbf{n}, \mathbf{e}). \end{aligned} \tag{4.65}$$

If we assume that vector perturbations have been generated at some time in the past, we can define the vector power spectrum as for the tensor case as

$$\left\langle \hat{\sigma}^{\pm}\left(\eta_S, \mathbf{k}\right) \hat{\sigma}^{\pm *}\left(\eta_{S'}, \mathbf{k}'\right)\right\rangle = \left(2\pi\right)^3 \delta^{(3)}\left(\mathbf{k} - \mathbf{k}'\right) P_\sigma\left(k\right) T_k\left(\eta_S\right) T_k\left(\eta_{S'}\right). \tag{4.66}$$

If we do not want to consider the case of early generation, we simply have to replace $P_\sigma(k)T_k(\eta_S)T_k(\eta_{S'})$ by a time-dependent power spectrum, $P_\sigma(k, \eta_S, \eta_{S'})$. The model under consideration (e.g., cosmic strings) then has to be used to determine this

time-dependent power spectrum. If, however, vector perturbations evolve freely, we can then compute the shear power spectrum as for tensors,

$$\langle n^i n^j \sigma_{ij} n'^l n'^k \sigma_{lk} \rangle = \frac{1}{4\pi} \sum_\ell (2\ell+1)\, \bar{c}_\ell(\eta,\eta') P_\ell\left(\mathbf{n}\cdot\mathbf{n}'\right), \tag{4.67}$$

finding (see Appendix 4.6.3)

$$\begin{aligned} \bar{c}_\ell &= \frac{2\ell\,(\ell+1)}{\pi\,(2\ell+1)^2} \int dk\; k^4 P_\sigma\left(k\right) T_k\left(\eta\right) T_k\left(\eta'\right) \\ &\quad \times \left[j'_{\ell-1}\left(kr\right) j'_{\ell-1}\left(kr'\right) + j'_{\ell+1}\left(kr\right) j'_{\ell+1}\left(kr'\right) \right]. \end{aligned} \tag{4.68}$$

As mentioned above, in more realistic scenarios, where vector perturbations are generated, e.g., via anisotropic stresses from topological defects or by second order perturbations, we obtain a shear power spectrum of the form $P_\sigma\left(k,\eta,\eta'\right)$, which cannot be factorized into a random initial spectrum and a deterministic transfer function.

In Appendix 4.6.3 we nevertheless, for sake of completeness, continue with expression (4.68) to derive the vector angular power spectrum for the luminosity distance fluctuations. We do not repeat the lengthy, complicated, and not very illuminating formulas here.

4.5 Conclusions and outlook

In this paper we have calculated the angular power spectrum of the linear vector and tensor fluctuations in the distance–redshift relation. For vector perturbations we have simply derived the formulas and for tensor fluctuations we have applied them to an initial spectrum of fluctuations from inflation. It is interesting to see that the tensor-distance fluctuation spectrum is not simply suppressed by a factor r as one might naively expect, but by about 8 orders of magnitude more. The reason for this is mainly that tensor fluctuations decay once they enter the horizon, while, on the contrary, scalar perturbations start growing. We therefore expect that the tensor signal generated from scalar perturbations at second order dominates over the small first order signal. The calculations of these second order contributions are left to a future project [116].

We have also found that the tensor signal is not monotonically increasing with redshift as we would expect it from a pure lensing signal. This is due to the fact that the total signal is the sum of a redshift part, $\propto -\delta z/(z+1)$, and a lensing part. At redshift $z_c \simeq 1.65$, which is close to the redshift where the angular diameter distance $D_A = (\eta_O - \eta_S)/(1+z)$ has a maximum, these terms cancel, and at higher redshifts the redshift-term dominates.

Acknowledgements

This work is supported by the Swiss National Science Foundation.

4.6 Appendix

4.6.1 Sachs focusing equation

Much of this work is based on the Sachs focusing equation [49]. It has been shown [104] that the distance can be defined as

$$D = \sqrt{|\det \mathcal{D}|}, \tag{4.69}$$

where $\mathcal{D}$ is the Jacobi matrix that satisfies the differential equation

$$\frac{d^2\mathcal{D}}{d\lambda^2} = \begin{pmatrix} -\mathcal{R} - \mathrm{Re}\,(F) & -\mathrm{Im}\,(F) \\ \mathrm{Im}\,(F) & -\mathcal{R} + \mathrm{Re}\,(F) \end{pmatrix} \mathcal{D}, \tag{4.70}$$

with $F = \frac{1}{2} R_{\alpha\mu\beta\nu} \bar{\epsilon}^{\alpha} \bar{\epsilon}^{\beta} k^{\mu} k^{\nu}$. The determinant of the Jacobi matrix $\mathcal{D}$ describes the area of the thin light beam and its square root is therefore a distance, (4.69), if the affine parameter λ is normalized such that $\omega_S = 1$. In general one can use the Sachs focusing equation also with a different affine parameter normalization. Indeed from the distance definition

$$D = \sqrt{\frac{dA_O}{d\Omega_S}} \tag{4.71}$$

and the solid angle aberration [49]

$$\frac{d\tilde{\Omega}}{d\Omega} = \left(\frac{k_\mu u^\mu}{k_\mu \tilde{u}^\mu} \right)^2 = \frac{\omega^2}{\tilde{\omega}^2}, \tag{4.72}$$

we find, setting $\omega = 1$,

$$\tilde{D} = \sqrt{\frac{dA_O}{d\tilde{\Omega}_S}} = \tilde{\omega} \sqrt{\frac{dA_O}{d\Omega_S}} = \tilde{\omega} D. \tag{4.73}$$

Since we are considering a light beam with a vertex at the source position, the initial conditions of the Sachs focusing equation are

$$D\,(\lambda_S) = 0, \qquad \left. \frac{dD\,(\lambda)}{d\lambda} \right|_{\lambda=\lambda_S} = 1, \tag{4.74}$$

if we normalize λ such that $\omega_S = 1$. The general initial conditions for an arbitrary affine parameter λ, are given by (4.6). Choosing $\omega_S = 1 + z$ one obtains the luminosity distance while $\omega_S = (1+z)^{-1}$ gives the angular diameter distance.

4.6.2 Details for tensor perturbations

Here we write down the nonvanishing Christoffel symbols and the Ricci tensor for the metric (4.18),

$$\Gamma^0_{ij} = \eta^{0l} \left(H_{il,j} + H_{lj,i} - H_{ij,l} \right) = \dot{H}_{ij} \quad \Rightarrow \quad \sum_i \Gamma^0_{ii} = 0, \tag{4.75}$$

$$\Gamma^i_{j0} = \eta^{ik} \left(H_{k0,j} + H_{jk,0} - H_{j0,k} \right) = \dot{H}_{ji}, \quad \Rightarrow \quad \Gamma^i_{i0} = 0, \tag{4.76}$$

$$\Gamma^i_{jl} = \eta^{ik} \left(H_{jk,l} + H_{kl,j} - H_{jl,k} \right) = H_{ji,l} + H_{il,j} - H_{jl,i}, \tag{4.77}$$

$$\Gamma^i_{ij} = H_{ij,i} + H_{ii,j} - H_{ij,i} = H_{ii,j} \quad \Rightarrow \quad \Gamma^i_{ij} = 0. \tag{4.78}$$

$$R_{00} = R_{i0} = 0, \tag{4.79}$$
$$R_{ij} = \ddot{H}_{ij} - H_{ij,ll} = -\Box H_{ij}. \tag{4.80}$$

These components lead to

$$\mathcal{R} = \frac{1}{2}\left(R_{00} + 2R_{i0}n^i + R_{ij}n^i n^j\right) = -\frac{1}{2}n^i n^j \Box H_{ij}. \tag{4.81}$$

4.6.3 Details for vector perturbations

Christoffel symbols and Ricci tensor

Here we write down the nonvanishing Christoffel symbols and the Ricci tensor for the metric (4.54),

$$\Gamma^i_{00} = -\dot{B}_i, \tag{4.82}$$
$$\Gamma^i_{j0} = \frac{1}{2}\left(\partial_\eta\left(H_{i,j} + H_{j,i}\right) - B_{i,j} + B_{j,i}\right), \tag{4.83}$$
$$\Gamma^i_{i0} = \dot{H}_{i,i} \quad \Rightarrow \quad \Gamma^i_{i0} = 0, \tag{4.84}$$
$$\Gamma^0_{ij} = \frac{1}{2}\left(B_{j,i} + B_{i,j} + \dot{H}_{i,j} + \dot{H}_{j,i}\right) = \sigma_{ij}, \tag{4.85}$$
$$\Gamma^0_{ii} = B_{i,i} + \dot{H}_{i,i} \quad \Rightarrow \quad \sum_i \Gamma^0_{ii} = 0, \tag{4.86}$$
$$\Gamma^i_{ij} = H_{i,ij} \quad \Rightarrow \quad \Gamma^i_{ij} = 0, \tag{4.87}$$
$$\Gamma^i_{jk} = H_{i,jk}, \tag{4.88}$$
$$\Gamma^i_{ik} = H_{i,ik} \quad \Rightarrow \quad \Gamma^i_{ik} = 0, \tag{4.89}$$

$$R_{00} = 0, \tag{4.90}$$
$$R_{i0} = \frac{1}{2}\left(B_{i,jj} + \dot{H}_{i,jj}\right) = \frac{1}{2}\nabla^2\sigma_i, \tag{4.91}$$
$$R_{ij} = \frac{1}{2}\left(\dot{B}_{j,i} + \dot{B}_{i,j} + \ddot{H}_{i,j} + \ddot{H}_{j,i}\right) = \dot{\sigma}_{ij}. \tag{4.92}$$

With these Ricci tensor components we can easily compute

$$\mathcal{R} = \frac{1}{2}\left(R_{00} + 2R_{i0}n^i + R_{ij}n^i n^j\right) = \frac{1}{2}\left(\nabla^2\sigma_i n^i + \dot{\sigma}_{ij}n^i n^j\right). \tag{4.93}$$

The c_ℓ coefficients

We first derive in detail Eq. (4.68). We use the relation

$$Y_{1,\pm1}(\mathbf{n}, \hat{\mathbf{k}}) = \sqrt{\frac{4\pi}{3}} \sum_{m'=-1}^{1} Y_{1m'}(\mathbf{n}, \mathbf{e})\, {}_{\mp1}Y^*_{1m'}(\hat{\mathbf{k}}, \mathbf{e}). \tag{4.94}$$

Here ${}_{\mp1}Y^*_{1m'}(\hat{\mathbf{k}},\mathbf{e})$ is the vector spherical harmonic. The general addition theorem for spin weighted spherical harmonics used in Eq. (4.94) above can be found, e.g., in [53]. Applying this to Eq. (4.65), we obtain

$$\begin{aligned} n^i n^j \sigma_{ij} &= \frac{(4\pi)^2}{3}\sum_{\ell m} i^\ell \sum_{m'=-1}^{1} Y_{1m'}(\mathbf{n}) Y_{\ell m}(\mathbf{n}) \\ &\quad \times \int \frac{d^3k}{(2\pi)^3} k j'_\ell(k\Delta\eta) Y^*_{\ell m}(\hat{\mathbf{k}}) \left(\hat{\sigma}^+ \, {}_{-1}Y^*_{1m'}(\hat{\mathbf{k}}) - \hat{\sigma}^- \, {}_{1}Y^*_{1m'}(\hat{\mathbf{k}})\right) . \end{aligned} \tag{4.95}$$

Here we omit the arbitrary unit vector $\mathbf{e}$ in the notation, and we have introduced the helicity basis,

$$\hat{\sigma}_i = \hat{\sigma}^+ e_i^{(+)} + \hat{\sigma}^- e_i^{(-)}$$

defined in Eq. (4.34). In the special case with $\mathbf{n} = \mathbf{e}$ we obtain

$$\begin{aligned} e^i e^j \sigma_{ij} &= \frac{4\pi}{\sqrt{3}} \sum_\ell i^\ell \sqrt{2\ell+1} \\ &\quad \times \int \frac{d^3k}{(2\pi)^3} k j'_\ell\left(k\Delta\eta\right) Y^*_{\ell 0}(\hat{\mathbf{k}}) \left(\hat{\sigma}^+ \, {}_{-1}Y^*_{10}(\hat{\mathbf{k}}) - \hat{\sigma}^- \, {}_{1}Y^*_{10}(\hat{\mathbf{k}})\right), \end{aligned} \tag{4.96}$$

where we have used

$$Y_{\ell m}\left(\mathbf{e},\mathbf{e}\right) = \sqrt{\frac{2\ell+1}{4\pi}}\delta_{m0}, \tag{4.97}$$

and Eq. (4.94) for $\mathbf{n} = \mathbf{e}$ which yields,

$$Y_{1,\pm1}(\mathbf{e},\hat{\mathbf{k}}) = \sqrt{\frac{4\pi}{3}} \sum_{m'=-1}^{1} Y_{1m'}(\mathbf{e},\mathbf{e}) \; {}_{\mp1}Y^*_{1m'}(\hat{\mathbf{k}},\mathbf{e}) = \; {}_{\mp1}Y^*_{10}(\hat{\mathbf{k}},\mathbf{e}). \tag{4.98}$$

Since the two point correlation function (4.67) depends on the angle $\mathbf{n}\cdot\mathbf{n}'$ only we can set $\mathbf{n}' = \mathbf{e}$ without loss of generality. With this we find

$$\begin{aligned} \langle n^i n^j \sigma_{ij} e^i e^j \sigma_{ij} \rangle &= \frac{8}{3\sqrt{3}} \sum_{\ell,m} \sum_{\tilde{\ell}} i^{\ell-\tilde{\ell}} \sqrt{2\tilde{\ell}+1} \; Y_{\ell m}\left(\mathbf{n}\right) \sum_{m'=-1}^{1} Y_{1m'}\left(\mathbf{n}\right) \\ &\quad \times \int dk \; k^4 j'_\ell(k\Delta\eta) j'_{\tilde{\ell}}(k\Delta\eta') P_\sigma\left(k\right) T_k(\eta) T_k(\eta') \\ &\quad \times \int d\Omega_{\hat{\mathbf{k}}} \; f_{m'}(\hat{\mathbf{k}}) Y^*_{\ell m}(\hat{\mathbf{k}}) Y_{\tilde{\ell}0}(\hat{\mathbf{k}}), \end{aligned} \tag{4.99}$$

where we have introduced

$$f_{m'}(\hat{\mathbf{k}}) = \; {}_{-1}Y^*_{1m'}(\hat{\mathbf{k}}) \; {}_{-1}Y_{10}(\hat{\mathbf{k}}) + \; {}_{1}Y^*_{1m'}(\hat{\mathbf{k}}) \; {}_{1}Y_{10}(\hat{\mathbf{k}}). \tag{4.100}$$

Since the spherical harmonics form an orthogonal basis on S_2, we can expand the product of two of them again in terms of spherical harmonics using the Clebsch–Gordan coefficients [123]. In the case of Eq. (4.99) we use

$$Y^*_{\ell m}(\hat{\mathbf{k}})Y_{\tilde{\ell}0}(\hat{\mathbf{k}}) = \sum_{L=|\ell-\ell'|}^{\ell+\ell'} \sqrt{\frac{(2\ell+1)\left(2\tilde{\ell}+1\right)}{4\pi\,(2L+1)}} \langle \ell, 0, \tilde{\ell}, 0|L, 0\rangle \langle \ell, m, \tilde{\ell}, 0|L, m\rangle Y^*_{Lm}(\hat{\mathbf{k}}). \tag{4.101}$$

The dependence of the spherical harmonics on the azimuthal angle ϕ,

$$Y^*_{Lm} \propto e^{-im\phi} \qquad \text{and} \qquad {}_{\pm1}Y^*_{1m'} \propto e^{-im'\phi} \tag{4.102}$$

implies that the integral over angles in Eq. (4.99) only contributes for $m' = -m$. Therefore also $m \in \{-1, 0, 1\}$. Since $f_{m'}(\hat{\mathbf{k}})$ contains only terms that either do not depend on θ or that are quadratic in $\sin(\theta)$ and $\cos(\theta)$ the only nonvanishing contributions are $L = 0$ or $L = 2$. Analogous to Eq. (4.101) we write

$$Y_{\ell,m}(\mathbf{n})\, Y_{1,-m}(\mathbf{n}) = \sum_n \sqrt{\frac{3\,(2\ell+1)}{4\pi(2n+1)}} \langle \ell, 0, 1, 0|n, 0\rangle \langle \ell, m, 1, -m|n, 0\rangle Y_{n0}(\mathbf{n})\,. \tag{4.103}$$

The addition theorem for the spherical harmonics implies

$$P_n(\mathbf{n}\cdot\mathbf{e}) = \sqrt{\frac{4\pi}{2n+1}} Y_{n0}(\mathbf{n})\,. \tag{4.104}$$

Using these identities we can rewrite the correlation function (4.99) as

$$\begin{aligned}\langle n^i n^j \sigma_{ij} e^i e^j \sigma_{ij}\rangle = &\sum_n \sum_{L=0,2} \sum_{\ell,\tilde{\ell}} \sum_{m=-1}^{1} \frac{i^{\ell-\tilde{\ell}}}{3\pi^{3/2}} (2\ell+1)\left(2\tilde{\ell}+1\right)(2L+1)^{-1/2} \\ &\times \langle \ell, 0, \tilde{\ell}, 0|L, 0\rangle \langle \ell, m, \tilde{\ell}, 0|L, m\rangle \langle \ell, 0, 1, 0|n, 0\rangle \langle \ell, m, 1, -m|n, 0\rangle \\ &\times \int dk k^4 j'_\ell(k\Delta\eta) j'_{\tilde{\ell}}(k\Delta\eta') P_\sigma(k) T_k(\eta) T_k(\eta') B_{Lm} P_n(\mathbf{n}\cdot\mathbf{e})\,,\end{aligned} \tag{4.105}$$

where we have introduced

$$B_{Lm} = \int d\Omega_{\hat{\mathbf{k}}}\; f_{-m}(\hat{\mathbf{k}}) Y^*_{Lm}(\hat{\mathbf{k}}). \tag{4.106}$$

The nonvanishing coefficients are given by

$$B_{00} = \frac{1}{\sqrt{\pi}}, \quad B_{2,\pm1} = \frac{1}{2}\sqrt{\frac{3}{5\pi}}, \quad B_{2,0} = -\frac{1}{\sqrt{5\pi}}. \tag{4.107}$$

Computing the sum of the Clebsch–Gordan coefficients, we find

$$\begin{aligned}\langle n^i n^j \sigma_{ij} e^i e^j \sigma_{ij}\rangle = &\sum_\ell \frac{\ell(\ell+1)}{2\pi(2\ell+1)} P_\ell(\mathbf{n}\cdot\mathbf{e}) \\ &\times \int dk\; k^4 P_\sigma(k) T_k(\eta) T_k(\eta') \left[j'_{\ell-1}(k\Delta\eta) j'_{\ell-1}(k\Delta\eta') + j'_{\ell+1}(k\Delta\eta) j'_{\ell+1}(k\Delta\eta')\right].\end{aligned} \tag{4.108}$$

Using this result for the $\bar{c}_\ell$'s defined in Eq. (4.67), we obtain directly Eq. (4.68).

Now we compute the full c_ℓ coefficient defined in (4.28). We use the Limber approximation (Appendix 4.6.4) to do the time integrals $\int d\eta T_k(\eta) j'_{\ell-1}(k(\eta_O - \eta))$. We start with the Doppler terms, the first line of Eq. (4.60), which contribute to the dipole term only

$$c_1^{\mathrm{D}} = \frac{4\pi}{3}\frac{\mathcal{H}_S^{-1}}{\Delta\eta_S}\frac{\mathcal{H}_{S'}^{-1}}{\Delta\eta_{S'}} < |\vec{v}_O|^2 > . \tag{4.109}$$

This dipole is the same as the one from the scalar analysis [9]. We cannot, of course, decide which part of the observer velocity comes from scalar perturbations and which part from vector perturbations. Since this dipole term is highly nonlinear, we neglect it in the subsequent analysis and consider only $\ell \geq 2$. We now determine the other terms. From the peculiar velocity of the source we obtain

$$c_\ell^{(1)} = \frac{2\ell\,(\ell+1)}{\pi\,(2\ell+1)^2}\left(1 - \frac{\mathcal{H}_S^{-1}}{\Delta\eta_S}\right)\left(1 - \frac{\mathcal{H}_{S'}^{-1}}{\Delta\eta_{S'}}\right) \times \int dk\; k^2 P_v\,(k)\, T_k^v\,(\eta_S)\, T_k^v\,(\eta_{S'}) \sum_{\tilde{\ell}=\ell-1,\ell+1} j_{\tilde{\ell}}\,(k\Delta\eta_S)\, j_{\tilde{\ell}}\,(k\Delta\eta_{S'})\,, \tag{4.110}$$

where we have introduced the velocity power spectrum defined by

$$\langle \hat{v}^{\pm}\,(\eta_S, \mathbf{k})\, \hat{v}^{\pm *}\,(\eta_{S'}, \mathbf{k}')\rangle = (2\pi)^3\, \delta^{(3)}\,(\mathbf{k} - \mathbf{k}')\, P_v\,(k)\, T_k^v\,(\eta_S)\, T_k^v\,(\eta_{S'}) \tag{4.111}$$

and $\hat{v}^{\pm}$ is the peculiar velocity in terms of the helicity basis defined in Eq. (4.34).

The second line of the redshift–distance relation (4.60) leads to

$$\begin{aligned} c_\ell^{(2)} \cong\; & \frac{\ell\,(1+\ell)}{2\pi\,(1+2\ell)^2}\frac{\mathcal{H}_S^{-1}}{\Delta\eta_S}\frac{\mathcal{H}_{S'}^{-1}}{\Delta\eta_{S'}}\int dk\; k^2 P_\sigma\,(k) \\ & \times \sum_{\tilde{\ell}=\ell-1,\ell+1}\Big[I_{\tilde{\ell}-1}^2 T_k^2\left(\eta_{\tilde{\ell}-1,k}\right)\Theta\left(\eta_{\tilde{\ell}-1,k} - \eta_S\right)\Theta\left(\eta_{\tilde{\ell}-1,k} - \eta_{S'}\right) \\ & + \left(\frac{\tilde{\ell}+1}{\tilde{\ell}}\right)^2 I_{\tilde{\ell}}^2 T_k^2\left(\eta_{\tilde{\ell},k}\right)\Theta\left(\eta_{\tilde{\ell},k} - \eta_S\right)\Theta\left(\eta_{\tilde{\ell},k} - \eta_{S'}\right) \\ & - \frac{\tilde{\ell}+1}{\tilde{\ell}} I_{\tilde{\ell}-1} I_{\tilde{\ell}} T_k\left(\eta_{\tilde{\ell}-1,k}\right) T_k\left(\eta_{\tilde{\ell},k}\right)\Big(\Theta\left(\eta_{\tilde{\ell},k} - \eta_S\right)\Theta\left(\eta_{\tilde{\ell}-1,k} - \eta_{S'}\right) \\ & + \Theta\left(\eta_{\tilde{\ell}-1,k} - \eta_S\right)\Theta\left(\eta_{\tilde{\ell},k} - \eta_{S'}\right)\Big)\Big]\,. \end{aligned} \tag{4.112}$$

Analogously the third line yields

$$
\begin{aligned}
c_\ell^{(3)} \;\cong\; & \frac{\ell\,(1+\ell)}{2\pi\,(1+2\ell)^2}\frac{1}{\Delta\eta_S}\frac{1}{\Delta\eta_{S'}}\int dk\; P_\sigma\,(k) \\
& \times \sum_{\tilde\ell=\ell-1,\ell+1}\Big[\Big(\tilde\ell-1\Big)^2 I_{\tilde\ell-1}^2 T_k^2\left(\eta_{\tilde\ell-1,k}\right)\Theta\left(\eta_{\tilde\ell-1,k}-\eta_S\right)\Theta\left(\eta_{\tilde\ell-1,k}-\eta_{S'}\right) \\
& \qquad + \Big(\tilde\ell+1\Big)^2 I_{\tilde\ell}^2 T_k^2\left(\eta_{\tilde\ell,k}\right)\Theta\left(\eta_{\tilde\ell,k}-\eta_S\right)\Theta\left(\eta_{\tilde\ell,k}-\eta_{S'}\right) \\
& \qquad - \Big(\tilde\ell^2-1\Big) I_{\tilde\ell-1} I_{\tilde\ell} T_k\left(\eta_{\tilde\ell-1,k}\right) T_k\left(\eta_{\tilde\ell,k}\right)\Big(\Theta\left(\eta_{\tilde\ell-1,k}-\eta_S\right)\Theta\left(\eta_{\tilde\ell,k}-\eta_{S'}\right) \\
& \qquad\qquad + \Theta\left(\eta_{\tilde\ell,k}-\eta_S\right)\Theta\left(\eta_{\tilde\ell-1,k}-\eta_{S'}\right)\Big)\Big]\,. \qquad (4.113)
\end{aligned}
$$

The fourth line is composed of the two terms that contribute to $\mathcal{R}$ given in Eq. (4.55). Denoting them with superscripts (41), (42), and their correlation with (412) we obtain

$$
\begin{aligned}
c_\ell^{(41)} \;\cong\; & \frac{\ell\,(1+\ell)}{8\pi\,(1+2\ell)^2}\frac{1}{\Delta\eta_S}\frac{1}{\Delta\eta_{S'}}\int dk\; k^2 P_\sigma\,(k)\sum_{\tilde\ell=\ell-1,\ell+1} \\
& \Big[\tilde\ell^2\left(\eta_{\tilde\ell,k}-\eta_S\right)\left(\eta_{\tilde\ell,k}-\eta_{S'}\right) I_{\tilde\ell}^2 T_k^2\left(\eta_{\tilde\ell,k}\right)\Theta\left(\eta_{\tilde\ell,k}-\eta_S\right)\Theta\left(\eta_{\tilde\ell,k}-\eta_{S'}\right)\Big] \qquad (4.114)
\end{aligned}
$$

$$
\begin{aligned}
c_\ell^{(42)} \;\cong\; & \frac{\ell\,(1+\ell)}{8\pi\,(1+2\ell)^2}\frac{1}{\Delta\eta_S}\frac{1}{\Delta\eta_{S'}}\int dk\; P_\sigma\,(k) \\
& \times \sum_{\tilde\ell=\ell-1,\ell+1}\Big[\left(\eta_{\tilde\ell-1,k}-\eta_S\right)\left(\eta_{\tilde\ell-1,k}-\eta_{S'}\right)\Big(\tilde\ell-1\Big)^2 I_{\tilde\ell-1}^2\dot T_k^2\left(\eta_{\tilde\ell-1,k}\right) \\
& \qquad \times \Theta\left(\eta_{\tilde\ell-1,k}-\eta_S\right)\Theta\left(\eta_{\tilde\ell-1,k}-\eta_{S'}\right) \\
& + \left(\eta_{\tilde\ell,k}-\eta_S\right)\left(\eta_{\tilde\ell,k}-\eta_{S'}\right)\Big(\tilde\ell+1\Big)^2 I_{\tilde\ell}^2\dot T_k^2\left(\eta_{\tilde\ell-1,k}\right)\Theta\left(\eta_{\tilde\ell,k}-\eta_S\right)\Theta\left(\eta_{\tilde\ell,k}-\eta_{S'}\right) \\
& - \Big(\tilde\ell^2-1\Big) I_{\tilde\ell-1} I_{\tilde\ell}\dot T_k\left(\eta_{\tilde\ell-1,k}\right)\dot T_k\left(\eta_{\tilde\ell,k}\right) \\
& \qquad \times\Big(\left(\eta_{\tilde\ell-1,k}-\eta_S\right)\left(\eta_{\tilde\ell,k}-\eta_{S'}\right)\Theta\left(\eta_{\tilde\ell-1,k}-\eta_S\right)\Theta\left(\eta_{\tilde\ell,k}-\eta_{S'}\right) \\
& \qquad\quad + \left(\eta_{\tilde\ell,k}-\eta_S\right)\left(\eta_{\tilde\ell-1,k}-\eta_{S'}\right)\Theta\left(\eta_{\tilde\ell,k}-\eta_S\right)\Theta\left(\eta_{\tilde\ell-1,k}-\eta_{S'}\right)\Big)\Big] \qquad (4.115)
\end{aligned}
$$

$$
\begin{aligned}
c_\ell^{(412)} \;\cong\; & \frac{\ell\,(1+\ell)}{8\pi\,(1+2\ell)^2}\frac{1}{\Delta\eta_S}\frac{1}{\Delta\eta_{S'}}\int dk\; k\; P_\sigma\,(k) \\
& \times \sum_{\tilde\ell=\ell-1,\ell+1}\Big[\left(\eta_{\tilde\ell,k}-\eta_S\right)\left(\eta_{\tilde\ell-1,k}-\eta_{S'}\right)\tilde\ell\,\Big(\tilde\ell-1\Big) I_{\tilde\ell-1} I_{\tilde\ell}\dot T_k\left(\eta_{\tilde\ell-1,k}\right) T_k\left(\eta_{\tilde\ell,k}\right) \\
& \qquad \times \Theta\left(\eta_{\tilde\ell,k}-\eta_S\right)\Theta\left(\eta_{\tilde\ell-1,k}-\eta_{S'}\right) \\
& \quad - \left(\eta_{\tilde\ell,k}-\eta_S\right)\left(\eta_{\tilde\ell,k}-\eta_{S'}\right)\tilde\ell\,\Big(\tilde\ell+1\Big) I_{\tilde\ell}^2 T_k\left(\eta_{\tilde\ell,k}\right)\dot T_k\left(\eta_{\tilde\ell,k}\right) \\
& \qquad \times \Theta\left(\eta_{\tilde\ell,k}-\eta_S\right)\Theta\left(\eta_{\tilde\ell,k}-\eta_{S'}\right)\Big] \\
& + (S\leftrightarrow S')\,. \qquad (4.116)
\end{aligned}
$$

Next, we compute the cross terms between the different lines of the distance–redshift relation (4.60). We start with the second and third lines,

$$
\begin{aligned}
c_\ell^{(23)} \;\cong\; & -\frac{\ell\,(1+\ell)}{2\pi\,(1+2\ell)^2}\frac{\mathcal{H}_S^{-1}}{\Delta\eta_S}\frac{1}{\Delta\eta_{S'}}\int dk\; k\; P_\sigma\,(k) \\
& \times \sum_{\tilde\ell=\ell-1,\ell+1}\Big[\Big(\tilde\ell-1\Big)\, I_{\tilde\ell-1}^2 T_k^2\left(\eta_{\tilde\ell-1,k}\right)\Theta\left(\eta_{\tilde\ell-1,k}-\eta_S\right)\Theta\left(\eta_{\tilde\ell-1,k}-\eta_{S'}\right) \\
& \qquad +\frac{\left(\tilde\ell+1\right)^2}{\tilde\ell} I_{\tilde\ell}^2 T_k^2\left(\eta_{\tilde\ell,k}\right)\Theta\left(\eta_{\tilde\ell,k}-\eta_S\right)\Theta\left(\eta_{\tilde\ell,k}-\eta_{S'}\right) \\
& \qquad -\Big(\tilde\ell+1\Big)\, I_{\tilde\ell-1} I_{\tilde\ell} T_k\left(\eta_{\tilde\ell-1,k}\right) T_k\left(\eta_{\tilde\ell,k}\right)\Theta\left(\eta_{\tilde\ell-1,k}-\eta_S\right)\Theta\left(\eta_{\tilde\ell,k}-\eta_{S'}\right) \\
& \qquad -\frac{\tilde\ell^2-1}{\tilde\ell} I_{\tilde\ell-1} I_{\tilde\ell} T_k\left(\eta_{\tilde\ell-1,k}\right) T_k\left(\eta_{\tilde\ell,k}\right)\Theta\left(\eta_{\tilde\ell,k}-\eta_S\right)\Theta\left(\eta_{\tilde\ell-1,k}-\eta_{S'}\right)\Big] \\
& + (S\leftrightarrow S')\,. \qquad (4.117)
\end{aligned}
$$

The second and fourth lines yield

$$
\begin{aligned}
c_\ell^{(241)} \;\cong\; & \frac{\ell\,(1+\ell)}{4\pi\,(1+2\ell)^2}\frac{\mathcal{H}_S^{-1}}{\Delta\eta_S}\frac{1}{\Delta\eta_{S'}}\int dk\; k^2 P_\sigma\,(k) \\
& \times \sum_{\tilde\ell=\ell-1,\ell+1}\Big[\tilde\ell\left(\eta_{\ell,k}-\eta_{S'}\right) I_{\tilde\ell-1} I_{\tilde\ell} T_k\left(\eta_{\tilde\ell-1,k}\right) T_k\left(\eta_{\tilde\ell,k}\right)\Theta\left(\eta_{\tilde\ell-1,k}-\eta_S\right)\Theta\left(\eta_{\tilde\ell,k}-\eta_{S'}\right) \\
& \qquad -\Big(\tilde\ell+1\Big)\left(\eta_{\tilde\ell,k}-\eta_{S'}\right) I_{\tilde\ell}^2 T_k^2\left(\eta_{\tilde\ell,k}\right)\Theta\left(\eta_{\tilde\ell,k}-\eta_S\right)\Theta\left(\eta_{\tilde\ell,k}-\eta_{S'}\right)\Big] \\
& + (S\leftrightarrow S')\,, \qquad (4.118)
\end{aligned}
$$

$$
\begin{aligned}
c_\ell^{(242)} \;\cong\; & \frac{\ell\,(1+\ell)}{4\pi\,(1+2\ell)^2}\frac{\mathcal{H}_S^{-1}}{\Delta\eta_S}\frac{1}{\Delta\eta_{S'}}\int dk\; k P_\sigma\,(k) \sum_{\tilde\ell=\ell-1,\ell+1} \\
& \Big[\left(\eta_{\tilde\ell-1,k}-\eta_{S'}\right)\Big(\tilde\ell-1\Big)\, I_{\tilde\ell-1}^2 T_k\left(\eta_{\tilde\ell-1,k}\right)\dot T_k\left(\eta_{\tilde\ell-1}\right)\Theta\left(\eta_{\tilde\ell-1,k}-\eta_S\right)\Theta\left(\eta_{\tilde\ell-1,k}-\eta_{S'}\right) \\
& -\left(\eta_{\tilde\ell,k}-\eta_{S'}\right)\Big(\tilde\ell+1\Big)\, I_{\tilde\ell-1} I_{\tilde\ell} T_k\left(\eta_{\tilde\ell-1,k}\right)\dot T_k\left(\eta_{\tilde\ell,k}\right)\Theta\left(\eta_{\tilde\ell-1,k}-\eta_S\right)\Theta\left(\eta_{\tilde\ell,k}-\eta_{S'}\right) \\
& -\left(\eta_{\tilde\ell-1,k}-\eta_{S'}\right)\frac{\tilde\ell^2-1}{\tilde\ell} I_{\tilde\ell-1} I_{\tilde\ell}\dot T_k\left(\eta_{\tilde\ell-1,k}\right) T_k\left(\eta_{\tilde\ell,k}\right)\Theta\left(\eta_{\tilde\ell,k}-\eta_S\right)\Theta\left(\eta_{\tilde\ell-1,k}-\eta_{S'}\right) \\
& +\left(\eta_{\tilde\ell,k}-\eta_{S'}\right)\frac{\left(\tilde\ell+1\right)^2}{\tilde\ell} I_{\tilde\ell}^2 T_k\left(\eta_{\tilde\ell,k}\right)\dot T_k\left(\eta_{\tilde\ell,k}\right)\Theta\left(\eta_{\tilde\ell,k}-\eta_S\right)\Theta\left(\eta_{\tilde\ell,k}-\eta_{S'}\right)\Big] \\
& + (S\leftrightarrow S')\,, \qquad (4.119)
\end{aligned}
$$

and, the third and fourth lines give

$$
\begin{aligned}
c_\ell^{(341)} \;\cong\; & -\frac{\ell\,(1+\ell)}{4\pi\,(1+2\ell)^2}\frac{1}{\Delta\eta_S}\frac{1}{\Delta\eta_{S'}}\int dk\; k\; P_\sigma\,(k)\sum_{\tilde\ell=\ell-1,\ell+1}\\
& \Big[\left(\eta_{\tilde\ell,k}-\eta_{S'}\right)\tilde\ell\left(\tilde\ell-1\right)I_{\tilde\ell-1}I_{\tilde\ell}T_k\left(\eta_{\tilde\ell-1,k}\right)T_k\left(\eta_{\tilde\ell,k}\right)\Theta\left(\eta_{\tilde\ell-1,k}-\eta_S\right)\Theta\left(\eta_{\tilde\ell,k}-\eta_{S'}\right)\\
& -\left(\eta_{\tilde\ell,k}-\eta_{S'}\right)\tilde\ell\left(\tilde\ell+1\right)I_{\tilde\ell}^2T_k^2\left(\eta_{\tilde\ell,k}\right)\Theta\left(\eta_{\tilde\ell,k}-\eta_S\right)\Theta\left(\eta_{\tilde\ell,k}-\eta_{S'}\right)\Big]\\
& +\left(S\leftrightarrow S'\right),
\end{aligned}
\tag{4.120}
$$

$$
\begin{aligned}
c_\ell^{(342)} \;\cong\; & -\frac{\ell\,(1+\ell)}{4\pi\,(1+2\ell)^2}\frac{1}{\Delta\eta_S}\frac{1}{\Delta\eta_{S'}}\int dk\; P_\sigma\,(k)\sum_{\tilde\ell=\ell-1,\ell+1}\\
& \Big[\left(\tilde\ell-1\right)^2\left(\eta_{\tilde\ell-1,k}-\eta_{S'}\right)I_{\tilde\ell-1}^2T_k\left(\eta_{\tilde\ell-1,k}\right)\dot T_k\left(\eta_{\tilde\ell-1,k}\right)\Theta\left(\eta_{\tilde\ell-1,k}-\eta_S\right)\Theta\left(\eta_{\tilde\ell-1,k}-\eta_{S'}\right)\\
& -\left(\tilde\ell^2-1\right)\left(\eta_{\tilde\ell,k}-\eta_{S'}\right)I_{\tilde\ell-1}I_{\tilde\ell}T_k\left(\eta_{\tilde\ell-1,k}\right)\dot T_k\left(\eta_{\tilde\ell,k}\right)\Theta\left(\eta_{\tilde\ell-1,k}-\eta_S\right)\Theta\left(\eta_{\tilde\ell,k}-\eta_{S'}\right)\\
& -\left(\tilde\ell^2-1\right)\left(\eta_{\tilde\ell-1,k}-\eta_{S'}\right)I_{\tilde\ell-1}I_{\tilde\ell}\dot T_k\left(\eta_{\tilde\ell-1,k}\right)T_k\left(\eta_{\tilde\ell,k}\right)\Theta\left(\eta_{\tilde\ell,k}-\eta_S\right)\Theta\left(\eta_{\tilde\ell-1,k}-\eta_{S'}\right]\big)\\
& +\left(\tilde\ell+1\right)^2\left(\eta_{\tilde\ell,k}-\eta_{S'}\right)I_{\tilde\ell}^2T_k\left(\eta_{\tilde\ell,k}\right)\dot T_k\left(\eta_{\tilde\ell,k}\right)\Theta\left(\eta_{\tilde\ell,k}-\eta_S\right)\Theta\left(\eta_{\tilde\ell,k}-\eta_{S'}\right)\Big]\\
& +\left(S\leftrightarrow S'\right).
\end{aligned}
\tag{4.121}
$$

To determine the correlation between the peculiar velocities and the shear on the constant time hypersurface σ_{ij} we need to specify the gravitation theory. We choose GR by using the Einstein's equations (4.61). Correlating the term for the peculiar velocity of the source v_S with the others, we find

$$
\begin{aligned}
c_\ell^{(12)} \;=\; & \frac{-1}{16\pi G a_S^2\left(\bar\rho_S+\bar p_S\right)}\left(1-\frac{\mathcal{H}_S^{-1}}{\Delta\eta_S}\right)\frac{\mathcal{H}_{S'}^{-1}}{\Delta\eta_{S'}}\frac{2\ell\,(\ell+1)}{\pi\,(2\ell+1)^2}\\
& \times\int dk k^5 P_\sigma\,(k)\,T_k\,(\eta_S)\sum_{\tilde\ell=\ell-1,\ell+1}j_{\tilde\ell}\,(k\Delta\eta_S)\int_{\eta_{S'}}^{\eta_O}d\eta T_k\,(\eta)\,j'_{\tilde\ell}\,(k\Delta\eta)\\
& +\left(S\leftrightarrow S'\right)\\
\cong\; & \frac{-1}{16\pi G a_S^2\left(\bar\rho_S+\bar p_S\right)}\left(1-\frac{\mathcal{H}_S^{-1}}{\Delta\eta_S}\right)\frac{\mathcal{H}_{S'}^{-1}}{\Delta\eta_{S'}}\frac{2\ell\,(\ell+1)}{\pi\,(2\ell+1)^2}\\
& \times\sum_{\tilde\ell=\ell-1,\ell+1}\Bigg[\frac{I_{\tilde\ell}\tilde\ell^4}{\Delta\eta_S^5}P_\sigma\left(\frac{\tilde\ell}{\Delta\eta_S}\right)T_{\tilde\ell/\Delta\eta_S}\,(\eta_S)\\
& \qquad\times\left(T_{\tilde\ell/\Delta\eta_S}\left(\eta_S+\frac{\Delta\eta_S}{\tilde\ell}\right)I_{\tilde\ell-1}\Theta\left(\eta_S-\eta_{S'}+\frac{\Delta\eta_S}{\tilde\ell}\right)\right.\\
& \qquad\left.-T_{\tilde\ell/\Delta\eta_S}\,(\eta_S)\,I_{\tilde\ell}\frac{\tilde\ell+1}{\tilde\ell}\Theta\left(\eta_S-\eta_{S'}\right)\right)\Bigg]\quad+\left(S\leftrightarrow S'\right),
\end{aligned}
\tag{4.122}
$$

$$
\begin{aligned}
c_\ell^{(13)} &= \frac{1}{16\pi G a_S^2\left(\bar{\rho}_S+\bar{p}_S\right)}\left(1-\frac{\mathcal{H}_S^{-1}}{\Delta\eta_S}\right)\frac{1}{\Delta\eta_{S'}}\frac{2\ell\left(\ell+1\right)}{\pi\left(2\ell+1\right)^2}\\
&\times\int dk k^5 P_\sigma\left(k\right)T_k\left(\eta_S\right)\sum_{\tilde{\ell}=\ell-1,\ell+1} j_{\tilde{\ell}}\left(k\Delta\eta_S\right)\int_{\eta_{S'}}^{\eta_O} d\eta\left(\eta_O-\eta\right)T_k\left(\eta\right)j'_{\tilde{\ell}}\left(k\Delta\eta\right)\\
&+\left(S\leftrightarrow S'\right)\\
&\cong \frac{1}{16\pi G a_S^2\left(\bar{\rho}_S+\bar{p}_S\right)}\left(1-\frac{\mathcal{H}_S^{-1}}{\Delta\eta_S}\right)\frac{1}{\Delta\eta_{S'}}\frac{2\ell\left(\ell+1\right)}{\pi\left(2\ell+1\right)^2}\\
&\times\sum_{\tilde{\ell}=\ell-1,\ell+1}\left[\frac{I_{\tilde{\ell}}\tilde{\ell}^3}{\Delta\eta_S^4}P_\sigma\left(\frac{\tilde{\ell}}{\Delta\eta_S}\right)T_{\tilde{\ell}/\Delta\eta_S}\left(\eta_S\right)\right.\\
&\quad\times\left(T_{\tilde{\ell}/\Delta\eta_S}\left(\eta_S+\frac{\Delta\eta_S}{\tilde{\ell}}\right)I_{\tilde{\ell}-1}\left(\tilde{\ell}-1\right)\Theta\left(\eta_S-\eta_{S'}+\frac{\Delta\eta_S}{\tilde{\ell}}\right)\right.\\
&\quad\left.\left.-T_{\tilde{\ell}/\Delta\eta_S}\left(\eta_S\right)I_{\tilde{\ell}}\left(\tilde{\ell}+1\right)\Theta\left(\eta_S-\eta_{S'}\right)\right)\right]\quad+\left(S\leftrightarrow S'\right), \qquad (4.123)\\
c_\ell^{(141)} &= \frac{1}{8\pi G a_S^2\left(\bar{\rho}_S+\bar{p}_S\right)}\left(1-\frac{\mathcal{H}_S^{-1}}{\Delta\eta_S}\right)\frac{1}{\Delta\eta_{S'}}\frac{2\ell\left(\ell+1\right)}{\pi\left(2\ell+1\right)^2}\\
&\times\int dk\ k^6 P_\sigma(k)\,T_k(\eta_S)\sum_{\tilde{\ell}=\ell-1,\ell+1} j_{\tilde{\ell}}(k\Delta\eta_S)\int_{\eta_{S'}}^{\eta_O} d\eta\left(\eta_O-\eta\right)\left(\eta-\eta_{S'}\right)T_k\left(\eta\right)j'_{\tilde{\ell}}\left(k\Delta\eta\right)\\
&+\left(S\leftrightarrow S'\right)\\
&\cong \frac{1}{8\pi G a_S^2\left(\bar{\rho}_S+\bar{p}_S\right)}\left(1-\frac{\mathcal{H}_S^{-1}}{\Delta\eta_S}\right)\frac{1}{\Delta\eta_{S'}}\frac{2\ell\left(\ell+1\right)}{\pi\left(2\ell+1\right)^2}\\
&\times\sum_{\tilde{\ell}=\ell-1,\ell+1}\left[\frac{I_{\tilde{\ell}}\tilde{\ell}^4}{\Delta\eta_S^5}P_\sigma\left(\frac{\tilde{\ell}}{\Delta\eta_S}\right)T_{\tilde{\ell}/\Delta\eta_S}\left(\eta_S\right)\right.\\
&\times\left(T_{\tilde{\ell}/\Delta\eta_S}\left(\eta_S+\frac{\Delta\eta_S}{\tilde{\ell}}\right)I_{\tilde{\ell}-1}\left(\tilde{\ell}-1\right)\left(\eta_S-\eta_{S'}+\frac{\Delta\eta_S}{\tilde{\ell}}\right)\Theta\left(\eta_S-\eta_{S'}+\frac{\Delta\eta_S}{\tilde{\ell}}\right)\right.\\
&\quad\left.\left.-T_{\tilde{\ell}/\Delta\eta_S}\left(\eta_S\right)I_{\tilde{\ell}}\left(\tilde{\ell}+1\right)\left(\eta_S-\eta_{S'}\right)\Theta\left(\eta_S-\eta_{S'}\right)\right)\right]+\left(S\leftrightarrow S'\right), \qquad (4.124)\\
c_\ell^{(142)} &= \frac{1}{8\pi G a_S^2\left(\bar{\rho}_S+\bar{p}_S\right)}\left(1-\frac{\mathcal{H}_S^{-1}}{\Delta\eta_S}\right)\frac{1}{\Delta\eta_{S'}}\frac{2\ell\left(\ell+1\right)}{\pi\left(2\ell+1\right)^2}\\
&\times\int dk\ k^4 P_\sigma(k)\,\dot{T}_k(\eta_S)\sum_{\tilde{\ell}=\ell-1,\ell+1} j_{\tilde{\ell}}\left(k\Delta\eta_S\right)\int_{\eta_{S'}}^{\eta_O} d\eta\left(\eta_O-\eta\right)\left(\eta-\eta_{S'}\right)\dot{T}_k(\eta)\,j_{\tilde{\ell}}(k\Delta\eta)\\
&+\left(S\leftrightarrow S'\right)\\
&\cong \frac{1}{8\pi G a_S^2\left(\bar{\rho}_S+\bar{p}_S\right)}\left(1-\frac{\mathcal{H}_S^{-1}}{\Delta\eta_S}\right)\frac{1}{\Delta\eta_{S'}}\frac{2\ell\left(\ell+1\right)}{\pi\left(2\ell+1\right)^2}\\
&\times\sum_{\tilde{\ell}=\ell-1,\ell+1}\left[\frac{I_{\tilde{\ell}}^2\tilde{\ell}^2}{\Delta\eta_S^3}P_\sigma\left(\frac{\tilde{\ell}}{\Delta\eta_S}\right)\dot{T}^2_{\tilde{\ell}/\Delta\eta_S}\left(\eta_S\right)\ \left(\eta_S-\eta_{S'}\right)\Theta\left(\eta_S-\eta_{S'}\right)\right]\\
&+\left(S\leftrightarrow S'\right). \qquad (4.125)
\end{aligned}
$$

4.6.4 Limber approximation

In this work we have used the Limber approximation [124] repeatedly. It approximates the integral of the product of a spherical Bessel function and a slowly varying function (e.g., a power law) by

$$\int_{x_1}^{x_2} dx f(x) j_\ell(x) \cong I_\ell f(\ell) \Theta(x_2 - \ell) \Theta(\ell - x_1) \tag{4.126}$$

for $x_2 > x_1$,where Θ denotes the Heaviside function defined by

$$\Theta(x) = \begin{cases} 0, & x \leq 0 \\ 1, & x > 0 \end{cases}, \tag{4.127}$$

and $I_\ell^2 = 1.58/\ell$ describes the area under the first peak of the spherical Bessel function $j_\ell(x)$. This rather crude approximation considers the contribution under the first peak only, and it usually gives an overestimation, but never by more than a factor of 2 [9]. Of course, if the function f varies heavily in the region of the first peak, $\ell - 1 < x < \ell + 1$, the approximation cannot be used.

We are, in particular, interested in (note that $\Delta\eta = \eta_O - \eta$ and $\Delta\eta' = \eta_O - \eta'$)

$$\int_{\eta_S}^{\eta_O} d\eta T(\eta) j_\ell(k\Delta\eta) \cong \frac{1}{k} T(\eta_{\ell,k}) I_\ell \Theta(\eta_{\ell,k} - \eta_S), \tag{4.128}$$

$$\int_{\eta_S}^{\eta_O} d\eta T(\eta) j'_\ell(k\Delta\eta) \cong \frac{1}{k} T(\eta_{\ell-1,k}) I_{\ell-1} \Theta(\eta_{\ell-1,k} - \eta_S) - \frac{1}{k} T(\eta_{\ell,k}) I_\ell \frac{\ell+1}{\ell} \Theta(\eta_{\ell,k} - \eta_S), \tag{4.129}$$

$$\int_{\eta_S}^{\eta} d\eta' \frac{\dot{T}(\eta')}{(k\Delta\eta')^2} j_\ell(k\Delta\eta') \cong \frac{1}{k\ell^2} \dot{T}(\eta_{\ell,k}) I_\ell \Theta(\eta_{\ell,k} - \eta_S) \Theta(\eta - \eta_{\ell,k}), \tag{4.130}$$

$$\int_{\eta_S}^{\eta_O} d\eta \int_{\eta_S}^{\eta} d\eta' \frac{\dot{T}(\eta')}{(k\Delta\eta')^2} j_\ell(k\Delta\eta') \cong \frac{1}{k^2\ell} \dot{T}(\eta_{\ell,k}) I_\ell \Theta(\eta_{\ell,k} - \eta_S), \tag{4.131}$$

$$\int_{\eta_S}^{\eta_O} d\eta (\eta - \eta_S)(\eta_O - \eta) \mathcal{H}(\eta) \dot{T}(\eta) \frac{j_\ell(k\Delta\eta)}{(k\Delta\eta)^2} \cong \frac{1}{\ell k^2} (\eta_{\ell,k} - \eta_S) I_\ell \mathcal{H}(\eta_{\ell,k}) \dot{T}(\eta_{\ell,k}) \Theta(\eta_{\ell,k} - \eta_S), \tag{4.132}$$

$$\int_{\eta_S}^{\eta_O} d\eta \int_{\eta_S}^{\eta} d\eta' T(\eta') j'_\ell(k\Delta\eta') \cong \frac{\ell-1}{k^2} T(\eta_{\ell-1,k}) I_{\ell-1} \Theta(\eta_{\ell-1,k} - \eta_S) - \frac{\ell+1}{k^2} T(\eta_{\ell,k}) I_\ell \Theta(\eta_{\ell,k} - \eta_S), \tag{4.133}$$

$$\int_{\eta_S}^{\eta_O} d\eta (\eta - \eta_S)(\eta_O - \eta) T_k(\eta) j_\ell(k\Delta\eta) \cong \frac{\ell}{k^2} (\eta_{\ell,k} - \eta_S) I_\ell T(\eta_{\ell,k}) \Theta(\eta_{\ell,k} - \eta_S), \tag{4.134}$$

$$\int_{\eta_S}^{\eta_O} d\eta\,(\eta-\eta_S)\,(\eta_O-\eta)\,\dot{T}\,(\eta)\,j'_\ell\,(k\Delta\eta)$$
$$\cong \frac{\ell-1}{k^2} I_{\ell-1}\,(\eta_{\ell-1,k}-\eta_S)\,\dot{T}\,(\eta_{\ell-1,k})\,\Theta\,(\eta_{\ell-1,k}-\eta_S)$$
$$-\frac{\ell+1}{k^2} I_\ell\,(\eta_{\ell,k}-\eta_S)\,\dot{T}\,(\eta_{\ell,k})\,\Theta\,(\eta_{\ell,k}-\eta_S)\,. \qquad (4.135)$$

We have used the following propriety of the spherical Bessel functions [123]:

$$j'_\ell\,(k\Delta\eta) = j_{\ell-1}\,(k\Delta\eta) - \frac{\ell+1}{k\Delta\eta} j_\ell\,(k\Delta\eta)\,. \qquad (4.136)$$

5

The CLASSgal code for Relativistic Cosmological Large Scale Structure

JOURNAL OF COSMOLOGY AND ASTROPARTICLE PHYSICS **11** 044 (2013)

The CLASSgal code for Relativistic Cosmological Large Scale Structure

Enea Di Dio, Francesco Montanari, Julien Lesgourgues and Ruth Durrer

We present accurate and efficient computations of large scale structure observables, obtained with a modified version of the CLASS code which is made publicly available. This code includes all relativistic corrections and computes both the power spectrum $C_\ell(z_1, z_2)$ and the corresponding correlation function $\xi(\theta, z_1, z_2)$ of the matter density and the galaxy number fluctuations in linear perturbation theory. For Gaussian initial perturbations, these quantities contain the full information encoded in the large scale matter distribution at the level of linear perturbation theory. We illustrate the usefulness of our code for cosmological parameter estimation through a few simple examples.

5.1 Introduction

Since many years now, cosmology is a data driven science. This became especially evident with the discovery of the apparent acceleration of the expansion of the universe, which was found by observations and still remains very puzzling on the theoretical side. The most blatant success story of cosmology, however, remains the agreement between predictions and observations of the cosmic microwave background (CMB) anisotropies, see [53, 98, 122], which is confirmed with the new Planck results [52, 125].

We now want to profit also in an optimal way from actual and future galaxy catalogs which contain information on the large scale matter distribution, termed large scale structure (LSS). Contrary to the CMB which is two dimensional, coming mainly from the surface of last scattering, galaxy catalogs are three dimensional and therefore contain potentially more, richer information. On the other hand, galaxy formation is a complicated non-linear process, and it is not clear how much cosmological information about the underlying matter distribution and about gravitational clustering can be inferred from the galaxy distribution. This is the problem of biasing which we do not address in this paper. Here we simply assume that on large enough scales, biasing is linear and local, an hypothesis which might turn out to be too simple [126].

When observing galaxies, we measure their redshift z and their angular position $-\mathbf{n} = (\sin\theta\cos\phi, \sin\theta\sin\phi, \cos\theta)$. Note that $\mathbf{n}$ is the photon direction, so from the source to the observer. Hence we see a galaxy in direction $-\mathbf{n}$. This observed three-dimensional data does not only contain information on the galaxy position, but also on the cosmic velocity field (redshift space distortions) and on perturbations of the

geometry, e.g., lensing effects. Therefore, by making optimal use of galaxy catalogs, we can learn not only about the large scale matter distribution but also about the velocity field and the geometry. Since Einstein's equations relate these quantities, this allows us to test general relativity or more generally the ΛCDM hypothesis, and to estimate cosmological parameters.

In this paper we present a new version of the Cosmic Linear Anisotropy Solving System (CLASS) code[1] [20, 127], incorporating several correction terms already presented in the theoretical works of Ref. [17, 18, 128, 129, 130]. This code is called CLASSgal and is made publicly available on a dedicated website[2]. The parts that concern the CMB have not been changed with respect to the main CLASS distribution. Several new features of CLASSgal will be merged with the main code in future CLASS versions.

In the next section, we describe the equations solved by CLASSgal and the initial input and final output. In section 5.3, we discuss the relevance of the different contributions to the observed power spectrum. In section 5.4, we present some forecasts for parameter estimation with future catalogs, in order to illustrate the usefulness of our code. The topic of this section is worked out in more detail in an accompanying publication [41]. In Section 5.5, we conclude with an outlook to future possibilities using our code. The detailed description of the modifications of the CLASS code as well as some derivations are deferred to two appendices.

5.2 CLASSgal, a code for LSS

When we observe galaxies at a given redshift z and direction $-\mathbf{n}$, we cannot infer their position $\mathbf{x}$. First of all, even in an unperturbed Friedman universe where $\mathbf{x} = -r(z)\mathbf{n}$, the radial comoving distance $r(z)$ depends on cosmological parameters. For small redshifts $z \ll 1$, we have simply $r(z) = zH_0^{-1}$, where H_0 denotes the present value of the Hubble parameter (the H_0 dependence can be removed by measuring distances in units of h^{-1}Mpc, where $H_0 = 100\,h\,\mathrm{km\,s^{-1}Mpc^{-1}}$). For redshifts of order unity and larger, this approximation is no longer sufficient, and one has to take into account the full time dependence of the Hubble parameter $H(z)$:

$$r(z) \;=\; \int_0^z \frac{dz'}{H(z')}\,. \tag{5.1}$$

Normalizing the scale factor a to unity today, $a_0 = 1$, one has

$$H^2(z) \;=\; H_0^2\left(a^{-3}\Omega_m + a^{-2}\Omega_K + \Omega_\Lambda\right)\,, \tag{5.2}$$

[1] http://class-code.net

[2] http://cosmology.unige.ch/tools/

where

$$\Omega_m = \frac{8\pi G\rho_m(t_0)}{3H_0^2} \quad \text{is the matter density parameter,} \tag{5.3}$$

$$\Omega_K = \frac{-K}{H_0^2} \quad \text{is the curvature parameter,} \tag{5.4}$$

and

$$\Omega_\Lambda = \frac{\Lambda}{3H_0^2} \quad \text{is the cosmological constant parameter.} \tag{5.5}$$

For a more complicated dark energy model, the expression involving Ω_Λ has to be modified correspondingly.

Note that both $\mathbf{x}$ and $r(z)$ are comoving distances. Hence, even in an unperturbed Friedmann universe, the three dimensional correlation function

$$\xi(|\mathbf{y}-\mathbf{x}|,t) = \frac{\langle\rho(\mathbf{x},t)\rho(\mathbf{y},t)\rangle}{\bar{\rho}(t)^2} - 1 \tag{5.6}$$

depends on cosmological parameters, and so does its Fourier transform, the power spectrum $P(k,t)$.

But this is not all. The observed redshifts are perturbed by peculiar motions and by fluctuations of the geometry. The first is manifest e.g. in the well known redshift space distortions [61, 106, 131, 132], while the latter is known e.g. through the effect of lensing on number counts [133, 134].

The gauge invariant expression for the perturbation of galaxy number counts, valid in a flat Friedmann universe, at first order in relativistic perturbation theory and ignoring bias, has been derived in Refs. [17, 18, 128, 129]. The result of [17] for the perturbation of number counts in direction $\mathbf{n}$ and at redshift z reads:

$$\begin{aligned}\Delta(\mathbf{n},z) = {} & D_g + \Phi + \Psi + \frac{1}{\mathcal{H}}\left[\Phi' + \partial_r(\mathbf{V}\cdot\mathbf{n})\right] \\ & + \left(\frac{\mathcal{H}'}{\mathcal{H}^2} + \frac{2}{r_S\mathcal{H}}\right)\left(\Psi + \mathbf{V}\cdot\mathbf{n} + \int_0^{r_S} dr(\Phi'+\Psi')\right) \\ & + \frac{1}{r_S}\int_0^{r_S} dr\left[2 - \frac{r_S - r}{r}\Delta_\Omega\right](\Phi+\Psi).\end{aligned} \tag{5.7}$$

Here Ψ and Φ are the Bardeen potentials or, equivalently, the temporal and spatial metric perturbations in the longitudinal gauge. The gauge-invariant quantities D_g and $\mathbf{V}$ coincide respectively with the density fluctuations in the spatially flat gauge and the peculiar velocity in the longitudinal gauge. $\mathcal{H}(z) = H(z)a$ is the comoving Hubble parameter and Δ_Ω denotes the angular Laplacian. Primes denote derivatives with respect to conformal time τ, to reflect the notations used in CLASS (while Ref. [17] used t for conformal time and dots for conformal time derivatives). In the first two lines, all perturbations are evaluated at the coordinates $(\tau(z), -r_S(z)\mathbf{n})$ corresponding to the *unperturbed* position of an object seen at a redshift z in the direction $-\mathbf{n}$. Inside the integral, metric perturbations are evaluated at conformal

time $(\tau_0 - r)$, where τ_0 is the conformal age of the universe, and at comoving radius r.

Eq. (5.7) is valid only for vanishing spatial curvature $K = 0$. In the remainder of this paper, as well as in the present version of the code CLASSgal we restrict ourselves to this case.

Note that in longitudinal gauge, the second parenthesis of the second line of Eq. (5.7) is simply $-\delta z(1+z)^{-1}$, see Ref. [17] for the general expression. When writing this line, we neglect a possible evolution of the number of counts, i.e. we assume that $a^3\bar{n}_S$ is constant, where $\bar{n}_S$ denotes the background number density. Allowing for evolution, one should add in the first parenthesis of the second line of Eq. (5.7) the term [18]

$$\frac{d\ln(a^3\bar{n}_S)}{\mathcal{H}d\tau_S} = -(1+z)\frac{d}{dz}\ln\left(\frac{\bar{n}_S}{(1+z)^3}\right) \equiv f_{\rm evo}(z)\,.$$

For $z \lesssim 1.5$ evolution can be parametrized, e.g., using the Schechter luminosity function [135, 136]. However, since $f_{\rm evo}(z)$ is very uncertain, we have set it to zero by default and simply allow the user to define his/her preferred evolution function $f_{\rm evo}(z)$, see Appendix 5.6.1 for more details.

Furthermore, as it stands, Eq. (5.7) gives the perturbation of the total number density. In practice, however, we cannot observe all galaxies, but only those with a flux which is larger than a certain limit, usually given in terms of a limiting magnitude m_* related to a limiting flux F_* by $m = -2.5\log_{10}F + \text{const.}$ (the constant depends on the units in which we measure the flux). If the fluctuation of the source number density depends on luminosity, the number count at a fixed observed flux F is given by

$$\begin{aligned}\Delta(\mathbf{n},z,F) &= \Delta(\mathbf{n},z) + \left.\frac{\partial\ln\bar{n}_S}{\partial\ln L_S}\right|_{\bar{L}_S}\times\frac{\delta L_S}{\bar{L}_S}\\ &= \Delta(\mathbf{n},z) + 2\left.\frac{\partial\ln\bar{n}_S}{\partial\ln L_S}\right|_{\bar{L}_S}\times\left[\left(\frac{1}{r_S\mathcal{H}}-1\right)\left(\Psi+\int_0^{r_S}dr(\Phi'+\Psi')+\mathbf{V}\cdot\mathbf{n}\right)\right.\\ &\quad\left.+\frac{1}{2r_S}\int_0^{r_S}dr\left[2-\frac{r_S-r}{r}\Delta_\Omega\right](\Phi+\Psi)-\Phi\right]. \qquad (5.8)\end{aligned}$$

up to some local monopole and dipole terms that we neglect for consistency. Here $\bar{L}_S$ is the background luminosity corresponding to a flux F. In the second equality, we made use of the fact that the fractional fluctuation in the luminosity at fixed flux is given by twice the fractional fluctuation in the luminosity distance which is computed e.g. in [9]. In Appendix 5.6.2 we show that the result of Ref. [9] is equivalent to the big bracket of Eq. (5.8).

Denoting the sources in direction $-\mathbf{n}$ at redshift z with magnitude $m < m_*$, i.e., flux $F > F_*$ by $N(\mathbf{n},z,m<m_*)dzd\Omega_0$, and its fractional perturbation by

$D_g(L > \bar{L}_*)$, we then obtain for its fluctuation, see [18]

$$\begin{aligned}\Delta^{(N)}(\mathbf{n}, z, m_*) &= D_g(L > \bar{L}_*) + (1+5s)\Phi + \Psi + \frac{1}{\mathcal{H}}\left[\Phi' + \partial_r(\mathbf{V}\cdot\mathbf{n})\right] + \\ &\left(\frac{\mathcal{H}'}{\mathcal{H}^2} + \frac{2-5s}{r_S\mathcal{H}} + 5s - f^N_{\rm evo}\right)\left(\Psi + \mathbf{V}\cdot\mathbf{n} + \int_0^{r_S} dr(\Phi' + \Psi')\right) \\ &+\frac{2-5s}{2r_S}\int_0^{r_S} dr\left[2 - \frac{r_S - r}{r}\Delta_\Omega\right](\Phi + \Psi)\,. \end{aligned} \tag{5.9}$$

with

$$f^N_{\rm evo} = \frac{\partial \ln\left(a^3 \bar{N}(z, L > \bar{L}_*)\right)}{\mathcal{H}\partial\tau_S}\,.$$

Here we have introduced the dependence of the number density on the luminosity via the logarithmic derivative,

$$s(z, m_*) \equiv \frac{\partial \log_{10} \bar{N}(z, m < m_*)}{\partial m_*} = \frac{\bar{n}_S(z, \bar{L}_*)}{2.5\bar{N}(z, L_S > \bar{L}_*)}\,, \tag{5.10}$$

where

$$\bar{N}(z, L_S > \bar{L}_*) \equiv \frac{\ln 10}{2.5}\int_{-\infty}^{m_*} \bar{n}_S(z, m)dm = \int_{F_*}^{\infty} \bar{n}_S(z, \ln F)d\ln F\,. \tag{5.11}$$

Using this definition and the fact that at fixed z partial derivatives w.r.t. L are the same as those w.r.t. F, one deduces:

$$\left.\frac{\partial \ln \bar{n}_S(z, \ln L_S)}{\partial \ln L_S}\right|_{\bar{L}_*} = -\frac{5}{2}s(z, m_*)\,,$$

which has been used to pass from Eqs. (5.7, 5.8) to (5.9). If the number density is independent of luminosity, s vanishes, and if we can neglect evolution, $f_{\rm evo} = 0$. Then Eq. (5.9) reduces to Eq. (5.7). In the present version of the CLASSgal code, the user can introduce a constant value for $s(z, m_*)$, depending on the limiting magnitude of the catalog she/he wants to analyze. The default value is $s = 0$.

Note that the dominant contribution to the redshift space distortions, the last term on the first line of (5.7), does not dependent on luminosity nor evolution, while the lensing term (third line of (5.7)) is affected by the luminosity dependence. This is the so called magnification bias.

In the code, instead of D_g, it is more convenient to use another gauge-invariant quantity D that coincides with the density fluctuations in comoving gauge. For non-relativistic matter it is related to D_g through [53]

$$D_g = D - 3\left(\frac{\mathcal{H}}{k}V + \Phi\right)\,. \tag{5.12}$$

Without mentioning it, D_g, D and V are always the corresponding quantities for matter (i.e. baryons, cold dark matter and possibly non-relativistic neutrinos) for

which we set $w_m = p_m/\rho_m = 0$. We never use the perturbed Einstein equations in these expressions, so that it is easy to change the code when one wants to consider a different dark energy model which may itself have perturbations, or models which modify gravity.

For the case of ΛCDM, the Einstein equations in the matter and Λ dominated era are simply [53]

$$4\pi G a^2 \rho_{\rm tot} D_{\rm tot} = \frac{3}{2}\mathcal{H}^2 \frac{\Omega_m}{\Omega_m + \Omega_\Lambda a^3} D = -k^2\Phi \ , \qquad \text{and} \quad \Phi = \Psi \, . \tag{5.13}$$

The matter density perturbation D in comoving gauge is related to the total density fluctuation it via $\delta\rho_m/\rho_{\rm tot}|_{\rm com} \equiv D_{\rm tot} = \frac{\Omega_m}{\Omega_m+\Omega_\Lambda a^3} D$.

We can expand Eq. (5.7) or (5.9) in spherical harmonics with redshift dependent amplitudes,

$$\Delta(\mathbf{n}, z) = \sum_{\ell m} a_{\ell m}(z) Y_{\ell m}(\mathbf{n}), \ \text{with} \ \ a_{\ell m}(z) = \int d\Omega_{\mathbf{n}} Y^*_{\ell m}(\mathbf{n}) \Delta(\mathbf{n}, z). \tag{5.14}$$

The star indicates complex conjugation. Denoting the angular power spectrum by

$$C_\ell(z_1, z_2) = \langle a_{\ell m}(z_1) a^*_{\ell m}(z_2) \rangle \tag{5.15}$$

a short calculation gives [17]

$$C_\ell(z_1, z_2) = 4\pi \int \frac{dk}{k} \mathcal{P}(k) \Delta_\ell(z_1, k) \, \Delta_\ell(z_2, k) \tag{5.16}$$

where $\mathcal{P}(k)$ is the primordial power spectrum, and

$$\begin{aligned}
\Delta_\ell(z,k) = {} & j_\ell(kr(z)) \Bigg[bD(\tau(z),k) + \left(\frac{\mathcal{H}'}{\mathcal{H}^2} + \frac{2-5s}{r(z)\mathcal{H}} + 5s - f^N_{\rm evo} + 1 \right) \Psi(\tau(z),k) \\
& + \ (-2+5s)\, \Phi(\tau(z),k) + \mathcal{H}^{-1} \Phi'(\tau(z),k) \Bigg] \\
& + \left[\frac{dj_\ell}{dx}(kr(z)) \left(\frac{\mathcal{H}'}{\mathcal{H}^2} + \frac{2-5s}{r(z)\mathcal{H}} + 5s - f^N_{\rm evo} \right) + \frac{d^2 j_\ell}{dx^2}(kr(z)) \frac{k}{\mathcal{H}} - 3 j_\ell(kr(z)) \frac{\mathcal{H}}{k} \right] V(\tau(z),k) \\
& + \int_0^{r(z)} dr \, j_\ell(kr) \Bigg[(\Phi(\tau,k) + \Psi(\tau,k)) \left(\frac{2-5s}{2} \right) \left(\ell(\ell+1) \frac{r(z)-r}{r(z)r} + \frac{2}{r(z)} \right) \\
& \qquad + (\Phi'(\tau,k) + \Psi'(\tau,k)) \left(\frac{\mathcal{H}'}{\mathcal{H}^2} + \frac{2-5s}{r(z)\mathcal{H}} + 5s - f^N_{\rm evo} \right)_{r(z)} \Bigg] \, .
\end{aligned} \tag{5.17}$$

Here the $j_\ell(x)$'s are the spherical Bessel functions, and all perturbations are the real transfer functions relating the corresponding variables to the power spectrum (we give more details about the definition of the primordial spectrum and of all the transfer functions in Appendix 5.6.1). The times $\tau(z) = \tau_0 - r(z)$ and $\tau = \tau_0 - r$ are conformal times of perturbations which we see at comoving distances $r(z)$ and r respectively. We have replaced D_g in Eq. (5.7) by D using the relation (5.12).

We have added a linear scale-independent bias b between the matter and galaxy density. The choice of adding galaxy bias to the density in the comoving gauge D is justified by the assumption that both galaxies and dark matter follow the same velocity field as they experience the same gravitational acceleration, and the linear bias prescription is valid in their rest frame. In the numerical calculations of the present paper we assume for simplicity $b = 1$, for a detailed discussion of galaxy bias in General Relativity see [137].

The first term in the first line of Eq. (5.17) is the usual density term. The third line collects all redshift space distortions terms and Doppler terms. The usual redshift space distortion derived by Kaiser [61] is the term proportional to $[d^2 j_\ell/dx^2]k/\mathcal{H}$, but sometimes, the subdominant term proportional to $2[dj_\ell/dx]/(r\mathcal{H})$ is also considered as part of the redshift space distortion. The first term on the fourth line is the lensing term. Note that this term is parametrically of the same order as the density and redshift space distortion terms, and therefore can become important in certain situations. The other terms are sometimes called "relativistic corrections". This name is somewhat misleading, since redshift space distortions are also (special) relativistic contributions, and of course the lensing term is also relativistic. We shall therefore simply call them "gravitational potential terms". They contain an integrated Sachs Wolfe effect (term on the last line), and several contributions from the potentials Φ and Ψ at redshift z.

In this equation, we have neglected terms evaluated at $z = 0$, at the observer position, which contribute only to the monopole. We have also neglected the term induced by the observer velocity, which contributes only to the dipole. These terms cannot be calculated reliably within linear perturbation theory. Nevertheless, $C_0(z_1, z_2)$ and $C_1(z_1, z_2)$ contain some interesting information on clustering, to which these local contributions would only add an uninteresting z-independent constant, see [41].

Equations (5.16, 5.17) are valid for a pair of infinitely thin shells located at redshift z_1 and z_2. For realistic redshift bins of finite thickness described by a set of window functions $W_i(z)$, e.g. a Gaussian centered at some redshift z_i, and a given number density of galaxies per redshift interval dN/dz (the integral of the product $W_i(z)dN/dz$ being normalised to unity), one can substitute $\Delta_\ell(z, k)$ with the integral

$$\Delta^i_\ell(k) = \int dz \frac{dN}{dz} W_i(z) \Delta_\ell(z, k) \ , \tag{5.18}$$

and define the power spectrum

$$C^{ij}_\ell = 4\pi \int \frac{dk}{k} \mathcal{P}(k) \Delta^i_\ell \Delta^j_\ell(k) \ . \tag{5.19}$$

For $i = j$, this quantity represents the auto-correlation power spectrum of relativistic density fluctuations observed in the shell around z_i. For $i \neq j$, it represents the cross-correlation power spectrum between two shells. When the window functions are Dirac distributions, we recover the expression $C_\ell(z_i, z_j)$.

Our code CLASSgal calculates C_ℓ^{ij} for a given cosmological model and for a set of window functions (that can be chosen to be Gaussian, Dirac or top-hat distributions). We continue to use the notation $C_\ell(z_i, z_j)$ in the case of Dirac window functions. We easily obtain angular correlation functions by summing up the C_ℓ's,

$$\begin{aligned}\xi(\theta, z_i, z_j) &\equiv \langle \Delta(\mathbf{n}, z_i)\Delta(\mathbf{n}', z_j)\rangle \\ &= \frac{1}{4\pi}\sum_{\ell=0}^{\ell_{\rm max}}(2\ell+1)C_\ell(z_i, z_j)P_\ell(\cos\theta)W_\ell\,, \end{aligned} \tag{5.20}$$

where $W_\ell = \exp\left[-\ell(\ell+1)/\ell_s^2\right]$ is a Gaussian smoothing introduced for convenience, which smoothes out sufficiently high multipoles to avoid unphysical small scales oscillations in $\xi(\theta)$ which are an artifact coming from the finiteness of $\ell_{\rm max}$. For $\ell_{\rm max} \sim 1000$ it is sufficient to choose $\ell_s \sim 600$. $P_\ell(\mu)$ is the Legendre polynomial of degree ℓ and θ is the angle between $\mathbf{n}$ and $\mathbf{n}'$, i.e., $\cos\theta = \mathbf{n}\cdot\mathbf{n}'$. For the case of thick shells,

$$\xi(\theta)^{ij} = \frac{1}{4\pi}\sum_{\ell=0}^{\ell_{\rm max}}(2\ell+1)C_\ell^{ij}P_\ell(\cos\theta)W_\ell\,. \tag{5.21}$$

5.3 Power spectra and correlation functions

In this section we show how CLASSgal can be used to estimate cosmological parameters. Of course, a truly measured correlation function will always have finite redshift and angular resolution, that can be described respectively by the shape and width of the window function, and by an appropriate instrumental noise function growing exponentially above a given ℓ or below a given angle. Furthermore, since we measure density fluctuations with a discrete tracer, namely galaxies, we must add Poisson noise to the error budget.

We first study the sensitivity of the different terms in the power spectrum to the redshift resolution. Throughout this section we set $s = f_{\rm evo} = 0$ in Eq. (5.17). We use a galaxy density distribution dN/dz inspired from the characteristics of a survey like DES[3],

$$\frac{dN}{dz} \propto \left(\frac{z}{0.55}\right)^2 \exp\left[-\left(\frac{z}{0.55}\right)^2\right]\,. \tag{5.22}$$

This assumption is convenient for the purpose of comparing our results with those of Ref. [63]. As explained in the second section of Appendix 5.6.1, CLASSgal allows the user to pass any selection function dN/dz analytically or in the form of tabulated values. For each redshift bin associated with a window function $W_i(z)$, the product $W_i(z)dN/dz$ is normalized to unity.

Fig. 5.1(a) shows the auto-correlation power spectrum of a given redshift bin i, defined in Eq. (5.19), for different types of window functions. In the case of a

[3] `www.darkenergysurvey.org`

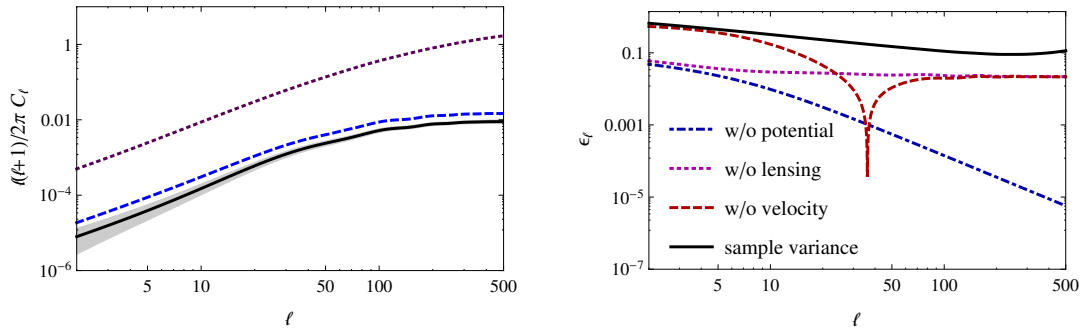

(a) (b)

Figure 5.1: Left panel: auto-correlation power spectrum, defined in Eq. (5.19), for a redshift bin centered around $z = 0.55$ and three different choices of window function: a Gaussian with half-width $\Delta z = 0.1$ (solid, black), a tophat of half-width $\Delta z = 0.1$ (dashed, blue), and a Dirac delta (dotted, purple). For the Gaussian window function we also indicate the error σ_{C_ℓ} as a shaded band.
Right panel: errors in Eq. (5.19) when neglecting gradually gravitational potential terms (dot-dashed, blue), lensing (dotted, purple) and velocity terms (Doppler and z-space distortions, dashed, red). The r.m.s. variance $\sigma_{C_\ell}/C_\ell^{\rm full}$ is also shown (solid, black). Results are computed for a Gaussian bin centered around $\bar{z} = 0.55$ and with half-width $\Delta z = 0.1$.

Gaussian window (solid curve) we plot also the r.m.s. variance given by

$$\sigma_{C_\ell} = \sqrt{\frac{2}{(2\ell+1) f_{\rm sky}}} \left(C_\ell^{ii} + \frac{1}{n_i} \right) \,, \tag{5.23}$$

where n_i is the number of galaxies per steradian inside the bin, and we assume full sky coverage, $f_{\rm sky} = 1$. We assumed the same value of n_i as in the table presented in Ref. [63], reflecting the characteristics of DES (see also footnote 6).

The Dirac delta case corresponds to a purely theoretical quantity. This signal is reduced significantly after the integration with a tophat or Gaussian window function. The tophat can be used if galaxy redshifts are known with spectroscopic precision. If we use a redshift resolution of $\Delta z = 0.001$, the signal is reduced roughly by a factor of 2 with respect to the Dirac delta window function. If only photometric redshift are available, then because of the relatively low z-resolution, the sharp tophat has to be replaced by a Gaussian.

Fig. 5.1(b) shows the errors made when neglecting one or several terms in Eq. (5.17), for a Gaussian bin centered around $\bar{z} = 0.55$ and with half-width $\Delta z = 0.1$. We define

$$\epsilon_\ell = \left| 1 - C_\ell^{\rm partial} / C_\ell^{\rm full} \right| \,, \tag{5.24}$$

where $C_\ell^{\rm full}$ is calculated with all the terms in Eq. (5.17), while in $C_\ell^{\rm partial}$ we gradually neglect the gravitational potential terms (G1-G5 in Eq. (5.44)), the lensing term

('Len' in Eq. (5.44)), and all velocity terms (redshift-space distortions and Doppler, 'Red' and 'Dop' in Eq. (5.44)). Similar comparisons have been presented in [17, 18] with a lower $\ell_{\rm max}$ and different choices of redshift and window functions. Note that when we neglect a contribution, we remove the corresponding auto-correlation as well as the correlations with other terms. Hence the difference ϵ_ℓ can become negative if it is dominated by a negative correlation term. Spikes toward $-\infty$ (in log scale) arise when the difference changes sign.

For comparison, we also show the r.m.s. sample variance $\sigma_{C_\ell}/C_\ell^{\rm full}$ (note that this quantity can in principle be larger than 1). As expected, this variance is more important for lower multipoles. After $\ell \approx 300$ it increases again because shot-noise starts dominating the error.

As expected, gravitational potential terms (dot-dashed) are always subdominant and most important on large scales. The lensing term (dotted) is nearly scale-independent. For the chosen configuration, namely a Gaussian window function centered at $\bar{z} = 0.55$ and with half-width $\Delta z = 0.1$, redshift-space distortions (dashed) represent the most important corrections to the plain density term, and neglecting these distortions introduces an error of the same order as the sample variance (solid) on large scales. At $\ell \gtrsim 38$, the difference ϵ_ℓ from redshift-space distortions changes sign and then become comparable to the lensing corrections. We stress, however, that we are not seeing here the non-linear Fingers-of-God effect, which is important on much smaller scales.

In a companion paper [41], we also consider situations where the redshift space distortion or the lensing term become significantly larger than the noise. There we see that wide window functions significantly reduce redshift space distortions but enhance the lensing term. Using single tracers, we have not yet found a configuration which is such that the potential terms raise above the noise. However, since they are largest on large scales, they are significantly affected by cosmic variance. A multi-tracer analysis may be considered to reduce cosmic variance [138]. Recently, it has also been shown that asymmetries in the correlation function between bright and faint galaxies are useful to enhance the relativistic terms [62].

Using Eq. (5.21), we can also compute the angular correlation function. Fig. 5.2(a) shows the auto-correlation in a redshift bin with either Gaussian, tophat or Dirac window function. In the Dirac case, the result has been divided by 10 for easier comparison using linear scales. In the Gaussian case, we also plot the r.m.s. sample variance.

Observational data on the angular correlation function must be interpreted with care since points at different angles are correlated. On the theoretical level, their non-diagonal covariance matrix is given by [139]

$$\mathrm{Cov}_{\theta\theta'} = \frac{2}{f_{\rm sky}} \sum_{\ell \geq 0} \frac{2\ell+1}{(4\pi)^2} P_\ell(\cos\theta) P_\ell(\cos\theta') \left(C_\ell + \frac{1}{n} \right)^2 , \tag{5.25}$$

and the error at a given angular scale can be estimated as

$$\sigma_{\xi_\theta} = \left(\mathrm{Cov}_{\theta\theta}\right)^{1/2} . \tag{5.26}$$

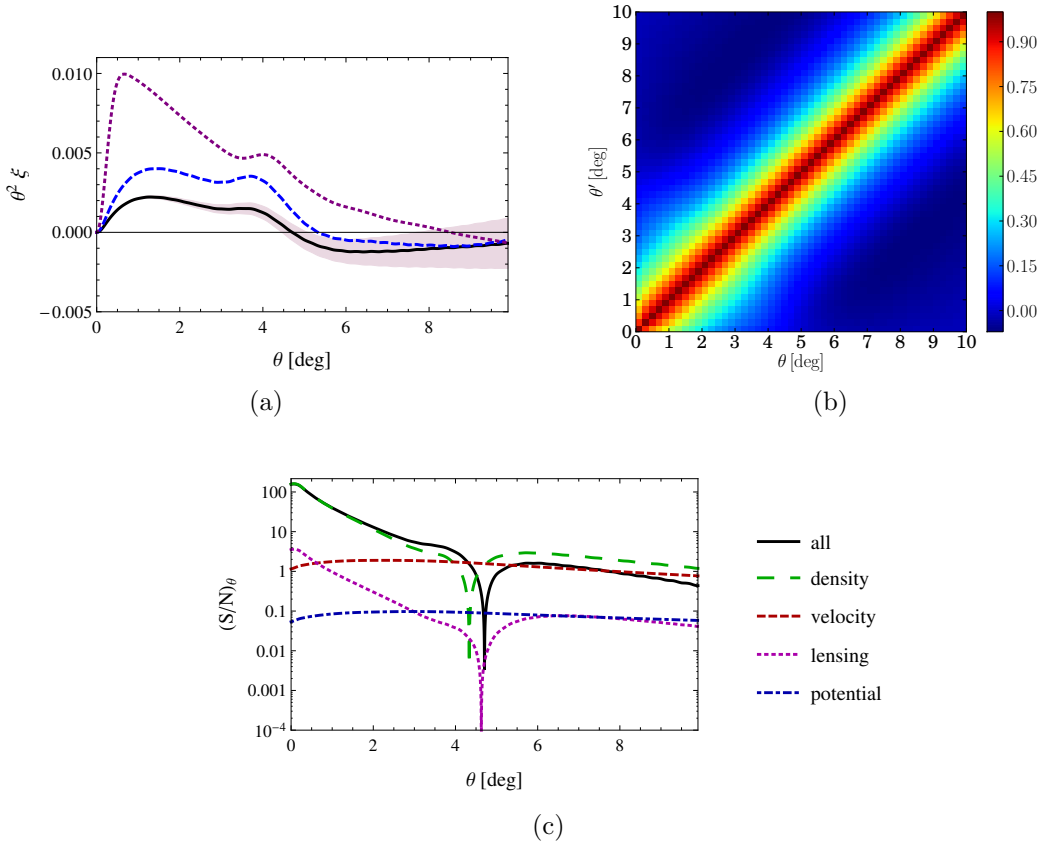

Figure 5.2: Upper left: the angular auto-correlation function, Eq. (5.21), for a bin centered at $\bar{z} = 0.55$ and for a Gaussian window function with $\Delta z = 0.1$ (solid, black), a tophat of half-width $\Delta z = 0.1$ (dashed, blue), and a Dirac delta (dotted, violet). For the Dirac delta case the correlation function has been divided by 10 for easier comparison. For the Gaussian window function we also indicate the error σ_{ξ_θ} as a shaded band. The bumps visible near four degrees correspond to the baryon acoustic feature. Upper right: the reduced covariance matrix of the angular correlation function (given by Eq. (5.25) rescaled by $\sigma_{\xi_\theta}\sigma_{\xi_{\theta'}}$). Bottom: the signal of the different contributions relative to the r.m.s. variance of the full ξ_θ. Results are computed for a Gaussian bin centered at $\bar{z} = 0.55$ and with half-width $\Delta z = 0.1$.

In Fig. 5.2(b) we show the non-diagonal structure of the reduced covariance matrix defined as $\mathrm{Cov}_{\theta\theta'}/\sigma_{\xi_\theta}\sigma_{\xi_{\theta'}}$, for a Gaussian window with half-width $\Delta z = 0.1$ centered at $\bar{z} = 0.55$. Along the diagonal, the reduced covariance matrix is equal to one by construction. Notice the small anti-correlations for $|\theta - \theta'| \gtrsim 6^o$ in dark blue.

Like for the power spectrum, we illustrate the impact of the different terms which appear in Eq. (5.17) on the total correlation function. Results are computed for a Gaussian bin centered around $\bar{z} = 0.55$ and with half-width $\Delta z = 0.1$. Fig. 5.2(c) shows the signal of different effects compared to the r.m.s. variance of the full cor-

relation function:

$$\left(\frac{S}{N}\right)_\theta = \frac{\xi(\theta)^{\rm partial}}{\sigma_{\xi_\theta}} \,, \tag{5.27}$$

where the nominator takes into account density, velocity terms (Doppler and z-space distortions), lensing and potential effects as well as their cross-correlations with previous terms, respectively. Therefore, e.g., the lensing curve considers not only lensing-lensing correlations but also cross-correlations of lensing with velocity and density terms. The curve corresponding to the total, observable, $\xi(\theta)$ is also plotted. The denominator of Eq. (5.27) is given by Eq. (5.26), which is computed considering the contribution of all the terms. Density and lensing curves as well as the total correlation function exhibit a spike to $-\infty$ (in log scale) at the angle for which $\xi(\theta)$ crosses zero. Note that the zero of the full correlation function moves from about 4.2^o to 4.6^o due to the presence of redshift space distortions. One also sees clearly that on large scales, $\theta > 4.5^o$ density and redshift space distortions are anti-correlated while on small scales they are correlated.

The $(S/N)_\theta$ curves show whether an effect gives a contribution larger than sample variance at a given scale, hence $(S/N)_\theta > 1$ suggests that in principle it the corresponding contribution is observable if it can be isolated from the other terms. The main contribution comes from density and redshift space distortions, consistent with Fig. 5.1(b). Lensing is mainly important at small scales, where linear perturbation theory which is adopted here is not longer sufficient since angles $\theta \lesssim 1^\circ$ correspond to comoving separations $r \lesssim 25\,{\rm Mpc}/h$. Potential terms have a signal-to-noise which is nearly scale-independent. Therefore they are more relevant at large separations where other effects decay. Nevertheless, due to cosmic variance $(S/N)_\theta$ of the potential terms never raises towards 1.

The code CAMBsources[4] [18] allows to calculate $C_\ell(z_1, z_2)$ for not too narrow smooth window functions and at not too large values of ℓ [5]. Whenever possible, we have checked that our results for the C_ℓ's agree with the output of CAMBsources, and that those for $\xi(\theta)$ agree with [106]. Our code CLASSgal has been optimized also for non-Gaussian window functions, narrower redshift bins and higher ℓ. It includes several extra options with respect to CAMBsources, that are described in section 5.2 of Appendix 5.6.1.

5.4 Example

As an example, we now determine the accuracy of Ω_m obtained from a galaxy survey, keeping all other parameters fixed, but varying the number of redshift bins $N_{\rm Bins}$ in

[4] `http://camb.info/sources/`

[5] The version of CAMBsources available at the time of this writing (October 2013) leads either to instabilities or to prohibitive memory requirements in the limit of thin Gaussian shells and/or large ℓ.

which we split the data. The Fisher matrix is defined as

$$F_{\alpha\beta} = \sum_{\ell} \frac{\partial C_\ell^{ij}}{\partial \lambda_\alpha} \frac{\partial C_\ell^{pq}}{\partial \lambda_\beta} \mathrm{Cov}^{-1}_{\ell,(ij),(pq)}, \tag{5.28}$$

where the covariance matrix of a given survey with sky coverage $f_{\rm sky}$ reads

$$\mathrm{Cov}_{[\ell,\ell'][(ij),(pq)]} = \delta_{\ell,\ell'} \frac{C_\ell^{\mathrm{obs},ip} C_\ell^{\mathrm{obs},jq} + C_\ell^{\mathrm{obs},iq} C_\ell^{\mathrm{obs},jp}}{f_{\rm sky}\,(2\ell+1)}, \tag{5.29}$$

and the spectra $C_\ell^{\mathrm{obs},ij}$ include a shot-noise contribution related to $n(i)$, the number of galaxies per steradian in the i-th redshift bin,

$$C_\ell^{\mathrm{obs},ij} = C_\ell^{ij} + \frac{\delta_{ij}}{n(i)}. \tag{5.30}$$

Since the spectra C_ℓ^{ij} form a symmetric matrix with $N_{\rm Bins}(N_{\rm Bins}+1)/2$ independent terms, the covariance matrix for each ℓ is of dimension $[N_{\rm Bins}(N_{\rm Bins}+1)/2]^2$. We will also consider an approximate version of the covariance matrix in which cross-correlation between bins are neglected: then the covariance matrix is only of dimension $[N_{\rm Bins}]^2$.

In Fig. 5.3 we show the Figure of Merit (FoM) for Ω_m when all other parameters are fixed, defined as the square root of the diagonal element of the Fisher matrix corresponding to Ω_m (see [41] for more details on this definition). We analyse how the FoM depends on the number of bins considering a spectroscopic survey (like DESspec) with a redshift range from $z = 0.45$ to $z = 0.65$. For comparison, we show the same FoM for an analysis of the observational data based on the reconstruction of the three-dimensional Fourier spectrum $P(k, \bar{z}_i)$ instead of the angular power spectra $C_\ell^{\mathrm{obs},ij}$, using the same number of redshift bins in both cases [41, 140].

Here we consider the same redshift binning strategy and the same shot-noise terms as in Ref. [63][6]. We also consider the same set of non-linearity wavenumbers, $k_{\rm max} = (0.05, 0.1, 0.2)h\mathrm{Mpc}^{-1}$. We limit $\ell < \ell_{\rm max}$ such that scales orthogonal to the line-of-sight and smaller than $\lambda_{\rm min} = 2\pi/k_{\rm max}$ (on which non-linearities are important) are not considered. This condition is equivalent to $[2\pi/\ell_{\rm max}]D_A(\bar{z}) = a(\bar{z})[2\pi/k_{\rm max}]$, giving $\ell_{\rm max} = r(\bar{z})k_{\rm max}$ in flat space. As shown in Fig. 5.3, more redshift bins lead to better constraints on the parameter Ω_m. Instead, the FoM of the 3D Fourier spectrum analysis is almost independent of $N_{\rm Bins}$. The approach based on the angular power spectrum performs significantly better beyond a certain value of $N_{\rm Bins}$ depending on $k_{\rm max}$, that can be read off from the figure. Our results cannot be immediately compared to those of [63] due to a different normalization of the FoM (see [41]). However they are consistent with [63], since the FoM of the two methods intersect each other at roughly the same value of $N_{\rm Bins}$.

[6] The shot noise is determined by the galaxy number density, assumed to be $n = 3.14 \times 10^{-3}h^3\mathrm{Mpc}^{-3}$. In Fig. 5.4, we also show for comparison some results, based on a larger shot noise assumption, with $n = 6.89 \times 10^{-4}h^3\mathrm{Mpc}^{-3}$.

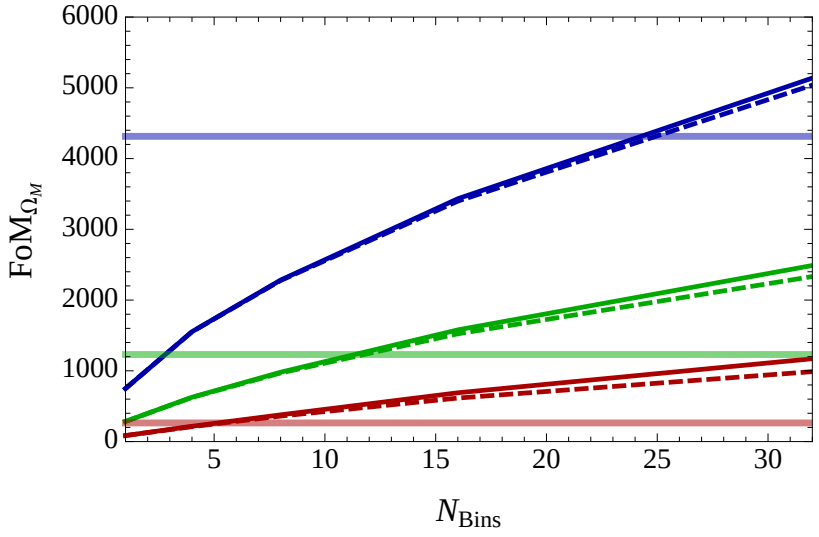

Figure 5.3: FoM as a function of bin number, for a spectroscopic survey (like DESspec). The analysis is performed with a cut-off at different wavenumbers (from top to bottom): $k_{\rm max} = 0.2\ h\ {\rm Mpc}^{-1}$ (blue), $k_{\rm max} = 0.1\ h\ {\rm Mpc}^{-1}$ (green), $k_{\rm max} = 0.05\ h\ {\rm Mpc}^{-1}$ (red). Different line styles show the figure of merit (FoM) considering all the cross correlation spectra between redshift bins (solid lines) or only auto-correlation spectra within redshift bins (dashed). The horizontal lines show the FoM computed for an analysis based on the 3D Fourier spectrum $P(k, \bar{z}_i)$, defined in detail in [41, 140]. In the latter case the dependence on $N_{\rm Bins}$ is negligible.

Our results do not show any saturation when considering more and more redshift bins. Naively one might think that, by considering smaller redshift bins, the shot-noise term would start to dominate at larger scales, since there are less galaxies per bin. But, as shown in Fig. 5.4, this effect is partially compensated by the growth of the signal which is integrated over a narrower window function and therefore less "washed out". Hence the scale at which the shot-noise term starts dominating changes very slowly when decreasing the width of the window function.

According to Fig. 5.4, we expect to start seeing a saturation of the FoM between 50 and 100 redshift bins, which is above the range of values of $N_{\rm Bins}$ shown in Fig. 5.3. This comment applies to the noise of the autocorrelation spectrum in each bin. The shot noise of cross-correlations spectra in pairs of bins is actually twice smaller, so we expect the saturation to occur at an even larger number of bins. We have not computed the FoM up to this level, because it would be computationally very expensive (the calculation time of the FoM scales like $N_{\rm Bins}^4$). Also, such a large number of bins probably becomes unrealistic as soon as one includes instrumental noise in the analysis.

Finally, in Fig. 5.5 we show the covariance matrix at two different ℓ values. The largest signal in the correlation matrix comes clearly from the auto-correlation in each redshift bin.

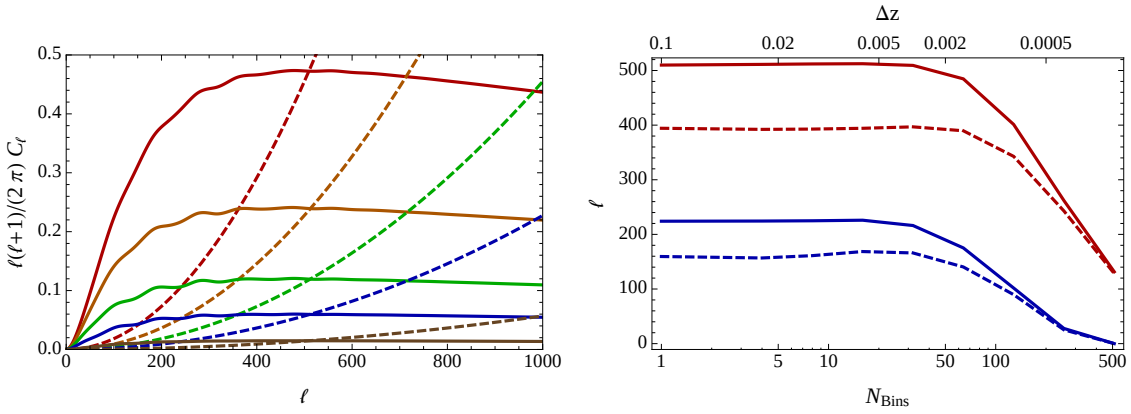

Figure 5.4: In the left panel we show the angular power spectrum C_ℓ (solid lines) and the shot-noise contribution (dashed lines) for different top-hat window functions of half-widths: $\Delta z = 0.1$ (brown), $\Delta z = 0.025$ (blue), $\Delta z = 0.0125$ (green), $\Delta z = 0.00625$ (orange), $\Delta z = 0.003125$ (red). All the window functions are centered at $z = 0.55$ and we consider a spectroscopic survey like DESspec for the shot-noise contribution (assuming the lowest shot noise mentioned in Footnote 6).
In the right panel we plot the multipole ℓ at which the shot-noise term starts to dominate. In red (upper lines) we consider low shot noise, while in blue (lower lines) higher shot noise is assumed (see Footnote 6). We consider top-hat (solid lines) and Gaussian window functions (dashed lines).

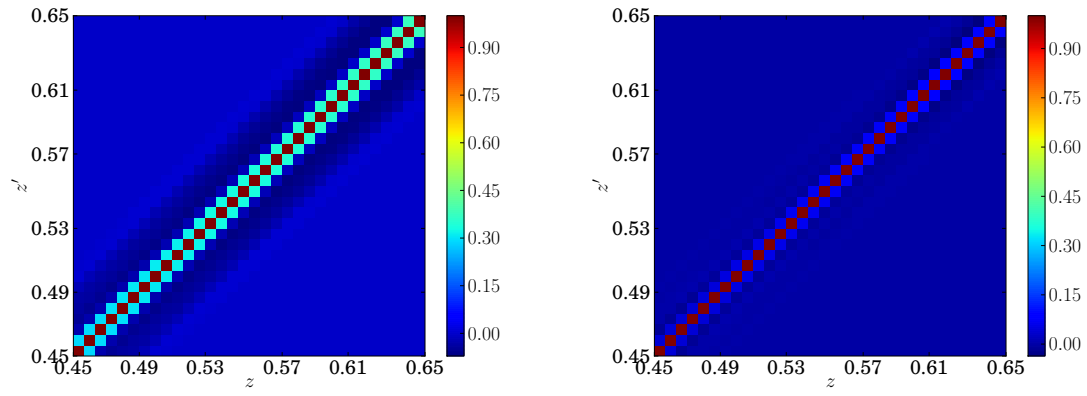

Figure 5.5: We show the correlations between different redshift bins. The left panel is computed for $\ell = 71$ corresponding to $k = 0.05\ h$ Mpc^{-1}, while the right panel shows $\ell = 285$ corresponding to $k = 0.2\ h$ Mpc^{-1} for the mean redshift $\bar{z} = 0.55$. We consider a tophat window function with half-width $\Delta z = 0.003125$.

5.5 Conclusions and outlook

In this paper, we introduce a new version of the CLASS code which computes the linear angular power spectra for large scale structure, C_ℓ^{ij}, in redshift bins described by a set of window functions $W_i(z)$. This code is called CLASSgal and includes all relativistic effects to first order in perturbation theory. The parts that concern the CMB have not been changed with respect to the main CLASS distribution. Several new features of CLASSgal will be merged with the main code in future CLASS versions.

The accuracy of the calculation is similar to the one of the original CLASS code, i.e., overall about 0.1% when using default precision, or up to 0.01% with boosted accuracy settings [141]. Whenever possible, we checked that CLASSgal agrees well with CAMBsources. CLASSgal offers the advantage of including by default several window functions and the possibility of passing tabulated selection and evolution redshift distributions, remaining accurate and efficient for narrow redshift bins and large values of ℓ. The code uses the Limber approximation as described in the Appendix, but for very accurate calculation one can turn off this approximation. For CLASS users, it should be absolutely straight forward to work with this code after reading the explanatory material presented in Appendix 5.6.1 of this work. A newcomer may want to read first the description of the original code in Ref. [127].

We have illustrated the utility of this code with an example where we determine Ω_m from a DES-like galaxy redshift survey. We have studied how the figure of merit depends on the number of redshift bins used, and to which extent slim redshift bins compensate for the increased shot noise by an enhanced signal. Our findings agree well with previous results [63] based on CAMBsources. More applications of our code are found in the accompanying paper [41].

Acknowledgments

We are grateful to Adam Amara, Camille Bonvin, Enrique Gaztañaga, Antony Lewis, Andrina Nicola, Alexandre Refregier and Carlo Schimd, for helpful discussions and for comparison of codes. We acknowledge financial support by the Swiss National Science Foundation. RD was supported in part by the (US) National Science Foundation under Grant No. NSF PHY11-25915.

5.6 Appendix

5.6.1 Differences between CLASS and CLASSgal

Conventions and notations used in the code

The CLASS code uses the notation of Ma & Bertschinger [142] for both Newtonian and synchronous gauge (as usual, the latter is fully specified by requiring in addition that $\theta_{\rm CDM}$ vanishes at initial time, and hence at all times). Conformal time is denoted τ and the prime stands for $' \equiv \partial_\tau$. Instead of $\mathcal{H}$, the code uses the standard

Hubble parameter $H = a'/a^2$ and its derivative $H' = a''/a^2 - 2aH^2$. Metric perturbations read (ϕ, ψ) in Newtonian gauge, and (η, h) in synchronous gauge. The gauge-invariant Bardeen potentials (Φ, Ψ) appearing in Eq. (5.7) are defined in such a way that in Newtonian gauge, they reduce to (ϕ, ψ), while in synchronous gauge, they are given by $([\eta - \mathcal{H}\alpha], [\mathcal{H}\alpha + \alpha'])$, with $\alpha \equiv (h' + 6\eta')/(2k^2)$ [142].

The quantities integrated by the code are not actual Fourier modes depending on $\vec{k}$, but transfer functions depending on k, normalized with respect to the curvature perturbation $\mathcal{R}$ (to be precise, this is true in the case of adiabatic initial conditions; for isocurvature initial conditions CLASS uses standard normalization conventions that can easily be read from the code). Hence, for any perturbation $A(\tau, \vec{k})$ with adiabatic initial conditions, the transfer function $A(\tau, k)$ is defined as

$$A(\tau, k) \equiv \frac{A(\tau, \vec{k})}{\mathcal{R}(\tau_{\rm ini}, \vec{k})} \ . \tag{5.31}$$

The power spectrum of A is then related to the primordial curvature power spectrum by

$$\langle A(\tau, \vec{k}) A^*(\tau, \vec{k'}) \rangle = A(\tau, k)^2 P_{\mathcal{R}}(k) \delta^{(3)}(\vec{k} - \vec{k'}) \ , \tag{5.32}$$

and the dimensionless primordial power spectrum is defined as $\mathcal{P}_{\mathcal{R}}(k) = \frac{k^3}{2\pi^2} P_{\mathcal{R}}(k)$.

Modifications to the `input` module

CLASSgal incorporates a few more optional input parameters than CLASS. In order to compute the angular power spectra including relativistic corrections, one should include at least `output = rCl, ...` in the input parameter file, instead of the usual flag `dCl` referring to the same quantity without relativistic corrections computed also by the main CLASS. The three fields `rCl_rsd`, `rCl_lensing`, `rCl_gr` are set by default to `yes`, but by setting one or several of them to `no`, one can turn off the contribution of redshift-space distortions + Doppler, of lensing, or of gravitational potential terms. The user can pass a value for linear, scale-independent galaxy bias (e.g. `bias = 1.2`). The density transfer function defined below in the first line of Eq. (5.44) is multiplied everywhere by this factor. Magnification bias, by default set to zero, is given by the option `s_bias` that allows constant values. Source evolution is controlled by the field `dNdz_evolution` (by default blank and hence neglecting evolution), that represents the number of sources per redshift and solid angle as a function of redshift. A tabulated evolution function can be considered by passing its file name, e.g., `dNdz_evolution = myevolution.dat`.

The minimum and maximum value of ℓ that will be computed are set by `l_max_lss` and `l_min`. The latter is set by default to 2 but can be decreased to 1 or 0. For $\ell = 0$ the usual output $[\ell(\ell+1)/2\pi]C_\ell$ would of course vanish, so there is an option `cl_rescale = yes/no` : if this is set to `no`, the code will simply output the C_ℓ's.

The shape and characteristics of window functions can be set like in the main CLASS, i.e. by a sequence of the type:

```
selection = gaussian
selection_mean = 1, 1.5, 1.8
```

`selection_width = 0.5,0.4,0.2`
where the shape can be set to `gaussian`, `tophat` or `dirac` (see the comments in the file `explanatory.ini` for more details). These window functions can be multiplied by a selection function common to all redshift bins. This feature is disabled when the field `dNdz_selection` is left blank. For an analytic selection function hard-coded in the source files, one should write `dNdz_selection = analytic`: by default it will point to the function dN/dz used in this paper. For reading a tabulated selection function from a file, one should pass the file name, e.g. `dNdz_selection = myselection.dat`.

The user is free to use the same tabulated redshift distribution for the evolution and the selection function, i.e. the survey observes all the sources. One should simply use the same file for `dNdz_evolution` and `dNdz_selection`.

In the matrix C_ℓ^{ij}, the user may wish to neglect some non-diagonal terms $i \neq j$ in order to speed up the code and get more compact output files. The number of non-diagonal elements is set by `non_diagonal`, that can be assigned between 0 and $N-1$, where N is the number of bins: 0 means 'only auto-correlations', 1 means 'only auto-correlations and adjacent bins', etc.

Modifications to the `perturbation` module

The role of the perturbation module is to integrate the coupled system of evolution equations for cosmological perturbations, and to store in memory a list of source functions $S_X(k,\tau)$ for discrete values of k and τ. These source functions are all linear combinations of transfer functions $A(\tau,k)$. In order to compute unlensed CMB spectra, one needs three well-known source functions $S_{T,E,B}$ described e.g. in [54, 143].

The perturbation module can store many other source functions $S_X(k,\tau)$, depending on the requested output. In the main code CLASS v1.7, they consist in:

- individual density or velocity transfer functions $\{\delta_i(\tau,k), \theta_i(\tau,k)\}$ (expressed in the gauge selected by the user);

- metric fluctuations if the lensing spectrum or lensed CMB spectrum are requested (the standard code stores only $S_g \equiv \Psi$ and assumes $\Phi = \Psi$, which is a good approximation for ΛCDM at late times, but not sufficient for the purposes of this work);

- to prepare the computation of the Fourier matter power spectrum, $P(k)$, or of the harmonic power spectrum of matter density in shells, $C_\ell^{\delta_i\delta_j}$, the code can either store the total fluctuations of non-relativistic matter in a given gauge, $S_{\delta_m} = \delta_m$, or the gravitational potential, $S_g = \Psi$, in view of inferring the total density fluctuation from the Poisson equation (in the sub-Hubble limit and assuming $\Phi = \Psi$). The user can use a flag to switch between these two schemes. Both of them provide approximations to the true observable density power spectrum built from Eq. (5.7), that we wish to compute with CLASSgal.

In CLASSgal, we need to store additional source functions corresponding to different terms in Eq. (5.7). These include the gauge-invariant matter density source function (including CDM, baryons and non-relativistic neutrinos – dubbed more generally non-cold dark matter (`ncdm`) in the code),

$$S_{\rm D} = \delta\rho_{\rm m}/\bar{\rho}_{\rm m} - 2\frac{H'}{H}\frac{\theta_{\rm m}}{k^2} \ , \qquad \text{(Newt. or synch.)} \tag{5.33}$$

the gauge-invariant velocity source function

$$S_\Theta = \theta_{\rm m} \ , \qquad \text{(Newt.)} \tag{5.34}$$
$$S_\Theta = \theta_{\rm m} + k^2\alpha \ , \qquad \text{(synch.)} \tag{5.35}$$

the gauge-invariant Bardeen potentials

$$S_\Psi = \{\psi \ \text{ or } \ \mathcal{H}\alpha + \alpha'\} \ , \tag{5.36}$$
$$S_\Phi = \{\phi \ \text{ or } \ \eta - \mathcal{H}\alpha\} \ , \tag{5.37}$$

and the sum $S_{(\Phi+\Psi)} = S_\Phi + S_\Psi$. The source functions $S_{\rm D}$ and S_Θ coincide with D and kV in Eq. (5.17). The code also needs to store the time derivatives $S_{\Phi'}$ and $S_{(\Phi+\Psi)'}$. In order to avoid heavy equations, these are not inferred from complicated differential combinations of the Einstein equations, but from finite differences: $S_{\Phi'}(\tau) \simeq [S_{\Phi'}(\tau + d\tau) - S_{\Phi'}(\tau - d\tau)]/[2d\tau]$. Since both Φ and Ψ vary only very slowly in the matter and dark energy dominated eras, this does not compromise the accuracy of the code.

Modifications to the `transfer` module

The role of the transfer module is to calculate harmonic transfer functions $\Delta_\ell^X(k)$ by convolving the source functions $S_X(\tau, k)$ with Bessel functions, sometimes using a kernel (accounting for selection functions, rescaling factors, etc.) For instance, in the standard version of CLASS and in the flat space limit, the density transfer function $\Delta_\ell^{\delta_i}(k)$ in a given redshift bin is computed using the Poisson equation

$$-\frac{k^2}{a^2}\psi = 4\pi G\rho_{\rm m}\delta_{\rm m} = \frac{3}{2}H^2\Omega_{\rm m}(\tau)\delta_{\rm m} \ , \tag{5.38}$$

Where $\Omega_{\rm m}(\tau)$ is the fractional density of matter at time τ, and $\delta_{\rm m}$ denotes the matter density fluctuation in synchronous gauge (CLASS also allows computations in Newtonian gauge). This relation neglects pressure from massive neutrinos which is however very small in the redshift range $z < 3$ where we use it. Then

$$\begin{aligned}\Delta_\ell^{\delta_i}(k) &= \int d\tau \, W_i(\tau) \, \delta_{\rm m}(\tau, k) \, j_\ell \left(k(\tau_0 - \tau)\right) \\ &= \int d\tau \, W_i(\tau) \, \frac{2k^2}{3(\Omega_{\rm m} a^2 H^2)_\tau} \, S_{\rm g}(\tau, k) \, j_\ell \left(k(\tau_0 - \tau)\right) \ .\end{aligned} \tag{5.39}$$

Here $W_i(\tau)$ stands for the selection function of the ith redshift bin of a given experiment, specified by the user. The selection functions readily available in CLASS

are Gaussians, top-hat distributions or Dirac distributions in redshift space, always normalized to $\int_0^\infty W_i(z) = 1$. Since they represent a number of galaxies per redshift interval, $W_i(z) = dN/dz$, the associated function $W_i(\tau)$ is calculated by the code according to

$$W_i(\tau) \equiv -\frac{dz}{d\tau} W_i(z) = -H(\tau(z))\, W_i(z) \ . \tag{5.40}$$

Each selection function is associated with a mean redshift $\bar{z}_i \equiv \int_0^\infty dz\, z W_i(z)$, and with a characteristic conformal time $\bar{\tau}_i \equiv \tau(\bar{z}_i)$. The calculation can be sped up by using the Limber approximation for small angular scales (large ℓ's) and nearby shells (small $\bar{z}_i$). We emphasize, however, that the Limber approximation must be used with care, since it may introduce significant errors especially for narrow z-window functions and for z-bin cross-correlations. The user can specify a value for the precision parameter $(\ell/z)_{\rm Limber}$ (set to 30 by default). When for given values of i and ℓ the condition

$$\ell > (\ell/z)_{\rm Limber}\ \bar{z}_i \tag{5.41}$$

is satisfied, the code switches to

$$\Delta_\ell^{\delta_i}(k) = W_i(\tau_L) \frac{2k}{3(\Omega_{\rm m} a^2 H^2)_{\tau_L}} S_{\rm g}(\tau_L, k) \sqrt{\frac{\pi}{(2\ell+1)}} \tag{5.42}$$

with $\tau_L \equiv \tau_0 - \frac{\ell+1/2}{k}$. This approximation corresponds to the first-order Limber approximation. The transfer module contains a routine allowing to switch to the second-order Limber approximation [124], but we checked that the difference between the two is small when the condition (5.41) is satisfied. The Limber approximation remains automatically switched off in the case of Dirac selection functions, for which the integral of Eq. (5.39) is replaced by

$$\Delta_\ell^{\delta_i}(k) = \frac{2k^2}{3(\Omega_{\rm m} a^2 H^2)_{\bar{\tau}_i}} S_{\rm g}(\bar{\tau}_i, k)\, j_\ell\left(k(\tau_0 - \bar{\tau}_i)\right) \ . \tag{5.43}$$

For high-precision calculations, the user can still avoid the Limber approximation for whatever selection function by setting $(\ell/z)_{\rm Limber}$ to a very large value. For non-Dirac selection functions, the code automatically adapts the τ-sampling of the source functions $S_X(k,\tau)$ to the width of the selection function, in order to perform an accurate integral in Eq.(5.39). Thin shells with a narrow $W_i(\tau)$ require a dense sampling of $S_X(k,\tau)$ in the vicinity of each $\bar{\tau}_i$, and increase the computation time and memory. Still, the approach described in these paragraphs represents the fastest and simplest way to calculate approximate density power spectra in shells. However the goal of this paper and of CLASSgal is to use a more involved calculation, accounting for all relativistic correction.

For that purpose, we need to compute many other transfer functions in CLASSgal,

corresponding to the different contributions in Eq. (5.17):

$$
\begin{aligned}
\Delta_\ell^{\mathrm{Den}_i} &= \int_0^{\tau_0} d\tau W_i\, b S_{\mathrm{D}}\, j_\ell \\
\Delta_\ell^{\mathrm{Len}_i} &= \ell(\ell+1)\int_0^{\tau_0} d\tau\, W_i^{\mathrm{L}}\, S_{\Phi+\Psi}\, j_\ell \\
\Delta_\ell^{\mathrm{D1}_i} &= \int_0^{\tau_0} d\tau\, W_i \left(\frac{1+\frac{H'}{aH^2}+\frac{2-5s}{(\tau_0-\tau)aH}+5s-f_{\mathrm{evo}}^N}{k}\right) S_\Theta\, \frac{dj_\ell}{dx} \\
\Delta_\ell^{\mathrm{D2}_i} &= \int_0^{\tau_0} d\tau\, W_i \left(-\frac{3aH}{k^2}\right) S_\Theta\, j_\ell \\
\Delta_\ell^{\mathrm{Red}_i} &= \int_0^{\tau_0} d\tau\, W_i \left(\frac{1}{aH}\right) S_\Theta\, \frac{d^2 j_\ell}{dx^2} \\
\Delta_\ell^{\mathrm{G1}_i} &= \int_0^{\tau_0} d\tau\, W_i \left(2+\frac{H'}{aH^2}+\frac{2-5s}{(\tau_0-\tau)aH}+5s-f_{\mathrm{evo}}^N\right) S_\Psi\, j_\ell \\
\Delta_\ell^{\mathrm{G2}_i} &= \int_0^{\tau_0} d\tau\, W_i\, (-2+5s)\, S_\Phi\, j_\ell \\
\Delta_\ell^{\mathrm{G3}_i} &= \int_0^{\tau_0} d\tau\, W_i \left(\frac{1}{aH}\right) S_{\Phi'}\, j_\ell \\
\Delta_\ell^{\mathrm{G4}_i} &= \int_0^{\tau_0} d\tau\, W_i^{\mathrm{G4}}\, S_{\Phi+\Psi}\, j_\ell \\
\Delta_\ell^{\mathrm{G5}_i} &= \int_0^{\tau_0} d\tau\, W_i^{\mathrm{G5}}\, S_{(\Phi+\Psi)'}\, j_\ell\ .
\end{aligned}
\tag{5.44}
$$

We have omitted all the arguments: k for the transfer functions, (τ, k) for the source functions, $x \equiv k(\tau_0-\tau)$ for the Bessel functions, and τ for selection and background functions. For the integrated terms 'Len', G4 and G5, we have defined

$$
\begin{aligned}
W_i^{\mathrm{L}}(\tau) &= \int_0^{\tau} d\tilde{\tau} W_i(\tilde{\tau}) \left(\frac{2-5s}{2}\right) \frac{(\tau-\tilde{\tau})}{(\tau_0-\tau)(\tau_0-\tilde{\tau})} \\
W_i^{\mathrm{G4}}(\tau) &= \int_0^{\tau} d\tilde{\tau} W_i(\tilde{\tau}) \frac{2-5s}{(\tau_0-\tilde{\tau})} \\
W_i^{\mathrm{G5}}(\tau) &= \int_0^{\tau} d\tilde{\tau} W_i(\tilde{\tau}) \left(1+\frac{H'}{aH^2}+\frac{2-5s}{(\tau_0-\tilde{\tau})aH}+5s-f_{\mathrm{evo}}^N\right)_{\tilde{\tau}}\ .
\end{aligned}
\tag{5.45}
$$

These expressions are valid in flat space, and can be easily generalized to curved space by replacing the spherical Bessel functions by hyper spherical Bessel functions (for an introduction, see [53]).

The evolution term f_{evo}^N has been explicitly implemented in terms of the number of sources per redshift and solid angle $\bar{n}(z)$, i.e. `dNdz_evolution`, according to [18],

$$
f_{\mathrm{evo}}^N = \frac{d}{\mathcal{H} d\tau}\left(\ln \frac{\bar{n}(z) H}{(\tau_0-\tau)^2}\right) = \frac{H'}{aH^2} + \frac{2}{Ha\,(\tau_0-\tau)} - \frac{1}{a}\frac{d\ln(\bar{n}(z))}{dz}. \tag{5.46}
$$

The previous remarks concerning the Limber approximation, the Dirac selection function, and time sampling issues for other selection functions, apply equally to CLASS and CLASSgal.

Modifications to the `spectra` module

The main task of the spectra module is to convolve the primordial spectrum with quadratic combinations of the transfer functions. For instance, in the standard CLASS version, auto-correlation ($i = j$) and cross-correlation ($i \neq j$) harmonic power spectra of matter density fluctuations in shells are given by

$$C_\ell^{\delta_i \delta_j} = 4\pi \int \frac{dk}{k} \mathcal{P}_\mathcal{R}(k) \Delta_\ell^{\delta_i}(k) \Delta_\ell^{\delta_j}(k) \ . \tag{5.47}$$

In CLASSgal, we compute a similar expression, with $\Delta_\ell^{\delta_i}(k)$ replaced by the sum

$$\begin{aligned} \Delta_\ell^i(k) &= \Delta_\ell^{\mathrm{Den}_i} && \text{(Density term)} \\ &+ \Delta_\ell^{\mathrm{Len}_i} && \text{(Lensing term)} \\ &+ \Delta_\ell^{\mathrm{D1}_i} + \Delta_\ell^{\mathrm{D2}_i} && \text{(Doppler term)} \\ &+ \Delta_\ell^{\mathrm{Red}_i} && \text{(Redshift space dist.)} \\ &+ \Delta_\ell^{\mathrm{G1}_i} ... + \Delta_\ell^{\mathrm{G5}_i}. && \text{(Gravity terms)} \end{aligned} \tag{5.48}$$

To show that this expression coincides with Eqs. (5.17, 5.18, 5.19), we replace everywhere H by $\mathcal{H}$, τ by $r = \tau_0 - \tau$ and $\tilde{\tau}$ by $\tilde{r} = \tau_0 - \tilde{\tau}$. Doing this we obtain

$$\begin{aligned} \Delta_\ell^i(k) = & \\ & \int_0^{\tau_0} dr \left\{ W_i(r) j_\ell(kr) \left[b S_\mathrm{D}(r,k) + \left(\frac{\mathcal{H}'}{\mathcal{H}^2} + \frac{2-5s}{r\mathcal{H}} + 5s - f_\mathrm{evo}^N + 1 \right)_r S_\Psi(r,k) \right. \right. \\ & \qquad \left. + (-2+5s)\, S_\Phi(r,k) + \frac{1}{\mathcal{H}(r)} S_{\Phi'}(r,k) \right] \\ & + W_i(r) \left[\left. \frac{dj_\ell}{dx} \right|_{kr} \left(\frac{\mathcal{H}'}{\mathcal{H}^2} + \frac{2-5s}{r\mathcal{H}} + 5s - f_\mathrm{evo}^N \right)_r + \left. \frac{d^2 j_\ell}{dx^2} \right|_{kr} \frac{k}{\mathcal{H}(r)} - 3 j_\ell(kr) \frac{\mathcal{H}}{k} \right] \frac{S_\Theta(r,k)}{k} \\ & + \int_r^{\tau_0} d\tilde{r}\, W_i(\tilde{r})\, j_\ell(kr) \left[\left(\frac{2-5s}{2} \right) \left(\ell(\ell+1) \frac{\tilde{r}-r}{\tilde{r}r} + \frac{2}{\tilde{r}} \right) S_{\Phi+\Psi}(r,k) \right. \\ & \qquad \left. \left. + \left(\frac{\mathcal{H}'}{\mathcal{H}^2} + \frac{2-5s}{\tilde{r}\mathcal{H}} + 5s - f_\mathrm{evo}^N \right) \right|_{\tilde{r}} S_{(\Phi+\Psi)'}(r,k) \right] \right\} \ . \end{aligned} \tag{5.49}$$

We can invert the order of the integrals over r and $\tilde{r}$, and rename the integration variables: we replace r in the first two lines and $\tilde{r}$ in the last line with r_S. With

this, the expression becomes

$$\begin{aligned}\Delta_\ell^i(k) = &\int_0^{\tau_0} dr_S W_i(r_S) \left\{ j_\ell(kr_S) \left[bS_{\rm D}(r_S,k) + \left(\frac{\mathcal{H}'}{\mathcal{H}^2} + \frac{2-5s}{r_S\mathcal{H}} + 5s - f^N_{\rm evo} + 1 \right)_{r_S} S_\Psi(r_S,k) \right.\right. \\ &\left.\left. + \ (-2+5s)\, S_\Phi(r_S,k) + \frac{1}{\mathcal{H}(r_S)} S_{\Phi'}(r_S,k) \right] \right. \\ &+ \left[\left.\frac{dj_\ell}{dx}\right|_{kr_S} \left(\frac{\mathcal{H}'}{\mathcal{H}^2} + \frac{2-5s}{r_S\mathcal{H}} + 5s - f^N_{\rm evo} \right)_{r_S} + \left.\frac{d^2 j_\ell}{dx^2}\right|_{kr_S} \frac{k}{\mathcal{H}(r_S)} - 3j_\ell(kr_S)\frac{\mathcal{H}}{k} \right] \frac{S_\Theta(r_S,k)}{k} \\ &+ \int_0^{r_S} dr\, j_\ell(kr) \left[S_{\Phi+\Psi}(r,k) \left(\frac{2-5s}{2} \right) \left(\ell(\ell+1)\frac{r_S - r}{r_S r} + \frac{2}{r_S} \right) \right. \\ &\left.\left. + \ S_{(\Phi+\Psi)'}(r,k) \left(\frac{\mathcal{H}'}{\mathcal{H}^2} + \frac{2-5s}{r_S\mathcal{H}} + 5s - f^N_{\rm evo} \right)\Big|_{r_S} \right] \right\} . \end{aligned} \tag{5.50}$$

which is identical to the thin shell expression in Eq. (5.17), with an additional integration over the window function, $dr_S W_i(r_S)$.

5.6.2 Luminosity fluctuations

In this appendix we derive in detail the luminosity fluctuation used in expression (5.8). We use the fact that the fractional fluctuation in the luminosity at fixed flux is given by twice the fractional fluctuation in the luminosity distance,

$$\frac{\delta L_S}{\bar{L}_S} = 2\frac{\delta D_L}{\bar{D}_L}.$$

We start from the luminosity distance fluctuation derived in [9] and we change the integration variable from the conformal time τ to $r = \tau_0 - \tau$

$$\begin{aligned}\frac{\delta D_L}{\bar{D}_L} &= \left(\frac{1}{r_S\mathcal{H}_S} - 1 \right) (\mathbf{v}_S\cdot\mathbf{n} + \Psi_S) + \frac{1}{2r_S}\int_0^{r_S} dr \left[2 - \frac{(r_S - r)}{r r_S}\Delta_\Omega \right] (\Psi + \Phi) \\ &+ \frac{1}{r_S\mathcal{H}_S}\int_0^{r_S} dr\,(\Psi' + \Phi') - \int_0^{r_S} dr \frac{r_S - r}{r_S}\,(\Psi' + \Phi') \\ &+ \frac{1}{2r_S}\int_0^{r_S} dr\,(r_S - r)\, r\,(\Psi'' + \Phi'') \\ &- \frac{1}{2r_S}\int_0^{r_S} dr\,(r_S - r)\, r \left[\partial_r^2 + \frac{2}{r}\partial_r \right] (\Psi + \Phi) + \frac{\Psi_S - \Phi_S}{2} \end{aligned} \tag{5.51}$$

where we have neglected the local monopole and dipole terms and we have written the Laplacian in spherical coordinates, $\Delta = \partial_r^2 + \frac{2}{r}\partial_r + \frac{1}{r^2}\Delta_\Omega$. We have also used $\mathbf{n}\cdot\nabla = -\partial_r$. The last term is not present in [9], since there it is assumed that $\Psi = \Phi$, however, it can be found e.g. in Ref. [113]. Considering the total derivative along the geodesic path

$$\frac{d\, f(\tau, \mathbf{x}(\tau))}{dr} = -\frac{d\, f(\tau, \mathbf{x}(\tau))}{d\tau} = -f' - \mathbf{n}\cdot\nabla f = -f' + \partial_r f. \tag{5.52}$$

we can rewrite the last integral of (5.51) as

$$\begin{aligned}
&\frac{1}{2r_S}\int_0^{r_S} dr\,(r_S-r)\,r\left[\partial_r^2+\frac{2}{r}\partial_r\right](\Psi+\Phi)\\
&\quad=\frac{1}{2r_S}\int_0^{r_S} dr\,(r_S-r)\,r\left[\frac{d^2}{dr^2}+2\frac{d\partial_\tau}{dr}+\partial_\tau^2+\frac{2}{r}\frac{d}{dr}+\frac{2}{r}\partial_\tau\right](\Psi+\Phi)\\
&\quad=\frac{\Psi_S+\Phi_S}{2}+\frac{1}{2r_S}\int_0^{r_S} dr\,(r_S-r)\,r\,(\Psi''+\Phi'')+\int_0^{r_S} dr\frac{r}{r_S}\,(\Psi'+\Phi') \quad (5.53)
\end{aligned}$$

Combining all terms together we finally arrive at

$$\begin{aligned}
\frac{\delta D_L}{\bar{D}_L} &= \left(\frac{1}{r_S\mathcal{H}_S}-1\right)\left(\mathbf{v}_S\cdot\mathbf{n}+\Psi_S+\int_0^{r_S} dr\,(\Psi'+\Phi')\right)\\
&+ \frac{1}{2r_S}\int_0^{r_S} dr\left[2-\frac{(r_S-r)}{rr_S}\Delta_\Omega\right](\Psi+\Phi)-\Phi_S.
\end{aligned}$$

6

Cosmological Parameter Estimation with Large Scale Structure Observations

JOURNAL OF COSMOLOGY AND ASTROPARTICLE PHYSICS **01** 042 (2014)

Cosmological Parameter Estimation with Large Scale Structure Observations

Enea Di Dio, Francesco Montanari, Ruth Durrer and Julien Lesgourgues

We estimate the sensitivity of future galaxy surveys to cosmological parameters, using the redshift dependent angular power spectra of galaxy number counts, $C_\ell(z_1, z_2)$, calculated with all relativistic corrections at first order in perturbation theory. We pay special attention to the redshift dependence of the non-linearity scale and present Fisher matrix forecasts for Euclid-like and DES-like galaxy surveys. We compare the standard $P(k)$ analysis with the new $C_\ell(z_1, z_2)$ method. We show that for surveys with photometric redshifts the new analysis performs significantly better than the $P(k)$ analysis. For spectroscopic redshifts, however, the large number of redshift bins which would be needed to fully profit from the redshift information, is severely limited by shot noise. We also identify surveys which can measure the lensing contribution and we study the monopole, $C_0(z_1, z_2)$.

6.1 Introduction

Observations and analysis of the cosmic microwave background (CMB) have led to stunning advances in observational cosmology [52, 53]. This is due on the one hand to an observational effort which has led to excellent data, but also to the theoretical simplicity of CMB physics. In a next (long term) step, cosmologists will try to repeat the CMB success story with observations of large scale structures (LSS), i.e. the distribution of galaxies in the Universe.

The advantage of LSS data is the fact that it is three-dimensional, and therefore contains much more information than the two-dimensional CMB. The disadvantage is that the interpretation of the galaxy distribution is much more complicated than that of CMB anisotropies. First of all, our theoretical cosmological models predict the fluctuations of a continuous density field, which we have to relate to the discrete galaxy distribution. Furthermore, on scales smaller than $30h^{-1}$Mpc, matter density fluctuations become large and linear perturbation theory is not sufficient to compute them. On these scales, in principle, we rely on costly N-body simulations.

In an accompanying paper [19] we describe a code, CLASSgal, which calculates galaxy number counts, $\Delta(\mathbf{n}, z)$, as functions of direction $\mathbf{n}$ and observed redshift z in linear perturbation theory. In this code all the relativistic effects due to peculiar motion, lensing, integrated Sachs Wolfe effect (ISW) and other effects of metric perturbations as described in [17, 18] are fully taken into account. Even if a realistic treatment of the problem of biasing mentioned above is still missing, the number counts have the advantage that they are directly observable as opposed to

the power spectrum of fluctuations in real space which depend on cosmological parameters. The problem how the galaxy distribution, number counts and distance measurements are affected by the propagation of light in a perturbed geometry has also been investigated in other works; see, e.g. [117, 128, 129, 130, 144, 145].

In this paper we use CLASSgal to make forecasts for the ability to measure cosmological parameters from Euclid-like and DES-like galaxy surveys. This also helps to determine optimal observational specifications for such a survey. The main goal of the paper is to compare the traditional $P(k)$ analysis of large scale structure with the new $C_\ell(z_1, z_2)$ method. To do this we shall study and compare the figure of merit (FoM) for selected pairs of parameters. As our goal is not a determination of the cosmological parameters but a comparison of methods, we shall not use constraints on the parameters from the Planck results or other surveys. We just use the Planck best fit values as the fiducial values for our Fisher matrix analysis. We mainly want to analyze the sensitivity of the results to redshift binning, and to the inclusion of cross correlations, i.e., correlations at different redshifts. We shall also study the signal-to-noise of the different contributions to $C_\ell(z_1, z_2)$ in order to decide whether they are measurable with future surveys.

In the next section we exemplify how the same number counts lead to different 3D power spectra when different cosmological parameters are employed. In Section 6.3 we use the Fisher matrix technique to estimate cosmological parameters from the number count spectrum. We pay special attention on the non-linearity scale which enters in a non-trivial way in the Fisher matrix. We then determine the precision with which we can estimate cosmological parameters for different choices of redshift bins and angular resolution. In Section 6.4 we discuss our results and put them into perspective. In Section 6.5 we conclude. Some details on the Fisher matrix technique and the basic formula for the number counts are given in the appendix.

6.2 Number counts versus the real space power spectrum

In this section we illustrate explicitly that the 3D power spectrum is not directly observable. This fact is not new, but it seems not to prevent the community from using the power spectrum which itself depends on cosmological parameters to estimate the latter. This is then usually taken into account by a recursive method: one chooses a set of cosmological parameters (usually the best fit parameters from CMB observations), determines the power spectrum under the assumption that this set correctly describes the background cosmology, and then estimates a new set of cosmological parameters. This process is repeated with the new parameters until convergence is reached, see [48, 146, 147, 148] and others. It is certainly possible to find the best fit parameters in this way, but a correct determination of the errors is more complicated, since not only the power spectrum but also its argument k depends on cosmological parameters. In Fig. 6.1 we show what happens when a measured correlation function is converted into a power spectrum using the wrong

cosmological parameters.

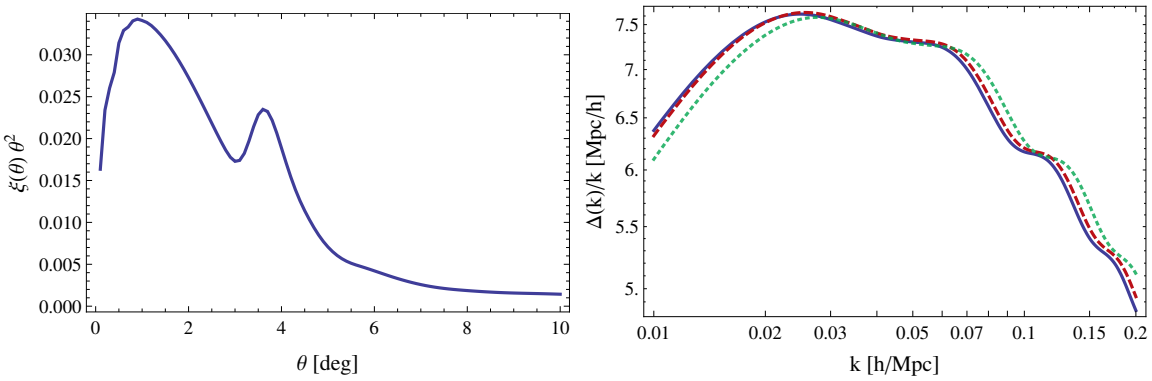

Figure 6.1: Left: the observable correlation function multiplied by θ^2, calculated according to [106] for $\Omega_m = 0.24$ and $z_1 = z_2 = 0.7$. Right: the power spectrum $\Delta^2(k) = k^3 P(k)/2\pi^2$ divided by k and scaled to $z = 0$, obtained by Fourier transforming the correlation function on the top, using three different assumptions to convert $\{\theta, z_1, z_2\}$ into comoving distances: either the fiducial value $\Omega_m = 0.24$ (solid, blue line), or two different values $\Omega_m = 0.3, 0.5$ (dashed, red line and dotted, green line, respectively). All other cosmological parameters are fixed to the WMAP7 best fit values.

The advantage of using the power spectrum is that different Fourier modes are in principle independent. Therefore, errors on the power spectrum are independent. Furthermore, for small redshifts, $z \ll 1$, the parameter dependence of the distance is simply $r(z) \simeq H_0^{-1} z,\ z \ll 1$, where H_0 denotes the Hubble constant. This is usually absorbed by measuring distances in units of h^{-1}Mpc. However, for large redshifts the relation becomes more complicated,

$$r(z) \;=\; \int_0^z \frac{dz'}{H(z')}\,, \tag{6.1}$$

where $H(z) = H_0 \left(\Omega_m (1+z)^3 + \Omega_K (1+z)^2 + \Omega_{\rm DE}(z)\right)^{1/2}$, $\Omega_m = 8\pi G\rho_m/(3H_0^2)$ denotes the present matter density parameter, $\Omega_K = -K/H_0^2$ is the present curvature parameter, and $\Omega_{\rm DE}(z) = 8\pi G\rho_{\rm DE}(z)/(3H_0^2)$ is the dark energy density parameter. $\rho_{\rm DE}$ is in principle redshift dependent, but for a cosmological constant we simply have

$$\rho_{\rm DE} = \rho_\Lambda = \frac{\Lambda}{8\pi G}\,, \qquad \Omega_{\rm DE} = \frac{\Lambda}{3H_0^2}.$$

Furthermore, we see perturbations which are far away from us, at an earlier stage of their evolution, when the power spectrum had a different amplitude.

We therefore propose here an alternative method to analyze large scale structure data. What we truly measure in a galaxy survey is the position of each galaxy in the sky, given by a direction $\mathbf{n}$ and a redshift z.

If we consider only the two dominant contributions, namely the density fluctuations and the redshift space distortions [61, 131, 132] in the number counts, we have [17, 106]

$$\Delta(\mathbf{n}, z) = D(r(z)\mathbf{n}, t(z)) + \frac{1}{\mathcal{H}(z)}\partial_r \left(\mathbf{V}(r(z)\mathbf{n}, t(z)) \cdot \mathbf{n}\right) . \tag{6.2}$$

Here D is the density fluctuation in comoving gauge and $\mathbf{V}$ is the peculiar velocity in longitudinal gauge. The full expression for $\Delta(\mathbf{n}, z)$ including lensing and other subdominant contributions from peculiar velocity and the gravitational potential is given in Appendix 6.6.1. Both $r(z)$ and the conformal time $t(z) \equiv t_0 - r(z)$ depend on the cosmology. To first order in perturbation theory, we can neglect the fact that the redshift and position $(z, \mathbf{n})$ that appear in the argument of D and $\mathbf{V}$ are also perturbed.

Fourier transforming Eq. (6.2), and noting that in Fourier space $\partial_r \to i\mathbf{k} \cdot \mathbf{n}$, we obtain

$$\Delta(\mathbf{k}, t(z)) = D(\mathbf{k}, t(z)) + \frac{k}{\mathcal{H}(z)}(\hat{\mathbf{k}} \cdot \mathbf{n})^2 V(\mathbf{k}, t(z)) . \tag{6.3}$$

Here V is the velocity potential such that $\mathbf{V}(\mathbf{k}) = i\hat{\mathbf{k}}V$ and $\mu = (\hat{\mathbf{k}} \cdot \mathbf{n}) = \cos\phi$, where ϕ denotes the angle between $\mathbf{k}$ and $\mathbf{n}$ and $\hat{\mathbf{k}} = \mathbf{k}/k$ is the unit vector in direction $\mathbf{k}$. For pure matter perturbations, the time dependence of D is independent of wave number such that

$$D(\mathbf{k}, t(z)) = G(z) D(\mathbf{k}, t_0) ,$$

where $G(z)$ describes the growth of linear matter perturbations. For pure matter perturbations, the continuity equation [53] implies

$$\frac{k}{\mathcal{H}(z)} V(\mathbf{k}, t(z)) = f(z) D(\mathbf{k}, t(z)) , \quad \text{where} \quad f(z) = \frac{1+z}{G}\frac{dG}{dz} = \frac{d\log G}{d\log(1+z)} \tag{6.4}$$

is the growth factor. Inserting this in Eq. (6.3), we obtain the following relation for a fixed angle between $\mathbf{k}$ and the direction of observation, and for a fixed redshift z:

$$P_\Delta(k, z) = G^2(z) \left(1 + \mu^2 f(z)\right)^2 P_D(k) . \tag{6.5}$$

If we have only one redshift bin at our disposition, the factor G^2 is in principle degenerate with a constant bias and the overall amplitude of $P_D(k)$. A more general expression for different redshifts and directions can be found in Ref. [106].

Measuring the redshift space distortions that are responsible for the angular dependence of P_Δ allows in principle to measure the growth factor, $f(z)$. Furthermore, assuming that density fluctuations relate to the galaxy density by some bias factor $b(z, k)$, while the velocities are not biased, the first term in Eq. 6.5 becomes proportional to $(b(z, k)G(z))^2$ while the second term behaves like $G(z)f(z)$. This feature allows in principle to reconstruct the bias function $b(z, k)$. It is an interesting question whether this bias can be measured better with our angular analysis or with the standard power spectrum analysis. However, since it is probably not

strongly dependent on cosmological parameters, its reconstruction with the power spectrum method seems quite adequate and probably simpler. In the remainder of the present work we shall therefore not address the interesting question of bias, see e.g. [149, 150].

However, in the above approximation, both relativistic effects which can be relevant on large scales as well as a possible clustering of dark energy are neglected. On top of that, the matter power spectrum in Fourier space is not directly observable. Several steps (like the relation between Fourier wave numbers and galaxy positions) can only be performed under the assumption of a given background cosmology. What we truly measure is a correlation function $\xi(\theta, z, z')$, for galaxies at redshifts z and z' in directions $\mathbf{n}$ and $\mathbf{n}'$, where θ is the angle between the two directions, $\mathbf{n} \cdot \mathbf{n}' = \cos\theta$. The correlation function analysis of cosmological surveys has a long tradition. But the correlation function has usually been considered as a function of the distance r between galaxies which of course has the same problem as its Fourier transform, the power spectrum: it depends on the cosmological parameters used to determine r.

For these reasons, we work instead directly with the correlation function and power spectra in angular and redshift space. They are related by

$$\xi(\theta, z, z') \equiv \langle \Delta(\mathbf{n}, z)\Delta(\mathbf{n}', z')\rangle \;=\; \frac{1}{4\pi}\sum_{\ell=0}^{\infty}(2\ell+1)C_\ell(z, z')P_\ell(\cos\theta)\,, \qquad (6.6)$$

where $P_\ell(x)$ is the Legendre polynomial of degree ℓ. The power spectra $C_\ell(z, z')$ can also be defined via

$$\Delta(\mathbf{n}, z) = \sum_{\ell m} a_{\ell m}(z)Y_{\ell m}(\mathbf{n})\,, \qquad C_\ell(z, z') = \langle a_{\ell m}(z)a^*_{\ell m}(z')\rangle\,, \qquad (6.7)$$

where the star indicates complex conjugation.

The full expression relating $\Delta(\mathbf{n}, z)$ or $C_\ell(z, z')$ to the the primordial power spectrum (given e.g. by inflation), valid at first order in perturbation theory and taking into account all relativistic effects, can be found in Refs. [17] or [19].

The disadvantage of this quantity w.r.t the power spectrum is the fact that the C_ℓ's at different redshifts are not independent. Their correlation is actually very important as it encodes, e.g., the radial BAO's (Baryon Acoustic Oscillations).

We finish this section with the conclusion that in order to measure quantities which are virtually independent of cosmological parameters the power spectrum analysis is sufficient and probably simpler, however when we want to constrain cosmological parameters or related quantities like the growth factor, the angular method proposed here is safer. It has the advantage that it is fully model independent.

6.3 The Fisher matrix and the nonlinearity scale

We consider galaxy number counts as functions of the observational direction and the observed redshift, $\Delta(\mathbf{n}, z)$. In Ref. [19] we describe how the code CLASSgal

calculates the corresponding power spectrum $C_\ell(z_1, z_2)$. We shall consider these spectra as our basic observables and assume that different ℓ-values are uncorrelated. The truly observed spectra have finite resolution in redshift, and are of the form

$$C_\ell^W(z, z') = \int W(z_1, z, \Delta z) W(z_2, z', \Delta z) C_\ell(z_1, z_2) dz_1 dz_2 \,. \tag{6.8}$$

Here $W(z_1, z, \Delta z)$ is a normalized window function centered around z with half-width Δz. We shall use Gaussian and top hat windows (with half-width Δz). Here C_ℓ^W are the Legendre coefficients of the smoothed angular correlation function

$$\xi^W(\theta, z, z') = \int W(z_1, z, \Delta z) W(z_2, z', \Delta z) \xi(\theta, z_1, z_2) dz_1 dz_2 \,. \tag{6.9}$$

6.3.1 Fisher matrix forecasts

We perform a Fisher matrix analysis to compare a forecast for future redshift surveys derived from the angular power spectrum $C_\ell(z_1, z_2)$ with the one derived from the three-dimensional Fourier power spectrum $P(k)$. For a given list of $N_{\rm bin}$ redshift bins with mean redshifts z_i, we denote the auto- and cross-correlation angular power spectra by $C_\ell^{ij} \equiv C_\ell^W(z_i, z_j)$. Since $C_\ell^{ij} = C_\ell^{ji}$, there are $[N_{\rm bin}(N_{\rm bin}+1)/2]$ power spectra to be considered. Assuming that the fluctuations are statistically homogeneous, isotropic and Gaussian distributed, the covariance matrix between different power spectra can be approximated as in Ref. [63],

$$\mathrm{Cov}_{[\ell,\ell'][(ij),(pq)]} = \delta_{\ell,\ell'} \frac{C_\ell^{{\rm obs},ip} C_\ell^{{\rm obs},jq} + C_\ell^{{\rm obs},iq} C_\ell^{{\rm obs},jp}}{f_{\rm sky}\,(2\ell+1)}, \tag{6.10}$$

where $f_{\rm sky}$ is the sky fraction covered by the survey. For each multipole ℓ, the covariance matrix is a symmetric matrix, $\mathrm{Cov}_{[\ell,\ell][(ij),(pq)]} = \mathrm{Cov}_{[\ell,\ell][(pq),(ij)]}$, of dimension $[N_{\rm bin}(N_{\rm bin}+1)/2)]^2$. The definition of the truly observable power spectrum $C_\ell^{{\rm obs},ij}$ takes into account the fact that we observe a finite number of galaxies instead of a smooth field. This leads to a shot noise contribution in the auto-correlation spectra,

$$C_\ell^{{\rm obs},ij} = C_\ell^{ij} + \frac{\delta_{ij}}{\Delta N(i)}, \tag{6.11}$$

where $\Delta N(i)$ is the number of galaxies per steradian in the i-th redshift bin. In principle also instrumental noise has to be added, but we neglect it here, assuming that it is smaller than the shot noise. More details about the Fisher matrix and the definition of 'figure of merit' (FoM) are given in Appendix 6.6.2.

6.3.2 The nonlinearity scale

Our code CLASSgal uses linear perturbation theory, which is valid only for small density fluctuations, $D = \delta\rho_m/\bar{\rho}_m \ll 1$. However, on scales roughly of the order of $\lambda \lesssim 30 h^{-1}$Mpc, the observed density fluctuations are of order unity and larger

at late times. In order to compute their evolution, we have to resort to Newtonian N-body simulations, which is beyond the scope of this work. Also, on non-linear scales, the Gaussian approximation used in our expression for likelihoods and Fisher matrices becomes incorrect. Hence, there exists a maximal wavenumber $k_{\rm max}$ and a minimal comoving wavelength,

$$\lambda_{\rm min} = \frac{2\pi}{k_{\rm max}}$$

beyond which we cannot trust our calculations. There are more involved procedures to deal with non-linearities instead of using a simple cutoff, see e.g. [151]. However, in this work we follow the conservative approach of a cutoff.

For a given power spectrum C_ℓ^{ij} this nonlinear cutoff translates into an ℓ-dependent and redshift-dependent distance which can be approximated as follows. The harmonic mode ℓ primarily measures fluctuations on an angular scale[1] $\theta(\ell) \sim 2\pi/\ell$. Let us consider two bins with mean redshifts $\bar{z}_i \leq \bar{z}_j$ and half-widths Δz_i and Δz_j. At a mean redshift $\bar{z} = (\bar{z}_i + \bar{z}_j)/2$ the scale $\theta(\ell)$ corresponds to a comoving distance $r_\ell = r(\bar{z})\theta(\ell)$, where $r(\bar{z})$ denotes the comoving distance to $\bar{z}$. Let us define the "bin separation" $\delta z_{ij} = z_j^{\rm inf} - z_i^{\rm sup}$, where $z_j^{\rm inf} = \bar{z}_j - \Delta z_j$ and $z_i^{\rm sup} = \bar{z}_i + \Delta z_i$. Hence δz_{ij} is positive for well-separated bins, and negative for overlapping bins (or for the case of an auto-correlation spectrum with $i = j$)[2].

When $\delta z_{ij} < 0$, excluding non-linear scales simply amounts in considering correlations only for distances $r_\ell > \lambda_{\rm min}$. When $\delta z_{ij} > 0$, the situation is different. The comoving radial distance corresponding to the bin separation δz_{ij} is $r_z = \delta z_{ij}\, H^{-1}(\bar{z})$. If $r_z > \lambda_{\rm min}$, we can consider correlations on arbitrarily small angular scales without ever reaching non-linear wavelengths (in that case, the limiting angular scale is set by the angular resolution of the experiment). Finally, in the intermediate case such that $0 < \delta z_{ij} H^{-1}(\bar{z}) < \lambda_{\rm min}$, the smallest wavelength probed by a given angular scale is given by $\sqrt{r_\ell^2 + r_z^2}$. In summary, the condition to be fulfilled by a given angular scale $\theta(\ell)$ and by the corresponding multipole ℓ is

$$\lambda_{\rm min} \;\leq\; \begin{cases} \frac{2\pi}{\ell} r(\bar{z}) & \text{if } \delta z_{ij} \leq 0\,, \\ \sqrt{\left(\frac{\delta z_{ij}}{H(\bar{z})}\right)^2 + \left(\frac{2\pi}{\ell} r(\bar{z})\right)^2} & \text{if } 0 \leq \delta z_{ij} \leq H(\bar{z})\lambda_{\rm min}\,. \end{cases} \tag{6.12}$$

[1] Here we refer to the angular scale separating two consecutive maxima in a harmonic expansion, and not to the scale separating consecutive maxima and minima, given by π/ℓ. Since we want to relate angular scales to Fourier modes, and Fourier wavelengths also refer to the distance between two consecutive maxima, the relation $\theta(\ell) = 2\pi/\ell$ is the relevant one in this context.

[2] In the case of a spectroscopic survey, we will use top-hat window functions. In this case there is no ambiguity in the definition of δz_{ij}, since $(z_i^{\rm sup},\, z_j^{\rm inf})$ are given by the sharp edges of the top-hats. In the case of a photometric survey, we will work with Gaussian window functions. Then $(z_i^{\rm sup},\, z_j^{\rm inf})$ can only be defined as the redshifts standing at an arbitrary number of standard deviations away from the mean redshifts $(\bar{z}_i,\, \bar{z}_j)$. In the following, the standard deviation in the i-th redshift bin is denoted Δz_i, and we decided to show results for two different definitions of the "bin separation", corresponding either to 2σ distances, with $z_j^{\rm inf} = \bar{z}_j - 2\Delta z_j$ and $z_i^{\rm sup} = \bar{z}_i + 2\Delta z_i$, or to 3σ distances, with $z_j^{\rm inf} = \bar{z}_j - 3\Delta z_j$ and $z_i^{\rm sup} = \bar{z}_i + 3\Delta z_i$.

The highest multipole fulfilling these inequalities is

$$\ell^{ij}_{\rm max} = \begin{cases} 2\pi r(\bar{z})/\lambda_{\rm min} & \text{if } \delta z_{ij} \leq 0\,, \\ \frac{2\pi r(\bar{z})}{\sqrt{\lambda^2_{\rm min} - \left(\frac{\delta z_{ij}}{H(\bar{z})}\right)^2}} & \text{if } 0 < \frac{\delta z_{ij}}{H(\bar{z})} < \lambda_{\rm min}\,, \\ \infty & \text{otherwise.} \end{cases} \tag{6.13}$$

In the last case, the cut-off is given by the experimental angular resolution, $\ell^{ij}_{\rm max} = 2\pi/\theta_{\rm exp}$. Only multipoles C^{ij}_ℓ which satisfy the condition $\ell \leq \ell^{ij}_{\rm max}$ are taken into account in our analysis. In the covariance matrix, for the spectra of redshift bins (ij) and (pq), we cut off the sum over multipoles in the Fisher matrix, Eq. (6.25) at

$$\ell_{\rm max} = \min(\ell^{ij}_{\rm max}, \ell^{pq}_{\rm max})\,. \tag{6.14}$$

The nonlinearity scale is fixed by the smallest redshift difference appearing in the two pairs (ij), (pq). This condition ensures that nonlinear scales do not contribute to the derivatives in the Fisher matrix, Eq. (6.25). This is an important limitation because nonlinear scales contain a large amount of information. Clearly, it will be necessary to overcome this limitation at least partially to profit maximally from future surveys. Notice that with $\ell_{\rm max}$ as in Eq. (6.14) the the Fisher matrix can still involve non-linear contributions, but these are confined to the inverse of the covariance matrix (6.10) where also the spectra (iq), (jp), (ip) and (jq) appear. Of course, we need to use values for the cosmological parameters to determine $r(z)$ and $H(z)$ in (6.12), but since this condition is approximate, this does not significantly compromise our results.

6.4 Results

We now present Fisher matrix forecasts for several different types of surveys. In the error budget we only take into account sample variance, shot noise and photometric redshift (photo-z) uncertainties. In this sense, our results are not very realistic: the true analysis, containing also instrumental noise, is certainly more complicated. Nevertheless, we believe that this exercise is useful for the comparison of different methods and different surveys.

In what follows we refer to the $P(k)$ analysis as the 3D case, and to the C_ℓ analysis as the 2D case. We assume a fiducial cosmology described by the minimal (flat) ΛCDM model, neglecting neutrino masses. We study the dependence on the following set of cosmological parameters: ($\omega_b \equiv \Omega_b h^2$, $\omega_{CDM} \equiv \Omega_{CDM} h^2$, H_0, A_s, n_s), which denote the baryon and CDM density parameters, the Hubble parameter, the amplitude of scalar perturbation and the scalar spectral index, respectively. We set the curvature $K = 0$.

6.4.1 A Euclid-like catalog

In this section we perform a Fisher matrix analysis for an Euclid-like catalog. We compare the galaxy surveys with spectral and photometric redshifts. We show the

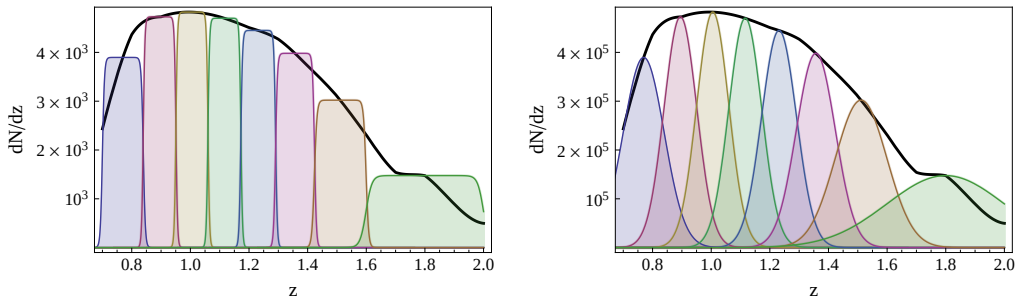

Figure 6.2: Optimal binning strategy for an Euclid-like survey. The black line is the galaxy redshift distribution [105]. We show the case in which the z-interval is divided into 8 bins. The width of every bin is chosen in order to have the same number of galaxies per bin. In the left panel we consider a spectroscopic survey, with tophat bins rounded at the edges to avoid numerical instabilities. (This rounding is not really necessary, but it allows us to use the same integration routine for both, tophat and Gaussian windows. Alternatively we can introduce hard limits in the case of tophat windows. We have compared both approaches and found that the difference is negligible.) On the right we show the case of a photometric survey, for which bins are chosen to be Gaussian because of photo-z uncertainties.

dependence of the FoM on redshift binning and on the nonlinearity scale. We concentrate on a few crucial observables since this is an illustration of our method and not a comprehensive forecast of a specific experiment. We defer to future work the inclusion of systematic errors and instrumental noise for a given experiment.

Methodology

We determine the FoM for the joint estimation of the Hubble parameter H_0 and of the CDM density parameter $\omega_{\rm CDM}$, marginalized over the other cosmological parameters (ω_b, A_s, n_s). We do the same for the joint estimation of the baryon density parameter ω_b and $\omega_{\rm CDM}$, marginalized over (H_0, A_s, n_s). We adopt two different non-linearity scales, $\lambda_{\rm min} = 34$ Mpc/h and $\lambda_{\rm min} = 68$ Mpc/h. We assume an angular resolution of about 3 arc minutes such that in addition to the condition given in Eqs. (6.13, 6.14) we impose $\ell_{\rm max} \leq 3000$. Note that we do not combine with known datasets like Planck to minimize the uncertainties on parameters. The goal here is not an optimal prediction of the improvement on cosmological parameter estimation by Euclid (for this we would need a detailed treatment of instrument errors). Here we want to compare two methods, the 3D and 2D analysis. In addition, we also study the importance of off–diagonal correlators and of the non-linearity scale.

Binning strategy

The overall galaxy redshift distribution of the survey in the considered range $0.7 < z < 2$ is the black line in Fig. 6.2, see [105][3]. Our binning strategy is to adjust the width of each bin such that there is the same number of galaxies per redshift bin. We verified that this choice gives higher FoM's than the choice of constant bin width, because it minimizes shot noise.

We consider a spectroscopic and a photometric survey. In the first case bins are tophat in redshift. In practice, to avoid numerical instabilities, CLASSgal uses rounded edges, see [19]. For the photometric case, we assume to dispose of 100 times more galaxies, but to take into account the uncertainties of the redshifts, we model the bins as Gaussian. The width of the bins must be consistent with the photo-z errors $0.05(1+z)$, for a splitting of the redshift interval $0.7 < z < 2$ this corresponds to about 6 bins. Instead, spectroscopic precision $0.001(1+z)$ is not an issue in our analysis.

In both cases (spectroscopic and photometric), we compare the results of a 2D and 3D analysis. For the 3D spectroscopic case, the FoM is nearly independent of the number of bins, within a few percent. Hence in the following plots we adopt a constant value computed with $N_{\rm bin} = 1$. The reason for this is that we assume a known redshift dependence of the growth factor, $f(z) = \Omega_M(z)^\gamma$ with $\gamma = 0.6$. If we would want to determine γ or to reconstruct the bias, $b(z)$, increasing the number of bins would be significant also for the 3D analysis. However, since this aspect is very similar for both, the 2D and the 3D analysis, we do not study it in this work.

In the 3D photometric case, the FoM is no longer constant, but rather decreases slowly with $N_{\rm bin}$. In fact, photometric uncertainties cause redshift bins to be correlated, hence the total Fisher matrix is not well approximated by the sum of the Fisher matrices of each bin, as assumed in [63] and in the present work. Since we wish to refer to the most favorable bin configuration in the 3D analysis, we will always compare 2D photometric results with the 3D photometric FoM obtained for $N_{\rm bin} = 1$.

2D and 3D performances

Not surprisingly, considering a smaller nonlinearity scale $\lambda_{\rm min}$ yields a larger FoM (compare the left and right panels of Figure 6.3). Naively, we expect to gain a factor 8 in the FoM when going from $\lambda_{\rm min} = 68h^{-1}$Mpc to $\lambda_{\rm min} = 34h^{-1}$Mpc, since we have 2^3 times more Fourier modes at our disposition. Fig. 6.3 quite accurately confirms this expectation for the 3D case (black lines). Interestingly, the 2D FoM degrades only by about a factor of 2 when the non-linearity scale is increased by 2. Since the redshift resolution is not affected by $\lambda_{\rm min}$, naively we would expect a degradation by a factor of 4 from the transverse directions, but it seems that the redshift information is as important as both transverse direction so that we only loose a factor of 2.

[3]See also `http://www.euclid-ec.org/`.

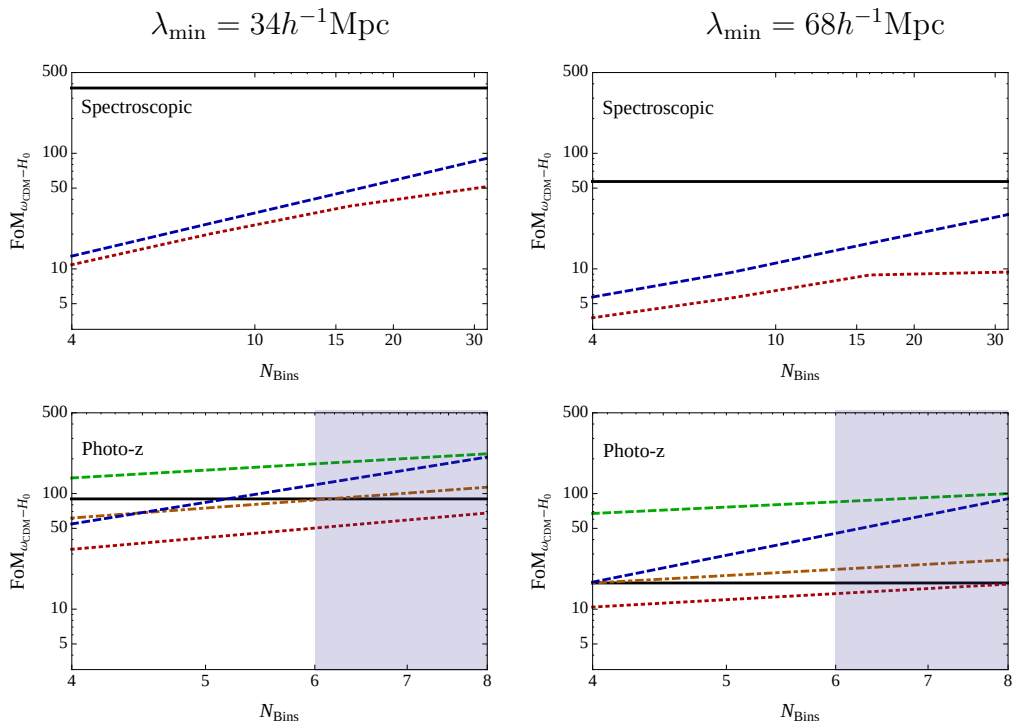

Figure 6.3: FoM for an Euclid-like survey for the non-linearity scales 34 Mpc/h, left panels, and 68 Mpc/h, right panels. Top panels refer to spectroscopic redshifts, bottom panels to photometric ones. For the 2D FoM we consider a cut at $\ell_{\rm max}$ values defined in Eq. (6.14) (dashed blue), and also the case in which cross-correlations of bins are neglected (dotted red). For the photometric survey, we plot the result derived from two different definitions of the bin separation (and hence of $\ell_{\rm max}$), defining ($z_i^{\rm sup}$, $z_j^{\rm inf}$) at either 2- (green) or 3-σ (blue), see Footnote 2. For this case we also plot the FoM for the $\ell_{\rm max}$ determination of Ref. [63] (dot-dashed orange). The solid black line shows the value of the 3D FoM for $N_{\rm bin} = 1$ and $\sigma_z = 0.05(1+\bar{z})$ in the photometric case. The shadowed region exceeds this z resolution.

In Figure 6.3, we also show the FoM adopting different definitions of $\ell_{\rm max}$ and including only auto-correlations of redshift bins. Apart from our definition of $\ell_{\rm max}$ given in Eqs. (6.13, 6.14), we also consider the definition $\ell_{\rm max} = r(\bar{z})2\pi/\lambda_{\rm min}$ used in [63], where $r(\bar{z})$ is the comoving distance to the mean redshift $\bar{z} = 1.35$ of the survey. While in the spectroscopic case this yields results which are within 30% of those obtained with our method, in the photometric case the FoM is significantly improved when using our definition, compare the (dot-dashed) orange and the (long dashed) green lines in the lower panels of Figure 6.3. The definition of Ref. [63] is sufficient for a narrow band survey, but not for a Euclid-like survey. This shows how much information can be gained by using our optimal definition of $\ell_{\rm max}$ given in Eq. (6.14) but also by taking into account cross-correlations (dashed blue lines) as compared to considering only the auto-correlation of redshift bins (dotted red lines). For photometric redshifts the result strongly depends on the value chosen for δz_{ij} which determines $\ell_{\rm max}^{ij}$. The larger is δz_{ij}, the more radial information is

lost. Compare the green (dashed, top) and blue (dashed, lower) lines for the photo-z FoM's, where we compare the choice of 2 and 3 standard deviation for δz_{ij}. This is the problem of Gaussian binning. It does spread the radial information considerably. Nevertheless, the reduction of shot noise (due to the fact that the photometric survey is assumed to contain a hundred times more galaxies) compensates for this, and leads to a better FoM from photometric surveys in the 2D analysis. However, in the spectroscopic case we could still increase the number of bins.

Interestingly, with the more conservative value of the non-linearity scale $\lambda_{\rm min} = 68$ Mpc$/h$ (right hand panels of Fig. 6.3), the difference between the full analysis (blue, dashed) and the one involving only auto-correlations (red, dotted) becomes very significant also for spectroscopic surveys. When considering only auto-correlations, the spectroscopic FoM reaches saturation at 16 bins. One reason for this is that shot noise affects auto-correlations more strongly than cross-correlations. But even neglecting shot noise, we still observe this saturation. We just cannot gain more information from the auto-correlations alone by increasing the number of bins, i.e. by a finer sampling of transverse correlations.

Comparing the spectroscopic with the photometric survey and sticking to the 2D analysis, we find that the photometric specifications yield a larger FoM. This is not surprising, since the latter case contains 100 times more galaxies than the spectroscopic survey, for which shot noise is correspondingly 100 times larger. Also, the FoM for the 2D analysis mainly comes from cross correlations. This is why different choices of δz_{ij} affect the final result so much.

The photometric FoM from the 3D analysis, however, is lower than the one from the spectroscopic survey. In the 3D case, the redshift uncertainties translate into uncertainties in the wavenumber k which are more relevant than the reduction of shot noise.

When the number of bins is large enough, our 2D analysis yields a better FoM than the standard $P(k)$ analysis. For the photometric survey this is achieved already at $N_{\rm bin} = 4 - 6$ while for the spectroscopic survey probably about 120 bins would be needed.

At some maximal number of bins the number of galaxies per bin becomes too small and shot noise starts to dominate. At this point nothing more can be gained from increasing the number of bins. However, since for slimmer redshift bins not only the shot noise but also the signal increases, see [19] for details, the optimal number of bins is larger than a naive estimate. In Ref. [19] it is shown that the shot noise, which behaves like $\ell(\ell+1)/2\pi$ (in a plot of $\ell(\ell+1)C_\ell/2\pi$), becomes of the order of the signal at somewhat smaller ℓ for slimmer redshift bins. Again, due to the increase of the signal this dependence is rather weak down to a redshift width of $\Delta z = 0.0065$. For redshift slices with $\Delta z < 0.005$, the signal does not increase anymore while the shot noise still does. For a DES-like survey, this maximal number of bins is about $N_{\rm max}^{\rm (DES)} \sim 50$, while for a Euclid-like survey it is of the order of $N_{\rm max}^{\rm (Euclid)} \sim 200$.

When using redshift bins which are significantly thicker than the redshift resolution of the survey, the 3D analysis, in principle, has an advantage since it makes use of the full redshift resolution in determining distances of galaxies, while in the

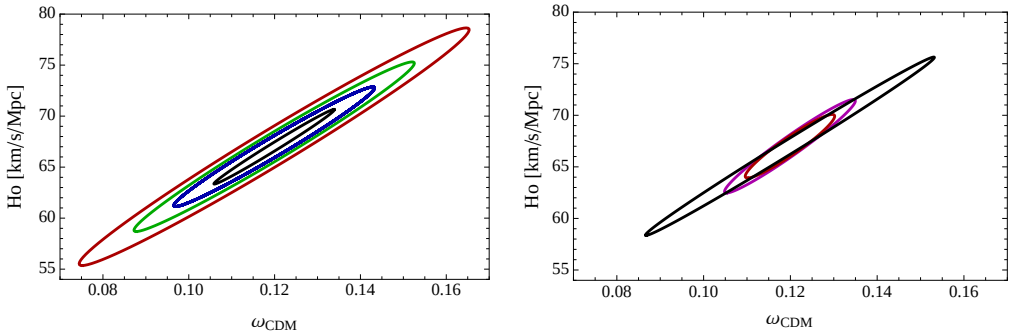

Figure 6.4: Confidence ellipses in the H_0–$\Omega_{\rm CDM}h$ plane (marginalized over the other cosmological parameters) for an Euclid-like survey computed with a non-linearity scale of 34 Mpc/h. Different colors indicate different redshift bin numbers: 4 bins (magenta), 8 bins (red), 16 bins (green), 32 bins (blue). Black contours refer to the 3D analysis for $N_{\rm bin} = 1$. We consider a spectroscopic survey (left panel) and a photometric one (right panel, for 2σ bin width).

2D analysis we do not distinguish redshifts of galaxies in the same bin. A redshift bin width of the order of the nonlinearity scale beyond which the power spectrum is not reliable, given by $r(\bar{z}, \Delta z) \sim 2\Delta z/H(\bar{z}) \simeq \lambda_{\rm min}$ is the minimum needed to recover the 3D FoM for spectroscopic surveys.

However, for spectroscopic surveys we can in principle allow for very slim bins with a thickness significantly smaller than the nonlinearity scale, and the maximal number of useful bins is decided by the shot noise. Comparing the C_ℓ^{ii} with C_ℓ^{jj}, e.g., of neighboring bins still contains some information, e.g., on the growth factor, even if $\ell^{ij}_{\rm max} \sim \ell^{ii}_{\rm max}$ for small $|i-j|$. In simpler terms, the fact that our analysis effectively splits transversal information coming from a given redshift and radial information from C_ℓ^{ij} with large ℓ, makes it in principle advantageous over the $P(k)$ analysis. It becomes clear from Fig. 6.3 (see also Fig. 6.7 below) that we need to use sufficiently many bins and our definition of $\ell^{ij}_{\rm max}$ to fully profit from this advantage.

The numerical effort of a Markov Chain Monte Carlo analysis of real data scales roughly like $N^2_{\rm bin}$. Running a full chain of, say 10^5 points in parameter space requires the calculation of about $10^5 N^2_{\rm bin}/2$ spectra with CLASS. (For comparison, a CMB chain requires 'only' 4×10^5 spectra).

Note also, that the advantage of the 2D method is relevant only when we want to estimate cosmological parameters. If the cosmology is assumed to be known and we want, e.g., to reconstruct the bias of galaxies w.r.t. matter density fluctuations, both methods are equivalent. But then, the redshift dependence also of $P(k)$ has to be studied and both power spectra, $P(k, \mu, z)$ and $C_\ell(z, z')$ are functions of three variables.

In Figure 6.4 we plot, as one of several possible examples, the confidence ellipses in the $H_0 - \omega_{\rm CDM}$ plane (marginalized over the other cosmological parameters) for an Euclid-like survey computed with a nonlinearity scale of 34 Mpc/h for different redshift bins. We do not assume any prior knowledge e.g. from Planck. Therefore

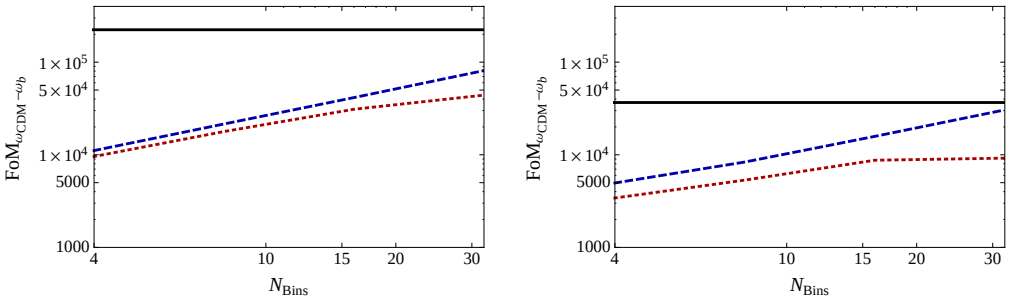

Figure 6.5: FoM for $\omega_{\rm CDM}$ - ω_b (marginalized over other cosmological parameters) for different nonlinearity scales (34 Mpc/h, left panels, and 68 Mpc/h, right panels) for a spectroscopic Euclid-like survey. For the 2D FoM we consider $\ell_{\rm max}$ as defined in Eq. (6.14) (dashed blue), and also the case in which cross-correlations of z-bins are neglected (dotted red). The solid black line shows the value of the 3D FoM for $N_{\rm bin} = 1$.

again, this is not a competitive parameter estimation but only a comparison of methods. We also show the dependence of the result on the number of bins. The strong degeneracy between H_0 and $\omega_{\rm CDM}$ comes from the fact that $\omega_{\rm CDM}$ is mainly determined by the break in the power spectrum at the equality scale $k_{\rm eq}$ which of course also depends on H_0. As is well known, the break in the power spectrum actually determines $\Omega_{\rm CDM}h \propto \omega_{\rm CDM}/H_0$. This determines the slope of the ellipse in Figure 6.4 which is extremely well constrained. Note also that the 2D and 3D ellipses have a slightly different slope, hence different principal axis. This implies that they do not constrain exactly the same combinations of H_0 and $\omega_{\rm CDM}$.

In Fig. 6.5 we show the FoM for $(\omega_b, \omega_{\rm CDM})$ for the spectroscopic Euclid survey. We marginalize over the other parameters, (H_0, n_s, A_s). Also in this case, the important contribution from cross–correlations, especially for the larger non-linearity scale is evident.

6.4.2 A DES-like catalog

We perform the same analysis as in the previous section also for a DES-like survey[4]. A similar analysis has been performed in Refs. [63, 152], and the goal of this section is to compare our results with these references. The novelties of the present analysis is that we marginalize over cosmological parameters which have been fixed in Refs. [63, 152] and we use a more sophisticated definition of the nonlinearity scale. Following [63] we consider a galaxy density distribution dN/dz given by

$$\frac{dN}{dz} \propto \left(\frac{z}{0.55}\right)^2 \exp\left[-\left(\frac{z}{0.55}\right)^2\right] , \tag{6.15}$$

in the redshift range $0.45 < z < 0.65$, which is divided in z-bins of the same size. The shot noise is determined by the galaxy number density, assumed to be

[4] `www.darkenergysurvey.org`

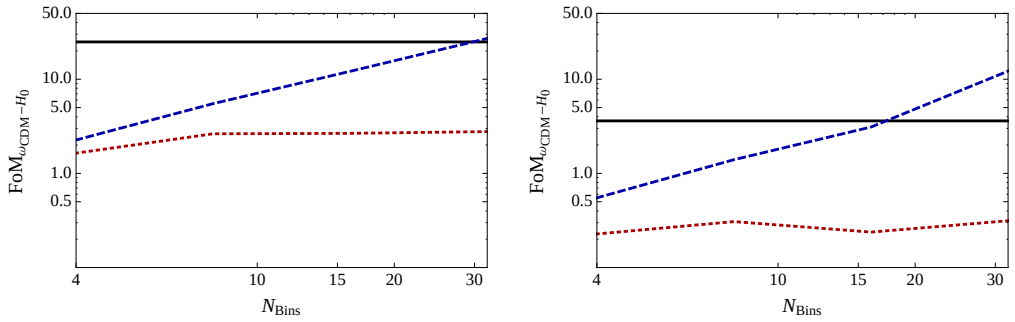

Figure 6.6: FoM for the nonlinearity scales 34 Mpc/h, left panels, and 68 Mpc/h, right panels for a spectroscopic, DES-like survey. For the 2D FoM we consider $\ell_{\rm max}$ as defined in Eq. (6.14) (dashed blue), and also the case in which cross-correlations between bins are neglected (dotted red). The solid black line shows the value of the 3D FoM for $N_{\rm bin} = 1$.

$n = 3.14 \times 10^{-3} h^3 {\rm Mpc}^{-3}$, constant in z. In this case we only consider a spectroscopic redshift resolution.

In Fig. 6.6 we show the FoM for the determination of $(H_0, \omega_{\rm CDM})$ from a DES-like survey, marginalizing over the remaining cosmological parameters. In this case, the FoM coming from autocorrelations alone saturates already at $N_{\rm bin} = 8$. The FoM including cross-correlations continues to grow and overtakes the one from the 3D analysis at $N_{\rm bin} = 30$.

In Fig. 6.7 we compare the FoM of each parameter in the 2D and 3D case for different values of the non-linearity scale. The mean number of bins at which the nonlinearity scale is reached, $\Delta z \simeq \lambda_{\rm min} H(\bar{z})/2$, is indicated as vertical grey bar. The number of bins where the 2D analysis becomes better than the 3D one, especially for the marginalized FoM, is typically nearly a factor of 2 larger than this naive estimate. This may come from the fact that we include correlations with small (or vanishing) angular separation only if $|z_j^{\rm inf} - z_i^{\rm sup}|$ is large enough while for most galaxies the mean bin distance $|\bar{z}_j - \bar{z}_i|$ would be relevant. In this sense our choice is conservative.

Interestingly, comparing Euclid and DES FoM's we find that while the $P(k)$ FoM for a Euclid-like survey is more than a factor of 10 times better than the one of a DES-like survey, this is no longer true when we compare the FoM's from our angular analysis at fixed number of redshift bins. However, to find the true (optimal but still realistic) FoM we have to increase the number of redshift bins until the FoM converges to its maximum. In practice at some point the instrumental noise which has been neglected in our treatment will prevent further growth of the FoM so that we refrained from going beyond $N_{\rm bin} = 32$ which would also be numerically too costly with our present implementation, but which will be interesting for a future analysis.

For completeness, we also show the FoM for $(\omega_b, \omega_{\rm CDM})$ for the DES like surveys marginalizing over (H_0, n_s, A_s) in Fig. 6.8. Again, the FoM from auto-correlations

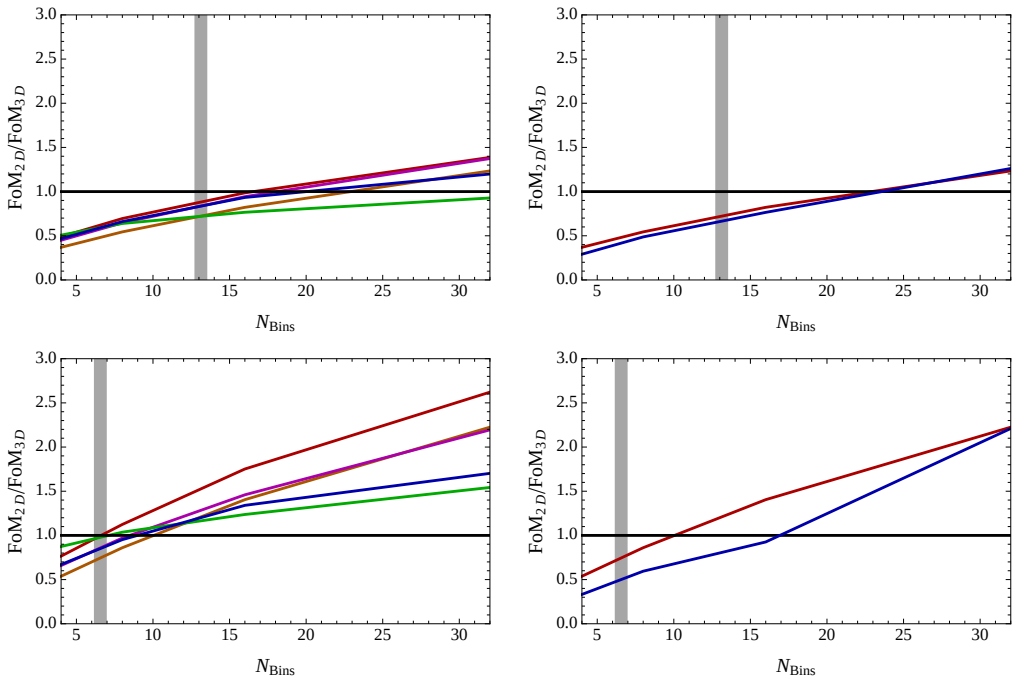

Figure 6.7: In the left panels we show the ratio between FoM 2D over 3D for each single parameter keeping the others fixed for a DES-like survey. Different colors indicate different parameters: ω_b (red), $\omega_{\rm CDM}$ (orange), n_s (magenta), H_0 (green) and A_s (blue). The vertical thick gray line shows when the bin size becomes of the same order of the non-linearity scale, where we expect that 2D and 3D analysis should roughly give the same result. This seems only approximately true. On the right panels we show the ratio between FoM's from 2D over 3D for ω_{CDM}. In red keeping the other cosmological parameters fixed, while in blue marginalizing over all other parameters. In the top panels we consider the nonlinearity scale $\lambda_{\rm min} = 34h^{-1}$Mpc while in the bottom panels we have $\lambda_{\rm min} = 68h^{-1}$Mpc.

only (red, dotted) saturated at about 8 redshift bins.

6.4.3 Measuring the lensing potential

It is well known that the measurement of the growth rate requires an analysis of galaxy surveys which are sensitive to redshift-space distortions [146, 153, 154, 155]. Isolating other effects can lead to an analysis which is more sensitive to other parameters. In this section we study especially how one can measure the lensing potential with galaxy surveys. The lensing potential is especially sensitive to theories of modified gravity which often have a different lensing potential than General Relativity, see, e.g. [107, 156, 157]. The lensing potential out to some redshift z is defined by [53]

$$\Psi_\kappa(\mathbf{n}, z) = \int_0^{r_s(z)} dr \frac{r_s - r}{r_s r} \left(\Psi(r\mathbf{n}, t) + \Phi(r\mathbf{n}, t)\right) . \tag{6.16}$$

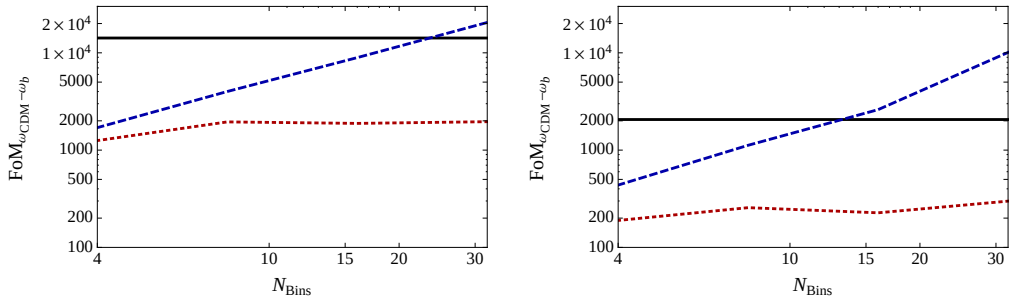

Figure 6.8: FoM for $\omega_{\rm CDM}$ - ω_b (marginalized over other cosmological parameters) for different nonlinearity scales (34 Mpc/h, left panel, and 68 Mpc/h, right panel) for a spectroscopic DES-like survey. For the 2D FoM we consider $\ell_{\rm max}$ as defined in Eq. (6.14) (dashed blue), and also the case in which cross-correlations of z-bins are neglected (dotted red). The solid black line shows the value of the 3D FoM for $N_{\rm bin} = 1$.

Denoting its power spectrum by $C_\ell^\Psi(z, z')$, we can relate it to the lensing contribution $C_\ell^{\rm lens}(z, z')$ [19] to the angular matter power spectrum $C_\ell(z, z')$ by

$$C_\ell^{\rm lens}(z, z') = \ell^2(\ell + 1)^2 C_\ell^\Psi(z, z') \,. \tag{6.17}$$

We shall see, that this lensing power spectrum can be measured from redshift integrated angular power spectra of galaxy surveys.

To study this possibility, we first introduce the signal-to-noise for the different terms which contribute to the galaxy power spectrum as defined in Ref. [19]. For completeness we list these terms in Appendix 6.6.1. The signal-to-noise for a given term is given by

$$\left(\frac{S}{N}\right)_\ell = \frac{\left|C_\ell - \tilde{C}_\ell\right|}{\sigma_\ell} \,. \tag{6.18}$$

where $\tilde{C}_\ell$ is calculated neglecting the term under consideration (e.g., lensing), and the r.m.s. variance is given by

$$\sigma_\ell = \sqrt{\frac{2}{(2\ell + 1) f_{\rm sky}}} \left(C_\ell + \frac{1}{n}\right) \,. \tag{6.19}$$

It is also useful to introduce a cumulative signal-to-noise that decides whether a term is observable within a given multipole band. We define the cumulative signal-to-noise by

$$\left(\frac{S}{N}\right)^2 = \sum_{\ell=2}^{\ell_{\rm max}} \left(\frac{C_\ell - \tilde{C}_\ell}{\sigma_\ell}\right)^2 \,. \tag{6.20}$$

Note that $C_\ell - \tilde{C}_\ell$ contains not only the auto-correlation of a given term, but also its cross-correlations with other terms so that it can be negative. Especially, for small

ℓ's the lensing term is dominated by its anti-correlation with the density term and is therefore negative.

Eq. (6.18) estimates the contribution of each term to the total signal. If its signal-to-noise is larger than 1, in principle it is possible measure this term and therefore to constrain cosmological variables determined by it. To evaluate the signal-to-noise of the total C_ℓ's, which is the truly observed quantity, we set $\tilde{C}_\ell = 0$.

In Figure 6.9 we show the signal-to-noise for different width of the redshift window function. We consider a tophat window for the narrowest case, $\Delta z = 0.01$ and Gaussian window functions with standard deviations $\Delta z \gtrsim 0.05(1+z)$, which corresponds to Euclid photometric errors [105] for the panels on the second line. The sky fraction, $f_{\rm sky}$, and the galaxy distribution dN/dz are compatible with Euclid specifications (see black lines in Fig. (6.2)). In particular, shot noise turns out to be negligible in this analysis. The shadowed regions in Figure 6.9 show the nonlinearity scales, estimated as $\ell_{\rm max} = 2\pi r(\bar{z})/\lambda_{\rm min}$, where $\bar{z}$ is the mean redshift of the bin and $\lambda_{\rm min} = 68h^{-1}$ Mpc.

As expected [17], redshift-space distortions and purely relativistic terms are mainly important at large scales, while lensing has a weaker scale dependence. For small Δz, apart from the usual density term, redshift-space distortions are the main contribution. Their signal-to-noise is larger than one, which allows to constrain the growth factor. As Δz increases, redshift-space distortions are washed out, and their signal decreases significantly. On the other hand, lensing and potential terms increase. This is due to the fact that these terms depend on integrals over z that coherently grow as the width of the z-window function increases. While potential terms always remain sub-dominant, the lensing signal-to-noise becomes larger than 1 for the value of $\Delta z = 0.5$ already at $\ell \approx 60$.

As a reference, we also show the signal-to-noise for an infinitesimal bin width (Dirac z-window function). This corresponds to the largest possible C_ℓ amplitude. As in the case $\Delta z = 0.01$, redshift-space distortion is of the same order as the density term. Note, however, that in reality for very narrow bins, shot noise becomes important and decreases $(S/N)_\ell$, especially for large multipoles.

The case of a uniform galaxy distribution between $0.5 < z < 2.5$ is also shown. We assume $f_{\rm sky} = 1$ and neglect shot noise. In this configuration the lensing term has a very large signal-to-noise. This can be used to constrain the lensing potential by comparing the observable (total) C_ℓ's to the theoretical models. In practice one may adapt this study to catalogs of radio galaxies, which usually cover wide z ranges but with poor redshift determination which is not needed for this case, for previous studies see, e.g., [158, 159, 160].

In Figure 6.10 the cumulative signal-to-noise, Eq. (6.20), is shown as function of the maximum multipole considered in the sum. Contrary to all the other terms, the cumulative signal-to-noise of the potential terms never exceeds 1. We therefore conclude that the considered experiment is not able to measure the potential terms. It is not clear, whether another feasible configuration would be sensitive to them. Notice also how the lensing term really 'kicks in' after the zero-crossing, when it is not longer dominated by its anti-correlation with the density term but by the

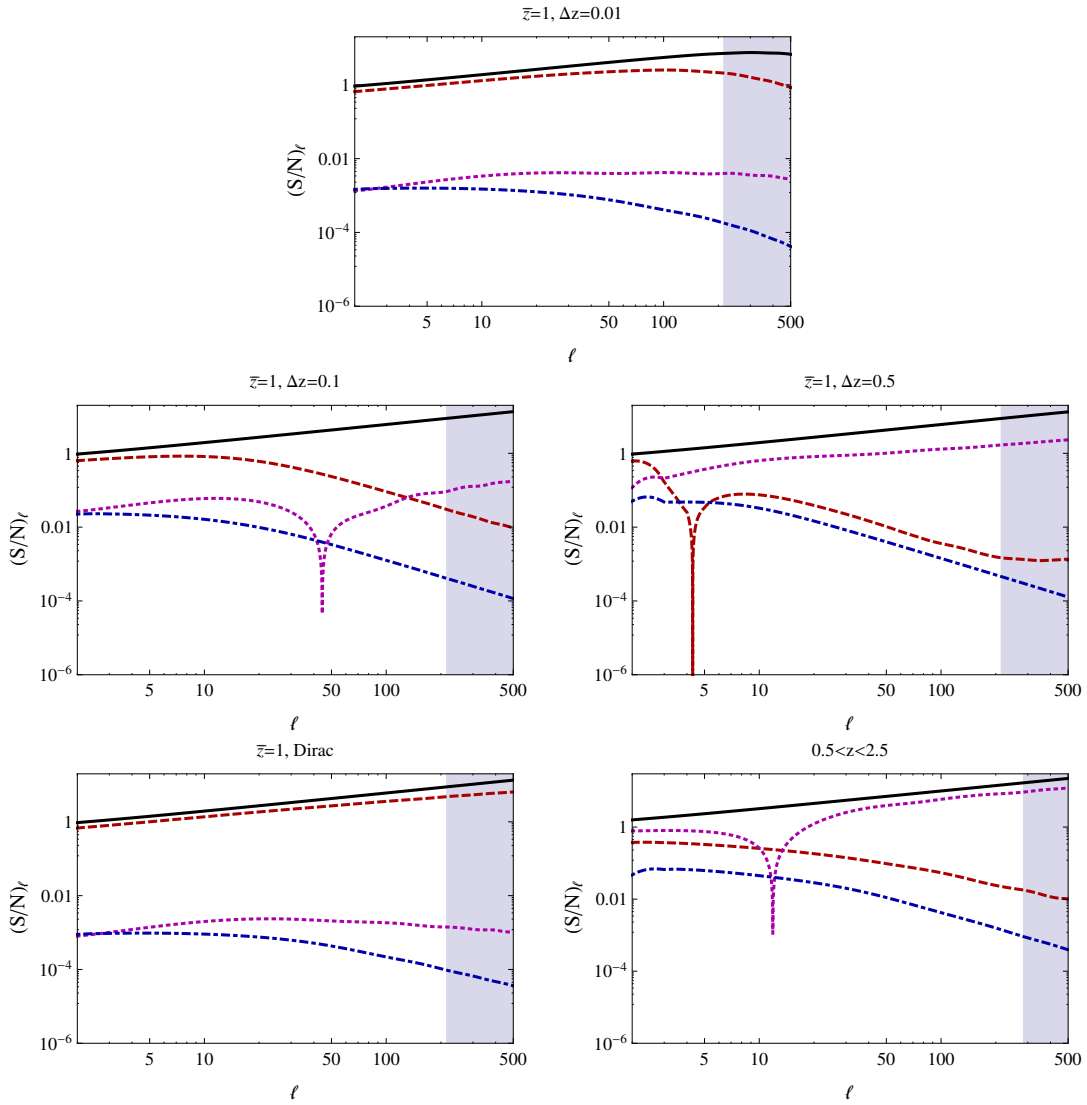

Figure 6.9: Signal-to-noise for different terms: total (solid, black), redshift-space distortions (dashed, red), lensing (dotted, magenta), potential terms (dot-dashed, blue). The plot in the top line is computed with a tophat window function with half-width $\Delta z = 0.01$. The cases in the second line correspond to Gaussian window functions of half-width $\Delta z = 0.1, 0.5$ around $\bar{z} = 1$. These three plots are compatible with Euclid specifications. In the third line, we show two extreme situations. The Dirac z-window function corresponds to an infinitesimal z-bin (left) and a very wide redshift range, $0.5 < z < 2.5$. This last case shows a large lensing signal. Notice the zero-crossing of the lensing term which is indicated by a downward spike in this log-plot. The shadowed regions correspond to nonlinearity scale estimated at the mean redshift of the bin.

contribution from the autocorrelation.

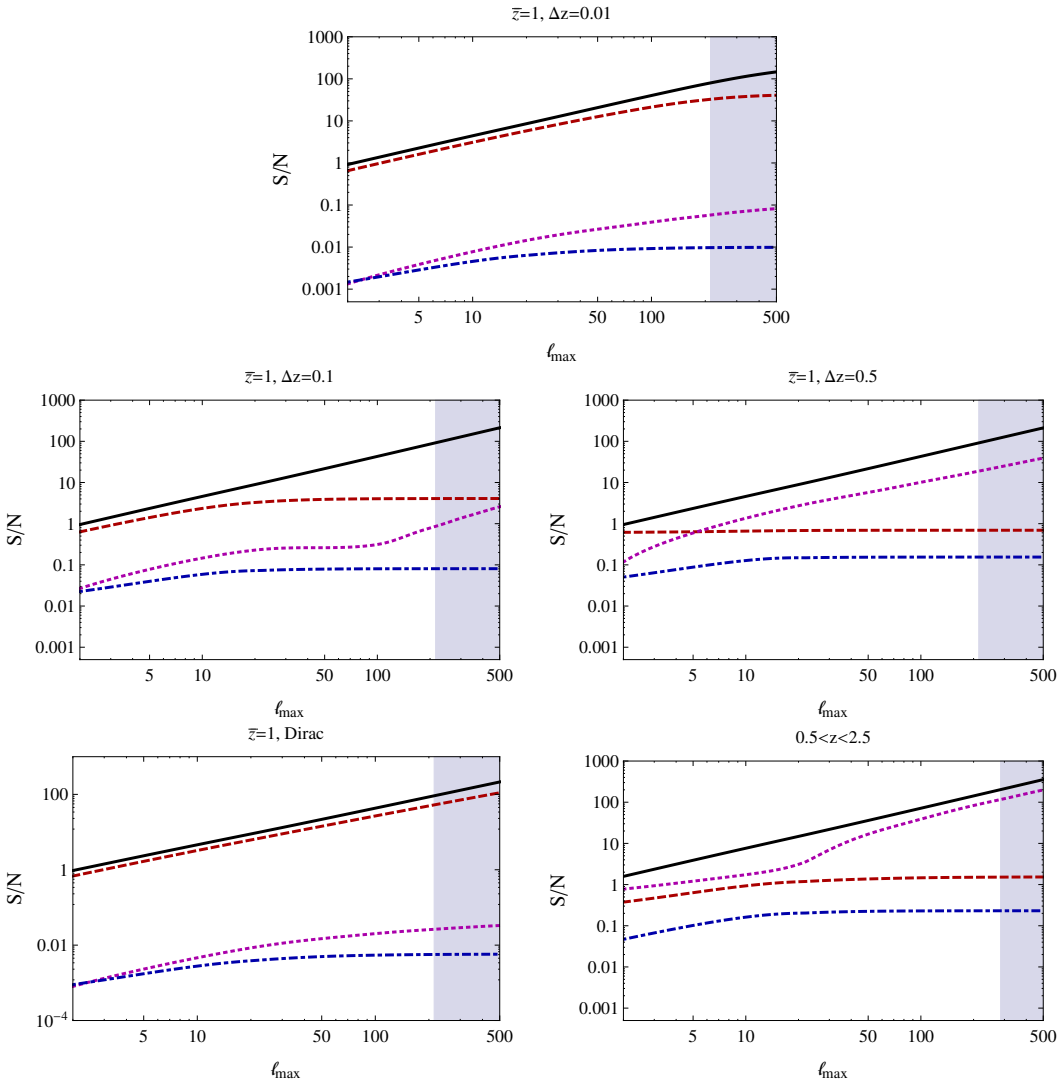

Figure 6.10: Cumulative signal-to-noise for different terms: total (solid, black), redshift-space distortions (dashed, red), lensing (dotted, magenta), potential terms (dot-dashed, blue). The different plots correspond to the same configurations as in Figure 6.9.

6.4.4 The correlation function and the monopole

So far we have not considered the observed monopole, C_0^{ij}, and dipole, C_1^{ij}, since the former is affected by the value of the gravitational potential and the density fluctuation at the observer position, while the latter depends on the observer velocity. These quantities are not of interest for cosmology and cannot be determined within linear perturbation theory.

However, there is an additional point which has to be taken into account when considering the correlation function. Usually, the correlation function is determined from an observed sample of galaxies by subtracting from the number of pairs with

given redshifts and angular separation the corresponding number for a synthetic, uncorrelated sample with the same observational characteristics (survey geometry, redshift distribution, etc.). This is the basis of the widely used Landy–Szalay estimator for the determination of the correlation function from an observed catalogue of galaxies [161]. For this estimator, by construction, the integral over angles vanishes, so that

$$C_0^{(\mathrm{LS})}(z_i, z_j) = 2\pi \int \xi_{\mathrm{LS}}(\theta, z_i, z_j) \sin\theta d\theta = 0\,. \tag{6.21}$$

Here $\xi_{\mathrm{LS}}(\theta, z_i, z_j)$ is already convolved with the redshift window function of the survey. If we want to compute the Landy–Szalay estimator for the correlation function we therefore have to subtract the monopole,

$$\xi_{\mathrm{LS}}(\theta, z_i, z_j) = \xi(\theta, z_i, z_j) - \frac{1}{4\pi} C_0^{ij}\,,$$

or

$$\xi_{\mathrm{LS}}(\theta, z_i, z_j) = \frac{1}{4\pi} \sum_{\ell=1}^{\ell_{\max}} (2\ell+1) C_\ell^{ij} P_\ell(\cos\theta)\,. \tag{6.22}$$

This is quite relevant as becomes clear when considering the radial and the transversal correlation function calculated in Ref. [106]. There this monopole is not subtracted and it is found that the transversal correlation function is nearly entirely positive while the radial correlation function is nearly entirely negative. Even though the integral of the theoretical correlation function over all of space, which is given by $P(0)$, vanishes for a Harrison-Zel'dovich spectrum, this is not the case, e.g., for the angular correlation function within a given a redshift slice or for the radial correlation function. It is therefore relevant whether the Landy–Szalay estimator for the correlation function is applied in each redshift slice or to the correlation function of the full survey.

Furthermore, even if C_0^{ij} depends on quantities at the observer position (note that in Eq. (6.24) the not observable monopole and dipole terms which come from quantities at the observer position are already neglected), we can use the fact that these are equal for all redshifts z_i, z_j and therefore differences like $C^{ij} - C^{ii}$ are independent of the observer position. We consider especially

$$\mathcal{M}(\bar{z}, \delta z) \equiv \frac{1}{2}\left[C_0(z_-, z_-) + C_0(z_+, z_+)\right] - C_0(z_-, z_+) \tag{6.23}$$

where $z_\pm = \bar{z} \pm \delta z/2$ (see [106]). This quantity which is the angular average of the radial correlation function for galaxies at redshifts z_+ and z_-, contains interesting clustering information.

In Fig. 6.11 we show the monopole as function of the radial redshift separation for a mean redshift $\bar{z} = 0.55$. Since here we are only interested in the theoretical modeling, we neglect redshift window functions and noise. The observable monopole for $\delta z = 0$ vanishes by definition, and it tends to a constant for large δz.

The difference between the density contribution only (black line) and full result (red dashed) is simply given by the redshift-space distortions, all other terms are

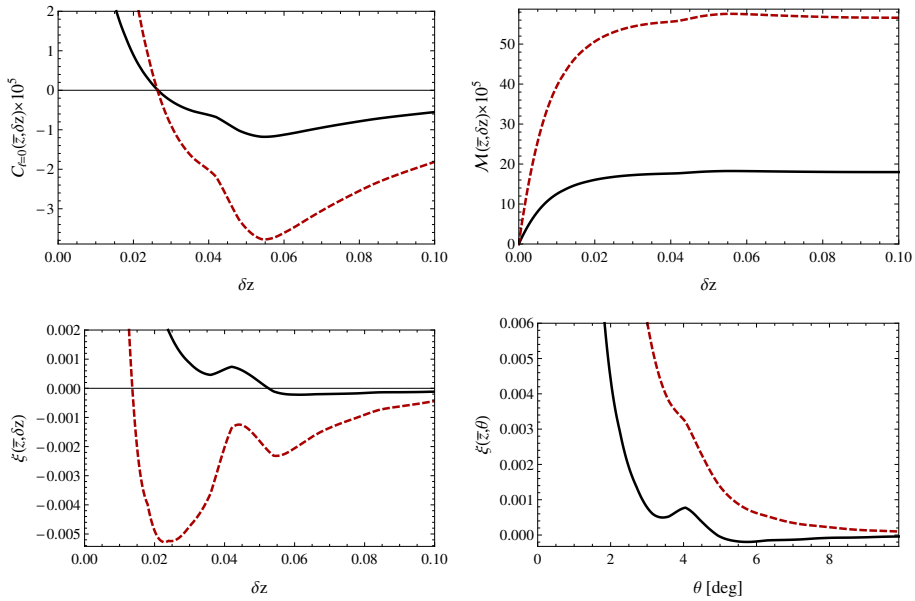

Figure 6.11: Top panel: the monopole $C_{\ell=0}(\bar{z},\delta z)$ and the observable monopole contribution $\mathcal{M}(\bar{z},\delta z)$ at mean redshift $\bar{z}=0.55$. Bottom panel: the radial (left) and the angular (right) correlation function at $\bar{z}=0.55$. Solid (black) lines include only density correlations, dashed (red) lines also include redshift-space distortions. The correlation functions are computed using Eq. (6.6); to wash out unphysical small scales oscillations, we use $\ell_s=80$ for $\xi(\bar{z},\delta z)$ and $\ell_s=400$ for $\xi(\bar{z},\theta)$, as defined in Eq. (5.20).

very small for this case. The Baryon Acoustic Oscillations (BAO) feature is clearly visible at $\delta z\approx 0.045$ in $C_0(\bar{z},\delta z)$. To confirm that this is indeed the BAO peak, the radial 2-point correlation function $\xi(\bar{z},\delta z)\equiv\xi(\theta=0,z_-,z_+)$ given by Eq. (6.6) but calculated from $\ell=0$ on (see [19] for more details) is also shown, presenting the same bump. A detailed study of the BAO peak in the angular power spectrum is left for future work. For completeness, also the transverse angular correlation function $\xi(\bar{z},\theta)\equiv\xi(\theta,\bar{z},\bar{z})$ is plotted, which shows the BAO peak at $\theta\approx 4^\circ$. Contrary to the radial case in which the BAO scales have negative correlation, the transverse function is always positive on these scales.

Since we neglect shot noise and assume total sky coverage, cosmic variance from Eq. (6.19), $\sigma_{\ell=0}=\sqrt{2}C_{\ell=0}(\bar{z},\delta z)$ leads to a signal-to-noise

$$\left(\frac{S}{N}\right)_{\ell=0}=\frac{C_{\ell=0}(\bar{z},\delta z)}{\sigma_{\ell=0}}=\frac{1}{\sqrt{2}}<1,$$

for one given redshift difference δz. This is also approximately the (S/N) for $\mathcal{M}$ for large enough δz. Hence, if we add $\mathcal{M}(\bar{z},\delta z)$ for several only weakly correlated redshifts we easily obtain a measurable signal with $S/N>1$.

6.5 Conclusions

We have shown how the new code CLASSgal [19] can be used to analyze galaxy surveys in an optimal way. With a few examples we have shown that the figure of merit from an analysis of the $C_\ell(z, z')$ spectra can be significantly larger, up to a factor of a few, than the one from a standard $P(k)$ analysis. This is due to the fact that this analysis makes optimal use of the redshift information and does not average over directions. Clearly, in the analysis of upcoming high quality surveys we will want to use this promising method.

We have also seen that the nonlinearity scale, the scale beyond which we can no longer trust the theoretically calculated spectrum, is of uttermost importance for the precision with which we estimate cosmological parameters. Within our conservative approach, and LSS data alone, cosmological parameters cannot be obtained with good precision, see Fig. 6.4. However, we hope that in the final data analysis we shall have accurate matter power spectra down to significantly smaller scales from N-body or approximation techniques. Furthermore, for an optimal determination of cosmological parameters, we shall of course combine LSS observations with CMB experiments, e.g. from Planck, and other cosmological data. As we have seen, the FoM of spectroscopic surveys increases significantly with the number of bins. However, the computational effort scales like $N_{\rm bin}^2$ and thus becomes correspondingly large. Nevertheless, the pre-factor in front of the scaling can be substantially smaller than one when we include only cross-correlations from bins within a given spatial distance.

We have also shown that deep angular galaxy catalogs can actually be used to measure the lensing potential. This is a novel method, alternative to the traditional lensing surveys, which can be used, e.g., to constrain modified gravity theories.

Since the power spectra of galaxy surveys depend on redshift, contrary to the CMB, here also the monopole contains cosmological information which can in principle be measured.

Acknowledgments

We thank Camille Bonvin, Enrique Gaztañaga, Anaïs Rassat and Alexandre Refregier for helpful discussions. This work is supported by the Swiss National Science Foundation. RD acknowledges partial support from the (US) National Science Foundation under Grant No. NSF PHY11-25915.

6.6 Appendix

6.6.1 The galaxy number power spectrum

The galaxy number counts in direction $\mathbf{n}$ at observed redshift z are given by [17, 19]

$$\begin{aligned}\Delta(\mathbf{n},z) &= D+\left[\frac{1}{\mathcal{H}}\partial_r(\mathbf{V}\cdot\mathbf{n})+\left(\frac{\mathcal{H}'}{\mathcal{H}^2}+\frac{2}{r(z)\mathcal{H}}\right)\mathbf{V}\cdot\mathbf{n}-3\mathcal{H}V\right]\\ &+\frac{1}{r(z)}\int_0^{r(z)}dr\left\{\left[2-\frac{r(z)-r}{r}\Delta_\Omega\right](\Phi+\Psi)\right\}+\left(\frac{\mathcal{H}'}{\mathcal{H}^2}+\frac{2}{r(z)\mathcal{H}}+1\right)\Psi\\ &+\frac{1}{\mathcal{H}}\Phi'-2\Phi+\left(\frac{\mathcal{H}'}{\mathcal{H}^2}+\frac{2}{r(z)\mathcal{H}}\right)\left(\Psi+\int_0^{r(z)}dr(\Phi'+\Psi')\right), \qquad (6.24)\end{aligned}$$

where V is the potential velocity defined throughout $\mathbf{V}=-\nabla V$. Here primes denote derivatives w.r.t. conformal time and the notation agrees with [19]. The first term is the density term, the term in square brackets is the redshift space distortion and the first term on the second line is the lensing term. The remaining gravitational potential contributions are sometimes also called "relativistic terms".

The C_ℓ's from this expression contain not only the auto-correlations of each term but also their cross-correlation with other contributions. We call the auto-correlation of the density term $C_\ell^\delta(z,z')$, the density term; the cross-correlation of density and velocity and the auto-correlation of the velocity term $C_\ell^z(z,z')$, the redshift space distortion term, the cross-correlation of the lensing contribution with density and velocity and its auto-correlation $C_\ell^{\rm lens}(z,z')$, the lensing term. We call the rest the "potential terms", $C_\ell^{\rm pot}(z,z')$. If the cross-correlation terms dominate, any of these spectra except C_ℓ^δ can in principle be negative even for $z=z'$. These are the definitions of the parts of the full angular power spectra which are used in Section 6.4.3. More details on how these spectra are calculated can be found in the accompanying paper [19].

6.6.2 Basics of Fisher matrix forecasts

The Fisher matrix is defined as the derivative of the logarithm of the likelihood with respect to pairs of model parameters. Assuming that the spectra C_ℓ^{ij} are Gaussian (which is not a good assumption for small ℓ but becomes reasonable for $\ell\gtrsim 20$), the Fisher matrix is given by (cf. [53, 162])

$$F_{\alpha\beta}=\sum\frac{\partial C_\ell^{ij}}{\partial\lambda_\alpha}\frac{\partial C_\ell^{pq}}{\partial\lambda_\beta}{\rm Cov}^{-1}_{\ell,(ij),(pq)}, \qquad (6.25)$$

where λ_α denotes the different cosmological parameters we want to constrain. The sum over ℓ runs from 2 to a value $\ell_{\rm max}$ related to the non-linearity scale $k_{\rm max}$: we discuss this issue in section 6.3.2. Note also that we sum over the matrix indices (ij) with $i\le j$ and (pq) with $p\le q$ which run from 1 to $N_{\rm bin}$.

In the Fisher matrix approximation, i.e. assuming that the likelihood is a multivariate Gaussian with respect to cosmological parameters (which usually is not the case), the region in the full parameter space corresponding to a given Confidence Level (CL) is an ellipsoid centered on the best-fit model with parameters $\bar\lambda_\alpha$, with

boundaries given by the equation $\sum_{\alpha,\beta}(\lambda_\alpha - \bar{\lambda}_\alpha)(\lambda_\beta - \bar{\lambda}_\beta)F_{\alpha\beta} = [\Delta\chi^2]$[5], and with a volume given (up to a numerical factor) by $[\det(F^{-1})]^{1/2}$ (see e.g. [53]). Since the smallness of this volume is a measure of the performance of a given experiment, one often uses the inverse of the square root of the determinant as a Figure of merit,

$$\mathrm{FoM} = \left[\det\left(F^{-1}\right)\right]^{-1/2} .$$

If we assume several parameters to be fixed by external measurements at the best-fit value $\bar{\lambda}_\alpha$, the 1σ ellipsoid for the remaining parameters is given by the same equation, but with the sum running only over the remaining parameters. Hence the volume of this ellipsoid is given by the square root of the determinant of the sub-matrix of F restricted to the remaining parameters, that we call $\hat{F}$. In that case, the FoM for measuring the remaining parameters reads

$$\mathrm{FoM}_{\mathrm{fixed}} = \left[\det\left((\hat{F})^{-1}\right)\right]^{-1/2} .$$

However, it is often relevant to evaluate how well one (or a few) parameters can be measured when the other parameters are marginalized over. In this case, a few lines of calculation show that the figure of merit is given by taking the sub-matrix of the inverse, instead of the inverse of the sub-matrix (see [53]),

$$\mathrm{FoM}_{\mathrm{marg.}} = \left[\det\left(\widehat{F^{-1}}\right)\right]^{-1/2} .$$

In particular, if we are interested in a single parameter λ_α and assume that all other parameters are marginalized over, the FoM for measuring λ_α is given by

$$\mathrm{FoM}_{\mathrm{marg.}} = \left[(F^{-1})_{\alpha\alpha}\right]^{-1/2} .$$

When the likelihood is not a multivariate Gaussian with respect to cosmological parameters, the 68% CL region is no longer an ellipsoid, but the FoM given above (with the Fisher matrix being evaluated at the best-fit point) usually remains a good indicator.

It is however possible to construct examples where the FoM estimate completely fails. For instance, if two parameters are degenerate in a such a way that their profile likelihood is strongly non-elliptical (e.g. with a thin and elongated banana shape). Then Fisher-based FoM will rely on a wrong estimate of the surface of the banana, and will return a very poor approximation of the true FoM. This happens e.g. when including isocurvature modes [164], for mixed dark matter models [165] or in some modified gravity models [166].

For the power spectrum analysis, following [140, 167], we define the Fisher matrix in each redshift bin as

$$F_{\alpha\beta} = \int_{-1}^{1}\int_{k_{\mathrm{min}}}^{k_{\mathrm{max}}} \frac{\partial \ln P_{\mathrm{obs}}}{\partial\lambda_\alpha}\frac{\partial \ln P_{\mathrm{obs}}}{\partial\lambda_\beta} V_{\mathrm{eff}} \frac{k^2 dk d\mu}{2(2\pi)^2}, \tag{6.26}$$

[5]The number $\Delta\chi^2$ depends both on the requested confidence level and on the number n of parameters: for $n = 1$ (resp. 2) and a 68%CL one should use $\Delta\chi^2 = 1$ (resp. 2.3). For other values see section 15.6 of [163].

where the effective volume $V_{\rm eff}$ is related to the actual volume $V_{\rm bin}$ of each redshift bin through

$$V_{\rm eff}(k,\mu,\bar{z}) = \left[\frac{P_{\rm obs}(k,\mu,\bar{z})}{P_{\rm obs}(k,\mu,\bar{z}) + 1/\bar{n}(\bar{z})}\right]^2 V_{\rm bin}(\bar{z})\,. \tag{6.27}$$

Here $\bar{z}$ is the mean redshift of the bin, and $\bar{n}(\bar{z})$ the average galaxy density in this bin, assumed to be uniform over the sky. In the case of several non-overlapping z-bins, we assume that measurements inside each of them are independent so that the total Fisher matrix is the sum of those computed for every bin. This expression is in principle valid in the flat-sky approximation. However, since it encodes all the statistical information, we can use it for a forecast analysis. The denominator in Eq. (6.27) features the two contributions to the variance of the observable power spectrum $P_{\rm obs}(k,\mu,\bar{z})$ coming from sampling variance and from shot noise. The observable power spectrum $P_{\rm obs}(k,\mu,\bar{z})$ (not including shot noise) is given in the minimal ΛCDM (Λ Cold Dark Matter) model by the theoretical power spectrum $P(k)$ calculated at $z = 0$, rescaled according to

$$P_{\rm obs}(k,\mu,\bar{z}) = \frac{\bar{D}_A(\bar{z})^2 H(\bar{z})}{D_A(\bar{z})^2 \bar{H}(\bar{z})} \left(1 + \mu^2 \Omega_M(\bar{z})^\gamma\right)^2 G(\bar{z})^2 P(k)\,. \tag{6.28}$$

The first ratio in Eq. (6.28) takes in account the volume difference for different cosmologies. The survey volume for galaxies in a redshift bin centered on $\bar{z}$ and of width δz is proportional to $D_A(\bar{z})^2 H(\bar{z})^{-1}\delta z$. The quantities $\bar{D}_A$ and $\bar{H}$ are evaluated at the fiducial cosmology. The parenthesis contains the Kaiser approximation to redshift-space distortions [61], which together with the density term is the dominant contribution in Eq. (6.24) for our analysis. We assume an exponent $\gamma = 0.6$ that is a good approximation to the growth factor from linear perturbation theory in ΛCDM. We have neglected the bias ($b = 1$) in order to compare the results with the FoM derived from the angular power spectrum $C_\ell(z_1, z_2)$ where we also set $b = 1$. When we consider photometric redshift surveys, we need take into account the loss of information in the longitudinal direction due to the redshift error σ_z. Following [167], we then multiply $P_{\rm obs}(k,\mu,\bar{z})$ with an exponential cutoff $e^{-(k\mu\sigma_z/H(z))^2}$.

In Eq. (6.26), the observable power spectrum and the effective volume are assumed to be expressed in Hubble-rescaled units, e.g. $[{\rm Mpc}/h]^3$, while wave numbers are expressed in units of $[h/{\rm Mpc}]$. In other words, it would be more rigorous to write everywhere ($[a_0^3 H_0^3 P_{\rm obs}]$, $[k/(a_0 H_0)]$, $[a_0^3 H_0^3 V_{\rm eff}]$) instead of ($P_{\rm obs}$, k, $V_{\rm eff}$): the quantities in brackets are the dimensionless numbers that are actually measured, see [168]. Using Hubble-rescaled units does make a difference in the calculation of the partial derivative with respect to the model parameter H_0: it is important to keep k/h and not k constant. Also, the wavenumber $k_{\rm max}$ corresponding to the non-linearity scale is given in units $h/{\rm Mpc}$, so that we fix $k_{\rm max}/h$.

Furthermore, since the computation of $P(k)$ involves the assumption of a cosmological model to convert observable angles and redshifts into distances, expressing the latter in ${\rm Mpc}/h$ mitigates the uncertainty introduced in this procedure since, to first approximation, distances $r(z) = \int dz/H(z)$ scale as h^{-1}.

7

A longitudinal gauge degree of freedom and the Pais Uhlenbeck field

JOURNAL OF HIGH ENERGY PHYSICS **04** 030 (2013)

A longitudinal gauge degree of freedom and the Pais Uhlenbeck field

Jose Beltrán Jiménez, Enea Di Dio, Ruth Durrer

We show that a longitudinal gauge degree of freedom for a vector field is equivalent to a Pais-Uhlenbeck scalar field. With the help of this equivalence, we can determine natural interactions of this field with scalars and fermions. Since the theory has a global $U(1)$ symmetry, we have the usual conserved current of the charged fields, thanks to which the dynamics of the scalar field is not modified by the interactions. We use this fact to consistently quantize the theory even in the presence of interactions. We argue that such a degree of freedom can only be excited by gravitational effects like the inflationary era of the early universe and may play the role of dark energy in the form of an effective cosmological constant whose value is linked to the inflation scale.

7.1 Introduction

The standard model of cosmology provides a very successful description of our Universe [98, 122]. However, it is based on the idea that about 96% of the energy density in the Universe stems from particles and fields which are not part of the standard model of particle physics and have never been observed in colliders. Dark matter, which amounts to about 26% of the Universe content, at least has the properties of typical non-relativistic particles, but dark energy, the component which makes up about 70% of the energy density of the Universe must be endowed with very exotic properties, like a strong negative pressure, in order to explain the observed current acceleration of the expansion of the Universe. This most unexpected discovery has been awarded the 2011 Nobel prize in physics [2, 4, 3, 169].

Even if a cosmological constant has the right properties and is in agreement with cosmological observations, this solution is unsatisfactory from a purely theoretical point of view, as its associated scale $(\rho_\Lambda)^{1/4} \simeq 10^{-3}$eV is so much smaller than the natural scale of gravity given by $M_p \simeq 10^{18}$ GeV. On the other hand, one could expect this scale to be related to some cutoff scale coming from particle physics, which should be, at least, the scale of supersymmetry $E_{\rm susy} > 1$TeV, again much larger than the value of the cosmological constant inferred from observations (see [170] for an extensive discussion about the cosmological constant problem).

This fine tuning issue of the cosmological constant has led the community to search for different solutions to the problem of accelerated expansion. Different dark energy models like e.g. quintessence or large scale modifications of gravity have been explored [107, 171, 172].

Researchers have also looked into theories with higher derivatives in the Lagrangian density, like e.g. the so-called $f(R)$ theories [68, 69] or the galileon field [70,

71, 72, 73]. Theories with higher derivatives look dangerous at first sight because they typically lead to the presence of ghosts (particles with negative kinetic energy) reflecting the Ostrogradski instability [74, 75]. This instability appears because these theories lead to higher than second order equations of motion, so that new degrees of freedom appear and they are usually ghost-like. It has been shown recently [173], that trying to eliminate the ghost by introducing additional constraints does not work in general, unless the corresponding phase space gets dimensionally-reduced. Even though without the presence of any interactions, the energy of a given field remains constant and the instability cannot develop, we expect that the coupling of such a field to other degrees of freedom or quantum effects will potentially provoke uncurable instabilities.

However, exceptions to this generic rule exist in degenerate theories like the aforementioned $f(R)$ theories of gravity and, more recently, the galileon fields where, thanks to the specific structure of the interactions, the equations remain of second order even though higher derivative terms are present in the action.

Interestingly, the dark energy problem, forces us to re-think our boundaries of what we can accept as sensible (effective) physical theories [174]. This is the youngest example of the cross fertilization of cosmological observations and fundamental theoretical physics.

The present paper inscribes in this framework. Here we show that the action for a vector field having only a residual gauge symmetry, which has already been proposed as a candidate for dark energy [175, 176, 177, 178], can be rewritten as an ordinary $U(1)$ gauge vector field theory together with a (degenerate) Pais-Uhlenbeck (PU) scalar field, the field version of the PU oscillator first discussed in [16]. Even though this is a higher derivative oscillator, it has been shown in [179, 180] that this model can be quantized with a positive spectrum for the Hamiltonian because it corresponds to a special class of Hamiltonians that, although being non-hermitian, exhibit a $\mathcal{PT}$ symmetry that allows to construct a quantum theory without negative energy states or a unitary evolution. However, such a construction relies on the presence of non-hermitian operators so that the classical limit of the theory remains unclear. In fact, the classical Hamiltonian is still unbounded and a prescription to go from the quantum theory to the classical solutions is lacking. Moreover, although it is an interesting construction to have a bounded spectrum for the quantum theory, the problem with higher derivative terms actually becomes manifest when interactions are introduced [181]. As a matter of fact, the free theory is not sick and provides a unitary evolution, even though the Ostrogradski ghostly degree of freedom is present. For special types of interactions, unitarity might be maintained [181, 182, 183].

Here we derive an alternative way to consistently quantize the degenerate PU field that makes use of the presence of another symmetry in which the field can be shifted by an arbitrary harmonic function. We use this symmetry to restrict the physical Hilbert space or to fix the gauge and quantize only the healthy physical mode. Then, we include interactions with charged scalars or fermions, in a way which is motivated by the interpretation of this field, and we show that our restriction of

the physical states remains intact.

The remainder of this paper is organized as follows: In the next section we show the relation of the vector field action with the residual gauge symmetry and the PU field. In Section 7.3 we include interactions. In Section 7.4 we discuss the quantization of the theory and show how it could play the role of dark energy or of the inflaton. (Even if in its present form the model does not propose a mechanism to end inflaton.) In Section 7.5 we conclude and discuss further investigations which can be performed to compare this model with standard ΛCDM.

7.2 The Stückelberg trick and the Pais Uhlenbeck field

7.2.1 From the Pais Uhlenbeck oscillator to the Pais Uhlenbeck field

We shall start by briefly introducing the PU oscillator [16] and showing how it can arise as the Fourier modes of a certain higher order field theory. The PU oscillator is described by the following action:

$$S_{PU} = \frac{\gamma}{2}\int \mathrm{d}t \left[\ddot{z}^2 - (\omega_1^2+\omega_2^2)\dot{z}^2 + \omega_1^2\omega_2^2 z^2\right], \tag{7.1}$$

where γ is an arbitrary parameter. Since the action depends on the second time derivative, this model is expected to exhibit the Ostrogradski instability. The corresponding Hamiltonian can be derived either by using the Dirac method [184, 185] or directly from the Ostrogradski Hamiltonian [74] as defined for higher order derivative theories. In either case, one obtains the expression

$$H_{PU}\left(z,x,p_z,p_x\right) = \frac{p_x^2}{2\gamma} + p_z x + \frac{\gamma}{2}(\omega_1^2+\omega_2^2)x^2 - \frac{\gamma}{2}\omega_1^2\omega_2^2 z^2, \tag{7.2}$$

where p_z and p_x are the canonical conjugate momenta of the canonical variables z and $x \equiv \dot{z}$ respectively. The term linear in the conjugate momentum, $p_z x$, represents the previously advertised Ostrogradski instability. At the classical level the instability may appear only by coupling the PU oscillator to other systems. The action (7.1) leads to the fourth order equation of motion

$$\frac{\mathrm{d}^4 z}{\mathrm{d}t^4} + (\omega_1^2+\omega_2^2)\frac{\mathrm{d}^2 z}{\mathrm{d}t^2} + \omega_1^2\omega_2^2 z = 0, \tag{7.3}$$

which is solved by the superposition of two modes with frequencies ω_1 and ω_2 in the non-degenerate case ($\omega_1 \neq \omega_2$):

$$z(t) = a_1 e^{-i\omega_1 t} + a_1^* e^{i\omega_1 t} + a_2 e^{-i\omega_2 t} + a_2^* e^{i\omega_2 t}. \tag{7.4}$$

From this solution we see that no instabilities in the form of exponentially growing modes appear in the classical solutions even though the Hamiltonian has the aforementioned linear term associated with the Ostrogradski instability. This should not

be surprising, since, at the classical level, only the introduction of interactions can develop the Ostrogradski instability by shifting the poles of the corresponding propagator off the real axis. Note the difference of these oscillating solutions to tachyons (i.e., modes with negative ω^2) where the above solutions would grow exponentially.

On the other hand, in the degenerate case ($\omega_1 = \omega_2$) we find

$$z\left(t\right) = \left(c_1 + c_2 t\right) e^{-i\omega t} + \left(c_1^* + c_2^* t\right) e^{i\omega t}, \tag{7.5}$$

where the term linear in t comes from the fact that the roots of the characteristic equation for the equation of motion (7.3) are degenerate (or, in other words, the propagator has a double pole). Even though this term is growing in time, its growth is milder than an exponentially growing mode. In particular there is no imaginary propagation speed that would signify a classical instability in the form of a tachyonic mode. This linear growth is independent of the presence of the Ostrograski instability, that is still present in the theory and can develop when interactions are introduced.

In summary, we have seen that the PU oscillator does not have tachyonic instabilities, although the Ostrogradski instability is still present and could turn the model out of control when interactions are introduced.

In the literature the PU oscillator has been already widely studied (cf. [16, 179, 180, 181, 186, 187]). Here we are interested in the field version of the PU model. Let us consider the action

$$\begin{aligned} S &= \xi \int \mathrm{d}^4x \Big[\phi \left(\Box + m_1^2\right) \left(\Box + m_2^2\right) \phi\Big] \\ &= \xi \int \mathrm{d}^4x \Big[(\Box\phi)^2 - (m_1^2 + m_2^2)\partial_\mu\phi\partial^\mu\phi + m_1^2 m_2^2 \phi^2\Big] \end{aligned} \tag{7.6}$$

where $\Box = \partial_\mu\partial^\mu$ is the d'Alembertian operator and ξ a dimensionless parameter whose value can be fixed by the normalization of ϕ. Note that the PU scalar field ϕ defined here is dimensionless in four spacetime dimensions.

We now show that each spatial Fourier mode of the PU field describes a PU oscillator where the frequencies ω_1 and ω_2 are determined by the masses m_1 and m_2. From the action (7.6) we derive the equation of motion

$$\left(\Box + m_1^2\right) \left(\Box + m_2^2\right) \phi = 0. \tag{7.7}$$

Expanding the PU field in spatial Fourier modes

$$\phi = \int \frac{\mathrm{d}^3k}{\left(2\pi\right)^{3/2}} \phi_k(t) e^{i\vec{k}\cdot\vec{x}} \tag{7.8}$$

the equation of motion for each mode ϕ_k becomes

$$\frac{\mathrm{d}^4\phi_k}{\mathrm{d}t^4} + \Big(2k^2 + m_1^2 + m_2^2\Big)\frac{\mathrm{d}^2\phi_k}{\mathrm{d}t^2} + \Big[k^4 + k^2\left(m_1^2 + m_2^2\right) + m_1^2 m_2^2\Big]\phi_k = 0. \tag{7.9}$$

Comparing Eqs. (7.3) and (7.9) we identify

$$\omega_1^2+\omega_2^2=2k^2+m_1^2+m_2^2 \quad \text{and} \quad \omega_1^2\omega_2^2=k^4+k^2(m_1^2+m_2^2)+m_1^2m_2^2, \tag{7.10}$$

so that, as expected, the frequencies are given by:

$$\begin{aligned}\omega_1^2&=k^2+m_1^2\\ \omega_2^2&=k^2+m_2^2.\end{aligned} \tag{7.11}$$

The action (7.6) describes two massive modes with positive masses m_1 and m_2 (none of them represents a tachyonic degree of freedom). However, one of them is actually a ghost, with the sign of $m_1^2-m_2^2$ determining which one of the two modes is the ghost. In the case where one of these parameters vanishes, one of the modes becomes massless. This corresponds to the case without the quadratic potential in the action, i.e., only the derivative terms remain despite the fact that one of the modes is massive. Finally, when both masses vanish $m_1=m_2=0$, we have a pure fourth order theory and the solutions of the characteristic equation are degenerate, i.e., both modes satisfy the usual dispersion relation for a massless mode. This is the aforementioned degeneracy leading to the term linearly growing with time appearing in (7.5). Each Fourier mode of a massless PU field is described by a degenerate PU oscillator and analogously for the massive case.

7.2.2 The Stückelberg trick

In the following we shall show how the degenerate PU field can be identified with a Stückelberg field. This field was first introduced in the Proca action for a massive vector field to restore the $U(1)$ gauge invariance of the theory [188]. Thus, the vector field could acquire a non-vanishing mass and still preserve the gauge symmetry in a somewhat simplified version of the Higgs mechanism. Here, we shall start from an action for a massless vector field, but with a modified kinetic term,

$$S=\int \mathrm{d}^4x\left[-\frac{1}{4}F_{\mu\nu}F^{\mu\nu}+\frac{1}{2}\xi(\partial_\mu A^\mu)^2\right], \tag{7.12}$$

with $F_{\mu\nu}=\partial_\mu A_\nu-\partial_\nu A_\mu$ and ξ and arbitrary dimensionless parameter (that can be fixed by the normalization of the longitudinal component of the vector field). In this action, $-F^2/4$ is the usual Maxwell term, whereas the second term is usually introduced in the quantization of the theory as a gauge-fixing term and partially breaks the gauge symmetry. However, here we shall not consider it as a purely gauge-fixing term, but as a fully physical term. This action is no longer invariant under general $U(1)$ transformations of the vector field, but only under residual gauge transformations $A_\mu\to A_\mu+\partial_\mu\theta$ which satisfy $\Box\theta=0$. In addition to the usual transverse modes associated with $F_{\mu\nu}$, this action has a third degree of freedom which appears here as longitudinal vector mode[1] and that is associated with $\partial_\mu A^\mu$.

[1]Here we refer to a 4-longitudinal mode such that $A^\mu k_\mu\neq 0$, as opposed with the usual terminology used in theories with massive vector fields where the longitudinal mode refers to the mode parallel to the 3-momentum $\vec{k}$.

Since such a mode gives a scalar physical quantity, we can alternatively interpret it as a scalar mode.

In the past [175, 176, 177, 178], it has been shown that this additional mode gives a contribution to the cosmological energy-momentum tensor that is proportional to the metric tensor so that its equation of state is $p = -\rho$ and it has therefore been suggested that this could play the role of the dark energy as an effective cosmological constant. So far, no evidences for longitudinal photons have been found in colliders and electromagnetism is unbroken in the real Universe to very high precision. Furthermore, there is no experimental evidence for the existence of an additional $U(1)$ gauge field in nature.

In this work, we show that when restoring $U(1)$ gauge invariance using the Stückelberg trick, this longitudinal mode becomes a scalar degree of freedom. Interestingly, it does not correspond to a normal scalar field but to the previously introduced (degenerate) Pais-Uhlenbeck field [16], which has second time derivatives in the action and fourth order equations of motion. The Ostrogradski ghost of the PU field will be related to the ghostly degree of freedom introduced by the gauge-fixing-like term in (7.12). In subsequent sections we shall see how to deal with such a ghost and consistently quantize the theory.

Let us now restore $U(1)$ gauge invariance by introducing a Stückelberg field. In other words, we replace $A_\mu \to A_\mu + \partial_\mu \phi$ so that the action becomes

$$\begin{aligned} S &= \int \mathrm{d}^4x \left[-\frac{1}{4} F_{\mu\nu} F^{\mu\nu} + \frac{1}{2}\xi \left(\partial_\mu (A^\mu + \partial^\mu \phi)\right)^2 \right] \\ &= \int \mathrm{d}^4x \left[-\frac{1}{4} F_{\mu\nu} F^{\mu\nu} + \frac{1}{2}\xi \left((\partial_\mu A^\mu)^2 + (\Box\phi)^2 + 2\partial_\mu A^\mu \Box\phi \right) \right] . \end{aligned} \tag{7.13}$$

This action is fully gauge-invariant under gauge transformations which act on both, A_μ and ϕ

$$\begin{aligned} A_\mu &\to A_\mu + \partial_\mu \Lambda, \\ \phi &\to \phi - \Lambda. \end{aligned} \tag{7.14}$$

The action (7.12) can thus be interpreted as the action (7.13) in a gauge such that $\Box\phi = 0$. In such a gauge, the residual gauge symmetry of (7.12) remains because the condition $\Box\phi = 0$ does not fix the gauge completely, but still is invariant under gauge transformations $A_\mu \to A_\mu + \partial_\mu \theta$, $\phi \to \phi - \theta$ which satisfy $\Box\theta = 0$. This is analogous to the residual gauge symmetry that remains in standard electromagnetism after imposing the Lorenz gauge condition. Since we have introduced the Stückelberg field to restore the full $U(1)$ gauge symmetry, one could also consider a mass term for the vector field, as in the original Stückelberg model. Then, one would obtain a massive PU field for the scalar field plus additional couplings to the vector field. We will not explore this possibility here because we are only interested in studying the massless vector field case. A way to prohibit the mass term (that would be allowed by the required symmetries of our action) is to impose the additional symmetry for the Stückelberg field $\phi \to \phi + \vartheta$ with ϑ a harmonic function. Our action (7.13) does

fulfill this symmetry, whereas the term $A_\mu \partial^\mu \phi$ that is generated from the mass term does not.

The equations of motion obtained from action (7.13) are

$$\partial_\nu F^{\mu\nu} + \xi \partial^\mu \left[\partial_\nu A^\nu + \Box\phi\right] = 0\,, \tag{7.15}$$

$$\Box\left(\Box\phi + \partial_\mu A^\mu\right) = 0\,. \tag{7.16}$$

Notice that the second equation is nothing but the 4-divergence of the first one. If we now fix to Lorenz gauge $\partial_\mu A^\mu = 0$, we are left with

$$\Box A_\mu = \xi \partial_\mu \Box\phi\,, \tag{7.17}$$

$$\Box^2\phi = 0\,. \tag{7.18}$$

The equation for the PU field completely decouples, whereas it acts as an effective external conserved current term for the vector field. Such an external source is determined by the gradient of $\Box\phi$ so that it only affects the longitudinal mode of A_μ. In other words, the transverse modes completely decouple from ϕ and only the longitudinal mode is affected. Indeed, if we introduce the field $B_\mu \equiv A_\mu - \xi\partial_\mu\phi$, the equations can be written as

$$\Box B_\mu = 0\,, \tag{7.19}$$

$$\Box^2\phi = 0 \tag{7.20}$$

where now we have $\partial_\mu B^\mu = -\xi\Box\phi$ as the gauge condition. The PU field determines the longitudinal mode of the vector field B_μ which, in addition, satisfies a free wave equation. In fact, since we still have the residual gauge symmetry, we can use it to set $B_0 = 0$ so that we obtain $\nabla \cdot \vec{B} = \xi\Box\phi$. In this gauge, we have the free wave equations of motion for the transverse modes of the vector field and for $\Box\phi$, whereas the longitudinal mode of the vector field is determined by the PU field (up to a residual gauge transformation). Notice that naively imposing the Lorenz gauge condition directly in the action (7.13) leads to

$$S = \frac{1}{2}\int \mathrm{d}^4x \left[-\partial_\mu A_\nu \partial^\mu A^\nu + \xi(\Box\phi)^2\right]\,. \tag{7.21}$$

This reproduces the correct equations of motion for the transversal modes of A_μ and for ϕ, but it does not yield the correct equation for the longitudinal mode of the vector field. We can alternatively use a gauge such that[2] $\partial_\mu A^\mu = -\frac{\xi}{1+\xi}\Box\phi$, which again leaves a residual gauge symmetry. Then, the equations of motion read:

$$\Box A_\mu = 0\,, \tag{7.22}$$

$$\Box^2\phi = 0. \tag{7.23}$$

[2]Since the quantity $\partial_\mu A^\mu + \Box\phi$ is gauge invariant, we cannot impose the condition $\partial_\mu A^\mu = -\Box\phi$. For our choice, this only happens in the limit $\xi \to \infty$.

When imposing this gauge at the level of the action we obtain:

$$S = \frac{1}{2}\int \mathrm{d}^4x \left[-\partial_\mu A_\nu \partial^\mu A^\nu + \frac{\xi}{1+\xi}(\Box\phi)^2\right] \tag{7.24}$$

which reproduces the correct equations of motion and, if we additionally impose the used gauge as a subsidiary condition, we also obtain the correct relation between $\partial_\mu A^\mu$ and $\Box\phi$. In any case, it is more clear by looking at the equations of motion directly that we have completely decoupled transverse modes for the vector field satisfying free wave equations plus the degenerate PU field which determines the longitudinal mode of the vector field. It will be useful to note that neither of the two gauges discussed fixes the gauge freedom completely, but they leave us with the residual gauge symmetry $A_\mu \to A_\mu + \partial_\mu\theta$, $\phi \to \phi - \theta$ with $\Box\theta = 0$. In addition to this residual symmetry, we also have the aforementioned symmetry that prevents the appearance of the mass term, i.e. $A_\mu \to A_\mu$, $\phi \to \phi + \vartheta$ with $\Box\vartheta = 0$. In other words, we can perform a residual gauge transformation with two different (harmonic) gauge parameters θ and $\vartheta - \theta$ for A_μ and ϕ respectively.

Interestingly, the transformation for the scalar field can be regarded as a generalized shift symmetry, since we can shift ϕ not only by a constant, like in the case of a Goldstone boson, or a linear function of the coordinates, like in the case of the galileon field, but by an arbitrary harmonic function. Of course, the constant shift and the Galilean transformations are particular cases of this more general symmetry.

We know that the Maxwell term describes a well behaved theory also at the quantum level and with interactions. However, the lack of stability under quantization is a common feature in higher order derivative Lagrangians. As we have already discussed, such theories suffer, for instance, from the Ostrogradski instability which implies that their Hamiltonian is not bounded from below [74, 75]. It has been argued, however, that the Ostrogradski ghost instability which is present in the PU oscillator can be *cured* and that the theory can be consistently quantized thanks to the presence of an unbroken $\mathcal{PT}$ symmetry that allows non-hermitian Hamiltonians to lead to unitary evolution [179, 180]. However, how to take the classical limit of theories quantized within such a framework remains unclear. In Section 7.4 we shall come back to this issue and develop an alternative consistent quantization procedure for the PU action based on the generalized shift symmetry and that makes no use of non-hermitian operators.

To end this Section, we want to mention that, in the same way that we can write the Maxwell Lagrangian in terms of the 2-form $\mathcal{F} = \mathrm{d}\mathcal{A} = \frac{1}{2}F_{\mu\nu}\mathrm{d}x^\mu \wedge \mathrm{d}x^\nu$, as $S_{\text{Maxwell}} = -\frac{1}{2}\int \mathcal{F}\wedge *\mathcal{F}$ for $\mathcal{A} = A_\mu \mathrm{d}x^\mu$, we find for the degenerate PU action,

$$S_{PU} = \frac{1}{2}\xi \int \mathrm{d}^4x\,(\Box\phi)^2 = \frac{1}{2}\xi\int \delta\mathrm{d}\phi \wedge *\delta\mathrm{d}\phi\,. \tag{7.25}$$

Hence $\mathrm{d}^4x\,(\Box\phi)^2 = \delta\mathrm{d}\phi\wedge *\delta\mathrm{d}\phi = *\mathrm{d}*\mathrm{d}\phi\wedge\mathrm{d}*\mathrm{d}\phi$. Here $\delta = -*\mathrm{d}*$ is the codifferential (on a 4-dimensional Lorentz manifold) and $*\omega$ denotes the Hodge dual of the p-form ω defined by

$$(*\omega)_{i_1\cdots i_{n-p}} = \frac{1}{p!}\eta^{i_1\cdots i_n}\omega_{i_{n-p}\cdots i_n}\,, \qquad \text{here } \eta \text{ is the volume form, } \eta = \sqrt{-g}\mathrm{d}x^1\wedge\cdots\wedge\mathrm{d}x^n\,.$$

Since $\delta\delta = 0$, the PU action is invariant under the transformation $\mathrm{d}\phi \to \mathrm{d}\phi + \delta\Sigma$ for some 2-form Σ which has the property that $\delta\Sigma = \mathrm{d}\theta$ for some scalar field θ. The field θ obviously satisfies $\Box\theta = \delta\mathrm{d}\theta = \delta\delta\Sigma = 0$. This is nothing else that the remaining gauge invariance or generalized shift symmetry of the PU action expressed in the language of forms.

7.3 Interactions

As we have already mentioned, it has been shown that the free PU oscillator can be quantized with a positive spectrum for the Hamiltonian. However, it happens very often that a free higher derivative theory can be fine but it becomes unstable once we introduce interactions. Actually, this is the real problem with higher order derivative theories. Let us investigate this issue for our theory. Since ϕ is the Stückelberg field of a $U(1)$ gauge field, its natural interaction will be to charged fields by means of a gauge interaction. In the following we shall consider two explicit examples, namely a complex scalar field and a charged fermion.

7.3.1 Charged scalars

Let us consider the action of a complex scalar field χ whose interaction is mediated by our Stückelberg field. We define the covariant derivative $D_\mu = \partial_\mu - i\partial_\mu\phi$ so that the action has a $U(1)$ gauge symmetry. Under a gauge transformation $\chi \to e^{i\theta}\chi$ and $\phi \to \phi + \theta$, the following action is invariant

$$\begin{aligned} S &= \int \mathrm{d}^4x \Big[D_\mu\chi (D^\mu\chi)^* - V(\chi\chi^*) \Big] \\ &= \int \mathrm{d}^4x \Big[\partial_\mu\chi\partial^\mu\chi^* + \chi\chi^*\partial_\mu\phi\partial^\mu\phi - i\partial_\mu\phi\big(\chi\partial^\mu\chi^* - \chi^*\partial^\mu\chi\big) - V(\chi\chi^*) \Big]. \end{aligned} \tag{7.26}$$

Here V is a potential which depends only on the modulus of χ. It is interesting to note that the scalar gauge field ϕ is automatically dynamical because it has derivative couplings to the charged field, unlike for the case of a gauge vector field. However, having a gauge symmetry, we can always remove it from action (7.26) by an appropriate gauge choice, so that it does not represent an actual physical degree of freedom of (7.26). Nevertheless, once we add the *free* PU action to the theory, ϕ can no longer be completely gauged away since the gauge symmetry is now reduced to gauge parameters satisfying $\Box\theta = 0$. Thus, the full interacting Lagrangian is given by

$$S = \int \mathrm{d}^4x \left[\partial_\mu\chi\partial^\mu\chi^* + \chi\chi^*\partial_\mu\phi\partial^\mu\phi - i\partial_\mu\phi\big(\chi\partial^\mu\chi^* - \chi^*\partial^\mu\chi\big) - V(\chi\chi^*) + \frac{1}{2}\xi(\Box\phi)^2 \right]. \tag{7.27}$$

With this additional kinetic term for the gauge field ϕ, it actually propagates two degrees of freedom, one of which can be removed using the gauge freedom so that ϕ

does now propagate one physical degree of freedom. Notice also that the addition of the PU term gives its corresponding propagator.

It is also interesting to note that if the potential $V(\chi\chi^*)$ leads to symmetry breaking, we obtain a non-degenerate PU model from the non-vanishing vacuum expectation value (vev) of $\chi\chi^*$. For instance, if we consider the usual renormalizable quartic potential $V(|\chi|) = \mu^2|\chi|^2 + \lambda|\chi|^4$ with $\mu^2 < 0$, then χ acquires a non-vanishing vev $\chi\chi^* \equiv v^2 = -\mu^2/\lambda$ and the quadratic term for ϕ is given by

$$S_\phi^{(2)} = \int \mathrm{d}^4x \left[\frac{1}{2}\xi(\Box\phi)^2 + v^2\partial_\mu\phi\partial^\mu\phi\right]. \tag{7.28}$$

Thus, we can generate the term with two derivatives analogous to the PU action with $m_1^2 = m_2^2 = -2v^2/\xi$ from a spontaneous symmetry breaking of the charged field.

The equations of motion derived from the above action are[3]

$$\xi\Box^2\phi - \partial_\mu j^\mu = 0, \tag{7.29}$$

$$D_\mu D^\mu\chi^* + \frac{\partial V}{\partial\chi} = 0, \tag{7.30}$$

$$D_\mu D^\mu\chi + \frac{\partial V}{\partial\chi^*} = 0\,, \tag{7.31}$$

where we have introduced the current

$$j^\mu = i\left(\chi^* D^\mu\chi - \chi D^\mu\chi^*\right) = i\left(\chi^*\partial^\mu\chi - \chi\partial^\mu\chi^*\right) + 2\chi\chi^*\partial^\mu\phi\,. \tag{7.32}$$

Notice that the first equation can be written as a conservation equation as follows:

$$\partial_\mu\left(\xi\partial^\mu\Box\phi - j^\mu\right) = 0 \tag{7.33}$$

so that we have a conserved charge given by

$$\mathcal{Q} = \int \mathrm{d}^3x \left(\xi\Box\dot{\phi} - j^0\right). \tag{7.34}$$

Interestingly, since the χ sector has a global $U(1)$ symmetry , the current j^μ is independently conserved on-shell, i.e., $\partial_\mu j^\mu = 0$ so that we have the usual conservation of the complex field charge

$$\mathcal{Q}_\chi = \int \mathrm{d}^3x\; j^0. \tag{7.35}$$

This conservation law also implies the conservation of the current $j_\phi^\mu = \partial^\mu\Box\phi$ that gives rise to the conserved charge

$$\mathcal{Q}_\phi = \int \mathrm{d}^3x\; \Box\dot{\phi} \tag{7.36}$$

[3]Here we use the fact that $D_\mu\chi^* = (D_\mu\chi)^*$ so that we will not distinguish between both.

associated with the PU field. The crucial fact here is that the χ-dependent term disappears from the equation of motion of ϕ. However, the equation of motion for χ still depends on ϕ. In other words, ϕ affects the dynamics of χ but is itself not affected by χ. It satisfies a "free" equation even in the presence of the coupling to χ. This surprising behavior will be useful for the quantization of the theory because we can use the procedure of the free field quantization to get rid of the ghost-mode and the coupling will not reintroduce the ghost into the theory.

To quantize the theory we write it in Hamiltonian form. The conjugate momenta are given by

$$\pi_\chi = \frac{\partial \mathcal{L}}{\partial \dot{\chi}} = D^0 \chi^*, \tag{7.37}$$

$$\phi_1 = \phi\,, \quad \Pi_1 = \frac{\partial \mathcal{L}}{\partial \dot{\phi}} - \frac{\mathrm{d}}{\mathrm{d}t}\frac{\partial \mathcal{L}}{\partial \ddot{\phi}} = 2\chi\chi^*\dot{\phi} - i\left(\chi\dot{\chi}^* - \dot{\chi}\chi^*\right) - \xi\Box\dot{\phi} = j^0 - \xi\Box\dot{\phi}, \tag{7.38}$$

$$\phi_2 = \dot{\phi}\,, \quad \Pi_2 = \frac{\partial \mathcal{L}}{\partial \ddot{\phi}} = \xi\Box\phi. \tag{7.39}$$

The conjugate momentum of χ^* is of course $\pi_{\chi^*} = \pi_\chi^* = D^0\chi$. Thus, the Hamiltonian density is

$$\begin{aligned}\mathcal{H} &= \dot{\chi}\pi_\chi + \dot{\chi}^*\pi_\chi^* + \dot{\phi}\Pi_1 + \ddot{\phi}\Pi_2 - \mathcal{L} \\ &= D_0\chi D^0\chi^* - D_i\chi D^i\chi^* + V\left(\chi\chi^*\right) + \frac{1}{2}\xi(\Box\phi)^2 + \xi\left(\left(\nabla^2\phi\right)\Box\phi - \dot{\phi}\Box\dot{\phi}\right).\end{aligned} \tag{7.40}$$

Writing this in terms of the momenta and the fields we obtain

$$\begin{aligned}\mathcal{H}(\chi,\phi_1,\phi_2,\pi_\chi,\Pi_1,\Pi_2) &= \pi_\chi\pi_\chi^* + i\phi_2\left(\chi\pi_\chi - \chi^*\pi_\chi^*\right) + \phi_2\Pi_1 + \frac{\Pi_2^2}{2\xi} + \Pi_2\nabla^2\phi_1 \\ &\quad + \nabla\chi\nabla\chi^* + \chi\chi^*\left(\nabla\phi_1\right)^2 - i\nabla\phi_1\left(\chi\nabla\chi^* - \chi^*\nabla\chi\right) + V\left(\chi\chi^*\right).\end{aligned} \tag{7.41}$$

7.3.2 Charged fermions

Here we shall briefly repeat the derivations of the previous section for a coupling of ϕ to a Dirac field ψ. Again, by using the covariant derivative $D_\mu = \partial_\mu - i\partial_\mu\phi$, the action for a charged fermion becomes

$$\begin{aligned}S &= \int \mathrm{d}^4x\left[-\bar{\psi}\left(\gamma^\mu D_\mu + m\right)\psi\right] \\ &= \int \mathrm{d}^4x\left[-\bar{\psi}\gamma^\mu\partial_\mu\psi + i\bar{\psi}\gamma^\mu\psi\partial_\mu\phi - m\bar{\psi}\psi\right].\end{aligned} \tag{7.42}$$

This action is invariant under a gauge transformation with $\psi \to e^{i\theta}\psi$ and $\phi \to \phi + \theta$. Again, having this symmetry at our disposal, the scalar field ϕ can, in principle, be gauged away. However, when we identify it with the PU field, it actually carries two degrees of freedom, one of which will be physical. Thus, the full interacting Lagrangian is

$$S = \int \mathrm{d}^4x\left[-\bar{\psi}\gamma^\mu\partial_\mu\psi + i\bar{\psi}\gamma^\mu\psi\partial_\mu\phi - m\bar{\psi}\psi + \frac{1}{2}\xi\left(\Box\phi\right)^2\right]. \tag{7.43}$$

This action leads to the following equations of motion

$$\xi\Box^2\phi - \partial_\mu j^\mu = 0, \tag{7.44}$$
$$D_\mu\bar{\psi}\gamma^\mu - m\bar{\psi} = 0, \tag{7.45}$$
$$D_\mu\gamma^\mu\psi + m\psi = 0, \tag{7.46}$$

where we have introduced the usual $U(1)$ current $j^\mu = i\bar{\psi}\gamma^\mu\psi$, which is conserved, i.e., $\partial_\mu j^\mu = 0$ so that we have the usual conserved fermionic charge

$$\mathcal{Q}_\psi = i\int \mathrm{d}^3x\bar{\psi}\gamma^0\psi. \tag{7.47}$$

Again, we also have the conserved current associated with the PU field $\mathcal{Q}_\phi$. Therefore, like for the case of a coupling to a charged scalar field, the PU field satisfies the "free" equation, i.e., its dynamics is not affected by the presence of the interaction with the fermionic field, however the PU field ϕ can, in principle, affects the dynamics of ψ.

To end this section and for completeness, we shall compute the Hamiltonian. The corresponding conjugate momenta are given by

$$\pi_\psi = \frac{\partial\mathcal{L}}{\partial\dot{\psi}} = -\bar{\psi}\gamma^0 \quad \Rightarrow \ \bar{\psi} = \pi_\psi\gamma^0, \tag{7.48}$$
$$\phi_1 = \phi\,, \quad \Pi_1 = \frac{\partial\mathcal{L}}{\partial\dot{\phi}} - \frac{\mathrm{d}}{\mathrm{d}t}\frac{\partial\mathcal{L}}{\partial\ddot{\phi}} = i\bar{\psi}\gamma^0\psi - \xi\Box\dot{\phi} = j^0 - \xi\Box\dot{\phi}, \tag{7.49}$$
$$\phi_2 = \dot{\phi}\,, \quad \Pi_2 = \frac{\partial\mathcal{L}}{\partial\ddot{\phi}} = \xi\Box\phi. \tag{7.50}$$

As we notice from Eq. (7.48), the field $\bar{\psi}$ is proportional to the conjugate momentum π_ψ and so we should not consider $\bar{\psi}$ as a field like ψ (cf. [189]). The Hamiltonian density reads

$$\begin{aligned}\mathcal{H} &= \pi_\psi\dot{\psi} + \Pi_1\dot{\phi} + \Pi_2\ddot{\phi} - \mathcal{L} \\ &= \Pi_1\phi_2 + \frac{\Pi_2^2}{2\xi} + \Pi_2\nabla^2\phi_1 + \pi_\psi\gamma^0\left(m + \gamma^i\partial_i\right)\psi + i\pi_\psi\left(\phi_2 - \gamma^0\gamma^i\partial_i\phi_1\right)\psi.\end{aligned} \tag{7.51}$$

In summary, in this Section we have shown explicitly that, by introducing interactions of the PU field to charged scalars or fermions following a minimal coupling principle, the dynamics of the PU field is not modified. The reason for this is that, although the quadratic term giving the free propagator for ϕ only respects a residual gauge symmetry, the full theory still preserves global $U(1)$ symmetry that gives rise to current conservation. Since it is the divergence of the conserved current that enters into the equation of motion of ϕ (which is guaranteed precisely by introducing it through a $U(1)$ covariant derivative), no effects from the charged particles on the PU field appear.

The above result that charged particles cannot excite the PU field can also been understood from standard electromagnetism results, where photons with polarization vector proportional to the 4-momentum k_μ cannot be generated out of conserved

currents. At the quantum level, this is ensured by the Ward identities according to which the amplitude of any process involving an external longitudinal photon (in the 4-dimensional sense) vanishes.

It is interesting to note that the above procedure to gauge a global $U(1)$ symmetry is similar to making it local by introducing a *longitudinal* vector field. In fact, if we consider the covariant derivative $D_\mu = \partial_\mu - iA_\mu$, nothing here imposes that the vector field A_μ must be transverse and only once we choose the fully gauge invariant kinetic term $-F^2/4$ for A_μ, the propagating vector boson becomes transverse. This is the natural choice if we want the gauge boson to carry a pure massless spin-1 representation of the Lorentz group and also if we want to keep the full $U(1)$ gauge invariance. However, other possibilities could be considered. One can, for instance, choose the kinetic term $(\partial_\mu A^\mu)^2/2$ for the vector field so that only its temporal component propagates. The price to pay is that only a residual gauge symmetry remains in the sector of the gauge boson. However, this is not too problematic in principle since the global $U(1)$ symmetry is maintained (A_μ does not change under a global transformation) and charge conservation is not affected. Notice also that, in addition to the coupling of the charged fields to ϕ, we can also couple them to the transverse gauge field A_μ, in principle with a different coupling constant, i.e., they can be differently charged under the *two different* $U(1)$ fields.

7.4 Discussion

In the previous sections we have introduced interactions for the degenerate PU field by following a symmetry principle, according to which all the interactions respect $U(1)$ gauge symmetry and ϕ is identified with the gauge field that allows to render the gauge symmetry local. It is precisely this way of coupling the PU field that facilitates to consistently quantize the theory. We have shown that the interactions of the PU field with charged scalars or fermions do not modify the equation of motion for ϕ, although ϕ itself can affect the dynamics of the charged fields. Thus, as we shall show below, one can quantize the free field and use the gauge symmetry to remove the ghost-like mode. The interactions will then not re-introduce it. After quantizing the field, we shall discuss its cosmological relevance and show how it can give rise to an effective cosmological constant.

7.4.1 Quantization and Stability of the PU field

A method to quantize the PU oscillator has been proposed in [179]. This method relies on the fact that even if a Hamiltonian is not hermitian, it leads to a unitary quantum theory if it exhibits an unbroken $\mathcal{PT}$-symmetry. In the original approach, the quantization procedure was developed for an isolated PU oscillator. Of course, being isolated, the ghostly degree of freedom is harmless [181]. One should actually check if couplings to other oscillators (or other dynamical systems) can be consistently added in such a way that the theory remains stable. In [190], the coupling of hermitian and non-hermitian Hamiltonians was explored and it was shown that

if the coupling constant is large enough, the energies can become complex. In some other works [182, 183], higher derivative supersymmetric theories are studied and it is shown that some special types of interactions do not spoil the unitarity of the theories. On the other hand, while the quantization method yields a system with positive energies, the classical Hamiltonian remains unbounded so that one needs to establish how the classical limit should be taken. Here we shall not make use of this quantization approach, but we shall take advantage of the existing residual gauge symmetry to get rid of the undesired degree of freedom. Moreover, we shall discuss how the quantization is consistent in view of the results of the previous Section.

The Hamiltonian for the free PU field in terms of the conjugate momenta,

$$\Pi_1 = \frac{\partial \mathcal{L}}{\partial \dot{\phi}} - \frac{\mathrm{d}}{\mathrm{d}t}\frac{\partial \mathcal{L}}{\partial \ddot{\phi}} = -\xi \Box \dot{\phi}, \tag{7.52}$$

$$\phi_2 = \dot{\phi}\,, \quad \Pi_2 = \frac{\partial \mathcal{L}}{\partial \ddot{\phi}} = \xi \Box \phi, \tag{7.53}$$

is given by

$$\mathcal{H}_0 = \Pi_1 \phi_2 + \frac{\Pi_2^2}{2\xi} + \Pi_2 \nabla^2 \phi\,, \tag{7.54}$$

where the expected Ostrogradski instability associated with Π_1 is represented by the unbounded first term. This is not fatal by itself, as we have discussed above, but it can, in general, lead to instabilities when we couple it to another field. At the classical level, this instability can show up by the excitation of arbitrarily many modes coupling to ϕ at the cost of lowering $\mathcal{H}_0$ indefinitely. As we have seen for the PU oscillator, we do not have any tachyonic instability, all the modes have real propagation speeds. Only for the degenerate case (that corresponds to our Stückelberg field) we have a mode that grows linearly with time, associated with having a double pole. This represents a much milder *instability* than those associated with tachyons.

On the other hand, we notice that this Hamiltonian does not have the gauge symmetry of the theory. However, it will obviously lead to a set of Hamilton equations that do satisfy the symmetry. This should not be surprising since the Hamiltonian, in general, does not preserve symmetries. In particular, it does not respect Lorentz symmetry, although the corresponding theory does. It is the set of physical observables that must respect the symmetries of the theory. For instance, one can always perform a canonical transformation that will change the form of the Hamiltonian, but will leave the equations of the dynamical system invariant. Moreover, in the case of a field theory, it is possible to add a 3-divergence or a total time derivative to the Hamiltonian density without modifying the quantum theory [189]. In terms of the canonical variables, the gauge symmetry of the action reads $\Pi_{1,2} \to \Pi_{1,2}$, $\phi_1 \to \phi_1 + \theta$, $\phi_2 \to \phi_2 + \dot{\theta}$ with θ an arbitrary harmonic function. In principle, one could try to construct a gauge-invariant Hamiltonian by using the aforementioned allowed modifications, although we shall not pursue this approach here. Instead, we

shall use the freedom given by the gauge symmetry to select a set of gauge-related modes for which the energy is positive.

For our equations of motion, the field can be expanded in Fourier modes as follows:

$$\phi = \int \frac{\mathrm{d}^3k}{(2\pi)^{3/2}} \frac{1}{(2k)^{3/2}} \left[(a_k + ib_k kt) e^{i(\vec{k}\cdot\vec{x}-kt)} + (a_k^* - ib_k^* kt) e^{-i(\vec{k}\cdot\vec{x}-kt)} \right]. \tag{7.55}$$

After quantization, a_k, b_k and a_k^*, b_k^* are promoted to operators $\mathbf{a}_k$, $\mathbf{b}_k$ and $\mathbf{a}_k^\dagger$, $\mathbf{b}_k^\dagger$ respectively. Notice that a_k is the pure gauge mode since it is modified by residual gauge transformations. In fact, gauge-invariant quantities (that will be determined by $\Box\phi$) only depend on b_k and b_k^*.

Using the above field decomposition, the Hamiltonian can be expressed as

$$H = \int \mathrm{d}^3x : \mathcal{H}_0 := \xi \int \mathrm{d}^3k k \left[\mathbf{b}_k^\dagger \mathbf{b}_k - \frac{1}{2} \left(\mathbf{a}_k^\dagger \mathbf{b}_k + \mathbf{b}_k^\dagger \mathbf{a}_k \right) \right], \tag{7.56}$$

where the double dots : : denote the normal ordering operator. As anticipated, the Hamiltonian is not gauge invariant which is reflected by its dependence on the gauge mode $\mathbf{a}_k$. Since we are free to perform a gauge transformation we could eliminate it from the physical spectrum by fixing some suitable gauge. Below, we explicitly show how to proceed.

Another approach is to impose an additional subsidiary condition à la Gupta-Bleuler[4] and to define a physical Hilbert space in which the expectation value of the gauge-dependent piece of the Hamiltonian vanishes. The easiest way to achieve this is to define the physical states as those which are annihilated by the gauge mode: $\mathbf{a}_k|\mathrm{phys}\rangle = 0$. In fact, this is too restrictive and can be relaxed, since imposing the more general condition $(\mathbf{a}_k - i\alpha\mathbf{b}_k)\,|\mathrm{phys}\rangle = 0$ with α some arbitrary real number, suffices to make the energy gauge invariant and positive for the physical Hilbert space. Moreover, if we only want to have positive energies, the parameter α of the subsidiary condition can also be complex, we just have to require that $\mathrm{Im}\ \alpha > -1$. This can be seen by computing the expectation value of the Hamiltonian in a physical state:

$$\langle H \rangle_{\mathrm{phys}} = \xi(1 + \mathrm{Im}\ \alpha) \int \mathrm{d}^3k k \langle \mathbf{b}_k^\dagger \mathbf{b}_k \rangle_{\mathrm{phys}}. \tag{7.57}$$

Notice that for the energy of the physical modes to be positive for α real we need $\xi > 0$ and it has canonical energy if $\xi = 1$. The case with $\mathrm{Im}\ \alpha = -1$ in which the expectation value of the Hamiltonian vanishes is also interesting. Then, the gauge mode exactly cancels the energy of the physical mode, rendering this case equivalent to the original Gupta-Bleuler formalism for which the temporal and longitudinal modes of the electromagnetic potential cancel each other so that there is no contribution from them to the energy[5]. The choice of the subsidiary condition with α real seems a natural choice because it fully eliminates the gauge-dependent

[4] See for instance [191].

[5] In the standard Gupta-Bleuler approach to quantize electromagnetism, one requires the weak Lorenz condition so that the positive frequency part of field operator $\partial_\mu A^\mu$ annihilates the physical

piece of the Hamiltonian and it amounts to identifying a physical state as the entire equivalence class of states that differ only by a gauge mode. In terms of the PU field, the subsidiary condition with α real can be written as $\phi^{(+)}(t_0)|\text{phys}\rangle = 0$ where $\phi^{(+)}$ is the positive frequency part of the field operator and t_0 some given time. In other words, the physical states are those for which the expectation value of ϕ vanishes at some time, i.e., $\langle\phi\rangle_{\text{phys}} = 0$ for some $t = t_0$.

For our bi-harmonic equation of motion, one can define the scalar product

$$\begin{aligned}\Big(\phi_k, \phi_{k'}\Big) &= i\int \mathrm{d}^3x\Big[\Phi_k^{*T}\Pi_{k'} - \Pi_k^{*T}\Phi_{k'}\Big] \\ &= -i\xi\int \mathrm{d}^3x\Big[\Big(\phi_k^*\Box\dot{\phi}_{k'} - \Box\dot{\phi^*}_k\phi_{k'}\Big) - \Big(\dot{\phi^*}_k\Box\phi_{k'} - \Box\phi_k^*\dot{\phi}_{k'}\Big)\Big] \quad (7.58)\end{aligned}$$

where T stands for the transpose and we have introduced the notation

$$\Phi_k \equiv \begin{pmatrix}\phi_k \\ \dot{\phi}_k\end{pmatrix} \qquad \Pi_k \equiv \xi\begin{pmatrix}-\Box\dot{\phi}_k \\ \Box\phi_k\end{pmatrix}. \quad (7.59)$$

The modes that we have used to decompose the field in (7.55) are not orthonormal with respect to this scalar product so that the corresponding operators do not satisfy the usual commutation relations, but they have the following commutation algebra:

$$\Big[\mathbf{a}_k, \mathbf{a}_{k'}^\dagger\Big] = \Big[\mathbf{a}_k, \mathbf{b}_{k'}^\dagger\Big] = \Big[\mathbf{b}_k, \mathbf{a}_{k'}^\dagger\Big] = -\frac{2}{\xi}\,\delta^{(3)}(\vec{k} - \vec{k}') \quad (7.60)$$

with all the other commutators vanishing. The modes that diagonalize the scalar product are[6]:

$$\phi_{1,k} = \frac{1}{(2\pi)^{3/2}}\frac{5^{-1/4}}{(2k)^{3/2}}\sqrt{\frac{2}{\xi}}\left(\frac{1-\sqrt{5}}{2} + ikt\right)e^{i(\vec{k}\cdot\vec{x}-kt)} \quad (7.61)$$

$$\phi_{2,k} = \frac{1}{(2\pi)^{3/2}}\frac{5^{-1/4}}{(2k)^{3/2}}\sqrt{\frac{2}{\xi}}\left(\frac{1+\sqrt{5}}{2} + ikt\right)e^{i(\vec{k}\cdot\vec{x}-kt)} \quad (7.62)$$

with eigenvalues $+1$ and -1 so that the modes $\phi_{2,k}$ have negative norm and this leads to a Hilbert space with indefinite metric. The PU field operator can be expanded as

$$\phi = \int \mathrm{d}^3k \sum_{\lambda=1,2}\Big(\mathbf{a}_{\lambda,k}\phi_{\lambda,k} + \mathbf{a}_{\lambda,k}^\dagger\phi_{\lambda,k}^*\Big), \quad (7.63)$$

states, which guarantees that $\langle\partial_\mu A^\mu\rangle_{\text{phys}} = 0$. This is imposed in order to recover the classical Maxwell equations or, equivalently, so that only the transverse photons contribute to physical observables. However, as shown in [192] one could relax this condition and only require that physical states $|\psi\rangle$ are such that they have positive norm on physical observables $\langle\mathcal{O}\psi|\mathcal{O}\psi\rangle$, where $\mathcal{O}$ belongs to the observables algebra, defined as those operators that commute with the generator of the residual gauge symmetry.

[6]Notice the interesting appearance of the golden ratio $\tau = \frac{1+\sqrt{5}}{2}$ and its inverse $\tau^{-1} = -\frac{1-\sqrt{5}}{2}$.

where now the modes are orthonormal with respect to the scalar product (7.58) and the annihilation and creation operators satisfy the commutation relations

$$\Big[\mathbf{a}_{\lambda,k}, \mathbf{a}^{\dagger}_{\lambda',k'}\Big] = \eta_{\lambda,\lambda'}\delta^{(3)}(\vec{k}-\vec{k}') \tag{7.64}$$

with $\eta_{\lambda\lambda'}$ =diag$(1,-1)$. Here we see how the negative norm modes appear in the commutation relations and lead to the indefinite metric for the corresponding Hilbert space. The relation of these operators with $\mathbf{a}_k$ and $\mathbf{b}_k$ is given by:

$$\mathbf{a}_k = \frac{5^{-1/4}}{\sqrt{2\xi}}\Big[\mathbf{a}_{1,k}+\mathbf{a}_{2,k}-\sqrt{5}(\mathbf{a}_{1,k}-\mathbf{a}_{2,k})\Big], \tag{7.65}$$

$$\mathbf{b}_k = \sqrt{\frac{2}{\xi}}5^{-1/4}\Big(\mathbf{a}_{1,k}+\mathbf{a}_{2,k}\Big). \tag{7.66}$$

Notice that the physical gauge-invariant mode $\mathbf{b}_k$ is now given by $(\mathbf{a}_{1,k}+\mathbf{a}_{2,k})$, i.e., $\Box\phi$ is given in terms of such a combination. The hamiltonian in terms of these operators reads:

$$H = \int \mathrm{d}^3k\frac{k}{\sqrt{5}}\left[\left(1+\sqrt{5}\right)\mathbf{a}^{\dagger}_{1,k}\mathbf{a}_{1,k}+\left(1-\sqrt{5}\right)\mathbf{a}^{\dagger}_{2,k}\mathbf{a}_{2,k}+\left(\mathbf{a}^{\dagger}_{1,k}\mathbf{a}_{2,k}+\mathbf{a}^{\dagger}_{2,k}\mathbf{a}_{1,k}\right)\right] \tag{7.67}$$

Now we can impose the subsidiary condition $(\mathbf{a}_k - i\alpha\mathbf{b}_k)|\mathrm{phys}\rangle = 0$ to obtain the physical Hilbert space. If we translate such a condition to the new operators it reads

$$\Big[(1-\sqrt{5}-2i\alpha)\mathbf{a}_{1,k}+(1+\sqrt{5}-2i\alpha)\mathbf{a}_{2,k}\Big]\Big|\mathrm{phys}\Big\rangle = 0 \tag{7.68}$$

and the expectation value of the Hamiltonian in a physical state is again gauge-independent and positive definite. Another way of quantizing the theory that takes advantage of the expansion in orthonormal modes is to fix the gauge such that we eliminate the negative norm mode and, then, quantizing the positive norm mode alone, in analogy to the quantization in the Coulomb gauge for standard QED. To do this, one has to fix the gauge $a_{2,k}=0$ a priori. This corresponds to choosing the gauge mode $a_k = -\tau^{-1}b_k$ and $a^*_k = -\tau^{-1}b^*_k$, with τ the golden ratio, for the classical amplitudes. Then, the PU field operator is expanded in terms of the remaining positive modes, i.e.:

$$\phi = \int \mathrm{d}^3k\Big[\mathbf{a}_{1,k}\phi_{1,k}+\mathbf{a}^{\dagger}_{1,k}\phi^*_{1,k}\Big]. \tag{7.69}$$

Thus, these modes are orthogonal with norm +1 so that the annihilation and creation operators satisfy the usual commutation relations $[\mathbf{a}_{1,k},\ \mathbf{a}^{\dagger}_{1,k'}] = \delta^{(3)}(\vec{k}-\vec{k}')$. We thus avoid having to work with negative norm states and negative energies from the beginning without having to impose a subsidiary condition. The disadvantage of this quantization procedure will be the lost of explicit gauge-invariance. In the quantization à la Gupta-Bleuler previously mentioned we work with all the modes. The expectation values of the physical observables are explicitly gauge-independent because they will only depend on $\mathbf{b}_k$ and $\mathbf{b}^{\dagger}_k$, which are the physical modes that cannot be removed by means of a gauge transformation.

The natural concern arising with the discussed procedure to identify the physical states is whether the introduction of interactions will spoil it. However, as we have shown in the previous section, if interactions are introduced following a symmetry principle, this will not be the case because, while the PU field will affect the sector of charged particles, its own equation of motion remains unaffected. The reason for this is that introducing the couplings as $U(1)$ gauge interactions leads to the presence of the associated Noether current, whose divergence is precisely the new term appearing in the equation of motion of the PU field. Thus, the conservation of this current also implies that the equation of the PU field is not modified. This is the crucial point to guarantee that the discussed procedure to identify the physical states remains unaffected when introducing interactions because the field decomposition given in (7.55) is also valid (and exact) in the presence of interactions with charged particles. The equivalent of this statement in standard QED comes from the fact that, due to current conservation, the divergence of the vector potential satisfies a decoupled free wave equation so that the selection of the Hilbert space is dynamically stable.

7.4.2 Cosmological relevance

Let us finally show how the PU field can actually play the role of dark energy. For that, we first note that $\Box\phi$ satisfies the usual equation for a massless scalar field which, for a homogeneous field in a FLRW universe with metric $ds^2 = dt^2 - a(t)^2 d\vec{x}^2$, reads

$$\left[\frac{\mathrm{d}^2}{\mathrm{d}t^2} + 3H\frac{\mathrm{d}}{\mathrm{d}t}\right]\Box\phi = 0. \tag{7.70}$$

The solution of this equation is given by

$$\Box\phi(t) = C_1 + C_2\int\frac{\mathrm{d}t}{a^3} \tag{7.71}$$

where $C_{1,2}$ are integration constants. Since the C_2-mode decays throughout the expansion of the universe, only the constant mode C_1 is relevant at late time. This is simply the well known result that a massless[7] scalar field is frozen on super-Hubble scales. If we now compute the energy-momentum tensor for the PU field we obtain

$$T_{\mu\nu} = \xi g_{\mu\nu}\left(\frac{(\Box\phi)^2}{2} + \partial_\lambda\phi\partial^\lambda\Box\phi\right) - 2\xi\partial_{(\mu}\phi\partial_{\nu)}\Box\phi. \tag{7.72}$$

Thus, it becomes apparent why the PU field can drive an accelerated expansion. At late times, $\Box\phi$ is constant so that we obtain that the above energy-momentum tensor is simply

$$T_{\mu\nu} = \frac{\xi}{2}\left(\Box\phi\right)^2 g_{\mu\nu}\,. \tag{7.73}$$

This is the form of the energy-momentum tensor of a cosmological constant with the value $\Lambda = 4\pi G\xi(\Box\phi)^2$. Notice that we must have $\xi > 0$ for the effective cosmological

[7] More precisely, a scalar field with a mass much smaller than the Hubble expansion rate.

constant to be positive. This is also what one would expect since, if $\Box\phi$ is constant, it contributes as a cosmological constant in the action. This result is in agreement with Ref. [193] where the cosmology of a theory whose action is a general function of the D'Alembertian of a scalar field is explored and it is found that de Sitter is an attractor for this type of theories. This is also expected from the results of Refs. [175, 176, 177, 178], where the symmetry breaking term $(\nabla_\mu A^\mu)^2$ gives rise to the appearance of an effective cosmological constant on super-Hubble scales. This relates to our result here because our PU field plays the role of the additional degree of freedom introduced by the symmetry breaking term there.

Since the field $\Box\phi$ behaves like a massless scalar field, the primordial power spectrum generated from its quantum fluctuations during a de Sitter inflationary phase will be the usual scale invariant one given by[8] $P_{\Box\phi} \simeq H_I^4$ where H_I is the constant Hubble parameter during inflation. Of course, in a more realistic quasi de Sitter inflationary phase, we expect a slightly tilted power spectrum with spectral index proportional to the slow roll parameters. However, the de Sitter expression will suffice for our purpose.

Interestingly, the scale of the effective cosmological constant is set by the scale of inflation $M_p^2\Lambda \simeq (\Box\phi)^2 \simeq H_I^4 \simeq (M_I^2/M_p)^4$, with M_I and M_p the inflationary and Planck scales respectively and we have used the Friedmann equation to relate H_I with M_I. Since we know that $\Lambda \simeq H_0^2$ where H_0 denotes the Hubble parameter today, we obtain $M_I^4 \simeq H_0 M_p^3$. If we use the corresponding values for H_0 and M_p we find $M_I \simeq 1$TeV, i.e., the electroweak scale. This is the result that was also found in Ref. [175, 176, 177, 178] where the role of effective cosmological constant is played by $(\nabla_\mu A^\mu)^2$. Also, in [78] it is shown that quantum fluctuations of a scalar field during inflation can produce dark energy provided its mass is smaller than the Hubble expansion rate today.

This is a general feature of this type of models: If we have an action without any dimensionfull parameter that effectively gives a massless scalar field and whose energy density is constant on super-Hubble scales, then the value of the effective cosmological constant that is generated during an inflationary phase taking place at the electroweak scale coincides with the observed value. However, the scalar field must arise from some non-standard mechanism, since the energy density of a standard scalar field is diluted by the expansion of the universe. In the present case, the effective scalar field is the physical degree of freedom remaining in the degenerate PU model that is associated with the d'Alembertian of the field, while in [175, 176, 177, 178] its role is played by the divergence of the vector field.

[8]The power of H_I^4 appearing here as opposed to the power H_I^2 found for the usual scalar field can be understood from dimensional arguments, but the underlying reason is that ϕ satisfies a fourth order equation so that it has a different normalization. Thus, although $\Box\phi$ satisfies the same equation as a massless scalar field, the power spectrum amplitude is different.

7.5 Conclusions and outlook

In this work we have shown that the degenerate Pais-Uhlenbeck field arises naturally as the Stückelberg field that restores the full $U(1)$ gauge symmetry in the action for a vector field including the usual Maxwell term plus a term $\propto (\partial_\mu A^\mu)^2$. We have seen that, in a given gauge, the Stückelberg field decouples from the vector field and satisfies the equation of motion of the degenerate PU field. Moreover, it determines the value of the longitudinal mode of the vector field so that it can be identified with it. After fixing to the decoupled gauge, we are left with the residual gauge symmetry analogous to the one remaining after imposing the Lorenz condition in standard electromagnetism. For the scalar field, this residual symmetry is an invariance under the addition of an arbitrary harmonic function so that it is a generalized version of the shift or galilean symmetries.

Although we have a fourth order theory, it propagates only one physical degree of freedom, since the second degree of freedom can be removed by the residual symmetry. Also the ghost-like mode that one expects from a fourth order theory can be removed from the physical spectrum by an appropriate gauge choice so that the free Hamiltonian only contains the gauge-invariant and positive energy of the physical degree of freedom. This can be achieved easily in the case of the free field, however, the introduction of interactions could spoil the mechanism by exciting the ghost-like mode. We have shown that if the couplings are introduced in a manner that the PU field acts as the gauge boson associated with a $U(1)$ symmetry, then the excising mechanism is not spoilt, i.e., the selection of the physical Hilbert space is dynamically stable.

We have explicitly worked out two particular cases: coupling to a complex scalar field and to a Dirac fermion. We have seen that in both cases, the equation of motion for the PU field remains unaffected thanks to the current conservation granted by the global $U(1)$ symmetry. This is crucial for the stability of the theory because guarantees that the ghost will not be reintroduced in the theory by the interactions and the quantization procedure remains consistent even in the presence of interactions.

Even though particles that are charged under such a $U(1)$ group are affected by the presence of the PU field, they cannot generate the PU field. One way in which it could be produced is from quantum fluctuations during the inflationary era in the early universe. Once the quantum fluctuations are amplified, the super-Hubble modes contribute as an effective cosmological constant to the energy-momentum tensor whose scale is determined by the scale of inflation. The homogeneous evolution is exactly the same as in standard ΛCDM. However, as the cosmological term is truly the dynamical PU field, it can be perturbed and the evolution of the cosmological perturbations including it will differ from standard ΛCDM. This provides us with a mechanism that can help to discriminate this model from a pure cosmological constant.

Acknowledgement

We would like to thank Antonio L. Maroto for very useful discussions and comments. We also thank Andrei Smilga for useful remarks. This work is supported by the Swiss National Science Foundation. JBJ is supported by the Ministerio de Educación under the postdoctoral contract EX2009-0305 and the Spanish MICINNs Consolider-Ingenio 2010 Programme under grant MultiDark CSD2009-00064 and project number FIS2011-23000.

8

Conclusions and outlook

During my thesis I have been working on different aspects of theoretical and observational relativistic cosmology. All addressed projects were related to the puzzling dark sector which contributes up to 96% of the present matter content of the universe. If Dark Matter seems to have the typical proprieties of non-relativistic particles, we do not have any clue about the nature of Dark Energy. From the theoretical side I have considered different approaches to explain the observed acceleration of the expansion of the universe, while on the observational side I have worked on Large Scale Structure observables, to understand how competitive a model independent analysis can be for future surveys, which will hopefully enlighten us about the nature of the dark sector.

The most conservative idea which has been proposed to explain the (apparent) acceleration of the expansion of the universe is definitively the so-called Back-Reaction. This idea does not require any new physics, but it is based on the fact that the universe is homogeneous on average only. Because Einstein's equations are highly non-linear, they do not commute with the average procedure. Starting from a FLRW metric as a background, and studying the perturbations around it, can be an oversimplification which could lead to a wrong interpretation of the cosmological observations. To study the validity of this idea is fundamental to analyze how inhomogeneities affect light propagation, since most of the observational evidences supporting Dark Energy come from distance-redshift relation measurements. We have considered a toy model, which exhibit unobserved symmetries which allow to solve exactly and fully relativistic the Einstein equations, and linear perturbation theory to compute the vector and tensor contributions to the luminosity distance. In the various cases that we have considered the effects induced by the inhomogeneities on the distance-redshift relation were far too small to explain the observations without assuming Dark Energy. In addition, we start having new evidences supporting Dark Energy, which do not rely on distance-redshift relation.

Even if all the attempts of using Back-Reaction to explain the apparent acceleration of the universe expansion have failed until now, these effects, which are typically on $1-2\%$ level, should be correctly and carefully taken into account in

future precision cosmology analysis. We need to understand how the accuracy of our measurements is affected by stochastic inhomogeneities. In particular, they may play a role in the determination of Dark Energy equation of state, which can discriminate between a cosmological constant and a Dark Energy or Modified Gravity model.

A less conservative approach consists in introducing an additional field which drives the late time acceleration. Many models have been studied in the last decade. Generically they dominate the matter content of the universe in the late time, but they suffer from fine-tuning problems or they exhibit superluminal propagation. In the past it has been shown that a longitudinal vector mode can play the role of an effective cosmological constant whose value is linked with the energy scale of inflation. In our work we have identified this mode with a scalar field described by an higher derivative theory, namely the Pais-Uhlenbeck field. The Pais-Uhlenbeck field has been introduced as a Stückelberg field to recover the $U(1)$ gauge invariance in the action for a massless vector field broken by a non-standard kinetic term. With this motivation we have determined a natural interaction for the Pais-Uhlenbeck field. Interestingly, its dynamics is not affected by the coupling with charged scalars or fermions. This feature assures that the ghost mode (related to the Ostrogradski instability for higher derivative theories) is not reintroduced by the interactions, once we get rid of it in the quantization of the free theory.

At the background level this model behaves like an effective cosmological constant. But at higher order in the perturbative expansion its dynamics can help us to discriminate it from a ΛCDM model. We expect indeed an imprint of the Pais-Uhlenbeck field perturbations on cosmological probes like CMB anisotropies or matter power spectrum $P(k)$. This analysis can be performed with current datasets, constraining the primordial amplitude and the tilt of the Pais-Uhlenbeck perturbations sourced during the inflationary era.

Nowadays in cosmology there are various models which still agree with observations. For many years the accuracy of the cosmological measurements was not enough to sensitively decrease the allowed parameter space. The limited amount of data required a model dependent analysis to extract some useful information. In the last years, with the successful CMB anisotropy experiments, we are entering in the so-called precision cosmology era, where we aim to reach a precision within the percent level. Future missions will be focused on observing Large Scale Structures. The galaxy distribution contains a wealthy information about the dark side of the universe. But to reveal the nature of the dark universe we need to face different problems, like the non-linear effects of structure formation or the galaxy bias. Moreover to reach the required precision we should consider new effects that could be neglected in previous surveys. The amount of data from future surveys will allow us to proceed in a model independent way. In this framework we have developed a numerical code CLASSgal which, accurately and efficiently, computes the Large Scale Structures observables including all the relativistic effects at linear order in pertur-

bation theory. We have then shown that an analysis based on observable quantities, namely the galaxy number counts, is competitive with respect to the traditional model dependent 3-dimensional analysis based on the matter power spectrum $P(k)$. We have also analyzed the amplitude of the effects that are neglected in the traditional analysis, finding that for deep redshift surveys the lensing contribution may become important. This opens the opportunity of measuring the lensing potential directly in galaxy surveys.

Our work was based on Fisher matrix analysis adopting a sharp cutoff for non-linear scales. So, in this perspective, a more realistic analysis based on Monte Carlo Markov Chain with mock data should be performed. It is also important to quantify the theoretical error induced by middle non-linear scales. Then, we need to quantify the impact on cosmological parameter estimation of the terms which are neglected in the usual analysis. They may induce a bias limiting the accuracy of the parameter estimation. In particular we have shown that the lensing contribution is not negligible. This means that future surveys will have the possibility to discriminate between General Relativity and theories of Modified Gravity which usually predict a different lensing potential. We are also interested in going to higher order correlation functions, like the 3-point function and the related bispectrum. Since at linear level a non-vanishing bispectrum requires non-gaussian perturbations, we can determine with which accuracy Large Scale Structure observables can constrain the primordial non-gaussianity. On the other hand CMB anisotropy experiments allow only for small deviations from gaussian initial conditions. In this case, to compute the 3-point function we need to re-derive the predicted galaxy number counts at least at second order in perturbation theory.

Cosmology is entering in a new era. Future large scale surveys will provide a wealthy amount of data challenging cosmologists to develop new approaches and tools to really profit of it. In the next decades we will have the opportunity of revealing the nature of the dark sector which contributes up to the 96% of the of the present matter content of the universe. Any discovery that will help physicists to understand the nature of Dark Energy and Dark Matter will be considered a milestone in the history and will lead us to a new physics, with new and deeper puzzling questions.

Bibliography

[1] F. Zwicky, *Die Rotverschiebung von extragalaktischen Nebeln*, Helvetica Physica Acta **6** (1933) 110–127.

[2] **Supernova Search Team** Collaboration, A. G. Riess et al., *Observational evidence from supernovae for an accelerating universe and a cosmological constant*, Astron.J. **116** (1998) 1009–1038, [astro-ph/9805201].

[3] **Supernova Search Team** Collaboration, B. P. Schmidt et al., *The High Z supernova search: Measuring cosmic deceleration and global curvature of the universe using type Ia supernovae*, Astrophys.J. **507** (1998) 46–63, [astro-ph/9805200].

[4] **Supernova Cosmology Project** Collaboration, S. Perlmutter et al., *Measurements of Omega and Lambda from 42 high redshift supernovae*, Astrophys.J. **517** (1999) 565–586, [astro-ph/9812133].

[5] E. Di Dio, M. Vonlanthen, and R. Durrer, *Back Reaction from Walls*, JCAP **1202** (2012) 036, [arXiv:1111.5764].

[6] J. Adamek, E. Di Dio, R. Durrer, and M. Kunz, *Distance-redshift relation in plane symmetric universes*, Phys.Rev. **D89** (2014) 063543, [arXiv:1401.3634].

[7] J. Adamek, D. Daverio, R. Durrer, and M. Kunz, *General Relativistic N-body simulations in the weak field limit*, Phys.Rev. **D88** (2013) 103527, [arXiv:1308.6524].

[8] L. Hui and P. B. Greene, *Correlated Fluctuations in Luminosity Distance and the (Surprising) Importance of Peculiar Motion in Supernova Surveys*, Phys.Rev. **D73** (2006) 123526, [astro-ph/0512159].

[9] C. Bonvin, R. Durrer, and M. A. Gasparini, *Fluctuations of the luminosity distance*, Phys.Rev. **D73** (2006) 023523, [astro-ph/0511183].

[10] C. Bonvin, R. Durrer, and M. Kunz, *The dipole of the luminosity distance: a direct measure of h(z)*, Phys.Rev.Lett. **96** (2006) 191302, [astro-ph/0603240].

[11] I. Ben-Dayan, M. Gasperini, G. Marozzi, F. Nugier, and G. Veneziano, *Backreaction on the luminosity-redshift relation from gauge invariant light-cone averaging*, JCAP **1204** (2012) 036, [arXiv:1202.1247].

[12] E. Di Dio and R. Durrer, *Vector and Tensor Contributions to the Luminosity Distance*, Phys.Rev. **D86** (2012) 023510, [arXiv:1205.3366].

[13] I. Ben-Dayan, G. Marozzi, F. Nugier, and G. Veneziano, *The second-order luminosity-redshift relation in a generic inhomogeneous cosmology*, JCAP **1211** (2012) 045, [arXiv:1209.4326].

[14] O. Umeh, C. Clarkson, and R. Maartens, *Nonlinear relativistic corrections to cosmological distances, redshift and gravitational lensing magnification. II - Derivation*, arXiv:1402.1933.

[15] J. B. Jimenez, E. Di Dio, and R. Durrer, *A longitudinal gauge degree of freedom and the Pais Uhlenbeck field*, JHEP **1304** (2013) 030, [arXiv:1211.0441].

[16] A. Pais and G. Uhlenbeck, *On Field theories with nonlocalized action*, Phys.Rev. **79** (1950) 145–165.

[17] C. Bonvin and R. Durrer, *What galaxy surveys really measure*, Phys.Rev. **D84** (2011) 063505, [arXiv:1105.5280].

[18] A. Challinor and A. Lewis, *The linear power spectrum of observed source number counts*, Phys.Rev. **D84** (2011) 043516, [arXiv:1105.5292].

[19] E. Di Dio, F. Montanari, J. Lesgourgues, and R. Durrer, *The CLASSgal code for Relativistic Cosmological Large Scale Structure*, JCAP **1311** (2013) 044, [arXiv:1307.1459].

[20] D. Blas, J. Lesgourgues, and T. Tram, *The Cosmic Linear Anisotropy Solving System (CLASS) II: Approximation schemes*, JCAP **1107** (2011) 034, [arXiv:1104.2933].

[21] A. Einstein, *Die grundlage der allgemeinen relativitätstheorie*, Annalen der Physik **354** (1916), no. 7 769–822.

[22] E. P. Hubble, *A spiral nebula as a stellar system, Messier 31.*, Astrophysical Journal **69** (Mar., 1929) 103–158.

[23] A. Einstein, *Kosmologische Betrachtungen zur allgemeinen Relativitätstheorie*, Sitzungsberichte der Königlich Preußischen Akademie der Wissenschaften (Berlin), Seite 142-152. (1917) 142–152.

[24] W. de Sitter, *Einstein's theory of gravitation and its astronomical consequences. Third paper*, Mon.Not.Roy.Astron.Soc. **78** (Nov., 1917) 3–28.

[25] A. Friedmann, *Über die Krümmung des Raumes*, Zeitschrift fur Physik **10** (1922) 377–386.

[26] G. Lemaître, *Un Univers homogène de masse constante et de rayon croissant rendant compte de la vitesse radiale des nébuleuses extra-galactiques*, Annales de la Societe Scietifique de Bruxelles **47** (1927) 49–59.

[27] V. M. Slipher, *The radial velocity of the Andromeda Nebula*, Lowell Observatory Bulletin **2** (1913) 56–57.

[28] C. Wirtz, *Einiges zur Statistik der Radialbewegungen von Spiralnebeln und Kugelsternhaufen*, Astronomische Nachrichten **215** (Apr., 1922) 349.

[29] C. Wirtz, *De Sitters Kosmologie und die Radialbewegungen der Spiralnebel*, Astronomische Nachrichten **222** (July, 1924) 21.

[30] G. Stromberg, *Analysis of radial velocities of globular clusters and non-galactic nebulae.*, Astrophysical Journal **61** (June, 1925) 353–362.

[31] E. P. Hubble, *Extragalactic nebulae.*, Astrophysical Journal **64** (Dec., 1926) 321–369.

[32] H. Nussbaumer and L. Bieri, Discovering the Expanding Universe. Cambridge University Press, Cambridge, U.K., 2009.

[33] E. Hubble, *A Relation between Distance and Radial Velocity among Extra-Galactic Nebulae*, Proceedings of the National Academy of Science **15** (Mar., 1929) 168–173.

[34] A. Einstein and W. de Sitter, *On the Relation between the Expansion and the Mean Density of the Universe*, Contributions from the Mount Wilson Observatory, vol. 3, pp.51-52 **3** (1932) 51–52.

[35] F. Zwicky, *On the Masses of Nebulae and of Clusters of Nebulae*, Astrophysical Journal, **86** (Oct., 1937) 217.

[36] M. Milgrom, *A modification of the Newtonian dynamics as a possible alternative to the hidden mass hypothesis*, Astrophysical Journal **270** (July, 1983) 365–370.

[37] M. Milgrom, *A modification of the Newtonian dynamics - Implications for galaxies*, Astrophysical Journal **270** (July, 1983) 371–389.

[38] J. D. Bekenstein, *Relativistic gravitation theory for the MOND paradigm*, Phys.Rev. **D70** (2004) 083509, [astro-ph/0403694].

[39] V. C. Rubin, W. K. J. Ford, and N. . Thonnard, *Rotational properties of 21 SC galaxies with a large range of luminosities and radii, from NGC 4605 (R = 4kpc) to UGC 2885 (R = 122 kpc)*, Astrophysical Journal **238** (June, 1980) 471–487.

[40] **BICEP2 Collaboration** Collaboration, P. Ade et al., *Detection of B-Mode Polarization at Degree Angular Scales by BICEP2*, Phys.Rev.Lett. **112** (2014) 241101, [arXiv:1403.3985].

[41] E. Di Dio, F. Montanari, R. Durrer, and J. Lesgourgues, *Cosmological Parameter Estimation with Large Scale Structure Observations*, JCAP **1401** (2014) 042, [arXiv:1308.6186].

[42] **SDSS Collaboration** Collaboration, D. J. Eisenstein et al., *Detection of the baryon acoustic peak in the large-scale correlation function of SDSS luminous red galaxies*, Astrophys.J. **633** (2005) 560–574, [astro-ph/0501171].

[43] M. M. Phillips, *The absolute magnitudes of Type IA supernovae*, Astrophysical Journal Letters **413** (Aug., 1993) L105–L108.

[44] I. M. H. Etherington, *On the Definition of Distance in General Relativity.*, Philosophical Magazine **15** (1933) 761.

[45] B. A. Bassett and M. Kunz, *Cosmic distance-duality as a probe of exotic physics and acceleration*, Phys.Rev. **D69** (2004) 101305, [astro-ph/0312443].

[46] P. Bull and T. Clifton, *Local and non-local measures of acceleration in cosmology*, Phys.Rev. **D85** (2012) 103512, [arXiv:1203.4479].

[47] R. Durrer, *What do we really know about Dark Energy?*, Phil.Trans.Roy.Soc.Lond. **A369** (2011) 5102–5114, [arXiv:1103.5331].

[48] C. Blake, K. Glazebrook, T. Davis, S. Brough, M. Colless, et al., *The WiggleZ Dark Energy Survey: measuring the cosmic expansion history using the Alcock-Paczynski test and distant supernovae*, Mon.Not.Roy.Astron.Soc. **418** (2011) 1725–1735, [arXiv:1108.2637].

[49] J. E. P. Schneider and E. Falco, Gravitational lenses. Springer Verlag, 1992.

[50] N. Straumann, General relativity with applications to astrophysics. Springer Verlag, 2004.

[51] N. Mustapha, B. Bassett, C. Hellaby, and G. Ellis, *Shrinking 2. The Distortion of the area distance redshift relation in inhomogeneous isotropic universes*, Class.Quant.Grav. **15** (1998) 2363–2379, [gr-qc/9708043].

[52] **Planck Collaboration** Collaboration, P. Ade et al., *Planck 2013 results. XVI. Cosmological parameters*, arXiv:1303.5076.

[53] R. Durrer, The Cosmic Microwave Background. Cambridge University Press, 2008.

[54] U. Seljak and M. Zaldarriaga, *A Line of sight integration approach to cosmic microwave background anisotropies*, Astrophys.J. **469** (1996) 437–444, [astro-ph/9603033].

[55] A. Lewis, A. Challinor, and A. Lasenby, *Efficient computation of CMB anisotropies in closed FRW models*, Astrophys.J. **538** (2000) 473–476, [astro-ph/9911177].

[56] M. Doran, *CMBEASY: an object oriented code for the cosmic microwave background*, JCAP **0510** (2005) 011, [astro-ph/0302138].

[57] F. Bernardeau, S. Colombi, E. Gaztanaga, and R. Scoccimarro, *Large scale structure of the universe and cosmological perturbation theory*, Phys.Rept. **367** (2002) 1–248, [astro-ph/0112551].

[58] M. Crocce and R. Scoccimarro, *Renormalized cosmological perturbation theory*, Phys.Rev. **D73** (2006) 063519, [astro-ph/0509418].

[59] M. Pietroni, *Flowing with Time: a New Approach to Nonlinear Cosmological Perturbations*, JCAP **0810** (2008) 036, [arXiv:0806.0971].

[60] J. J. M. Carrasco, M. P. Hertzberg, and L. Senatore, *The Effective Field Theory of Cosmological Large Scale Structures*, JHEP **1209** (2012) 082, [arXiv:1206.2926].

[61] N. Kaiser, *Clustering in real space and in redshift space*, Mon.Not.Roy.Astron.Soc. **227** (1987) 1–27.

[62] C. Bonvin, L. Hui, and E. Gaztanaga, *Asymmetric galaxy correlation functions*, Phys.Rev. **D89** (2014) 083535, [arXiv:1309.1321].

[63] J. Asorey, M. Crocce, E. Gaztanaga, and A. Lewis, *Recovering 3D clustering information with angular correlations*, arXiv:1207.6487.

[64] A. Albrecht, G. Bernstein, R. Cahn, W. L. Freedman, J. Hewitt, et al., *Report of the Dark Energy Task Force*, astro-ph/0609591.

[65] I. Zlatev, L.-M. Wang, and P. J. Steinhardt, *Quintessence, cosmic coincidence, and the cosmological constant*, Phys.Rev.Lett. **82** (1999) 896–899, [astro-ph/9807002].

[66] C. Armendariz-Picon, V. F. Mukhanov, and P. J. Steinhardt, *Essentials of k essence*, Phys.Rev. **D63** (2001) 103510, [astro-ph/0006373].

[67] C. Bonvin, C. Caprini, and R. Durrer, *A no-go theorem for k-essence dark energy*, Phys.Rev.Lett. **97** (2006) 081303, [astro-ph/0606584].

[68] T. P. Sotiriou and V. Faraoni, *f(R) Theories Of Gravity*, Rev.Mod.Phys. **82** (2010) 451–497, [arXiv:0805.1726].

[69] A. De Felice and S. Tsujikawa, *f(R) theories*, Living Rev.Rel. **13** (2010) 3, [arXiv:1002.4928].

[70] A. Nicolis, R. Rattazzi, and E. Trincherini, *The Galileon as a local modification of gravity*, Phys.Rev. **D79** (2009) 064036, [arXiv:0811.2197].

[71] C. de Rham and L. Heisenberg, *Cosmology of the Galileon from Massive Gravity*, Phys.Rev. **D84** (2011) 043503, [arXiv:1106.3312].

[72] C. de Rham and A. J. Tolley, *DBI and the Galileon reunited*, JCAP **1005** (2010) 015, [arXiv:1003.5917].

[73] C. Burrage, C. de Rham, and L. Heisenberg, *de Sitter Galileon*, JCAP **1105** (2011) 025, [arXiv:1104.0155].

[74] M. Ostrogradsky, *Mémoire sur les équations différentielles relatives aux problèmes des isopérimètres*, Mem. Ac. St. Petersburg **6** (1850) 385.

[75] R. P. Woodard, *Avoiding dark energy with 1/r modifications of gravity*, Lect.Notes Phys. **720** (2007) 403–433, [astro-ph/0601672].

[76] K. S. Stelle, *Renormalization of higher-derivative quantum gravity*, Phys. Rev. D **16** (Aug, 1977) 953–969.

[77] A. Salam and J. Strathdee, *Remarks on high-energy stability and renormalizability of gravity theory*, Phys. Rev. D **18** (Dec, 1978) 4480–4485.

[78] C. Ringeval, T. Suyama, T. Takahashi, M. Yamaguchi, and S. Yokoyama, *Dark energy from primordial inflationary quantum fluctuations*, Phys.Rev.Lett. **105** (2010) 121301, [arXiv:1006.0368].

[79] R. Amanullah, C. Lidman, D. Rubin, G. Aldering, P. Astier, et al., *Spectra and Light Curves of Six Type Ia Supernovae at 0.511 lt z lt 1.12 and the Union2 Compilation*, Astrophys.J. **716** (2010) 712–738, [arXiv:1004.1711].

[80] **SNLS Collaboration** Collaboration, J. Guy et al., *The Supernova Legacy Survey 3-year sample: Type Ia Supernovae photometric distances and cosmological constraints*, Astron.Astrophys. **523** (2010) A7, [arXiv:1010.4743].

[81] T. Holsclaw, U. Alam, B. Sanso, H. Lee, K. Heitmann, et al., *Nonparametric Dark Energy Reconstruction from Supernova Data*, Phys.Rev.Lett. **105** (2010) 241302, [arXiv:1011.3079].

[82] N. Suzuki, D. Rubin, C. Lidman, G. Aldering, R. Amanullah, et al., *The Hubble Space Telescope Cluster Supernova Survey: V. Improving the Dark Energy Constraints Above zgt1 and Building an Early-Type-Hosted Supernova Sample*, Astrophys.J. **746** (2012) 85, [arXiv:1105.3470].

[83] J. Dunkley, R. Hlozek, J. Sievers, V. Acquaviva, P. Ade, et al., *The Atacama Cosmology Telescope: Cosmological Parameters from the 2008 Power Spectra*, Astrophys.J. **739** (2011) 52, [arXiv:1009.0866].

[84] C. Vale and . White, Martin J., *Simulating weak lensing by large scale structure*, Astrophys.J. **592** (2003) 699–709, [astro-ph/0303555].

[85] K. Kainulainen and V. Marra, *Accurate Modeling of Weak Lensing with the sGL Method*, Phys.Rev. **D83** (2011) 023009, [arXiv:1011.0732].

[86] S. Rasanen, *Backreaction: directions of progress*, Class.Quant.Grav. **28** (2011) 164008, [arXiv:1102.0408].

[87] G. Lemaitre, *The expanding universe*, Gen.Rel.Grav. **29** (1997) 641–680.

[88] R. C. Tolman, *Effect of imhomogeneity on cosmological models*, Proc.Nat.Acad.Sci. **20** (1934) 169–176.

[89] K. Bolejko, M.-N. Celerier, and A. Krasinski, *Inhomogeneous cosmological models: Exact solutions and their applications*, Class.Quant.Grav. **28** (2011) 164002, [arXiv:1102.1449].

[90] V. Marra and A. Notari, *Observational constraints on inhomogeneous cosmological models without dark energy*, Class.Quant.Grav. **28** (2011) 164004, [arXiv:1102.1015].

[91] P. Szekeres, *A Class of Inhomogeneous Cosmological Models*, Commun.Math.Phys. **41** (1975) 55.

[92] A. Krasinski and K. Bolejko, *Redshift propagation equations in the $\beta' \neq 0$ Szekeres models*, Phys.Rev. **D83** (2011) 083503, [arXiv:1007.2083].

[93] N. Meures and M. Bruni, *Redshift and distances in a ΛCDM cosmology with non-linear inhomogeneities*, Mon.Not.Roy.Astron.Soc. **419** (2012) 1937, [arXiv:1107.4433].

[94] H. Collins, *The influence of inhomogeneities on the large-scale expansion of the universe*, arXiv:1011.2046.

[95] A. Zakharov, *Nonlinear plane-symmetric perturbations of a spatial-plane friedman universe filled with an ideal dust*, Soviet Physics Journal **30** (1987) 1015–1019.

[96] J. Plebanski and A. Krasinski, An Introduction to General Relativity and Cosmology. Cambridge University Press, 2006.

[97] C.-M. Yoo, T. Kai, and K.-i. Nakao, *Solving Inverse Problem with Inhomogeneous Universe*, Prog.Theor.Phys. **120** (2008) 937–960, [arXiv:0807.0932].

[98] **WMAP Collaboration** Collaboration, E. Komatsu et al., *Seven-Year Wilkinson Microwave Anisotropy Probe (WMAP) Observations: Cosmological Interpretation*, Astrophys.J.Suppl. **192** (2011) 18, [arXiv:1001.4538].

[99] H. El-Ad and T. Piran, *Voids in the large scale structure*, Astrophys.J. **491** (1997) 421, [astro-ph/9702135].

[100] S. Seitz, P. Schneider, and J. Ehlers, *Light propagation in arbitrary space-times and the gravitational lens approximation*, Class.Quant.Grav. **11** (1994) 2345–2374, [astro-ph/9403056].

[101] V. Marra, E. W. Kolb, S. Matarrese, and A. Riotto, *On cosmological observables in a swiss-cheese universe*, Phys.Rev. **D76** (2007) 123004, [arXiv:0708.3622].

[102] P. Bull, T. Clifton, and P. G. Ferreira, *The kSZ effect as a test of general radial inhomogeneity in LTB cosmology*, Phys.Rev. **D85** (2012) 024002, [arXiv:1108.2222].

[103] C.-M. Yoo, T. Kai, and K.-i. Nakao, *Redshift Drift in LTB Void Universes*, Phys.Rev. **D83** (2011) 043527, [arXiv:1010.0091].

[104] V. Perlick, *Gravitational lensing from a spacetime perspective*, Living Rev.Rel. **7** (2004) 9.

[105] **EUCLID Collaboration** Collaboration, R. Laureijs et al., *Euclid Definition Study Report*, arXiv:1110.3193.

[106] F. Montanari and R. Durrer, *A new method for the Alcock-Paczynski test*, Phys.Rev. **D86** (2012) 063503, [arXiv:1206.3545].

[107] R. Durrer and R. Maartens, *Dark Energy and Dark Gravity*, Gen.Rel.Grav. **40** (2008) 301–328, [arXiv:0711.0077].

[108] P. Szekeres, *Quasispherical Gravitational Collapse*, Phys.Rev. **D12** (1975) 2941.

[109] S. R. Green and R. M. Wald, *Newtonian and Relativistic Cosmologies*, Phys.Rev. **D85** (2012) 063512, [arXiv:1111.2997].

[110] N. E. Chisari and M. Zaldarriaga, *Connection between Newtonian simulations and general relativity*, Phys.Rev. **D83** (2011) 123505, [arXiv:1101.3555].

[111] W. Israel, *Singular hypersurfaces and thin shells in general relativity*, Nuovo Cim. **B44S10** (1966) 1.

[112] K. Enqvist, *Lemaitre-Tolman-Bondi model and accelerating expansion*, Gen.Rel.Grav. **40** (2008) 451–466, [arXiv:0709.2044].

[113] E. Di Dio, *Light propagation in an arbitrary space-time*, Master's thesis, ETHZ, 2010.

[114] T. H.-C. Lu, K. Ananda, and C. Clarkson, *Vector modes generated by primordial density fluctuations*, Phys.Rev. **D77** (2008) 043523, [arXiv:0709.1619].

[115] K. N. Ananda, C. Clarkson, and D. Wands, *The Cosmological gravitational wave background from primordial density perturbations*, Phys.Rev. **D75** (2007) 123518, [gr-qc/0612013].

[116] E. Di Dio and R. Durrer, "in preparation.".

[117] F. Schmidt and D. Jeong, *Cosmic Rulers*, Phys.Rev. **D86** (2012) 083527, [arXiv:1204.3625].

[118] D. Jeong and F. Schmidt, *Large-Scale Structure with Gravitational Waves I: Galaxy Clustering*, Phys.Rev. **D86** (2012) 083512, [arXiv:1205.1512].

[119] G. Ellis, B. Bassett, and P. Dunsby, *Lensing and caustic effects on cosmological distances*, Class.Quant.Grav. **15** (1998) 2345–2361, [gr-qc/9801092].

[120] R. Durrer, *Gauge invariant cosmological perturbation theory: A General study and its application to the texture scenario of structure formation*, Fund.Cosmic Phys. **15** (1994) 209, [astro-ph/9311041].

[121] R. Durrer and T. Kahniashvili, *CMB anisotropies caused by gravitational waves: A Parameter study*, Helv.Phys.Acta **71** (1998) 445–457, [astro-ph/9702226].

[122] D. Larson, J. Dunkley, G. Hinshaw, E. Komatsu, M. Nolta, et al., *Seven-Year Wilkinson Microwave Anisotropy Probe (WMAP) Observations: Power Spectra and WMAP-Derived Parameters*, Astrophys.J.Suppl. **192** (2011) 16, [arXiv:1001.4635].

[123] M. Abramowitz and I. Stegun, Handbook of Mathematical Functions. Dover Publications, New York, 9th printing ed., 1970.

[124] M. LoVerde and N. Afshordi, *Extended Limber Approximation*, Phys.Rev. **D78** (2008) 123506, [arXiv:0809.5112].

[125] **Planck Collaboration** Collaboration, P. Ade et al., *Planck 2013 results. I. Overview of products and scientific results*, arXiv:1303.5062.

[126] J. Beltran Jimenez and R. Durrer, *Effects of biasing on the matter power spectrum at large scales*, Phys.Rev. **D83** (2011) 103509, [arXiv:1006.2343].

[127] J. Lesgourgues, *The Cosmic Linear Anisotropy Solving System (CLASS) I: Overview*, arXiv:1104.2932.

[128] J. Yoo, A. L. Fitzpatrick, and M. Zaldarriaga, *A New Perspective on Galaxy Clustering as a Cosmological Probe: General Relativistic Effects*, Phys.Rev. **D80** (2009) 083514, [arXiv:0907.0707].

[129] J. Yoo, *General Relativistic Description of the Observed Galaxy Power Spectrum: Do We Understand What We Measure?*, Phys.Rev. **D82** (2010) 083508, [arXiv:1009.3021].

[130] D. Bertacca, R. Maartens, A. Raccanelli, and C. Clarkson, *Beyond the plane-parallel and Newtonian approach: Wide-angle redshift distortions and convergence in general relativity*, JCAP **1210** (2012) 025, [arXiv:1205.5221].

[131] A. Hamilton, *Measuring Omega and the real correlation function from the redshift correlation function*, Astrophys.J. **385** (1992) L5–L8.

[132] A. Raccanelli, L. Samushia, and W. J. Percival, *Simulating Redshift-Space Distortions for Galaxy Pairs with Wide Angular Separation*, arXiv:1006.1652.

[133] M. Lima, B. Jain, M. Devlin, and J. Aguirre, *Submillimeter Galaxy Number Counts and Magnification by Galaxy Clusters*, Astrophys.J. **717** (2010) L31, [arXiv:1004.4889].

[134] Y. D. Hezaveh and G. P. Holder, *Effects of Strong Gravitational Lensing on Millimeter-Wave Galaxy Number Counts*, Astrophys.J. **734** (2011) 52, [arXiv:1010.0998].

[135] E. Zucca, O. Ilbert, S. Bardelli, L. Tresse, G. Zamorani, et al., *The VIMOS VLT Deep Survey - Evolution of the luminosity functions by galaxy type up to z=1.5 from first epoch data*, Astron.Astrophys. (2005) [astro-ph/0506393].

[136] Y. Peng, S. Lilly, K. Kovac, M. Bolzonella, L. Pozzetti, et al., *Mass and environment as drivers of galaxy evolution in SDSS and zCOSMOS and the origin of the Schechter function*, Astrophys.J. **721** (2010) 193–221, [arXiv:1003.4747].

[137] T. Baldauf, U. Seljak, L. Senatore, and M. Zaldarriaga, *Galaxy Bias and non-Linear Structure Formation in General Relativity*, JCAP **1110** (2011) 031, [arXiv:1106.5507].

[138] P. McDonald and U. Seljak, *How to measure redshift-space distortions without sample variance*, JCAP **0910** (2009) 007, [arXiv:0810.0323].

[139] M. Crocce, A. Cabre, and E. Gaztanaga, *Modeling the angular correlation function and its full covariance in Photometric Galaxy Surveys*, Mon.Not.Roy.Astron.Soc. **414** (2011) 329–349, [arXiv:1004.4640].

[140] M. Tegmark, *Measuring cosmological parameters with galaxy surveys*, Phys.Rev.Lett. **79** (1997) 3806–3809, [astro-ph/9706198].

[141] J. Lesgourgues, *The Cosmic Linear Anisotropy Solving System (CLASS) III: Comparision with CAMB for LambdaCDM*, arXiv:1104.2934.

[142] C.-P. Ma and E. Bertschinger, *Cosmological perturbation theory in the synchronous and conformal Newtonian gauges*, Astrophys.J. **455** (1995) 7–25, [astro-ph/9506072].

[143] T. Tram and J. Lesgourgues, *Optimal polarisation equations in FLRW universes*, JCAP **1310** (2013) 002, [arXiv:1305.3261].

[144] D. Jeong, F. Schmidt, and C. M. Hirata, *Large-scale clustering of galaxies in general relativity*, Phys.Rev. **D85** (2012) 023504, [arXiv:1107.5427].

[145] D. Jeong and F. Schmidt, *Cosmic Clocks*, Phys.Rev. **D89** (2014) 043519, [arXiv:1305.1299].

[146] B. A. Reid, L. Samushia, M. White, W. J. Percival, M. Manera, et al., *The clustering of galaxies in the SDSS-III Baryon Oscillation Spectroscopic Survey: measurements of the growth of structure and expansion rate at z=0.57 from anisotropic clustering*, arXiv:1203.6641.

[147] S. Nuza, A. Sanchez, F. Prada, A. Klypin, D. Schlegel, et al., *The clustering of galaxies at z 0.5 in the SDSS-III Data Release 9 BOSS-CMASS sample: a test for the LCDM cosmology*, Mon.Not.Roy.Astron.Soc. **432** (2013) 743–760, [arXiv:1202.6057].

[148] L. Anderson, E. Aubourg, S. Bailey, F. Beutler, A. S. Bolton, et al., *The clustering of galaxies in the SDSS-III Baryon Oscillation Spectroscopic Survey: Measuring D_A and H at z=0.57 from the Baryon Acoustic Peak in the Data Release 9 Spectroscopic Galaxy Sample*, arXiv:1303.4666.

[149] C. Carbone, O. Mena, and L. Verde, *Cosmological Parameters Degeneracies and Non-Gaussian Halo Bias*, JCAP **1007** (2010) 020, [arXiv:1003.0456].

[150] V. Desjacques, *Local bias approach to the clustering of discrete density peaks*, Phys.Rev. **D87** (2013), no. 4 043505, [arXiv:1211.4128].

[151] B. Audren, J. Lesgourgues, S. Bird, M. G. Haehnelt, and M. Viel, *Neutrino masses and cosmological parameters from a Euclid-like survey: Markov Chain Monte Carlo forecasts including theoretical errors*, JCAP **1301** (2013) 026, [arXiv:1210.2194].

[152] J. Asorey, M. Crocce, and E. Gaztanaga, *Redshift-space distortions from the cross-correlation of photometric populations*, arXiv:1305.0934.

[153] N. P. Ross, J. da Angela, T. Shanks, D. A. Wake, R. D. Cannon, et al., *The 2dF-SDSS LRG and QSO Survey: The 2-Point Correlation Function and Redshift-Space Distortions*, Mon.Not.Roy.Astron.Soc. **381** (2007) 573–588, [astro-ph/0612400].

[154] **WiggleZ Collaboration** Collaboration, C. Contreras et al., *The WiggleZ Dark Energy Survey: measuring the cosmic growth rate with the two-point galaxy correlation function*, Mon.Not.Roy.Astron.Soc. **430** (Aprile, 2013) 924–933, [arXiv:1302.5178].

[155] S. de la Torre, L. Guzzo, J. Peacock, E. Branchini, A. Iovino, et al., *The VIMOS Public Extragalactic Redshift Survey (VIPERS). Galaxy clustering and redshift-space distortions at z=0.8 in the first data release*, arXiv:1303.2622.

[156] S. Asaba, C. Hikage, K. Koyama, G.-B. Zhao, A. Hojjati, et al., *Principal Component Analysis of Modified Gravity using Weak Lensing and Peculiar Velocity Measurements*, JCAP **1308** (2013) 029, [arXiv:1306.2546].

[157] I. D. Saltas and M. Kunz, *Anisotropic stress and stability in modified gravity models*, Phys.Rev. **D83** (2011) 064042, [arXiv:1012.3171].

[158] C. Blake, T. Mauch, and E. M. Sadler, *Angular clustering in the SUMSS radio survey*, Mon.Not.Roy.Astron.Soc. **347** (2004) 787, [astro-ph/0310115].

[159] M. Negrello, F. Perrotta, J. G.-N. Gonzalez, L. Silva, G. De Zotti, et al., *Astrophysical and Cosmological Information from Large-scale sub-mm Surveys of Extragalactic Sources*, Mon.Not.Roy.Astron.Soc. **377** (2007) 1557–1568, [astro-ph/0703210].

[160] R. Subrahmanyan, R. Ekers, L. Saripalli, and E. Sadler, *A deep survey of the low-surface-brightness radio sky*, PoS **MRU** (2007) 055, [arXiv:0802.0053].

[161] S. D. Landy and A. S. Szalay, *Bias and variance of angular correlation functions*, Astrophys.J. **412** (1993) 64.

[162] L. Verde, *Statistical methods in cosmology*, Lect.Notes Phys. **800** (2010) 147–177, [arXiv:0911.3105].

[163] W. V. W.H. Press, S.A. Teukolsky and B. Flannery, Numerical Recipes 3rd Edition: The Art of Scientific Computing. Cambridge University Press, Cambridge U.K., 2007.

[164] **Planck Collaboration** Collaboration, P. Ade et al., *Planck 2013 results. XXII. Constraints on inflation*, arXiv:1303.5082.

[165] A. Boyarsky, J. Lesgourgues, O. Ruchayskiy, and M. Viel, *Lyman-alpha constraints on warm and on warm-plus-cold dark matter models*, JCAP **0905** (2009) 012, [arXiv:0812.0010].

[166] B. Audren, D. Blas, J. Lesgourgues, and S. Sibiryakov, *Cosmological constraints on Lorentz violating dark energy*, JCAP **1308** (2013) 039, [arXiv:1305.0009].

[167] H.-J. Seo and D. J. Eisenstein, *Probing dark energy with baryonic acoustic oscillations from future large galaxy redshift surveys*, Astrophys.J. **598** (2003) 720–740, [astro-ph/0307460].

[168] G. M. J. Lesgourgues, G. Mangano and S. Pastor, Neutrino Cosmology. Cambridge University Press, Cambridge U.K., 2013.

[169] **Supernova Cosmology Project** Collaboration, S. Perlmutter et al., *Discovery of a supernova explosion at half the age of the Universe and its cosmological implications*, Nature **391** (1998) 51–54, [astro-ph/9712212].

[170] J. Martin, *Everything You Always Wanted To Know About The Cosmological Constant Problem (But Were Afraid To Ask)*, Comptes Rendus Physique **13** (2012) 566–665, [arXiv:1205.3365].

[171] E. J. Copeland, M. Sami, and S. Tsujikawa, *Dynamics of dark energy*, Int.J.Mod.Phys. **D15** (2006) 1753–1936, [hep-th/0603057].

[172] S. Nojiri and S. D. Odintsov, *Introduction to modified gravity and gravitational alternative for dark energy*, eConf **C0602061** (2006) 06, [hep-th/0601213].

[173] T.-j. Chen, M. Fasiello, E. A. Lim, and A. J. Tolley, *Higher derivative theories with constraints: Exorcising Ostrogradski's Ghost*, JCAP **1302** (2013) 042, [arXiv:1209.0583].

[174] A. Adams, N. Arkani-Hamed, S. Dubovsky, A. Nicolis, and R. Rattazzi, *Causality, analyticity and an IR obstruction to UV completion*, JHEP **0610** (2006) 014, [hep-th/0602178].

[175] J. Beltran Jimenez and A. L. Maroto, *The Dark Magnetism of the Universe*, Mod.Phys.Lett. **A26** (2011) 3025–3039, [arXiv:1112.1106].

[176] J. Beltran Jimenez and A. L. Maroto, *The electromagnetic dark sector*, Phys.Lett. **B686** (2010) 175–180, [arXiv:0903.4672].

[177] J. Beltran Jimenez and A. L. Maroto, *Cosmological electromagnetic fields and dark energy*, JCAP **0903** (2009) 016, [arXiv:0811.0566].

[178] J. Beltran Jimenez and A. L. Maroto, *Dark energy: The Absolute electric potential of the universe*, Int.J.Mod.Phys. **D18** (2009) 2243–2248, [arXiv:0905.2589].

[179] C. M. Bender and P. D. Mannheim, *No-ghost theorem for the fourth-order derivative Pais-Uhlenbeck oscillator model*, Phys.Rev.Lett. **100** (2008) 110402, [arXiv:0706.0207].

[180] P. D. Mannheim, *Solution to the ghost problem in fourth order derivative theories*, Found.Phys. **37** (2007) 532–571, [hep-th/0608154].

[181] A. Smilga, *Comments on the dynamics of the Pais-Uhlenbeck oscillator*, SIGMA **5** (2009) 017, [arXiv:0808.0139].

[182] A. V. Smilga, *Benign versus malicious ghosts in higher-derivative theories*, Nucl.Phys. **B706** (2005) 598–614, [hep-th/0407231].

[183] D. Robert and A. V. Smilga, *Supersymmetry vs ghosts*, J.Math.Phys. **49** (2008) 042104, [math-ph/0611023].

[184] P. A. Dirac, *Generalized Hamiltonian dynamics*, Can.J.Math. **2** (1950) 129–148.

[185] P. Dirac, Lectures on quantum mechanics,. Courier Dover Publications, 2001.

[186] C. M. Bender and P. D. Mannheim, *Exactly solvable PT-symmetric Hamiltonian having no Hermitian counterpart*, Phys.Rev. **D78** (2008) 025022, [arXiv:0804.4190].

[187] C. M. Bender and P. D. Mannheim, *Giving up the ghost*, J.Phys. **41** (2008) 304018, [arXiv:0807.2607].

[188] E. Stueckelberg, *Interaction energy in electrodynamics and in the field theory of nuclear forces*, Helv.Phys.Acta **11** (1938) 225–244.

[189] S. Weinberg, The Quantum theory of fields. Vol. 1: Foundations. Cambridge University Press, Cambridge U.K., 1995.

[190] C. M. Bender and H. F. Jones, *Interactions of Hermitian and non-Hermitian Hamiltonians*, J.Phys. **A41** (2008) 244006, [arXiv:0709.3605].

[191] C. Itzykson and J. Zuber, Quantum field theory. McGraw-Hill, New York U.S.A., 1980.

[192] D. Zwanziger, *Physical States in Quantum Electrodynamics*, Phys.Rev. **D14** (1976) 2570.

[193] A. Anisimov, E. Babichev, and A. Vikman, *B-inflation*, JCAP **0506** (2005) 006, [astro-ph/0504560].